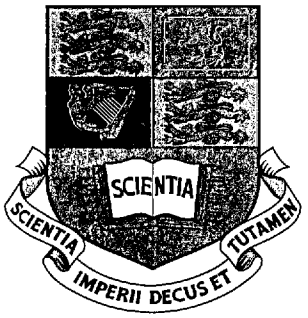
Imperial College
London



Crystal Structure and Defect Property Predictions in Ceramic Materials.

A dissertation submitted to the University of London for the degree of Doctor of Philosophy and the Diploma of Imperial College

by Mark R. Levy

Department of Materials

Imperial College of Science, Technology and Medicine

January 2005

Abstract

Atomic scale computer simulation techniques have been employed to predict the crystal structures and defect properties of ceramic materials. The techniques use energy minimization procedures to relax ion positions subject to interatomic forces. Application has been made to a number of related solid state systems.

Initial investigations were made of ABO_3 perovskite materials. Crystal structure predictions were an essential precursor to more in depth studies of the perovskite defect structures. The two cations A and B were restricted to being trivalent, and the anion to be oxygen; in total 96 separate compositions were studied. Structural changes between rhombohedral $R\bar{3}c$, orthorhombic Pnma, hexagonal $P6_3cm$ perovskite and cubic bixbyite Ia3 were correlated to cation radii via a two dimensional contour map.

Calculations of the internal energies for intrinsic defect formation were then undertaken over the extensive ABO_3 compositional range. These results were then compared to previous work on a series of pyrochlore materials. The motivation stemmed from a correlation that had been made between intrinsic defect formation and radiation tolerance in the pyrochlore materials. Using this same idea, the relative radiation tolerance between different ABO_3 compounds is proposed and the relative radiation tolerance compared to pyrochlores is discussed. It was found that

of the compositions under consideration, only the Ia3 bixbyite materials could be as tolerant as the pyrochlore materials.

Maintaining the theme of energy systems, the suitability of a subset of the perovskite oxides was assessed for their application as solid oxide fuel cell components. This required a consideration of the defect behaviour of these materials when aliovalently doped. Thus an investigation into the possible compensation mechanisms operating when a range of divalent cations are substituted into the materials was carried out. The lowest energy solution mechanisms involved charge compensation via oxygen vacancies and the specific solution site was dependent on both the crystal structure of the perovskite and the size of the divalent ion.

The dielectric behaviour of lithium doped zinc fluoride was also investigated. Previously it had been determined experimentally that lithium doping of zinc fluoride results in an anisotropic dielectric relaxation. The mechanism has been unresolved since the early 1970s, however, through atomistic simulations it has been possible to develop a defect model that is able to describe this anisotropy. A new defect model involving a split lithium interstitial defect cluster formation is proposed.

The different solid state issues addressed by this thesis are linked through a central theme which emphasises the importance of atomic scale defect processes in inorganic materials, and their interaction with different crystal structures.

Copyright

The copyright of this thesis rests with the author and no quotation from it or information derived from it may be published without prior written consent of the author.

© Mark R. Levy 2005

Acknowledgements

I would like to acknowledge EPSRC for my studentship and also John Maguire of the United States Air Force for my case award which was made available through EOARD contract No. F61775-01-WW064. David Iddles and Cannell of Filtronic Comtek for their continued interest and funding.

Kurt Sickafus and James Valdez, of Los Alamos National Laboratory, are greatly thanked for their experimental investigations into the radiation tolerance of ceramic materials. I am indebted to them for many useful discussions and also financial assistance which enabled me to visit them at LANL. Also at LANL I would like to acknowledge conversations with Ken Mclellan and for allowing me to stay over, take me skiing on the last day of the season, getting me drunk in several states Chris Stanek. Thanks are also extended to Alan Atkinson for supervision.

Ahead of all others I must thank Robin for the guidance, discussion, frequent moments of madness, and inspiration that keep us all sane and more importantly for putting up with me!

My deepest thanks go to KJWA for his invaluable help, discussing my work and the more important life issues such as beer. On a similar note, I should also thank all those that help me with computing issues when I felt completely overwhelmed; Kurt,

Gerdjan, Michael and Alex (who also seems to find my work far more interesting than his own).

For telling me that I am a fool when discussing the finer points of a topic I point to Jon. Thanks are also extended to all others in the group; Alex, Antony, Averyl, Kaajal and Nick and those that are almost in the group simply for being around so much, thanks Seema! I should also thank Rachel for being an escape from the world of computer simulation.

I also thank my family for their continued support both financial and mental, without them I would not be here today. Finally I would like to thank someone that has kept my spirits up when I felt down, made me feel happy when sad, and most importantly is able to put up with my bizarre ravings ... Cindy I thank you from the bottom of my heart.

Contents

Abstract 4

Copyright 5

Acknowledgements 7

Table of Contents 10

List of Tables 13

List of Figures 17

1 Introduction **22**

2 Methodology **25**

2.1 Introduction 25

2.2 Crystal Data 27

2.3 The Perfect Lattice 30

2.3.1 The Long Range Interaction: The Ewald Summation 32

2.3.2 The Short Range Interaction 37

2.3.3 Electronic Polarisability 44

2.3.4 Cauchy Violation 45

2.3.5 Potential Parameters: Fitting 46

2.3.6 Potential Model Variation 51

2.4 The Defective Lattice 63

2.5 Energy Minimization 67
2.6 Ion Migration Activation Energies 69
2.7 Quantum Mechanical Calculations 71
2.7.1 General Considerations 71
2.7.2 The Hartree-Fock approach 74
2.7.3 Density Functional Theory 74
2.8 Simulation Codes 76
2.9 Contour Plots 77

3 Perovskite Perfect Lattice **79**
3.1 Perovskite Compositions 79
3.2 Crystallography of The Perovskite Structure 80
3.3 Crystal Structure Predictions 88
3.4 Dissociation to Garnet 97
3.5 Discontinuity in the Dielectric Constant 108
3.6 Potential Fitting Improvements 110
3.7 Quantum Mechanical Structure Predictions 112

4 Disorder processes in $A^{3+}B^{3+}O_3$ compounds: implications for radiation tolerance. **115**
4.1 Introduction 115
4.1.1 Motivation 115
4.1.2 Radioactive Waste 116
4.1.3 Crystallography 128
4.2 Results and Discussion 130
4.2.1 Disorder Processes 130
4.2.2 Comparing Defect Processes 139

4.2.3 Implications for Radiation Tolerance 141
4.2.4 Comparison to Pyrochlore/Fluorite 142
4.3 Conclusion 144

5 Extrinsic Defect Reactions in Perovskite Materials 148
5.1 Introduction 148
5.2 Defect Equilibria 152
5.3 Results and Discussion 155
5.4 Conclusions 166

6 Dielectric relaxation of lithium doped ZnF_2 168
6.1 Introduction 168
6.1.1 Dielectric Relaxation of lithium doped ZnF_2 169
6.2 Results for Undoped ZnF_2 174
6.3 Solution mechanisms for LiF doped ZnF_2 175
6.4 Discussion on the Dielectric Relaxation 186

7 Conclusions 190
7.1 Crystal Structure Predictions for Perovskites 190
7.2 Intrinsic Defect Processes in Perovskites: Implications for Radiation Tolerance 191
7.3 Extrinsic Defect Processes in Perovskites 193
7.4 Lithium doped Zinc Fluoride 194

8 Further Work 195
8.1 Simulation Studies 195
8.2 Experimental Studies 200

Bibliography 203

A Thermodynamics and Normalisation **232**

A.1 Reaction Equilibria 232

A.2 Thermodynamic Approximations 234

A.3 Normalisation Factor Worked Examples 235

A.3.1 Schottky Defect Process 235

A.3.2 Anion Frenkel disorder and extrinsic defects in ZnF_2 237

B Presentations and Publications **240**

List of Tables

2.1 12 co-ordinate effective cation radii. 29

2.2 6 co-ordinate effective cation radii. 29

2.3 $C_{6,ij}$ term determination for the A site cations 41

2.4 $C_{6,ij}$ term determination for the B site cations 42

2.5 The percentage agreement with experimental unit cell volumes for the compounds used for the derivation of the cation - anion potentials. 50

2.6 Short-range potential parameters used for perovskite materials. 52

2.7 Short-range potential parameters used for fluoride materials. 52

2.8 Shell Parameter for O^{2-} 53

2.9 Short-range potential parameters used for perovskite materials based on the site dependent $C_{6,ij}$ term. 54

2.10 Comparison between the effective radius and co-ordinate specific radius $C_{6,ij}$ value (eVÅ^6). 55

2.11 Comparison between the Binks [1] and Catlow O^{2-}-O^{2-} potentials. . 56

2.12 Short-range potential parameters used for perovskite materials based on the double exponential oxygen term. 56

2.13 Damped coulombic model parameters for input into the general potential for GULP. 60

2.14 Short-range potential parameters used for perovskite materials based on the damped coulombic model. 60
2.15 Cation shell parameters 62
2.16 Short-range potential parameters used for perovskite materials with cation shells. 63

3.1 Atomistic positions in cubic perovskites. 81
3.2 Atomistic positions in orthorhombic perovskites. 83
3.3 Atomic positions for rhombohedral perovskites. 84
3.4 Atomic positions for hexagonal perovskites. 85
3.5 Atomic positions for cubic bixbyite. 86
3.6 Experimentally determined cubic perovskites. 88
3.7 Experimentally determined orthorhombic perovskites. 89
3.8 Experimentally determined rhombohedral perovskites. 91
3.9 Atomic positions for cubic ($Ia\bar{3}d$) garnet 97
3.10 Atomic positions for monoclinic ($P2_1/c$) garnet 99
3.11 Quantum mechanically calculated lattice energies for a subset of perovskite compositions. 113

4.1 Atomic positions for pyrochlore oxides. 130
4.2 The position of the oxygen interstitial defect as used in the oxygen Frenkel reaction 131
4.3 Comparison of the total defect energies for isolated defects and clusters $\{A_B^X : B_A^X\}^X$ for different compositions of perovskite and pyrochlore oxides. 143

5.1 VIII coordinate effective cation radii for the divalent dopant ions. . . 155

6.1 Comparison of calculated and experimental lattice parameters for ZnF_2. 174

6.2 Calculated and experimental elastic constants for ZnF_2. 174

6.3 Normalised, intrinsic defect process energies for ZnF_2. 175

6.4 Solution and cluster binding energies for Li^+ accommodation in ZnF_2. 177

6.5 $\{Li_i^{\bullet} : V_{Zn}'' : Li_i^{\bullet}\}$ cluster energies (eV). 186

List of Figures

2.1 Comparison of predicted and ionic radii with those of Shannon. . . . 28

2.2 The long and short range interactions of the total forces 30

2.3 The development of ψ_1 component of the Ewald summation. 34

2.4 Graphical representation of ψ_2 of the Ewald summation. 34

2.5 The form of the Buckingham Potential for O^{2-}-O^{2-} interaction illustrating how the energy tends to minus infinity as the ion separation tends to zero. 43

2.6 A schematic of the shell model. 45

2.7 The smooth change in ion radius due to the lanthanide contraction allows for an imposed order onto the potential parameters (a) A_{ij}, (b) ρ_{ij} and (c) $C_{6,ij}$. 49

2.8 (a) Comparison between the O^{2-}-O^{2-} potentials from Binks [1], Catlow [2] and the double exponential model; (b) modification of the Al^{3+}-O^{2-} interaction energy. 57

2.9 Comparison of the effective co-ordination and damped coulombic potentials for the La^{3+}-O^{2-} interaction. 61

2.10 Representation of the Multi Region Approach 64

2.11 Defect energy variations with changing region size for an antisite defect, A_B^X. 65

2.12 Example ion migration plot. 70
2.13 Schematic of ion migration calculations in ZnF_2. 70
2.14 Migration energy contour plot for ion migration in ZnF_2 71
2.15 Example contour map used to display results presented in this thesis. 78

3.1 Schematic of compositions under study. 80
3.2 Cubic perovskite unit cell 81
3.3 Pnma, orthorhombic perovskite unit cell 83
3.4 $R\bar{3}c$ rhombohedral perovskite unit cell 84
3.5 $P6_3cm$ hexagonal perovskite unit cell 85
3.6 Bixbyite unit cell 86
3.7 Perovskite distortion from cubic to orthorhombic 87
3.8 Lattice Energy Contour Map. 92
3.9 Classical Tolerance Factor variations as a function of cation radii. . . 94
3.10 Comparison between experimental crystal structures and crystal structure predictions. 95
3.11 Comparison between experimentally determined and predicted unit cell volumes. 96
3.12 Garnet ($Ia\bar{3}d$) unit cell. 98
3.13 Garnet ($P2_1/c$) unit cell. 98
3.14 Phase diagrams for the Al_2O_3 - RE_2O_3 system. 100
3.15 Phase diagrams for the Cr_2O_3 - RE_2O_3 system. 101
3.16 Phase diagrams for the Ga_2O_3 - RE_2O_3 system. 103
3.17 Phase diagrams for the Fe_2O_3 - RE_2O_3 system. 104
3.18 Phase diagrams for the Sc_2O_3 - RE_2O_3 system. 105
3.19 Phase diagrams for the In_2O_3 - RE_2O_3 system. 106
3.20 Summary of the compositions which form garnets. 107

3.21 Experimentally determined high frequency dielectric constant for rare earth aluminate perovskites 109
3.22 Static dielectric constant predictions for the $A^{3+}B^{3+}O_3$ compounds. . 110
3.23 High frequency dielectric constant predictions for the $A^{3+}B^{3+}O_3$ compounds. 111

4.1 Full unit cell of pyrochlore oxide 129
4.2 Schottky reaction energy contour map. 132
4.3 Oxygen Frenkel reaction energy contour map. 134
4.4 A^{3+} cation Frenkel reaction energy contour map. 135
4.5 B^{3+} cation Frenkel reaction energy contour map. 136
4.6 Antisite reaction energy contour map. 138

5.1 Schematic of a solid oxide fuel cell. 150
5.2 Divalent cation solution into $LaScO_3$. 156
5.3 Divalent cation solution into $LaInO_3$. 157
5.4 Divalent cation solution into $GdScO_3$. 158
5.5 Divalent cation solution into $GdInO_3$. 159
5.6 Lowest energy mechanisms for divalent cation solution into $LaScO_3$. . 161
5.7 Lowest energy mechanisms for divalent cation solution into $LaInO_3$. . 162
5.8 Lowest energy mechanisms for divalent cation solution into $GdScO_3$. . 163
5.9 Lowest energy mechanisms for divalent cation solution into $GdInO_3$. . 164

6.1 The ZnF_2 tetragonal unit cell. The orange spheres represent fluorine ions and the brown spheres represent zinc ions. 169
6.2 Basal plane of ZnF_2 showing the configuration of the split interstitial fluorine cluster. 172
6.3 The three disorder mechanisms for Li doped ZnF_2 173

6.4 Isolated Interstitial Li^+ migration in the [001]. The line indicates the lowest energy pathway. 180

6.5 Isolated Interstitial Li^+ migration in the ab plane. The line indicates the lowest energy pathway. 181

6.6 Isolated Substitutional Li^+ migration in the ab plane. The line indicates the lowest energy pathway. 183

6.7 Isolated substitutional Li^+ migration in the ac plane. The line indicates the lowest energy pathway. 184

6.8 Li^+ migration in the ab plane starting from the split defect orientation. The line indicates the lowest energy pathway. 185

6.9 The tetragonal ZnF_2 unit cell showing the three different unrelaxed neighbour positions of the Li^+ interstitial defect. 188

8.1 Proposed extension to the crystallographic space modelled. 197

Abbreviations, Symbols and nomenclature

List of Abbreviations

Abbreviation	Full Meaning
ANSTO	Australian Nuclear Science and Technology Organization
BPEO	Best Practicable Environmental Option
DFT	Density Functional Theory
DoE	United States Department of Energy
EPA	Environmental Protection Agency
GGA	Generalised Gradient Approximation
HADES	Harwell Automatic Defect Examination System code
HF	Hartree-Fock
HLW	High Level Waste
ILW	Intermediate Level Waste
IT-SOFC	Intermediate Temperature SOFC
LDA	Local Density Approximation
LLW	Low Level Waste
MC	Monte Carlo
MCFC	Molten Carbonate Fuel Cell
MD	Molecular Dynamics
MINATOM	Russian Ministry for Atomic Energy
NRC	Nuclear Regulatory Commission

Abbreviation	Full Meaning
PAFC	Phosphoric Acid Fuel Cell
PEMFC	Proton Exchange Fuel Cell
SOFC	Solid Oxide Fuel Cell
US	United States
UK	United Kingdom
VLLW	Very Low Level Waste
WIPP	Waste Isolation Pilot Plant
YAG	Cubic Yttrium Aluminium Garnet
YAM	Monoclinic Yttrium Aluminium Garnet
YAP	Yttrium Aluminium Perovskite
QMD	Quantum Molecular Dynamics

List of Symbols

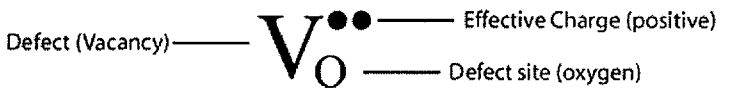
Symbol	Meaning
Å	Angstrom
Bq	Becquerel
Cm	Coulomb meter
N	Newton
m	meter
ppm	parts per million
K	Kelvin
eV	electron volt
ΔH_F	Enthalpy of Formation
t	tolerance factor
R_A	A cation radius
R_B	B cation radius
R_O	Oxygen anion radius
α_D	Dielectric Polarisability
[]	Miller notation for a direction
<>	Miller notation for a family of directions
()	Miller notation for a plane
{}	Miller notation for a family of planes

Kröger-Vink Nomenclature

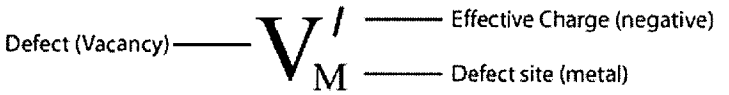
Kröger and Vink proposed a nomenclature to describe defect chemical reactions [3]. The point defects are assumed to be dilute species, with the solid being the solvent. The nomenclature has three constituents; the body, the superscript and the subscript. The body represents the chemistry of the defect itself, ie. V for a vacancy or Mg for a magnesium ion. The superscript represents the effective charge of the defect relative to the perfect lattice; an effective positive charge is represented by a dot ($^{\bullet}$), a negative charge by a prime ($'$). The subscript represents the site of

the defect, eg. $_i$ indicates a defect at an interstitial site, $_{Mg}$ represents a magnesium lattice site.

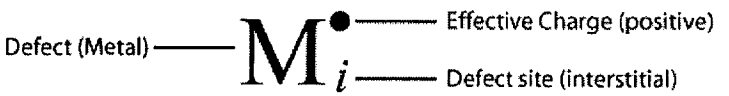
Assuming a binary metal oxide (MO_2), using Kröger-Vink nomenclature, an oxygen vacancy is:



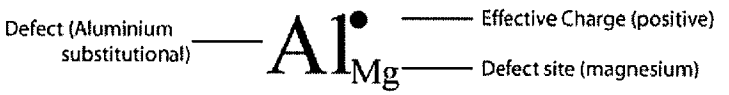
a metal vacancy is:



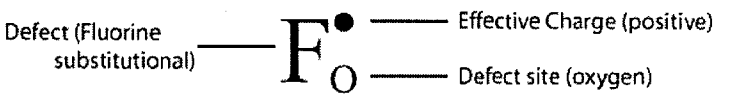
a metal interstitial is:



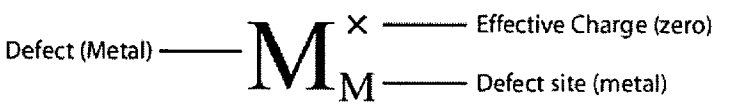
a cation substitutional is:



an anion substitutional is:



and a metal ion on its lattice site is:



Chapter 1

Introduction

Atomic scale computer simulation techniques have been used to predict the crystal structure and defect properties of a series of ceramic materials. The techniques incorporate energy minimization and equivalent procedures to relax ion positions subject to interatomic forces. Application has been made to a number of related solid state systems.

Initial investigation was made to the crystal structure of perovskite materials. Crystal structure predictions are an essential precursor to a more in depth study of the perovskite compounds. Since there is a multitude of compositions that are possible when one considers that the A cations are able to adopt 1+, 2+ and 3+ valence states, B cations are able to adopt 5+, 4+ and 3+ valence states, and the anion need not be oxygen, some limitations need to be imposed to make a viable study. Here, the two cations were restricted to being trivalent, and the anion to be oxygen, further to this, the large A cation was limited to be a rare earth ion. Once structural determinations were made, further work was conducted on more application specific

considerations.

The problem of adequately dealing with High-Level Nuclear waste (HLW) is escalating, and pressure from environmental organisations is increasing the importance of the issue on the global political scene. Previous studies [4, 5] that considered pyrochlore ceramics as possible encapsulation materials have shown that assessing the structural stability of complex oxides is a suitable method in determining the applicability for HLW storage. Here, perovskites were investigated using a similar approach. That is, atomistic computer modelling techniques have been employed to examine several possible candidate materials. As such, the radiation damage of an extensive range of perovskite oxides were investigated for their suitability to be incorporated in nuclear waste forms via a consideration of the intrinsic defect processes. These results were then compared to the previous work on a series of pyrochlore materials. This leads to a series of propositions concerning the relative radiation tolerance of perovskite to pyrochlore oxides.

With dwindling fossil fuel reserves and increasing awareness of global warming attention is being directed towards renewable and non-polluting energy systems. The Kyoto protocol was created to set targets for industrialised nations to cut their greenhouse gas emissions. As part of this drive for a non-polluting, energy efficient system, solid oxide fuel cells (SOFCs) are being rigorously investigated. Maintaining the energy theme, the suitability of a subset of the perovskite oxides was assessed for their application to solid oxide fuel cell (SOFC) components. This required consideration of the defect behaviour of the materials when doped and an investigation into the compensation mechanisms operating when divalent cations were introduced into the materials.

The same approach used for the perovskite materials has then been translated to

the dielectric behaviour of doped zinc fluoride. The lithium doping of zinc fluoride has been shown experimentally to exhibit an anisotropic dielectric relaxation. The mechanism of this was previously a matter of contention, however, through atomistic simulations it has been possible to develop a defect model that is able to describe this anisotropy.

This thesis encompasses a variety of different solid state issues, all linked through a central theme which emphasises the importance of atomic scale defect processes in inorganic materials, and their interaction with different crystal structures. The structure of this thesis allows each issue to be viewed as a separate, self-contained chapter, incorporating a literature review, a presentation of the results obtained from simulation studies, and a critical discussion with summary conclusions.

This Introduction (Chapter 1) sets the scene for the thesis by establishing the themes, aims and objectives of the research, and describes the layout of the following chapters. The methodology used throughout the research is detailed in Chapter 2, preceding four self-contained chapters concerning pertinent solid state issues. Firstly, the perfect lattice is presented and discussed in Chapter 3, followed by the questioning of the suitability of perovskites as radioactive hosts in Chapter 4. Chapter 5 discusses extrinsic defect reactions and the application of perovskites to SOFC technology, while Chapter 6 investigates the anisotropic dielectric behaviour of lithium doped zinc fluoride. All issues are brought together in Chapter 7 for further discussion and conclusions and suggestions for areas of further work are given in Chapter 8. Finally, Appendix A details the thermodynamic approximations inherent in the mass action method.

Chapter 2

Methodology

2.1 Introduction

Over the past twenty years, one of the major developments in the physical and biological sciences is the use of computer modelling. For example, impressive achievements have been made in molecular biology [6,7], protein science [8], polymer science [9,10], physical chemistry [11], liquid crystals [12, 13] and solid-state materials [14, 15]. Previously, computer modelling has been concerned with reproducing experimental data; in essence it has been trying to prove itself. However, it is increasingly becoming a predictive tool, and is moving towards more realistic and accurate predictions of complex systems [16]. Much of this advancement is a consequence of the rapid increase in computational resources available, which is illustrated by the continued increase in the number density of transistors incorporated on an integrated circuit, still in accordance Moore's Law [17].

The modelling methodologies, which are used within the field of solid-state physics,

fall into two categories, those that rely upon the use of a simple description of interatomic forces, and those that take a quantum mechanical approach by solving Schrödinger's equation [14]. Interatomic potentials are numerical functions that attempt to describe the variation in energy of an atomic or ionic interaction as a function of separation. Such potentials can be used to perform either static [14, 18] or dynamic calculations.

This thesis utilises static-lattice calculations, and these are described in more depth later. Molecular dynamics (MD) calculations are methods that allow the crystal lattice to vibrate, where this vibration is described by Newtonian laws [14]. One popular method for quantum molecular dynamic (QMD) calculations is based on the Car-Parrinello approximation [19] and use Density Functional Theory (see Section 2.7) to calculate the energy of the system, and thus, the interatomic forces. Monte Carlo (MC) methods have their basis in statistical physics and make changes to the system by randomly swapping components and then deciding whether to accept or reject the change via a set of rules. MC can be used in conjunction with energy minimization to evolve structures by swapping ions within a lattice in a random fashion and decision criterion is the evaluation of the energy via energy minimization, this is then compared to the previous result [20].

Molecular dynamics calculations are more computationally intensive than the static-lattice approach. They are limited by the very short time-scales they can predict (typically nanoseconds). The timestep between calculations must be on a scale smaller than the characteristic time of any important process in the system (e.g. an atomic vibration), hence a value of the order of 10^{-15} s is typically used [14]. A technique recently proposed by Voter [21] may help to resolve this timescale problem by running the simulation at elevated temperatures in order to accelerate the system

dynamics. The electronic structure calculations that attempt to solve Schrödinger's equation are even more computationally expensive. They are however, considered less reliant on empirical approximations and so may yield more accurate results. One important role of highly accurate quantum mechanical calculation is in determining reliable parameters for interatomic potentials [16].

The calculations presented in this study employ predominantly the static-lattice, energy minimization approach whilst some use a quantum mechanical approach. The minimum energy configuration is determined by an iterative relaxation of the atom positions with respect to the forces acting on them.

Static-lattice simulations are very versatile and have been extended to a wide range of applications and provide a good working description of many important properties of ionic crystals [18, 22–28]. Nevertheless they do have limitations in their scope, for example, they are unable to model any property that depends explicitly on electronic structure. They can, however, model charged defects, from which an electronic defect can be inferred [14], for example, a lattice ion can be ionized (a hole) or can assume an extra charge (a small polaron or localized electron).

2.2 Crystal Data

Initial crystallographic data were obtained by a search of research literature using the Inorganic Crystal Structure Data file (ICSD), which is part of the Chemical Data Service at Daresbury [29]. These data are presented in Tables 3.6, 3.7, and 3.8.

Effective ionic radii were taken from Shannon [30]. The 12 co-ordinate effective radii

were not available for all ions, thus for these the radii were calculated by fitting a function to the changes in ionic radius as the co-ordination increased from 6 to 8 and then applying this to the increase from 8 to 12. Predictions were then validated against known 12 coordinate radii. The ionic radii used for this work are given in Tables 2.1 and 2.2 and the relationship between 8 and 12 coordinated ionic radii is shown in Figure 2.1 where it can be seen that there is good correlation between the predicted and experimental ionic radii.

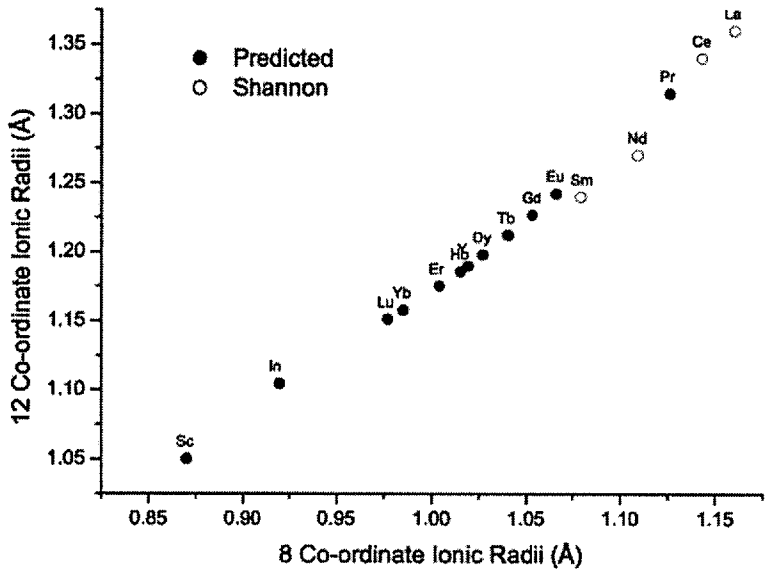


Figure 2.1: Comparison of predicted and ionic radii with those of Shannon.

Table 2.1: 12 co-ordinate effective cation radii.

Cation	Effective ionic radius Å
Sc^{3+}	1.0503
In^{3+}	1.1044
Lu^{3+}	1.1509
Yb^{3+}	1.1578
Er^{3+}	1.175
Ho^{3+}	1.1857
Y^{3+}	1.1897
Dy^{3+}	1.198
Tb^{3+}	1.2122
Gd^{3+}	1.227
Eu^{3+}	1.2424
Sm^{3+}	1.24*
Nd^{3+}	1.27*
Pr^{3+}	1.3147
Ce^{3+}	1.34*
La^{3+}	1.36*

* Ionic Radii from Shannon [30].

Table 2.2: 6 co-ordinate effective cation radii [30].

Cation	Effective ionic radius Å
Al^{3+}	0.535
Cr^{3+}	0.615
Ga^{3+}	0.62
Fe^{3+}	0.645
Sc^{3+}	0.745
In^{3+}	0.8

2.3 The Perfect Lattice

Static lattice calculations are based on the classical Born model [31, 32] of ionic solids in which the lattice is constructed from an arrangement of spherical, charged ions. A pair-potential description of the forces between ions is used [18], in which the interaction energy between the ions is a function of their separation (and hence atomic position). These forces can be resolved into two components (Figure 2.2): (i) long-range Coulombic interactions and (ii) short-range interactions.

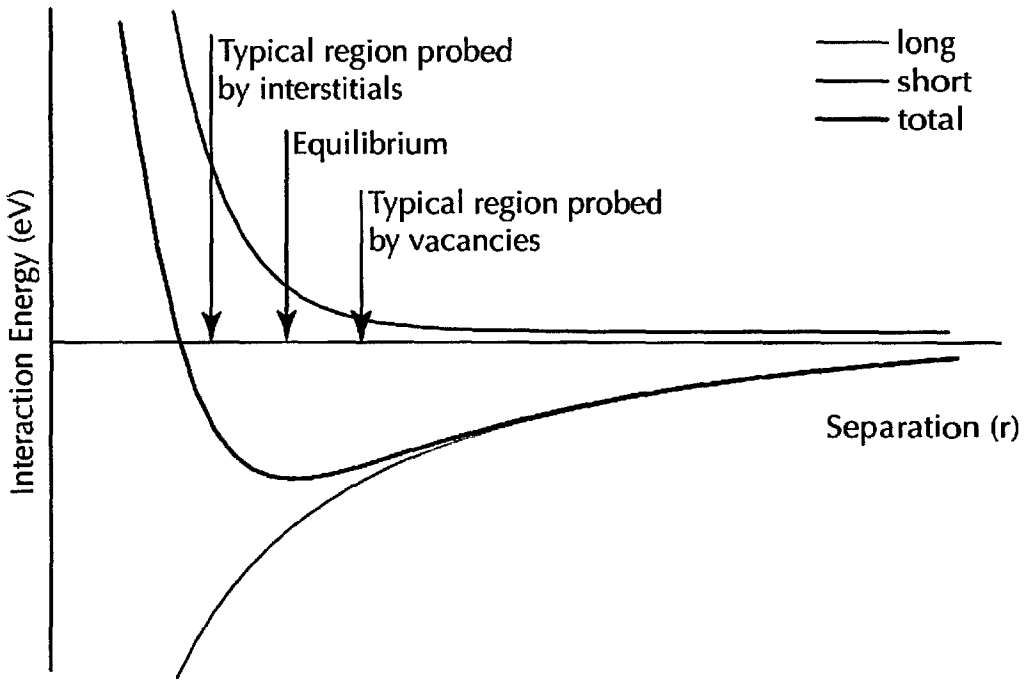


Figure 2.2: The long and short range interactions of the total forces (adapted from Harding [33]).

Since there are many atoms interacting with each other within the lattice, the total interaction can be expressed as a series summation, with increasing numbers of ions such that:

$$\Phi = \Phi_0 + \sum_{ij} \Phi_2(r_{ij}) + \sum_{ijk} \Phi_3(r_{ijk}) + \sum_{ijkl} \Phi_4(r_{ijkl}) + \ldots \tag{2.1}$$

In this sum, Φ_0 is a function of the local environment, and is traditionally ignored since it is differences in energies that are usually of importance, i.e. it defines the energy zero. $\Phi_2(r_{ij})$ is the interaction acting over ion pairs, $\Phi_3(r_{ijk})$ is the interaction acting over ion triplets etc. For ionic materials, the pair interactions are usually assumed to be dominant and all higher interactions are considered to be negligible [33]. Consequently we only include the two body $\Phi_2(r_{ij})$ terms and choose to ignore three body $\Phi_3(r_{ijk})$ and higher terms explicitly. This is the *pair potential approximation* [33]. The total energy (E_T) for the interaction between two ions (i and j) takes the form [34]:

$$E_T = \frac{q_i q_j}{4\pi\epsilon_0 r_{ij}} + \phi_{sr} \tag{2.2}$$

where the first term represents the long range Coulombic interaction; q_i, q_j are the charge on ions i and j; r_{ij} is the ionic separation; and ϵ_0 is the permittivity of free space. The second term, ϕ_{sr}, is the short-range interaction energy (described in Section 2.3.2). All interactions in a lattice can be summed to give the total lattice energy (E_L):

$$E_L = \sum_{j>i} \sum_{i} \left(\frac{q_i q_j}{4\pi\epsilon_0 r_{ij}} + \phi_{sr} \right) \tag{2.3}$$

2.3.1 The Long Range Interaction: The Ewald Summation

A significant computational problem exists in the summation of the long range Coulombic forces. The issue is that these forces typically fall off as r^{-d}, where d is the system dimensionality [35, 36]. It therefore proves very difficult to sum the forces to determine the true interaction energy of the system. Consequently, a new mathematical approach was needed to facilitate the summation: the first such method was provided by crystallographer Paul Ewald in 1921 [37].

The Ewald summation technique was derived to calculate the electrostatic interaction between one ion and all remaining ions in the crystal lattice. The formal mathematical derivation is rather complex and a detailed explanation is beyond the scope of this thesis. Therefore, the following section describes the important aspects of the summation method; a similar abridged derivation can be found in early editions of Kittel's book, Introduction to Solid State Physics [38], and is attibuted to an unpublished paper by Ewald and Shockley. Later editions of Kittel's book (e.g. [39]) introduce a structure factor into the derivation for the case where the unit cell contains more that one ion. A third good derivation is given by Tosi [40].

In deriving the Ewald sum, an assumption is made that the lattice is constructed of spherical ions with charges of the same magnitude (whether positive or negative) and that they do not overlap. With this in mind, the total potential, ψ, experienced at a specific reference lattice point, $\vec{r}$, can be partitioned into two distinct, but related components, one in reciprocal space, ψ_1 (Figure 2.3), and one in real space, ψ_2 (Figure 2.4).

$$\psi = \psi_1 + \psi_2 \tag{2.4}$$

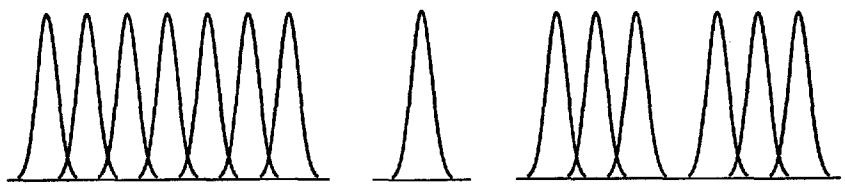
The potential ψ_1 is that of a lattice with a Gaussian distribution of charges fixed at each lattice point with the same signs as the ions occupying those lattice points in the real crystal. The potential ψ_2 is that of a lattice of point charges, with the addition of a Gaussian distribution of opposite sign superimposed upon the point charges. The reason for the splitting of the potential into two components, is that by choosing a suitable parameter, η, for the width of the Gaussian peaks, both parts can be made to converge rapidly at the same time. A highly optimal value for this width parameter has been determined by Catlow and Norgett [41] and is given by:

$$\eta = \left(\frac{N\pi^3}{V_c^2}\right)^{\frac{1}{6}} \tag{2.5}$$

where N is the total number of species and V_c is the unit cell volume. When the two component potentials are summed, the overall potential reduces to the original set of point charges, i.e. Gaussian distributions cancel, and the overall potential is independent of parameters, such as the width parameter, used during the convergence of the components ψ_1 and ψ_2.

The definition of the Madelung constant mandates that the charge distribution on the reference point is not considered to contribute to the potentials ψ_1 or ψ_2, i.e. ions cannot experience their own electrostatic potential as illustrated in Figure 2.3. It follows that the potential ψ_1 can be described as the difference between two potentials, ψ_a, being the potential of a continuous series of Gaussian distributions and ψ_b, being the potential of the single Gaussian distribution of the reference point.

$$\psi_1 = \psi_a - \psi_b \tag{2.6}$$



(a) ψ_a (b) ψ_b (c) $\psi_1 = \psi_a - \psi_b$

Figure 2.3: The development of the potential as a consequence of the definition of the Madelung constant, from a lattice of Gaussian distributions and a Gaussian charge distribution at the reference point.

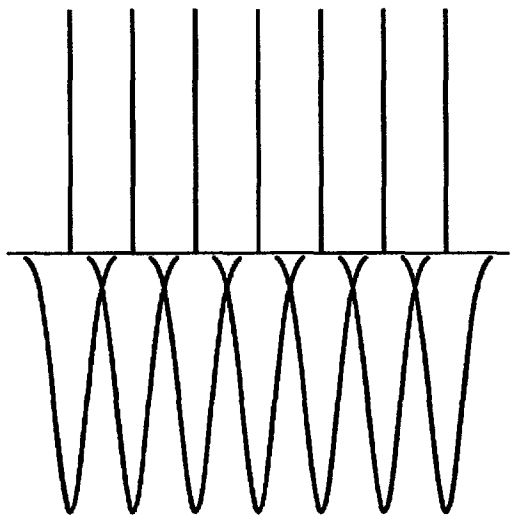


Figure 2.4: Graphical representation of ψ_2 of the Ewald summation.

In order to calculate the potential of the continuous Gaussian distribution, ψ_a, it and its associated charge density, ρ, are expanded in terms of a Fourier series:

$$\psi_a = \sum_k c_k \exp(i(\vec{k} \cdot \vec{r})) \tag{2.7}$$

$$\rho = \sum_k \rho_k \exp(i(\vec{k} \cdot \vec{r})) \tag{2.8}$$

where c_k and ρ_k are coefficients and $\vec{k}$ is 2π times the reciprocal lattice vectors. The series converges with increasing $\vec{k}$ and decreasing c_k and ρ_k. The charge density is related to the electrostatic potential via the Poisson equation [35]:

$$\nabla^2 \psi_a = -4\pi\rho \tag{2.9}$$

so that

$$\rho_k = \frac{c_k k^2}{4\pi} \tag{2.10}$$

The Gaussian charge density for a single ion of charge q_i with half width $\sqrt{\frac{ln2}{\eta}}$ is:

$$\rho = q_i \left(\frac{\eta}{\pi}\right)^{\frac{3}{2}} \exp(-\eta \vec{r}^2) \tag{2.11}$$

It is possible to evaluate the charge density, ρ_k, by multiplying both sides of Equations (2.8) and (2.11) by $e^{-i\vec{k}\cdot\vec{r}}$, and integrating (2.8) over the unit cell volume, V_c, and (2.11) over the whole crystal. These two integrations should result in identical charge densities, so that:

$$\int_{V_\infty} q_i \left(\frac{\eta}{\pi}\right)^{\frac{3}{2}} \exp(-\eta \vec{r}^2) \exp(-i\vec{k} \cdot \vec{r}) dr = \rho_k \int_{V_c} \exp(i\vec{k} \cdot \vec{r}) \exp(-i\vec{k} \cdot \vec{r}) d\vec{r} = V_c \rho_k \tag{2.12}$$

Integrating over the unit cell results in a charge distribution that originates from both the lattice point within the cell, and the tails of the distributions from all other lattice points.

It is then possible by considering Equations (2.7) and (2.10) and combining with the above result to derive,

$$\psi_a = \sum_k \frac{4\pi}{k^2 V_c} \int \left(\frac{\eta}{\pi}\right)^{\frac{3}{2}} \exp(i\vec{k}\cdot\vec{r}) \exp(-\eta r^2) \exp(-i\vec{k}\cdot\vec{r}) d\vec{r} \tag{2.13}$$

which can be integrated to yield

$$\psi_a = \frac{4\pi}{V_c} \sum_k \frac{\exp(i\vec{k}\cdot\vec{r} - \frac{k^2}{4\eta})}{k^2} \tag{2.14}$$

When $\vec{k} = 0$, the potential ψ_a tends to infinity. However, since it is assumed that the overall charge of a neutral unit cell is zero, this term can be ignored.

The potential at the reference point in the lattice, (i.e. at $\vec{r} = 0$) is ψ_b; the contribution of this to the field is due to the central Gaussian distribution:

$$\psi_b = \int_0^\infty \frac{1}{\epsilon_0} r^2 \frac{\rho}{\vec{r}} d\vec{r} = \frac{1}{2\epsilon_0} q_i \frac{\eta^{\frac{1}{2}}}{\pi^{\frac{3}{2}}} \tag{2.15}$$

Therefore, combining Equations (2.14) and (2.15) it is possible to obtain an expression for ψ_1:

$$\psi_1 = \frac{4\pi}{V_c} \sum_k \frac{\exp(i\vec{k}\cdot\vec{r} - \frac{k^2}{4\eta})}{k^2} - \frac{1}{2\epsilon_0} q_i \frac{\eta^{\frac{1}{2}}}{\pi^{\frac{3}{2}}} \tag{2.16}$$

The remaining contribution to the net potential, ψ_2, must now be evaluated at the reference point, this is non zero since it has a contribution due to the tails of the Gaussian distributions from the other lattice points overlapping the reference point. The potential has three contributions from each lattice point: the point charge associated with the ion j, the Gaussian distribution contained within the sphere of radius r_{ij} at the j lattice point and the Gaussian distribution occurring outside the same sphere.

$$\psi_2 = \frac{1}{4\pi\epsilon_0}\sum_j q_j \left[\frac{1}{r_j} - \frac{1}{r_j}\int_0^{r_j} \rho d\vec{r} - \int_{r_j}^{\infty} \frac{\rho}{\vec{r}} d\vec{r}\right] = \frac{1}{4\pi\epsilon_0}\sum_j \frac{q_j}{r_j}\mathrm{erfc}(\eta^{\frac{1}{2}} r_j) \quad (2.17)$$

Now, with expressions for ψ_1 and ψ_2 determined, it is possible to expand Equation (2.4) by combining Equations (2.16) and (2.17):

$$\psi = \frac{4\pi}{V_c}\sum_k \frac{\exp(i\vec{k}\cdot\vec{r} - \frac{k^2}{4\eta})}{k^2} - \frac{1}{2\epsilon_0} q_i \frac{\eta^{\frac{1}{2}}}{\pi^{\frac{3}{2}}} + \frac{1}{4\pi\epsilon_0}\sum_j \frac{q_j}{r_j}\mathrm{erfc}(\eta^{\frac{1}{2}} r_j) \quad (2.18)$$

2.3.2 The Short Range Interaction

The short-range interaction energy has both repulsive and attractive components. The repulsive interactions occur due to an increase in nuclear repulsion through electron cloud overlap between the ions as they approach; this only acts over small separations. The attractive force operates over intermediate distances and results from the formation of instantaneous dipoles between the ions (one type of the van der Waals interaction). The magnitude of the attractive force is determined by the charges on the ions.

In theory, there should not be a problem in defining a potential since, as an energy surface exists, an algorithm that describes it will constitute the potential. Many different models exit, and are useful for different approaches, for instance the Lennard-Jones potential is very popular for molecular dynamics simulations. Early attempts at determining empirical potentials were overly simplistic such as that determined by Kapustinskii [42, 43] and required no information about the crystal structure in order to yield the lattice energy (see Equation 2.19).

$$\Delta U = -\frac{1.07 \times 10^5 v \mid q_i \mid\mid q_j \mid}{r_{ij}} \tag{2.19}$$

where U is the system lattice energy, v is the number of ions in the molecule, q_i, q_j are the ionic charges and r_{ij} is the ion separation.

The first attempt to describe a true interionic potential was by Born and Landé [44] who described the functional form:

$$\phi_{sr}(r_{ij}) = \frac{b}{r_{ij}^n} \tag{2.20}$$

where b and n are constants that are chosen to reproduce the equilibrium interionic separation and r_{ij} is the nearest distance between two unlike ions. This form, though very simple, works well for very highly ionic materials such as the alkali halides. To account for the new information from quantum mechanics, Born and Mayer [32] introduced a short range repulsive function of the form:

$$\phi_{sr}(r_{ij}) = A_{ij} \exp(\frac{-r_{ij}}{\rho_{ij}}) \tag{2.21}$$

where A_{ij} and ρ_{ij} are adjustable parameters. An attractive term of the form $C_{6,ij}/r_{ij}^6$, was also then added to Equation 2.20 to account for the van der Waals interaction which had just been determined via work from van der Waals, London and Margenau [45–48]. This combination results in the aforementioned Lennard-Jones potential [49–51]:

$$\phi_{sr}(r_{ij}) = \frac{b}{r_{ij}^n} - \frac{C_{6,ij}}{r_{ij}^6} \tag{2.22}$$

When the short range repulsive and the attractive van der Waals terms are combined, the Buckingham potential model is formed:

$$\phi_{sr}(r_{ij}) = A_{ij} \exp\left(\frac{-r_{ij}}{\rho_{ij}}\right) - \frac{C_{6,ij}}{r_{ij}^6} \tag{2.23}$$

where the A_{ij} parameter can be approximated as a measure of the number of electrons within the ion; ρ_{ij} can be approximated as a measure of the electron density; and $C_{6,ij}$ is an approximate description of the polarisability of the ion. It is however, important to note that the potential terms are purely numerical in nature, and whilst comparison with physical properties may be possible (and helpful) for some cases, caution should be exercised. The $C_{6,ij}$ term takes the correlation effect into consideration and as such has an intermediate-range effect. The justification for the $C_{6,ij}$ term inclusion in the short-term potential form is that it is small beyond a few lattice spacings and so the contribution to the system energy is minimal. As such, the $C_{6,ij}$ term is subjected to a cut-off of 20 Å. The $C_{6,ij}$ parameter was calculated via the Slater-Kirkwood formula [52]:

$$C_{6,ij} = \frac{\frac{3}{2}\alpha_i\alpha_j}{\left(\frac{\alpha_i}{P_i}\right)^{\frac{1}{2}}\left(\frac{\alpha_j}{P_j}\right)^{\frac{1}{2}}} \tag{2.24}$$

where α_i, α_j are the static polarisabilities of ions i and j, and P_i, P_j are the number of electrons that contribute significantly to the polarisability of ions ions i and j, i.e. the effective electron numbers of ions i and j. Consequently, $C_{6,ij}$ a function of the ionic radius, and as such depends on the coordination of the ions.

The determination of the $C_{6,ij}$ term requires knowledge of the in-crystal radius and the polarisability, α_D, of the relevant ions and was calculated using Equation 2.25 [53, 54]. The polarisabilities and $C_{6,ij}$ are presented in Tables 2.3 and 2.4

$$\alpha_D = \frac{8}{9}a_0\,(2\ell+1)\,[a_0 < r^2 >]^2 \tag{2.25}$$

where ℓ is the orbital angular momentum quantum number of the electron subshell concerned, i.e. the outermost occupied/paritially occupied electron shell, the factor $[a_0 < r^2 >]^2$ is a form of mean square radius of the outer electron orbit (r is the radius in dimensionless atomic units and a_0 is the radius of the first Bohr orbit in hydrogen).

The Buckingham potential model has proved to be successful in simulating many oxide systems [55, 56] and other ionic solids [57, 58]. On this justification, this was the potential model implemented to describe the short-range interactions in this study, however a significant problem with the Buckingham potential is that the energy tends to minus infinity as the ion separation goes to zero (see Figure 2.5)); this region must be inaccessible by making the barrier sufficiently large, this is particularly problematic in molecular dynamics [43].

Table 2.3: $C_{6,ij}$ term determination for the A site cations. See Equations 2.24 and 2.25.

Ion Interaction	Radius (CN8) (Å)	Modified Crystal Radius, r (Å) [53,54]	Polarisability, α_D (Å^3)	Effective No. of Electrons, P [53,54]	$C_{6,ij}$ (eVÅ^6)
O^{2-}–O^{2-}	1.42	1.20	2.01	5.93	5.20
Ce^{3+}–O^{2-}	1.14	1.21	6.15	17.86	15.86
Dy^{3+}–O^{2-}	1.03	1.11	4.07	13.99	10.94
Er^{3+}–O^{2-}	1.00	1.09	3.81	13.64	10.34
Eu^{3+}–O^{2-}	1.07	1.15	4.53	14.64	12.00
Gd^{3+}–O^{2-}	1.05	1.14	4.37	14.35	11.62
Ho^{3+}–O^{2-}	1.02	1.10	3.97	13.93	10.72
La^{3+}–O^{2-}	1.16	1.23	6.07	17.00	15.51
Lu^{3+}–O^{2-}	0.98	1.06	3.64	13.74	10.01
Nd^{3+}–O^{2-}	1.11	1.18	5.01	15.23	13.07
Pr^{3+}–O^{2-}	1.13	1.19	5.32	15.97	13.83
Pu^{3+}–O^{2-}	-	1.20	4.67	13.80	12.10
Sm^{3+}–O^{2-}	1.08	1.16	4.74	15.03	12.49
Tb^{3+}–O^{2-}	1.04	1.12	4.25	14.33	11.37
Yb^{3+}–O^{2-}	0.99	1.07	3.58	13.34	9.81

Table 2.4: $C_{6,ij}$ term determination for the B site cations. See Equations 2.24 and 2.25.

Ion Interaction	Radius (CN8) (Å)	Modified Crystal Radius, r (Å) [53,54]	Polarisability, α_D (Å^3)	Effective No. of Electrons, P [53,54]	$C_{6,ij}$ (eVÅ^6)
Al^{3+}–O^{2-}	0.54	0.74	0.79	6.22	2.54
Cr^{3+}–O^{2-}	0.62	0.82	1.45	9.28	4.47
Fe^{3+}–O^{2-}	0.65	0.85	2.29	13.64	6.96
Ga^{3+}–O^{2-}	0.62	0.82	1.50	9.49	4.62
In^{3+}–O^{2-}	0.80	1.00	2.62	11.14	7.40
Sc^{3+}–O^{2-}	0.75	0.95	2.81	13.38	8.14
Y^{3+}–O^{2-}	0.90	1.10	3.81	13.39	10.30

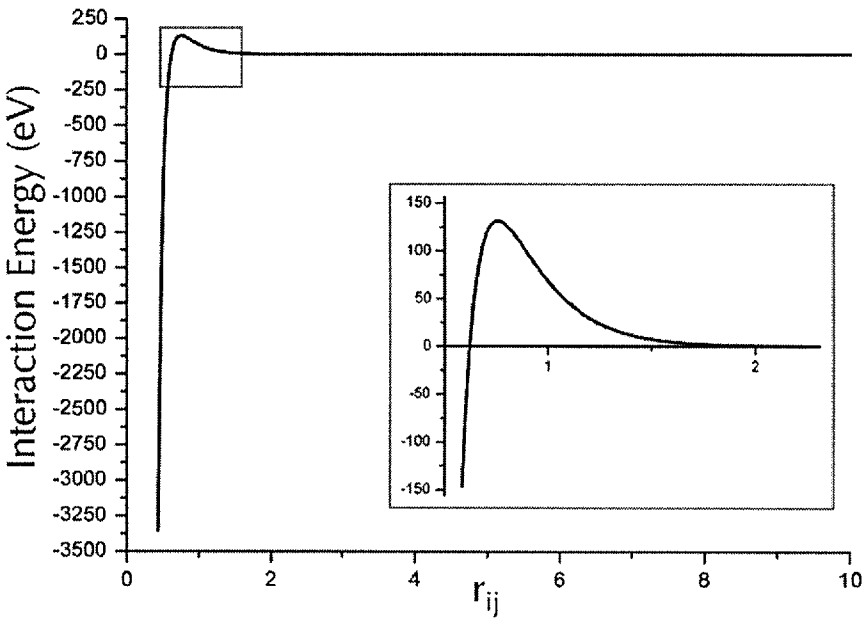


Figure 2.5: The form of the Buckingham Potential for O^{2-}-O^{2-} interaction illustrating how the energy tends to minus infinity as the ion separation tends to zero (see Table 2.6 for parameter values).

2.3.3 Electronic Polarisability

It is noteworthy that the Buckingham potential is a pair-potential model, i.e. it operates between two ions at a time (i and j). Other interactions may occur that operate between three or more ions at a time (many-body interactions). A many body term is included, through the shell model since the two-body interactions operate between shells (or shell to the core of those ions that are treated as without a shell). Since the position of the shell (relative to the core) depends on the assumed electro-static interactions from all ions in the crystal, the two-body forces are mediated via a many-body shell position.

The electronic polarisability of species was determined using the Shell Model which was originally developed by Dick and Overhauser [59] while Faux and Lidiard [60] proved its value to defect calculations. The ion is described as having a massless shell (usually for static lattice calculations, for MD a shell can be assigned a mass) around a central massive core. The core and shell are linked by an isotropic, harmonic spring with a force constant, k (Figure 2.6). When an electric field is applied to the ion, the shell is allowed to move relative to the core in such a way that it develops a dipole and thus simulates the dielectric polarisability of the lattice. The core and the shell are assigned positive ($X \cdot e$) and negative ($Y \cdot e$) charges respectively such that the sum is equal to the charge on the ion ($(X + Y) \cdot e$). The polarisability, α_e, of an isolated ion is given by:

$$\alpha_e = \frac{1}{4\pi\epsilon_0}\left(\frac{Y^2}{k}\right) = 14.3994\left(\frac{Y^2}{k}\right) \tag{2.26}$$

where Y is the shell charge in electronic charge units, ϵ_o is the permittivity of free space, α_e and k are in units of Å^3, and eVÅ^{-2} respectively. For this work, only the

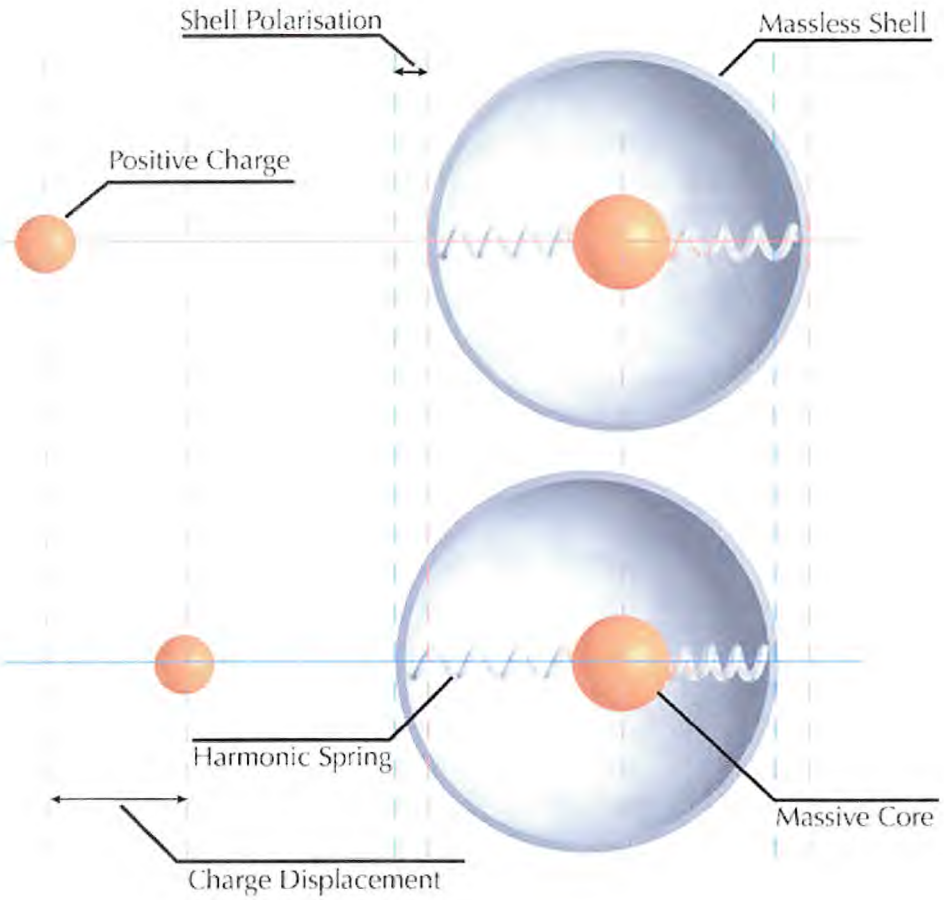


Figure 2.6: A schematic of the shell model.

oxygen ion is treated as polarisable, and the parameters for this are presented in Table 2.8.

2.3.4 Cauchy Violation

One of the assumptions made in this model is that the potential is merely a function of the separation of the ions and not their direction [33]. In other words this is a centrosymmetric model. This is clearly an approximation since it implies that the elastic constants c_{12} and c_{44} are equal (for a cubic crystal); this is known as the

Cauchy relationship [61]. Unfortunately this is not found experimentally, and for many materials the difference between the elastic constants is quite considerable.

The centrosymmetric nature of the model is also manifested in the Shell Model since this assumes that only dipolar distortions to spherical symmetry are allowed. Modifications can be made to the shell model in order to model the Cauchy violation. Schroder allowed the shell to distort in a spherical manner, adjusting the radius of the shell to create what is known as the *breathing shell* [62]. The problem with this model is that it is only able to account for cases where $c_{12} < c_{44}$. Sangster developed a further modification to describe the case where $c_{12} > c_{44}$ by allowing the shell to distort in an ellipsoidal manner [63]. However, these models are hard to parameterise due to the limited amount of data available. Fortunately for calculating defect properties and parameters, the centrosymmetric shell model approximation has proven very successful [33].

2.3.5 Potential Parameters: Fitting

There are two types of approach for determining valid interatomic potentials. These are empirical fitting (to match experimental data) and energy surface fitting. In the latter approach, a high quality quantum mechanical technique is used to predict the interaction energy between ions as a function of ion separation. Parameters are then chosen to reproduce this energy surface. Throughout this work only potentials determined empirically were used.

Empirical potential derivation consists of a least squares procedure, whereby the difference between observed (experiment) and calculated properties are minimized, i.e.:

$$F = \sum [f_{observable} - f_{calculated}]^2 \tag{2.27}$$

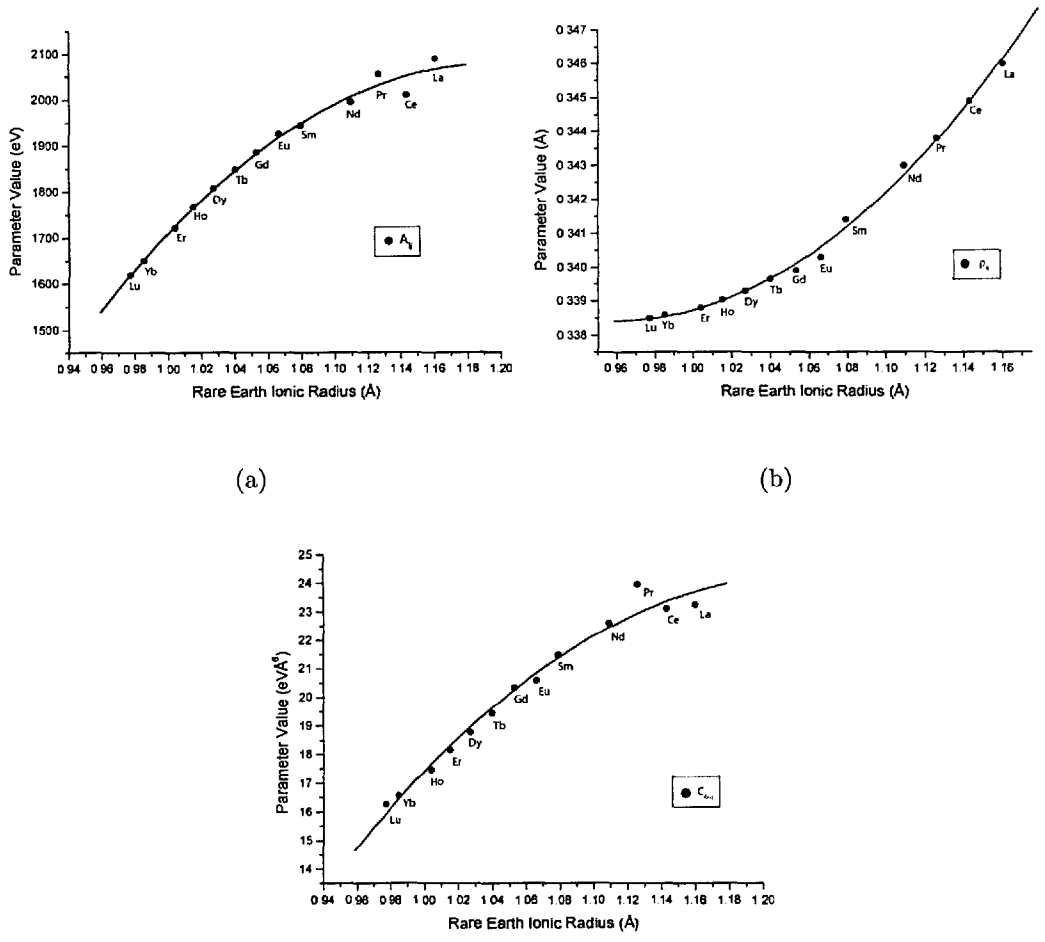
Almost all properties of the material can be used in the derivation process, including elastic and dielectric constants, lattice energy and phonon data. The prerequisite, however, is a knowledge of the crystal structure, including the ionic positions and lattice parameters. Care must be taken when phonon modes are included in the derivation process since their order can change during the fitting, thus they are commonly used only to used to ensure that the minimum energy structure is stable (i.e. all the phonons are positive). It is often the case with empirical fitting that only the crystal structure is known with any degree of certainty.

Often, more than one set of parameter values can reproduce the physical properties of the material [64]. However, the test of a successful potential model is the transferability of the parameters to systems not included in the initial parameter selection. If the potential set is only able to reproduce the structure for which it was fitted against, then it is of little use.

The transferability and reliability of the potentials can be improved by including as much information about the structure as possible (e.g. high frequency and static dielectric constants, bulk modulus and elastic constants) in the fitting procedure. Unfortunately, a potential may reproduce such perfect lattice properties, and yet when defect calculations are performed, its shortcomings become evident. Experience suggests that such problems are generally avoided if the potential is fitted over a broad range of interionic separations to allow for the consideration of interstitial and vacancy defects which alter the equilibrium separation (see Figure 2.2). A useful method for accomplishing this is to use multi-fitting. Here a cation - anion interac-

tion is determined against a large number of related compositions with varying ion separations. This has the added benefit that any errors in the experimental crystal properties are minimized (see Table 2.5 for examples).

When a range of compositions and interactions are to be studied, it is possible to impose a self-consistency between them. For example, in this work where the rare earth elements were to be modelled, the potential parameters were required to vary in a smooth manner. This is due to the steady decrease in the size of the ions with increasing atomic number accompanied by a corresponding increase in the number of electrons in the 4f orbital (the lanthanide contraction). This smooth order can be imposed onto the potential parameters as a function of the radius of the ion for which they describe. This imposed order can be seen in the smooth transitions in the A_{ij} (Figures 2.7(a)), ρ_{ij} (Figure 2.7(b)) and $C_{6,ij}$ (Figure 2.7(c)) terms.



(a) (b)

(c)

Figure 2.7: The smooth change in ion radius due to the lanthanide contraction allows for an imposed order onto the potential parameters (a) A_{ij}, (b) ρ_{ij} and (c) $C_{6,ij}$.

The potential parameters used for this study are presented in Tables 2.6 and 2.7 and were derived via a multi-structure empirical fitting procedure. The A_{ij} and ρ_{ij} terms of the Buckingham potential were altered in such a way that they gave good agreement to the crystallographic properties taken from experimental observations,

Table 2.5: The percentage agreement with experimental unit cell volumes for the compounds used for the derivation of the cation - anion potentials.

		B Cation						
		Ga	**Cr**	**Al**	**Sc**	**Fe**	**Pr**	**Averages**
A Cation	**La**	100.47	100.57	101.00	-	99.76	-	100.45
	Ce	100.48	98.44	100.73	-	-	-	99.89
	Pr	100.97	97.95	101.37	-	99.90	-	100.05
	Nd	100.11	100.49	101.19	-	99.88	-	100.42
	Sm	-	98.49	101.37	-	100.62	-	100.16
	Eu	-	-	-	100.10	-	-	100.10
	Gd	99.91	100.65	-	100.33	100.01	-	100.23
	Tb	-	-	100.22	-	99.95	-	100.09
	Dy	-	100.70	-	-	99.84	-	100.27
	Ho	-	-	100.17	-	100.15	-	100.16
	Er	-	100.33	-	-	100.06	-	100.19
	Yb	-	-	-	-	100.15	-	100.15
	Lu	-	-	-	-	100.46	99.99	100.22
	Averages	100.39	99.70	100.86	100.21	100.07	99.99	-

in particular, the aim was that the average unit cell volume was fitted to within 1% over the series, both horizontal and vertical, to ensure that the relative Madelung energies of the lattices were correct. It is important that the potentials are able to reproduce experimental data so that when they are used to predict structures for which there is no experimental data, confidence in the model predictions is maintained. Similar fitting methods have been used by Binks *et al.* [34] and Minervini *et al.* [5,26]. The terms in the Shell model were taken from Minervini *et al.* (Table 2.8) [5]. A more detailed explanation of the fitting procedure used and a discussion of the merits of this and other potential fitting methods is given by Gale [43].

2.3.6 Potential Model Variation

The results presented in this thesis were based on Buckingham pair potentials (Equation 2.23). However, in order to improve crystal structure predictions (Figure 3.10) the potential model was altered. Such modifications were however, within the scope of the Buckingham model and involved changes in and extensions to the standard Buckingham model by simple additions to its functional form as follows:

- Changes in the co-ordination dependency of the $C_{6,ij}$ term.
- The addition of a double exponential term for the oxygen-oxygen interaction.
- The addition of a damped coulombic interaction.

Table 2.6: Short-range potential parameters used for perovskite materials.

Species	A_{ij} (eV)	ρ_{ij} (Å)	$C_{6,ij}$ (eVÅ^6)
O^{2-}-O^{2-}	9547.96	0.2192	32.0
Al^{3+}-O^{2-}	1365.79	0.30096	2.538
Ce^{3+}-O^{2-}	2034.18	0.34380	15.86
Cr^{3+}-O^{2-}	1452.25	0.30918	4.472
Dy^{3+}-O^{2-}	1767.64	0.33770	10.94
Er^{3+}-O^{2-}	1678.21	0.33781	10.81
Eu^{3+}-O^{2-}	1886.71	0.33975	11.997
Fe^{3+}-O^{2-}	1478.98	0.31306	6.960
Ga^{3+}-O^{2-}	1456.72	0.30988	4.616
Gd^{3+}-O^{2-}	1868.75	0.33880	11.62
Ho^{3+}-O^{2-}	1726.29	0.33776	10.72
In^{3+}-O^{2-}	1595.65	0.32960	7.402
La^{3+}-O^{2-}	2051.32	0.34585	15.51
Lu^{3+}-O^{2-}	1561.36	0.33854	10.01
Nd^{3+}-O^{2-}	1979.11	0.34148	13.07
Pr^{3+}-O^{2-}	2025.54	0.34270	13.83
Sc^{3+}-O^{2-}	1587.95	0.32190	8.143
Sm^{3+}-O^{2-}	1944.44	0.34080	12.49
Tb^{3+}-O^{2-}	1818.00	0.33845	14.33
Y^{3+}-O^{2-}	1721.23	0.33821	10.29
Yb^{3+}-O^{2-}	1616.68	0.33798	13.34

Table 2.7: Short-range potential parameters used for fluoride materials.

Interaction	A_{ij} (eV)	ρ_{ij} (Å)	$C_{6,ij}$ (eVÅ^6)
F^--F^-	1317.50	0.27530	13.8
Li^+-F^-	574.80	0.25530	0.0
Zn^{2+}-F^-	918.41	0.28481	0.0

Co-ordination Dependency of $C_{6,ij}$

The value of the $C_{6,ij}$ term is determined via calculation by using the Slater-Kirkwood equation (Equation 2.24). This approach requires the use of the in crys-

Table 2.8: Shell Parameter for O^{2-} [5,34]

Species	Y (e)	k (eVÅ^{-2})
O^{2-}	-2.04	6.3

tal ion radius. The $C_{6,ij}$ derived for this work used an effective ionic radius for all cation - anion potentials. This effective ionic radius was taken from Grimes and Grimes [53,54]. However, cations at different lattice sites were subjected to different anion coordinations and consequently exhibited different cationic radii (the A cation being 12 fold oxygen co-ordinated has a larger radius than a B cation which is 6 fold coordinated). The values of Grimes and Grimes [53, 54] represent an average (roughly 6 co-ordinate). It was therefore pertinent that the potential should reflect this difference between the A and B cation co-ordination. As such, a co-ordination specific model was determined, whereby the cation radii were chosen to match the coordinations of the relevant ion. It can be seen from Tables 2.1 and 2.2 that the 12 co-ordinate radius is larger than the corresponding 6 co-ordinate radius. This co-ordination specific radius was then used to determine a modified value for $C_{6,ij}$ and then in turn, the A_{ij} and ρ_{ij} potential parameters were re-derived (the site specific $C_{6,ij}$ potentials are shown in Table 2.9). The effective co-ordinate and co-ordinate specific $C_{6,ij}$ values are shown in Table 2.10.

Double Exponential Oxygen

The next step was to consider altering the O^{2-}-O^{2-} Buckingham potential although, of course this interaction affects all others in the system. There have been many different oxygen interactions used, however one that has proved successful is that used by Catlow [2]. In order to incorporate this Catlow oxygen interaction into the

Table 2.9: Short-range potential parameters used for perovskite materials based on the site dependent $C_{6,ij}$ term.

Species	A_{ij} (eV)	ρ_{ij} (Å)	$C_{6,ij}$ (eVÅ^6)
O^{2-}-O^{2-}	9547.96	0.2192	32.0
Al^{3+}-O^{2-}	1365.79	0.30096	1.499
Ce^{3+}-O^{2-}	2034.18	0.34380	18.30
Cr^{3+}-O^{2-}	1452.28	0.30918	2.827
Dy^{3+}-O^{2-}	1767.64	0.33770	12.24
Er^{3+}-O^{2-}	1678.21	0.33781	11.59
Eu^{3+}-O^{2-}	1886.71	0.33975	13.53
Fe^{3+}-O^{2-}	1478.98	0.31306	6.127
Ga^{3+}-O^{2-}	1456.72	0.30988	2.930
Gd^{3+}-O^{2-}	1868.75	0.33880	13.013
Ho^{3+}-O^{2-}	1726.29	0.33776	12.00
In^{3+}-O^{2-}	1595.65	0.32960	5.211
La^{3+}-O^{2-}	2051.32	0.34585	17.70
Lu^{3+}-O^{2-}	1561.36	0.33854	11.32
Nd^{3+}-O^{2-}	1979.11	0.34148	14.96
Pr^{3+}-O^{2-}	2025.54	0.34270	16.05
Sc^{3+}-O^{2-}	1587.95	0.32190	5.581
Sm^{3+}-O^{2-}	1944.44	0.34080	14.15
Tb^{3+}-O^{2-}	1818.00	0.33845	12.76
Y^{3+}-O^{2-}	1721.23	0.33821	7.550
Yb^{3+}-O^{2-}	1616.68	0.33798	11.55

oxygen interaction already in use for this work, a double exponential oxygen model was introduced. The form of this can be seen in Equation 2.28.

$$V(r_{ij}) = \left(\frac{A_{ij}}{2}\right)\exp\left(\frac{-r_{ij}}{\rho_{ij,1}}\right) + \left(\frac{B_{ij}}{2}\right)\exp\left(\frac{-r_{ij}}{\rho_{ij,2}}\right) - \frac{C_{6,ij}}{r_{ij}^6} \qquad (2.28)$$

Here, the A_{ij} and $C_{6,ij}$ terms are those taken from the Binks oxygen potential [1],

Table 2.10: Comparison between the effective radius and co-ordinate specific radius $C_{6,ij}$ value (eVÅ^6).

Interaction	Effective Co-ordination	Site Specific Co-ordination
O^{2-}-O^{2-}	32.0	32.0
Al^{3+}-O^{2-}	2.538	1.499
Ce^{3+}-O^{2-}	15.86	18.300
Cr^{3+}-O^{2-}	4.472	2.827
Dy^{3+}-O^{2-}	10.94	12.240
Er^{3+}-O^{2-}	10.81	11.590
Eu^{3+}-O^{2-}	11.997	13.530
Fe^{3+}-O^{2-}	6.960	6.127
Ga^{3+}-O^{2-}	4.616	2.930
Gd^{3+}-O^{2-}	11.62	13.013
Ho^{3+}-O^{2-}	10.72	12.000
In^{3+}-O^{2-}	7.406	5.211
La^{3+}-O^{2-}	15.51	17.700
Lu^{3+}-O^{2-}	10.01	11.320
Nd^{3+}-O^{2-}	13.07	14.96
Pr^{3+}-O^{2-}	13.83	16.05
Sc^{3+}-O^{2-}	8.143	5.581
Sm^{3+}-O^{2-}	12.49	14.15
Tb^{3+}-O^{2-}	14.33	12.76
Y^{3+}-O^{2-}	10.29	7.550
Yb^{3+}-O^{2-}	13.34	11.55

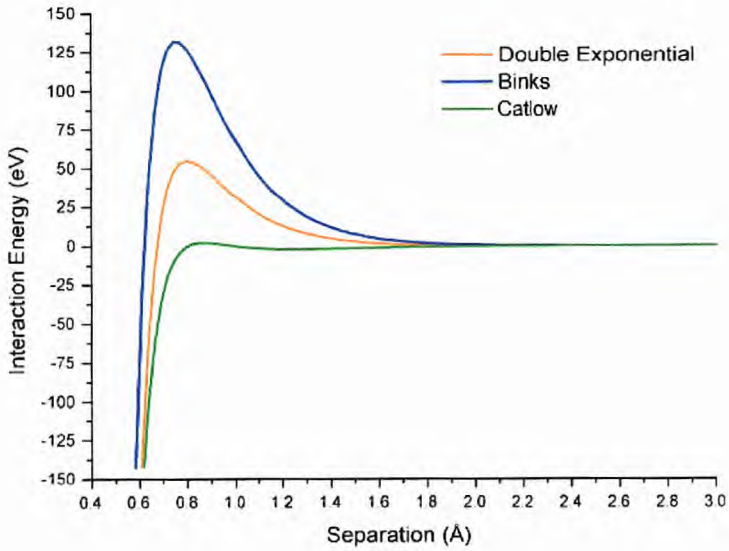
while the B_{ij} is the A_{ij} term from the Catlow potential [2]. The two potentials are shown in Table 2.11 and the forms are shown in Figure 2.8(a).

Table 2.11: Comparison between the Binks [1] and Catlow O^{2-}-O^{2-} potentials.

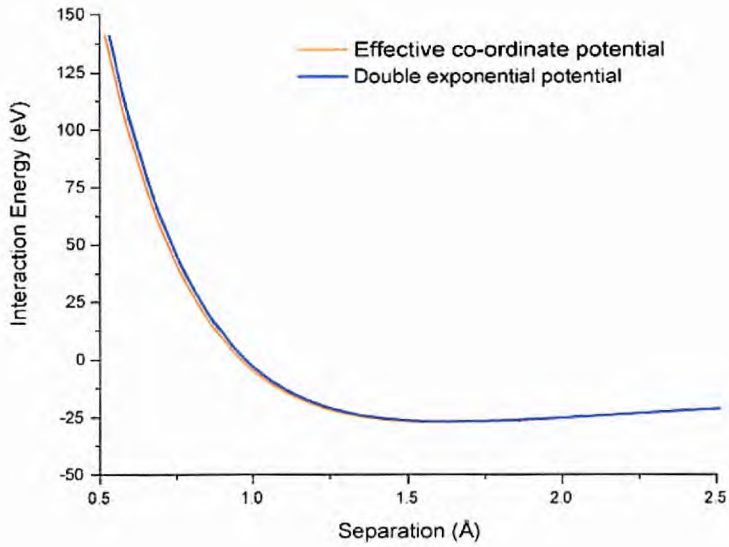
Potential	A_{ij} (eV)	ρ_{ij} (Å)	$C_{6,ij}$ (eVÅ^6)
Binks	9547.96	0.2192	32.0
Catlow	22764.3	0.1490	27.8

Table 2.12: Short-range potential parameters used for perovskite materials based on the double exponential oxygen term.

Species	A_{ij} (eV)	ρ_{ij} (Å)	$C_{6,ij}$ (eVÅ^6)
O^{2-}-O^{2-}	4773.98	0.21910	32.00
O^{2-}-O^{2-}	11382.15	0.14900	0.0
Al^{3+}-O^{2-}	1412.20	0.30096	2.538
Ce^{3+}-O^{2-}	2032.94	0.34380	15.86
Cr^{3+}-O^{2-}	1500.68	0.30918	4.472
Dy^{3+}-O^{2-}	1778.50	0.33770	10.94
Er^{3+}-O^{2-}	1700.81	0.33705	10.34
Eu^{3+}-O^{2-}	1888.10	0.33974	11.997
Fe^{3+}-O^{2-}	1510.00	0.31306	6.960
Ga^{3+}-O^{2-}	1488.22	0.30988	4.616
Gd^{3+}-O^{2-}	1854.73	0.33880	11.62
Ho^{3+}-O^{2-}	1735.99	0.33776	10.72
In^{3+}-O^{2-}	1600.35	0.32960	7.402
La^{3+}-O^{2-}	2040.50	0.34572	15.51
Lu^{3+}-O^{2-}	1625.65	0.33680	10.01
Nd^{3+}-O^{2-}	1985.63	0.34095	13.07
Pr^{3+}-O^{2-}	2015.13	0.34258	13.83
Sc^{3+}-O^{2-}	1610.47	0.32190	8.143
Sm^{3+}-O^{2-}	1925.16	0.34080	12.49
Tb^{3+}-O^{2-}	1815.81	0.33900	14.33
Y^{3+}-O^{2-}	1708.82	0.33821	10.29
Yb^{3+}-O^{2-}	1658.86	0.33695	13.34



(a)



(b)

Figure 2.8: (a) Comparison between the O^{2-}-O^{2-} potentials from Binks [1], Catlow [2] and the double exponential model; (b) modification of the Al^{3+}-O^{2-} interaction energy.

Damped Coulombic Potential

This potential model aims to better account for the large amount of electronic overlap between the cations and the oxygen ions at the short interatomic separations that occur at lower coordination states (e.g. 5 and 7 coordination with respect to the 6 and 12 coordination for the classical perovskites see Chapter 3) Physically, this reduces the coulomb interaction between formal charged ions at short separations. The coordination states should thus be biased toward Pnma from $P6_3cm$. For this purpose, a potential model was developed by Grimes and Redfern and termed a "damped Coulombic Potential" [65]. In essence, this model is equivalent to the standard partial charge model at short separations however at larger distances, the effect of the dampening is negligible and ions interact as formal charged species. For this model, the scale of the electrostatic interaction between ions decreases exponentially with decreasing ionic separation. The general form of the potential is:

$$V(r_{ij}) = \frac{q_i q_j}{4\pi\epsilon_0 r_{ij}} \left(1 - \exp\left(\frac{-r_{ij}}{\rho_{ij}}\right)\right) \tag{2.29}$$

Since this new potential form is not one of the standard "classical" potential forms included for use with GULP, the damped coulombic model has to be modified such that it fits the GULP general potential model:

$$V(r_{ij}) = D_{ij} \exp\left(\frac{-r_{ij}}{\rho_{ij}}\right) r_{ij}^{-m} - C r_{ij}^{-n} \tag{2.30}$$

It is clear how this is achieved if Equation 2.29 is expanded as;

$$V(r_{ij}) = \frac{q_i q_j}{4\pi\epsilon_0 r_{ij}} - \left(\frac{q_i q_j}{4\pi\epsilon_0 r_{ij}}\right) exp\left(\frac{-r_{ij}}{\rho_{ij}}\right) \tag{2.31}$$

The initial coulombic interaction term is then the standard coulombic interaction and is treated as usual within the code. The remaining "damped coulombic" term is rearranged such that it fits a general potential model (Equation 2.30):

$$V(r_{ij}) = \frac{D_{ij}}{r_{ij}} \exp\left(\frac{-r_{ij}}{\rho_{ij}}\right) \tag{2.32}$$

The damped coulombic term of the potential can now be compared to this new general potential form in order to elucidate the constant terms:

$$-\frac{q_i q_j}{4\pi\epsilon_0 r_{ij}} \exp\left(\frac{-r_{ij}}{\rho_{ij}}\right) = \frac{D_{ij}}{r_{ij}} \exp\left(\frac{-r_{ij}}{\rho_{ij}}\right) \tag{2.33}$$

In Equation 2.30, the C value is set to zero, the exponent m is set to 1, and the D_{ij} term is:

$$D_{ij} = -\frac{q_i q_j}{4\pi\epsilon_0} \tag{2.34}$$

thus, the only variable input into the general potential equation is the ρ_{ij} which here is fixed so that the damped coulombic contribution to the total energy is only 1% at the sum of the six coordinate ionic radii $(R_i + R_j)$, i.e.:

$$\exp\left(\frac{-r_{ij}}{\rho_{ij}}\right) = 0.01|_{r_{ij}=(R_i+R_j)} \tag{2.35}$$

Tables 2.13 and 2.14 show a limited set of parameters that were used for the general potential. Figure 2.9 shows a comparison of the effective co-ordination potential and the damped coulombic potential for the La^{3+}-O^{2-} interaction. It is clear that the energy minima is translated to higher separations, thus biasing the high co-ordinations. The motivation for the derivation of this model was an attempt to predict the dissociation of the perovskite into two distinct garnet phases.

Table 2.13: Damped coulombic model parameters for input into the general potential for GULP.

Interaction			D_{ij}	ρ_{ij}
Al^{3+} core	-	$O^{0.04+}$ core	-0.10785	0.42018
Al^{3+} core	-	$O^{2.04-}$ shell	5.50038	0.42018
Al^{3+} core	-	Al^{3+} core	-8.08880	0.34027
Al^{3+} core	-	La^{3+} core	-8.08880	0.34027
La^{3+} core	-	$O^{0.04+}$ core	-0.10785	0.52810
La^{3+} core	-	$O^{2.04-}$ shell	5.50038	0.52810
La^{3+} core	-	La^{3+} core	-8.08880	0.34027
$O^{0.04+}$ core	-	$O^{0.04+}$ core	-0.00144	0.60801
$O^{0.04+}$ core	-	$O^{2.04-}$ shell	0.07334	0.60801
$O^{2.04-}$ shell	-	$O^{0.04+}$ core	0.07334	0.60801
$O^{2.04-}$ shell	-	$O^{2.04-}$ shell	-3.74026	0.60801

Table 2.14: Short-range potential parameters used for perovskite materials based on the damped coulombic model.

Species	A_{ij} (eV)	ρ_{ij} (Å)	$C_{6,ij}$ (eVÅ^6)
O^{2-}-O^{2-}	9547.96	0.21910	32.00
Al^{3+}-O^{2-}	1359.79	0.30096	2.538
La^{3+}-O^{2-}	2044.32	0.34572	15.51

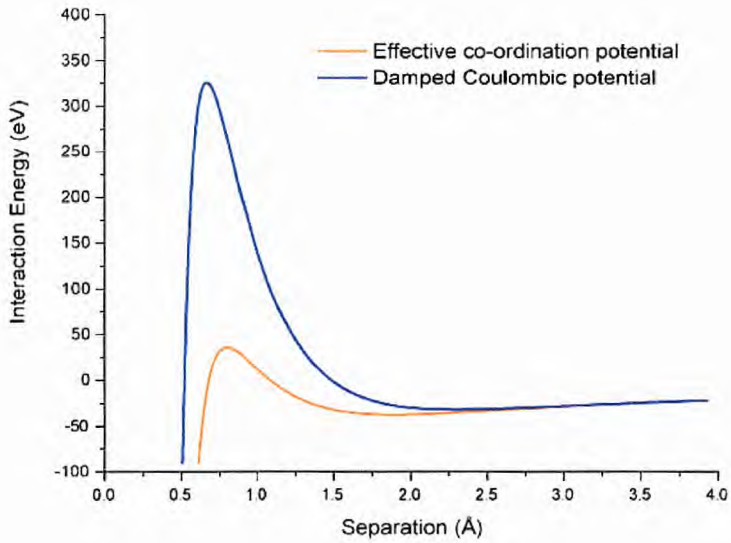


Figure 2.9: Comparison of the effective co-ordination and damped coulombic potentials for the La^{3+}-O^{2-} interaction.

Cation Shell Model

In addition to predicting the crystal structure of the wide range of perovskite compositions, a potential model should also be able to predict dielectric properties. An important contribution to the dielectric constant of a material is from the electronic behaviour. This is modelled using the shell model. In order to improve predictions of the dielectric constant, the shell model was investigated and shells were added to the cations (leaving the oxygen shell unaltered). The addition of these cation shells was designed to increase the contributions to the dielectric constant.

The rationale behind the decision to define the shell charge as negative (with a positive core) lies with the make-up of the atom. This consists of a positive nucleus surrounded by a negative cloud of electrons, therefore it was logical to translate this to the shell model. The value assigned to the shell charge was determined from the the ratio of the effective electron number taken from Grimes and Grimes [53, 54]

to the shell charge on the oxygen ion. Therefore the shell charges are consistent throughout. These modified effective electron numbers (shell charges) are shown in Tables 2.3 and 2.4. The shell spring constant was also determined in a consistent manner, and is related to the ionic polarisability taken again from Grimes and Grimes [53, 54]. The shell parameters for these potentials are shown in Table 2.15, with the Buckingham potentials corresponding to those shown in Table 2.16.

Table 2.15: Cation shell parameters.

Species	Y (e)	k (eVÅ^{-2})
Al^{3+}	-0.193	275.1
Ce^{3+}	-0.56	292.42
Cr^{3+}	-0.293	333.73
Dy^{3+}	-0.44	270.2
Er^{3+}	-0.427	274.4
Eu^{3+}	-0.46	265.82
Fe^{3+}	-0.427	456.4
Ga^{3+}	-0.3	337.23
Gd^{3+}	-0.453	264.77
Ho^{3+}	-0.44	274.57
In^{3+}	-0.353	266.17
La^{3+}	-0.53	267.4
Lu^{3+}	-0.43	291.37
Nd^{3+}	-0.48	260.05
Pr^{3+}	-0.5	269.32
Sc^{3+}	-0.42	357.87
Sm^{3+}	-0.473	267.75
Tb^{3+}	-0.453	271.42
Y^{3+}	-0.453	264.42
Yb^{3+}	-0.453	279.3

Table 2.16: Short-range potential parameters used for perovskite materials with cation shells.

Species	A_{ij} (eV)	ρ_{ij} (Å)	$C_{6,ij}$ (eVÅ^6)
O^{2-}-O^{2-}	9547.96	0.2192	32.0
Al^{3+}-O^{2-}	1765.52	0.2873	2.538
Ce^{3+}-O^{2-}	1080.51	0.3815	15.86
Cr^{3+}-O^{2-}	1292.28	0.31646	4.472
Dy^{3+}-O^{2-}	840.00	0.3866	10.94
Er^{3+}-O^{2-}	790.926	0.388	10.34
Eu^{3+}-O^{2-}	925.00	0.386	11.997
Fe^{3+}-O^{2-}	1505.98	0.312	6.960
Ga^{3+}-O^{2-}	1335.72	0.315	4.616
Gd^{3+}-O^{2-}	900.25	0.385	11.62
Ho^{3+}-O^{2-}	820.77	0.387	10.72
In^{3+}-O^{2-}	775.81	0.37954	7.402
La^{3+}-O^{2-}	1115.79	0.38147	15.51
Lu^{3+}-O^{2-}	710.81	0.3932	10.01
Nd^{3+}-O^{2-}	1002.47	0.3819	13.07
Pr^{3+}-O^{2-}	1050.00	0.3813	13.83
Sc^{3+}-O^{2-}	754.43	0.37183	8.143
Sm^{3+}-O^{2-}	950.664	0.3848	12.49
Tb^{3+}-O^{2-}	870.00	0.3868	14.33
Y^{3+}-O^{2-}	825.00	0.3862	10.29
Yb^{3+}-O^{2-}	750.008	0.391	13.34

2.4 The Defective Lattice

In order to efficiently simulate the lattice relaxation around defects, a multi region approach is adopted which stems from the work of Mott and Littleton [33,66]. The lattice is partitioned into concentric spherical regions centred on the defect (Figure 2.10). The area surrounding the defect is termed Region I, here lattice relaxation is

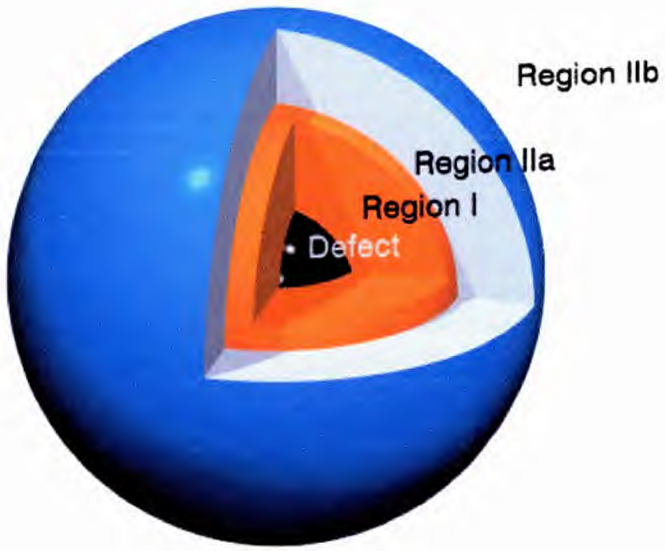


Figure 2.10: Representation of the Multi Region Approach

large, so all interactions are calculated explicitly, while all ions are relaxed to zero force using a Newton-Raphson minimization procedure [18]. Beyond Region I, the lattice relaxation is smaller and as such a more approximate approach can be used. This region is termed Region II, here the interaction is treated as arising from the net charge effect of the defect.

The size of Region I was chosen such that a further increase yields no appreciable change (less than 0.1 eV for an increase in region size of 1 Å) in the defect energy, whilst being small enough for computational efficiency (see Figure 2.11).

Within the two-region approach the defect formation energy, E_d, can be expressed as [25, 67]:

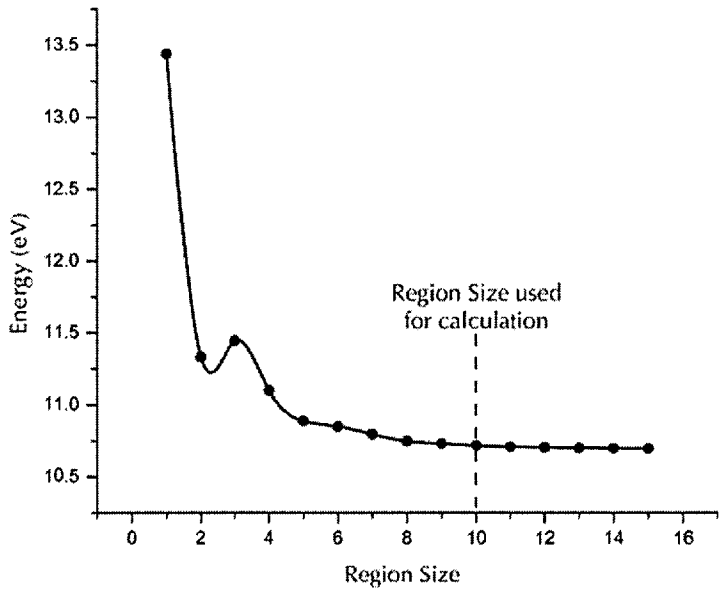


Figure 2.11: Defect energy variations with changing region size for an antisite defect, A_B^X.

$$E_d = E_I(\overline{r}) + E_{I-II}(\overline{r}, \overline{\zeta}) + E_{II}(\overline{\zeta}) \tag{2.36}$$

where E_I is the energy due to the interactions of ions in region I while $\overline{r}$ is their displacement vector; E_{II} is the energy of region II for which the displacement vector is $\overline{\zeta}$; and E_{I-II} is the energy of the interaction between regions I and II. Since region II extends to infinity, E_{II} is the summation of an infinite number of displacements and as such cannot be solved exactly. If, however, it is assumed that all displacements within region II are small, then the quasi-harmonic approximation is valid, such that:

$$E_{II} = \frac{1}{2}\overline{\zeta}.A.\overline{\zeta} \tag{2.37}$$

where A is the force constant matrix. Substituting Equation 2.37 into Equation 2.36, and differentiating with respect to $\overline{\zeta}$, the equilibrium displacements in region II are given by:

$$\frac{\delta E}{\delta \overline{\zeta}} = \frac{\delta E_{I-II}(\overline{r}, \overline{\zeta})}{\delta \overline{\zeta}}|_{\overline{\zeta}=\overline{\zeta_e}} + A\overline{\zeta_e} \tag{2.38}$$

where $\overline{\zeta_e}$ is the equilibrium value of $\overline{\zeta}$ corresponding to $\overline{r}$. When this is substituted into Equation 2.37 and then into Equation 2.36, the explicit dependence of E_d on energy of region II, E_{II}, is removed allowing a far more convenient solution:

$$E_d = E_1(\overline{r}) + E_{I-II}(\overline{r}, \overline{\zeta}) - \frac{1}{2}\frac{\delta E_{I-II}(\overline{r}, \overline{\zeta})}{\delta \overline{\zeta}}|_{\overline{\zeta}=\overline{\zeta_e}} \cdot \overline{\zeta_e} . \overline{\zeta_e} \tag{2.39}$$

Original versions of this method only partitioned the lattice into two regions. However, in order to ensure a smooth transition between Region I and Region II, Region II is split into areas called Region IIa and Region IIb. In Region IIa, which acts as a transition region between Region I and Region IIb, the Mott-Littleton approximation [33, 66] is used to calculate the polarisation, P, at a distance, r, from the defect of charge, q:

$$P(r) = \frac{q\overline{r}}{4\pi r^3}\left(1 - \frac{1}{\epsilon_0}\right) \tag{2.40}$$

where ϵ_0 is the static dielectric constant of the crystal (note: the above uses atomic units). Within Region IIa the displacements of the ions are calculated via direct summation, using the Mott-Littleton approximation due to all defect components within Region I.

2.5 Energy Minimization

Once a model has been adequately validated, in order to be made useful in a predictive manner, it must be combined with energy minimization. This reduces the system to a state of mechanical equilibrium. The criterion used for determining the accuracy of the model is that the ion displacements in the optimised structure from the experimental configuration are minimal. During energy minimization, all ionic interactions are calculated and each ion moves a distance proportional to the force acting on it through an iterative process.

Two conditions exist to minimize the lattice energy at equilibrium: constant volume and constant pressure (it is also possible to equilibrate under constant stress conditions but this is not discussed further.). Under constant volume minimization, the lattice energy is minimized only by varying the internal coordinates of the ions within the unit cell relative to the strains on individual ions, whilst the lattice parameters are not allowed to change. Under constant pressure minimization, the unit cell dimensions are also adjusted, accounting for the strains on both the individual ions and the unit cell. Since there are fewer degrees of freedom for the constant volume calculations, they are computationally faster. Consequently, most early calculations were constant volume. Due to the increase in computation power available, nearly all modern calculations are of the constant pressure type, including all those included in this thesis.

If the lattice energy (U_L) of a system with N ions with coordinates, r, is $U_L(r)$, then after one minimization step, the lattice energy at a new set of coordinates, r' is:

$$U_L(r') = U_L(r) + \vec{g^T} \cdot \vec{\delta} + \frac{1}{2}\vec{\delta^T} \cdot \mathbf{W} \cdot \vec{\delta} \tag{2.41}$$

where $\mathbf{W}$ is a matrix that contains the corresponding second derivatives (Equation 2.45); $\vec{\delta}$ is a generalised strain vector with $3N$ displacement components; $\vec{\delta r}$, and 6 independent bulk strain components; $\vec{\delta\varepsilon}$ of the symmetric strain matrix $\mathbf{E}$, which is the Voigt matrix representation of the vector $\vec{\delta\varepsilon}$:

$$\mathbf{E} = \begin{pmatrix} \delta\varepsilon_1 & \frac{1}{2}\delta\varepsilon_6 & \frac{1}{2}\delta\varepsilon_5 \\ \frac{1}{2}\delta\varepsilon_6 & \delta\varepsilon_2 & \frac{1}{2}\delta\varepsilon_4 \\ \frac{1}{2}\delta\varepsilon_5 & \frac{1}{2}\delta\varepsilon_4 & \delta\varepsilon_3 \end{pmatrix} \tag{2.42}$$

therefore the set of new coordinates, r' is related to the original set, r, by:

$$r' = \mathbf{E} \cdot (r + \delta r) \tag{2.43}$$

The vector $\vec{g}$, refers to the first derivative of the lattice energy with respect to the ion displacements and strain components;

$$\vec{g} = \left(\frac{\partial U_L}{\partial r}, \frac{\partial U_L}{\partial \delta\varepsilon} \right) \tag{2.44}$$

while the matrix $\mathbf{W}$ contains the corresponding second derivatives;

$$\mathbf{W} = \begin{pmatrix} \frac{\partial^2 U_L}{\partial r \cdot r} & \frac{\partial^2 U_L}{\partial r \cdot E} \\ \frac{\partial^2 U_L}{\partial E \cdot r} & \frac{\partial^2 U_L}{\partial E \cdot E} \end{pmatrix} = \begin{pmatrix} W_{rr} & W_{rE} \\ W_{Er} & W_{EE} \end{pmatrix} \tag{2.45}$$

The system is then relaxed iteratively, adjusting the coordinates of the ions until the forces on the ions are zero. Since the first derivative of the lattice energy with

respect to distance (coordinates) is the force, it is possible to write this convergence aim as:

$$\frac{\partial U_L}{\partial r} = F = 0 \tag{2.46}$$

in practice, the minimization proceeds for a pre-set number of iterations or until a point where at subsequent steps, the total energy of the system changes by less than a predetermined value.

2.6 Ion Migration Activation Energies

The bulk transport properties of intrinsic defects can be calculated very simply by performing numbers of static lattice defect calculations at different points throughout the lattice. This method is only applicable when the migration process is controlled via a thermally activated hopping mechanism. When this is the case, then the energy difference between a migrating ion at a saddle point (local energy maximum, see Figure 2.12) and an isolated ion represents the energy barrier for migration of that ion. The location of this saddle point is determined by compiling contour plots of defect energies between the start and end points of the migration. It is then assumed that the defect will follow a lowest energy pathway, and hence the migration path and saddle point energy can be determined. The saddle point is confirmed by carrying out energy calculations perpendicular to the migration pathway.

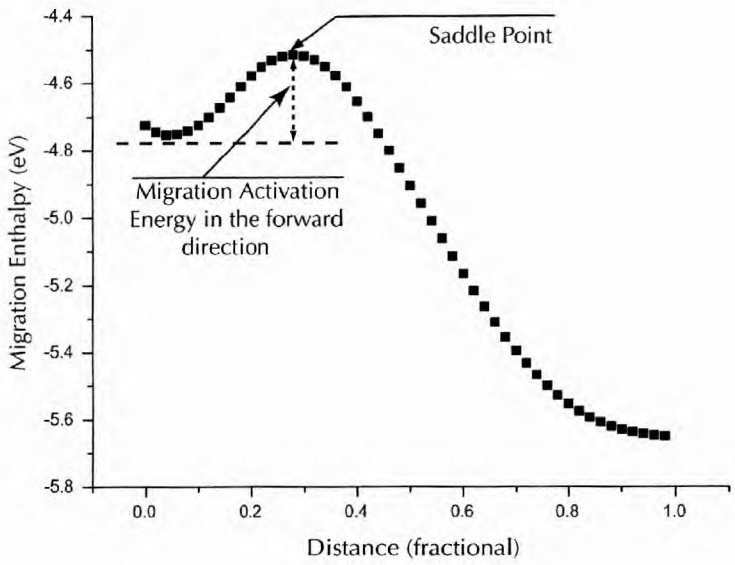


Figure 2.12: Example ion migration plot.

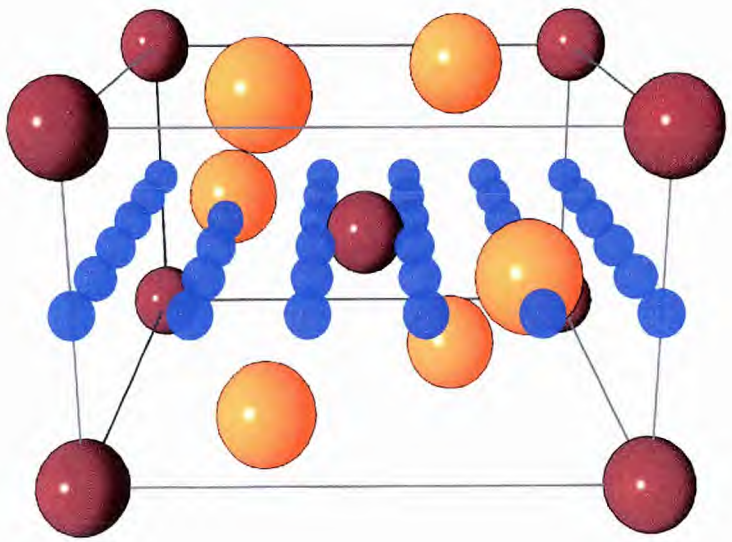


Figure 2.13: Schematic of ion migration calculations in ZnF_2.

In order to calculate this energy contour, the migrating defect is rastered across a plane parallel to the direction of migration and to ensure that a valid minimum is located, planes either side of this are also calculated, and one perpendicular. An

example of this approach, whereby an interstitial defect is migrating in the (100) of a ZnF_2 lattice, is shown in Figure 2.13, and the associated contour plot is shown in Figure 2.14 (the results are discussed in Chapter 6).

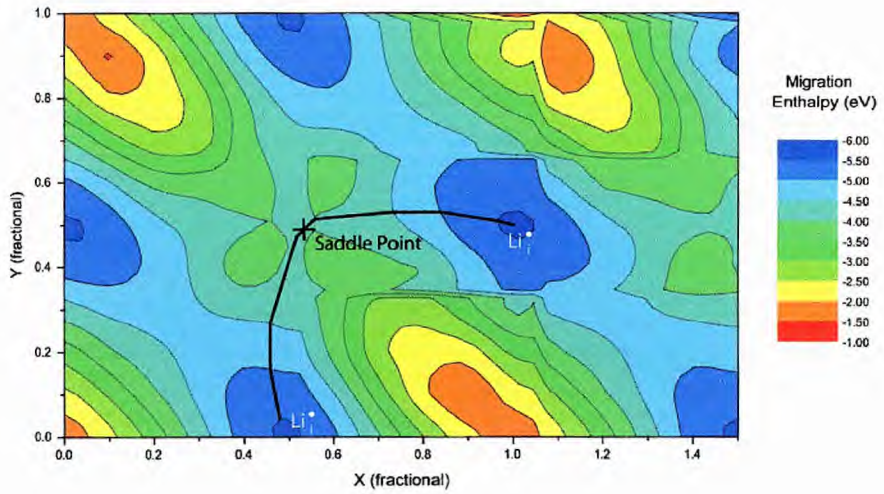


Figure 2.14: Migration energy contour plot for ion migration in ZnF_2

Other more automated techniques such as nudged elastic band methods [68, 69] maybe used in the future. However they are far more computationally expensive.

2.7 Quantum Mechanical Calculations

2.7.1 General Considerations

Quantum mechanics provides a reliable method to calculate the total energy of an ensemble of electrons and atomic nuclei in a perfect or defective lattice. One of the postulates of quantum mechanics is that the state of a system can be fully described by a mathematical function $\Psi(r_1, r_2, ..., t)$ where r_1, r_2 are the spacial coordinates of particles 1, 2 etc. that constitute the system and t is the time. This is known as

the wavefunction of the system and can be evaluated by solving a wave equation, known as the Schrödinger equation [70]. All the properties of the system can be evaluated from the wavefunction. Such analysis can involve calculations based on fundamental quantum mechanical relationships so that the Schrödinger's equation is solved without the use of prior chosen parameters to describe the electrons in that material. However, even in this case the equations are usually subject to approximations such as the Born-Oppenheimer [71]. In that case, the positions of the nuclei can be considered static and only the electrons are considered subject to the static field of the nuclei (this is based on the assumption that the electron velocity is so much higher than that of the nuclei that the position of the latter is effectively fixed). The problem with such *ab initio* approaches is that exact solutions are immensely computationally demanding for a system involving anything other than a single electron in a simple potential. This is due to the complex interactions between electrons.

In general, the problem is handled by approximating electron interactions so that each electron is assumed to be in an effective potential generated by all the other electrons and the nuclei. The specific interactions are thus managed in an average manner within this potential so that one electron is dealt with at a time, i.e. the interactions are decoupled and the wave function is now:

$$\Psi(\vec{r_1}, \vec{r_2}, \vec{r_3}, ..., \vec{r_n}) = \Psi(\vec{r_1})\Psi(\vec{r_2})\Psi(\vec{r_3})...\Psi(\vec{r_n}) \tag{2.47}$$

where Ψ_n are the n one-electron wavefunctions. This reduces the problem to solving a series of coupled one-electron Schrödinger equations of the form:

$$H\Psi_n = \left(-\frac{\hbar^2}{2m}\nabla^2 + V_{ext} + V_{eff}\right)\Psi_n = \epsilon_i\Psi_n \tag{2.48}$$

where V_{ext} is the external potential, either due to the nuclei and/or other applied field and V_{eff} is the effective potential. In general, calculations of this type involve writing part of the electron-electron interaction in terms of a mean-field. The difference between this average approach and one in which electron motions are able to take explicit account of each other is called the correlation (i.e. where the electron paths are correlated).

There are two possible descriptions of the wavefunction, local orbital and plane-wave. In the local orbital approach, the wavefunctions are located at single atomic nuclei and was originally developed for molecules. This approach was not used in these studies.

The plane-wave approach describes an infinite periodic system, in other words a perfect solid. The plane-wave approach has the benefits that all space is treated the same, it is mathematically simple, and does not depend upon the atomic positions. However disadvantages also exist, such that empty space is treated to the same level as an area of importance for property determination such as electron overlap. The quality of the calculation depends on a single energy cut-off parameter. This parameter is expressed as the energy of a free electron whose wavefunction has the same wavevector as the smallest plane wavevector. All plane waves of energy less than this cut-off energy are used in the calculation [72].

Problems occur with both approaches when defects are involved, i.e. when there is a local defect placed within an infinite solid. For such calculations neither approach is perfect but here calculations of the plane-wave variety were chosen for this work.

2.7.2 The Hartree-Fock approach

An early approach for the development of a computational method was developed by Hartree [73, 74] who set V_{eff} to the average of the Coulomb potential between an electron and all other electrons in the system. The Hartree method neglects exchange and correlation, and therefore yields somewhat poor results. Exchange is a result of the indistinguishability of electrons and results from the fact that the wavefunction describing the pair must be anti-symmetric [75] (a requirement of the Pauli exclusion Principle [76]). When Fermi statistics are added to this approach, the Hartree-Fock (HF) method is formed. This now calculates the exchange energy exactly, however, it still neglects the correlation energy. This technique has enabled many advances, and is often the platform from which more accurate calculations are built.

2.7.3 Density Functional Theory

A subtly different approach to HF is that of density functional theory (DFT). The popularity of DFT is due to the fact that it is less computationally demanding than HF calculations and that predictions for systems involving d-block metals agree more closely to experiment than those for HF [77]. This technique was initially developed by Hohenberg, Kohn and Sham [78–80], and resulted in a Nobel prize for chemistry in 1998 for Walter Kohn and John Pople [72]. DFT is based on two simple principles [72, 78]. First, the total energy of a system of electrons and nuclei is a unique functional of the electron probability density, i.e. the density uniquely determines the potential acting on the electrons. The second principle, is that the variational minimum of the energy is exactly equivalent to the true ground

state. The variation principle seeks the parameter values that minimize the energy, with the resulting wavefunction being the optimum wavefunction of the selected form [81]. The concept of the density functional for the energy is the basis of early approximate models such as the Fermi-Thomas method [82, 83] and the Hartree-Fock-Slater method [84]. It was not until 1964 that a formal proof was derived to show that the ground state electronic properties can be uniquely determined by the electron density [78]. However, these do not suggest the form that any functional should take, only that one exists.

The benefit of DFT is that no attempt is made to calculate the many-body wavefunction. The energy is instead simply written in terms of the electron density. This, in effect, removes with the huge complexity of a multidimensional wavefunction. Although the simplification is immense, the theory remains general. The energy is then written:

$$E = E[\rho(r)] = \int dr V_{ext}(r)\rho(r) + F[\rho(r)] \tag{2.49}$$

where $\rho(r)$ is the charge density function and F is a universal functional of the charge density and a function of the electron kinetic energy, Hartree Coulomb term, and the exchange-correlation functional. The method works so long as the energy of Equation 2.49 is a minimum for the correct density function.

The problem remains that a value for the exchange-correlation energy (E_{xc}) is unknown. The benefit of DFT is that very simple approximate functionals work. A widely used approximation is the local-density approximation (LDA). LDA states that E_{xc} can be calculated by assuming that for each infinitesimally small element, the E_{xc} is that of a uniform electron gas. This is clearly inadequate since the charge

density is highly non-uniform about an atom. However, LDA is a very effective method for calculating E_{xc} and hence, LDA methods yield good results and works for many cases [85, 86]. Instances where this approximation are poor are generally due to spatial variations in the charge density. As such, the generalized-gradient approximation (GGA) is used which includes the gradient dependence of the density [85].

It is important to note that despite the successes of DFT through LDA and GGA, these are still far from ideal and rely on not only an assumption but also parameters for the functionals. The functionals for E_{xc} are the major approximation and are postulated from physically reasonable assumptions, and their use is justified *a posteriori* by their success.

2.8 Simulation Codes

Two simulation codes were employed to conduct static lattice calculations, CASCADE (Cray Automatic System for the Calculation of Defect Energies) [87] and GULP (General Utility Lattice Program) [88, 89]. CASCADE was originally developed at the Daresbury Laboratory for the CRAY-1 computer and was based on the original HADES (Harwell Automatic Defect Examination System) code [90, 91]. GULP was written as an improved code and incorporates automatic empirical potential fitting routines and calculation of phonon spectra. GULP was used for simultaneous multi-structure fitting of potential parameters.

The CASTEP code [72] was used for all quantum mechanical calculations, and is a part of the Accelrys Materials Studio Package.

2.9 Contour Plots

Due to the nature of many of the results presented in this thesis, contour plot representations of the data have been employed as they facilitate easy identification of regions of compositional interest. An example contour plot is given in Figure 2.15. The plots are generated by ordering the A and B cation radii along x and y axes, respectively. Compounds for which a property has been calculated therefore form a grid of points. The materials property of interest (the independent variable) is displayed by the contours of varying colour. Warm colours represent high values, whilst cool colours represent low values. The compositions for which calculations have been performed are shown by different points overlaid on the plot. The contour lines themselves connect equal property values. In order to facilitate comparisons between different crystal structures, all results are plotted against the VI coordinate ionic radii taken from Shannon [30] so that a full set of consistent ionic radii are available. The ionic radii are simply used as an order parameter.

Data values that fall between simulation results were interpolated via the Kriging method. The Kriging method is a modified weighted average interpolation approach. The weights are calculated by solving sets of linear equations based on the variance of the data being interpolated [92,93]. The benefit of the Kriging method over that of other interpolation schemes, is that the original dataset remains unchanged after the interpolation has been performed. The Kriging method has its roots in geology and the analysis of maps.

The data interpolation and the generation of the resulting contours were performed using MicroCal Origin Pro 6.1 [94].

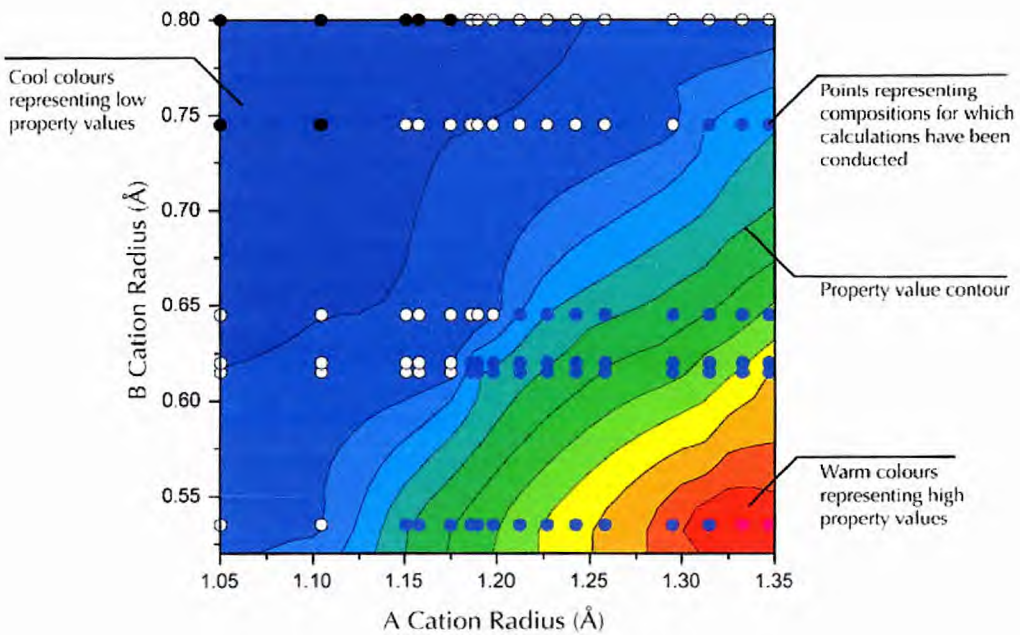


Figure 2.15: Example contour map used to display results presented in this thesis.

Chapter 3

Perovskite Perfect Lattice

3.1 Perovskite Compositions

The mineral perovskite ($CaTiO_3$) is named after a Russian mineralogist, Count Lev Aleksevich von Perovski, and was discovered and named by Gustav Rose in 1839 from samples found in the Ural Mountains [95]. Since then considerable attention has been paid to the perovskite family of compositions. The perovskite is a true engineering ceramic material with a plethora of applications spanning energy production (SOFC technology) [96], environmental containment (radioactive waste encapsulation) [97] and communications (dielectric resonator materials) [98]. Of the more exotic applications, $LaGaO_3$, $PrGaO_3$ and $NdGaO_3$ are being considered as substrates for epitaxy of high T_c superconductors [99].

3.2 Crystallography of The Perovskite Structure

The perovskite structure has the general stoichiometry ABX_3, where "A" and "B" are cations and "X" is an anion. The "A" and "B" cations can have a variety of charges and in the original Perovskite mineral ($CaTiO_3$) the A cation is divalent and the B cation is tetravalent. However, for the purpose of this study, the case where both the A and B cations adopt a trivalent state were considered and the A cations were restricted to being rare earths. Due to the large number of perovskite compositions possible from combinations of cations on the lattice site, 96 compositions were chosen. The ions occupying the A and B lattice sites are detailed in Figure 3.1.

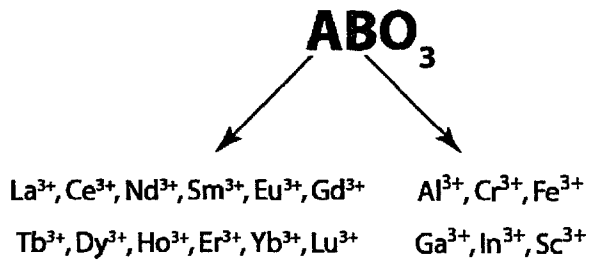


Figure 3.1: Schematic of compositions under study.

The traditional view of the perovskite lattice is that it consists of small B cations within oxygen octahedra, and larger A cations which are XII fold coordinated by oxygen. This structural family is named after the mineral $CaTiO_3$ which exhibits an orthorhombic structure with space group Pnma [100, 101]. For the $A^{3+}B^{3+}O_3$ perovskites the most symmetric structure observed is rhombohedral $R\bar{3}c$ (e.g. $LaAlO_3$) which involves a rotation of the BO_6 octahedra with respect to the cubic structure. However, this distortion from the perfect cubic symmetry is slight [100].

The structure of an ideal cubic perovskite is shown in Figure 3.2, where the A cations

are shown at the corners of the cube, and the B cation in the centre with oxygen ions in the face-centred positions. The spacegroup for cubic perovskites is $Pm\bar{3}m$ (221) [102]; the equivalent positions of the atoms are detailed in Table 3.1.

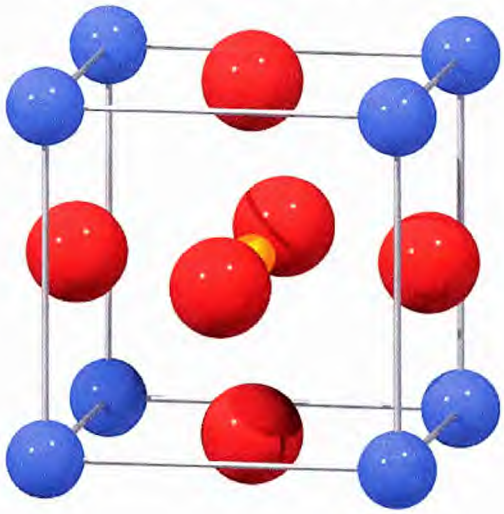


Figure 3.2: Cubic perovskite unit cell. Blue spheres represent the A cations, yellow spheres represent the B cations, and red spheres represent oxygen anions forming an octahedra.

Table 3.1: Atomistic positions in cubic perovskites [103]

Site	Location	Co-ordinates
A cation	(2a)	(0, 0, 0)
B cation	(2a)	$(\frac{1}{2}, \frac{1}{2}, \frac{1}{2})$
O anion	(6b)	$(\frac{1}{2}, \frac{1}{2}, 0)$ $(\frac{1}{2}, 0, \frac{1}{2})$ $(0, \frac{1}{2}, \frac{1}{2})$

The rare earth perovskites have been widely studied using X-ray diffraction and neutron scattering techniques (see Section 3.3). The first study was carried out in 1927 by Goldshmidt [104] which concentrated on $YAlO_3$ and $LaFeO_3$ [105]. Many early studies reported that the perovskites showed mainly cubic or pseudocubic structure, but as work on these systems continued, the number of proposed symmetries increased. The lack of conclusive structural determinations amongst these early stud-

ies are likely due to the relative inaccuracies of the X-ray photographic techniques and are compounded by the small magnitude of the structural distortions [105]. Recent studies have been able to more accurately determine the structure of some perovskites that can then be used as a foundation for subsequent modelling. Literature suggests that many of the materials exhibit the orthorhombic Pnma [106] (or Pbnm) [99, 107] distorted structure at room temperature. This distorted structure can be seen in Figure 3.3 (it is double the size of the cubic cell). Special positions for the Pnma distortion are given in Table 3.2. A further distortion is also possible resulting in a rhombohedral structure with the space group $R\bar{3}c$ [102, 108, 109]. The rhombohedral structure is shown in Figure 3.4; special positions are given in Table 3.3. A further distortion can be seen with the formation of an hexagonal $P6_3cm$ structure, which can be seen in Figure 3.5, with special positions given in Table 3.4. In this variant, the lattice distortions are so great that the A cations are now VII coordinate and the B cations are V coordinate and the structure has lost its direct similarity with the perovskite symmetry. As such, although these are sometimes referred to as perovskites, they are not strictly perovskite structures and are best considered as intermediate between the perovskite and bixbyite or garnet structures.

Beyond the hexagonal region, a cubic bixbyite (space group Ia3) [110] structure is formed illustrated in Figure 3.6, details are given in Table 3.5. For this structure, the cation sites are equivalently octahedrally coordinated by oxygen, and as such the difference between the A and B lattice sites are negligible.

One description of the perfect perovskite structure is to consider corner linked BO_6 octahedra with interstitial A cations as discussed by Hines *et al.* [112]. In an idealised cubic perovskite constructed of rigid spheres, each cation is the perfect size to be in contact with an oxygen anion; the radii of the ions can then be related:

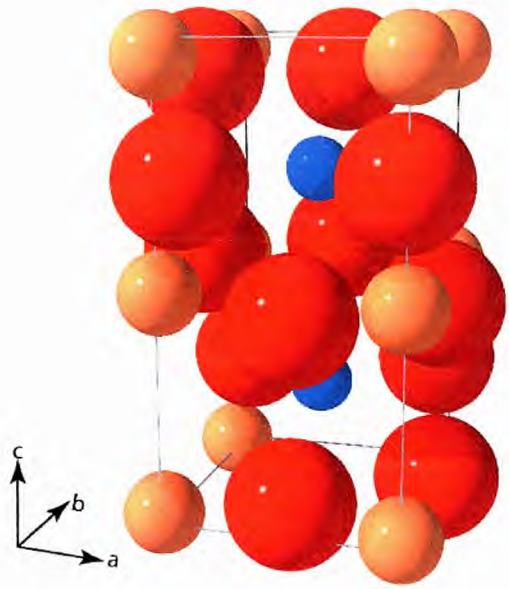


Figure 3.3: Pnma, orthorhombic perovskite unit cell. Blue spheres represent the A cations, yellow spheres represent the B cations, with red spheres representing oxygen ions.

Table 3.2: Atomistic positions in orthorhombic perovskites [103].

Site	Location	Co-ordinates
A cation	(4c)	$\pm$[(u, v, $\frac{1}{4}$) ($\frac{1}{2}$-u, v+$\frac{1}{2}$, $\frac{1}{4}$)]
B cation	(4b)	($\frac{1}{2}$, 0, 0) ($\frac{1}{2}$, $\frac{1}{2}$, 0) (0, 0, $\frac{1}{2}$) (0, $\frac{1}{2}$, $\frac{1}{2}$)
O(1) anion	(4c)	$\pm$[(m, n, $\frac{1}{4}$) ($\frac{1}{2}$-m, n+$\frac{1}{2}$, $\frac{1}{4}$)]
O(2) anion	(8d)	$\pm$[(x, y, z) ($\frac{1}{2}$-x, y+$\frac{1}{2}$, $\frac{1}{2}$-z) (-x, -y, z+$\frac{1}{2}$) (x+$\frac{1}{2}$, $\frac{1}{2}$-y, -z)]

u, v, m, n are dependent on the particular structure under consideration.

$$R_A + R_O = \sqrt{2}(R_B + R_O) \tag{3.1}$$

where, R_A, R_B, and R_O are the relative ionic radii of the A site and B site cations and the oxygen ion respectively.

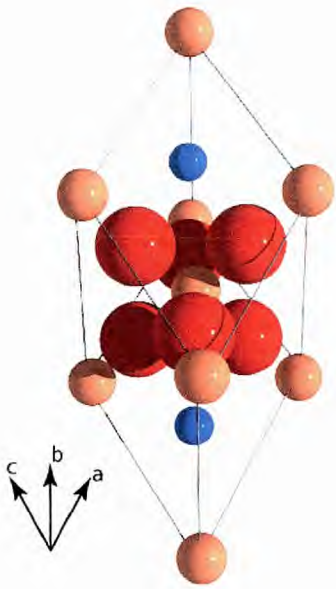


Figure 3.4: R$\bar{3}$c rhombohedral perovskite unit cell. Blue spheres represent the A cations, yellow spheres represent the B cations, and red spheres represent oxygen.

Table 3.3: Atomic positions for rhombohedral perovskites [102].

Site	Location	Co-ordinates
A cation	(6a)	(0, 0, $\frac{1}{4}$)
B cation	(6b)	(0, 0, 0)
O anion	(18e)	(x, 0, $\frac{1}{4}$)

n.b. the above co-ordinates are based on hexagonal axes.

However, with decreasing A cation size, a point will be reached where the cations will be too small to remain in contact with the anions in the cubic structure. Therefore the B-O-B links bend slightly, tilting the BO_6 octahedra to bring some anions into contact with the A cations [112]. To allow for this distortion, a constant, t, is introduced into the above equation, thus:

$$R_A + R_O = t\sqrt{2}(R_B + R_O) \tag{3.2}$$

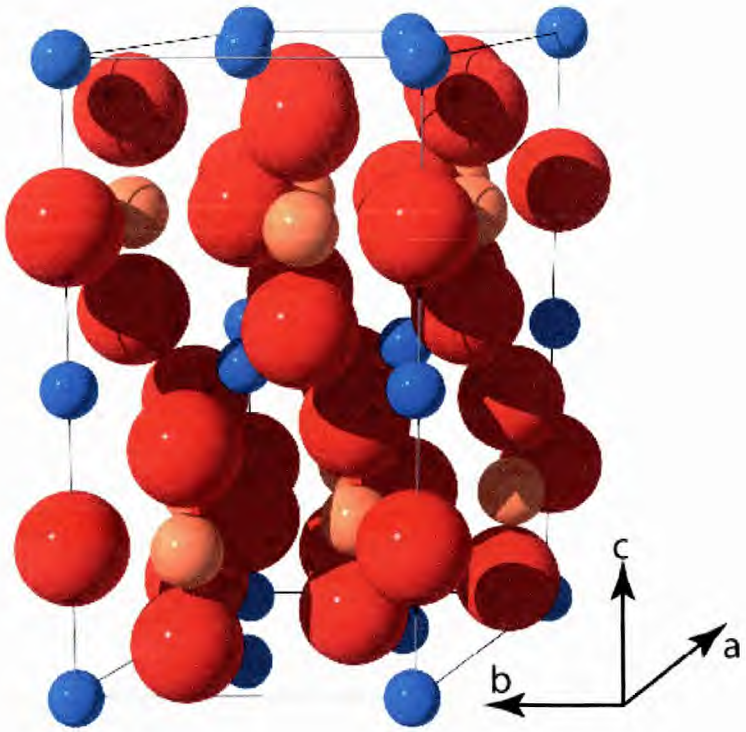


Figure 3.5: $P6_3cm$ hexagonal perovskite unit cell. Blue spheres represent the A cations, yellow spheres represent the B cations, and red spheres represent oxygen.

Table 3.4: Atomic positions for hexagonal perovskites [111].

Site	Location	Co-ordinates
A cation	2a	(0, 0, z)
A cation	4b	$(\frac{1}{3}, \frac{2}{3}, z)$
B cation	6c	(x, 0, z)
O(1) anion	6c	(x, 0, z)
O(2) anion	6c	(x, 0, z)
O(3) anion	2a	(0, 0, z)
O(4) anion	4b	$(\frac{1}{3}, \frac{2}{3}, z)$

The constant, t, is known as the tolerance factor and can be used as a measure of the degree of distortion of a perovskite from ideal cubic. Therefore, the closer to cubic, the closer the value of the tolerance factor is to unity [113]. This distortion

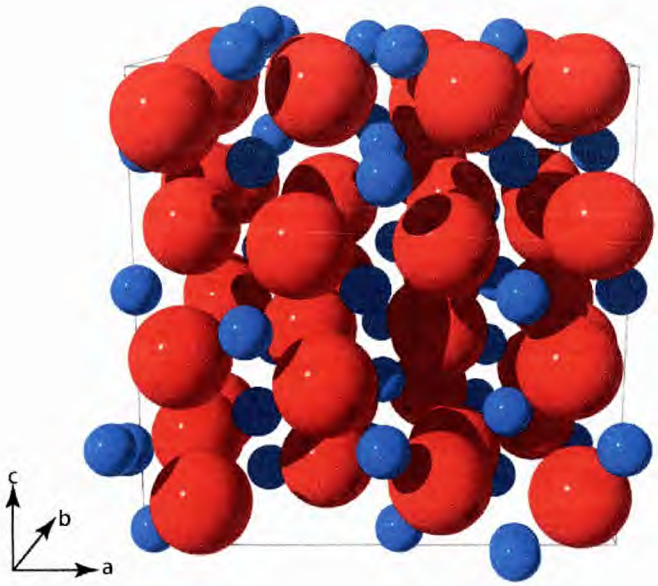
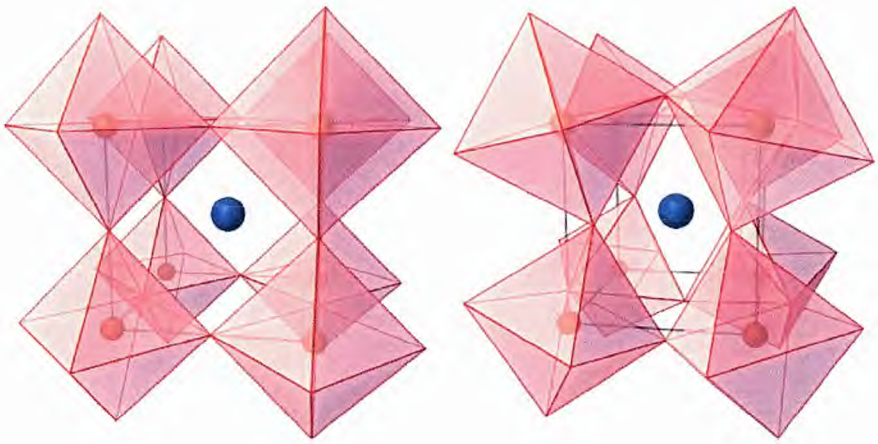


Figure 3.6: Bixbyite unit cell. Blue spheres represent the cations, and red spheres represent oxygen. The A and B cations are distributed over all of the cation sites.

Table 3.5: Atomic positions for cubic bixbyite [110]

Site	Location	Co-ordinates
A/B cation	8b	$(\frac{1}{4}, \frac{1}{4}, \frac{1}{4})$
A/B cation	24d	$(x, 0, \frac{1}{4})$
O anion	48e	(x, y, z)

from cubic to orthorhombic is shown in Figure 3.7. All perovskite distortions that maintain the A and B site oxygen coordinations involve the tilting of the BO_6 octahedra and an associated displacement of the A cation. For the orthorhombic structure, these octahedra tilt about the b and c axes, while in the rhombohedral structure the octahedra tilt about each axis [99]. This octahedral tilting is related to the sizes of the A and B cations (as described by the tolerance factor), for example $AGaO_3$ is more distorted than $AAlO_3$ [99].



(a) Cubic (b) Orthorhombic

Figure 3.7: Perovskite distortion from (a) cubic to (b) orthorhombic.

On the basis of tolerance factor values, it has been proposed [114] that compositions with $1.00 < t < 1.13$ will exhibit hexagonal symmetry. It is therefore not surprising that $LaAlO_3$ adopts the highly symmetric $R\bar{3}c$ structure since its tolerance factor is 1.02, based on the appropriate VI and XII coordinate radii of Shannon [30]. As the A cation radius decreases and/or B cation radius increases, the tolerance factor decreases. In the perovskite family, this is associated with the octahedra tilting to yield lower symmetry arrangements which, here, gives rise to an orthorhombic structure with space group Pnma. This is only in broad agreement with the predictions provided by the tolerance factor where compositions with $t < 1.00$ are associated with cubic and orthorhombic symmetry [114]. Even greater deviations lead to a structure with hexagonal $P6_3cm$ crystallography [108].

Limiting values for the tolerance factor have been determined through experiment. For example, Hines *et al.* suggested (solely by analysis of the tolerance factor) that the perovskite will be cubic if $0.9 < t < 1.0$, and orthorhombic if $0.75 < t <$

0.9 [112]. If the value of t drops below 0.75 the compound has been seen to adopt an hexagonal ilmenite structure ($FeTiO_3$) [112]. Such an analysis works better for 2+, 4+ perovskites (for which the tolerance factor was originally determined) than for the 3+, 3+ perovskites which were considered here.

3.3 Crystal Structure Predictions

Initial crystallographic data were collected from published literature. Tables 3.6, 3.7 and 3.8 show these data and the corresponding references for the experimentally determined crystal structures for perovskite compositions. A particularly important resource utilised is the Inorganic Crystal Structure Database which is part of the Chemical Data Service at Darebury [29].

Table 3.6: Experimentally determined cubic perovskites.

Compound	Space Group	Lattice Parameter (a) Å	Reference
$CeCrO_3$	$Pm\bar{3}m$	3.89	[115]
$CeFeO_3$	-	3.9	[103]
$CeGaO_3$	-	3.879	[103,116]
$GdMnO_3$	-	3.82	[103]
$PrCoO_3$	$Pm\bar{3}m$	3.78	[115]
$PrMnO_3$	-	3.82	[103]
$SmCoO_3$	$Pm\bar{3}m$	3.75	[115]
$SmCrO_3$	$Pm\bar{3}m$	3.86	[115]
$SmVO_3$	-	3.89	[115]

Table 3.7: Experimentally determined orthorhombic perovskites.

Compound	Space Group	Lattice Parameters Å			Reference
		a	b	c	
$CeAlO_3$	P4/mmm	3.7669	3.7669	3.7967	[117]
$CeVO_3$	Pbnm	5.514	5.557	7.808	[118]
$CrBiO_3$	Tetragonal	7.77	-	8.08	[103]
$DyAlO_3$	Pbnm	5.21	5.31	7.4	[108]
$DyFeO_3$	Pbnm	5.302	5.598	7.623	[119]
$DyMnO_3$	Pnma	5.842	7.378	5.28	[120]
$ErFeO_3$	Pbnm	5.263	5.582	7.591	[119]
$EuAlO_3$	Pbnm	5.271	5.292	7.458	[121]
$EuFeO_3$	Pbnm	5.372	5.606	7.685	[119]
$GdAlO_3$	Pbnm	5.247	5.304	7.447	[108]
$GdCoO_3$	-	3.732	3.807	3.676	[116]
$GdCrO_3$	Pbnm	5.312	5.515	7.6 15	[103, 122]
$GdFeO_3$	Pbnm	5.349	5.611	7.669	[119]
$GdScO_3$	Pnma	5.742	7.926	5.482	[123]
$HoFeO_3$	Pbnm	5.278	5.591	7.602	[119]
$LaCrO_3$	Pnma	5.479	7.7562	5.5161	[124]
$LaFeO_3$	Pnma	5.5647	7.8551	5.556	[125]
$LaGaO_3$	Pbnm	5.5245	5.4922	7.774	[126]
$LaMnO_3$	Pbnm	5.5367	5.7473	7.6929	[127]
$LaRhO_3$	Pbnm	5.524	5.679	7.9	[128]
$LaScO_3$	Pbnm	-	-	-	[103]
$LaTiO_3$	Pbnm	5.6301	5.5844	7.901	[129]
$LaVO_3$	Pnma	5.5518	7.848	5.554	[130]
$LuFeO_3$	Pbnm	5.213	5.547	7.565	[119]
$NdCoO_3$	Pnma	5.3312	7.5482	5.3461	[131]
$NdCrO_3$	Pnma	5.4798	7.6918	5.4221	[132]
$NdFeO_3$	Pnma	5.587	7.761	5.4505	[133]
$NdGaO_3$	Pbnm	5.4276	5.4979	7.7078	[107]
$NdMnO_3$	Pnma	5.7119	7.589	5.4119	[106]
$NdScO_3$	Pbnm	5.555	5.744	7.972	[134]

Table 3.7: continued...

Compound	Space Group	Lattice Parameters Å			Reference
		a	b	c	
$NdVO_3$	Pbnm	5.461	5.58	7.762	[118]
$PrCrO_3$	Pbnm	5.444	5.484	7.71	[113]
$PrFeO_3$	Pbnm	5.482	5.578	7.786	[119]
$PrGaO_3$	Pbnm	5.4526	5.4947	7.121	[99]
$PrMnO_3$	Pbnm	5.450	5.786	7.589	[135]
$PrVO_3$	-	5.48	5.59	7.76	[113]
$PuCrO_3$	-	5.46	5.51	7.76	[113]
$PuMnO_3$	Pbnm	5.4	5.786	7.589	[135]
$PuVO_3$	Pbnm	5.48	5.61	7.78	[113]
$ScAlO_3$	Pbnm	4.937	5.2321	7.2045	[136, 137]
$SmAlO_3$	Pbnm	5.2912	5.2904	7.474	[119]
$SmFeO_3$	Pbnm	5.4	5.597	7.711	[119]
$SmVO_3$	-	5.4	5.591	7.68	[138]
$TbFeO_3$	Pbnm	5.3268	5.5978	7.6406	[139]
$YAlO_3$	Pbnm	5.1377	5.2736	7.3085	[140]
$YbFeO_3$	Pbnm	5.233	5.557	7.57	[119]
$YCrO_3$	Pbnm	5.247	5.518	7.54	[141]
$YFeO_3$	Pbnm	5.2819	5.5957	7.6046	[142]
$YScO_3$	Pbnm	5.431	5.712	7.894	[103]

In order to elucidate trends, all compositions must be compared in a single figure. This was achieved by ordering the A cations by size (assuming the XII coordinate radii values throughout) along an x-axis and the B cations (using the VI coordinate values) along a y-axis, thereby forming a 2D grid of compounds. Such a plot (contour map) is shown in Figure 3.8 for all 96 compounds for which calculations were performed. (Of course, for the $P6_3cm$ and Ia3 structures, the cations are not XII and VI coordinations, but these values are maintained in order to facilitate comparisons. The radii are therefore simply an order parameter.)

Table 3.8: Experimentally determined rhombohedral perovskites.

Compound	Space Group	Lattice Parameters Å			Angles			Reference
		a	b	c	α	β	γ	
$BiFeO_3$	R3CH	5.5775	5.5775	13.8616	90	90	120	[143]
$CeFeO_3$	-	3.9	-	-	90	90	90	[103]
$CrBiO_3$	-	7.77	-	8.08	90	90	90	[103]
$GdAlO_3$	-	10.56	10.56	12.89	90	90.6	90	[108]
$GdCrO_3$	-	-	-	-	-	-	-	[144]
$LaAlO_3$	$R\bar{3}c$	5.3647	-	13.1114	60.1	90	90	[102]
$LaCoO_3$	$R\bar{3}CR$	5.3416	5.3416	5.3416	60.99	60.99	60.99	[145]
$LaNiO_3$	$R\bar{3}CH$	5.4573	5.4573	13.1601	90	90	120	[125]
$NdAlO_3$	$R\bar{3}c$	5.3223	5.3223	12.9292	90	90	120	[102]
$PrAlO_3$	$R\bar{3}c$	5.3337	5.3337	12.9766	90	90	120	[113, 121]
$PuAlO_3$	-	5.33	-	-	56.07	90	90	[113]

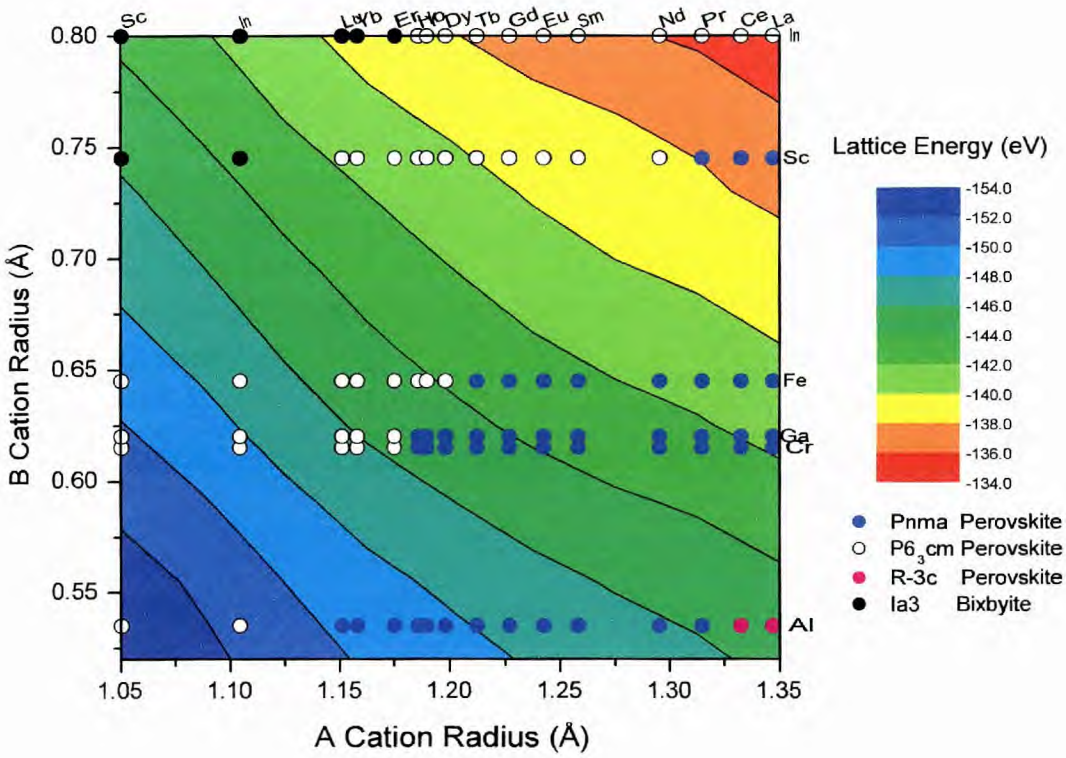


Figure 3.8: Lattice Energy Contour Map.

The lattice energy for each compound was calculated according to Equation 2.3, assuming each of 17 possible crystal structures reported in the literature for materials with the ABO_3 stoichiometry (including the four mentioned above). From these data the lowest lattice energy was identified for each compound so that an energy value was assigned to each composition. Each composition is also identified in Figure 3.8 by a symbol which indicates its lowest energy structure. Lattice energy contours were then generated (see Chapter 2 for details). Such maps facilitate comparisons and allow identification of compositional ranges that are of particular significance. In this case it was at once clear that the compounds fall into four groups: rhombohedral

$R\bar{3}c$, orthorhombic Pnma, hexagonal $P6_3cm$, and bixbyite Ia3. In this regard it is important to note that although 17 different crystal structures have been reported for ABO_3 compounds in general, some have only been reported for $A^{2+}B^{4+}O_3$ materials and others represent only slight distortions from those already mentioned.

By studying Figure 3.8 it is apparent that for the situation when the A cation is large and the B cation is small (e.g. $LaAlO_3$) the lowest energy structure is the rhombohedral $R\bar{3}c$. As the A cation radius decreases and the B cation radius increases, the lowest energy structure changes to be orthorhombic Pnma. Further decreases in A cation radius and increases in B cation radius result in the formation of the hexagonal $P6_3cm$ structure in which the perovskite structure can only be inferred rather than seen directly. Beyond this hexagonal regime, all resemblance of the perovskite structure is lost and a cubic bixbyite is formed with Ia3 symmetry. Now the A and B cation radii are very similar, and in bixbyite both cation sites are VI coordinated by oxygen. Although dissimilar to perovskite, it is possible to consider bixbyite in terms of a defective fluorite structure [146] (the importance of this is discussed in relation to the radiation tolerance of these phases in Chapter 4).

It is also important to note that despite the abrupt crystallographic changes that are predicted (rhombohedral to orthorhombic to hexagonal to bixbyite) the lattice energy contours are continuous across the boundaries. Thus the lattice or internal energy does not change significantly with the changes in the crystallographic structure.

The prediction of structural types is in overall agreement with experimental data and are consistent with changes in the tolerance factor (see Figure 3.9). The tolerance factor decreases from the point where the rhombohedral structure is dominant (high A cation radius and low B cation radius) to where the bixbyite structure is the lowest

energy phase (low A cation radius and high B cation radius). This is consistent with the phase rules derived by Hines *et al.* [112].

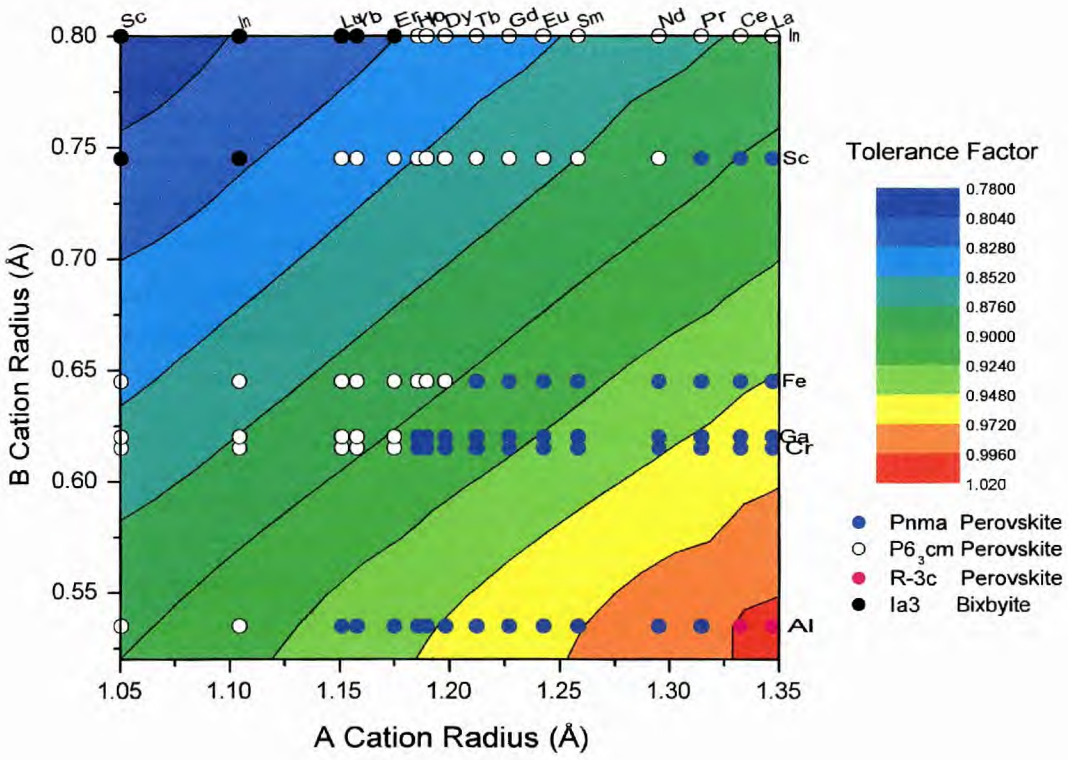


Figure 3.9: Classical Tolerance Factor variations as a function of cation radii.

Figure 3.10 shows a comparison between the lowest lattice energy structure predictions to those determined experimentally and presented in Tables 3.6, 3.7 and 3.8. In particular, where an orthorhombic structure is predicted, experimental structures are known to be orthorhombic in most cases. The same holds true for the hexagonal and rhombohedral structures. However, within the orthorhombic and hexagonal regimes, certain compounds are reported experimentally to exhibit slight variations from Pnma and $P6_3cm$ respectively. A similar high degree of correlation is seen for

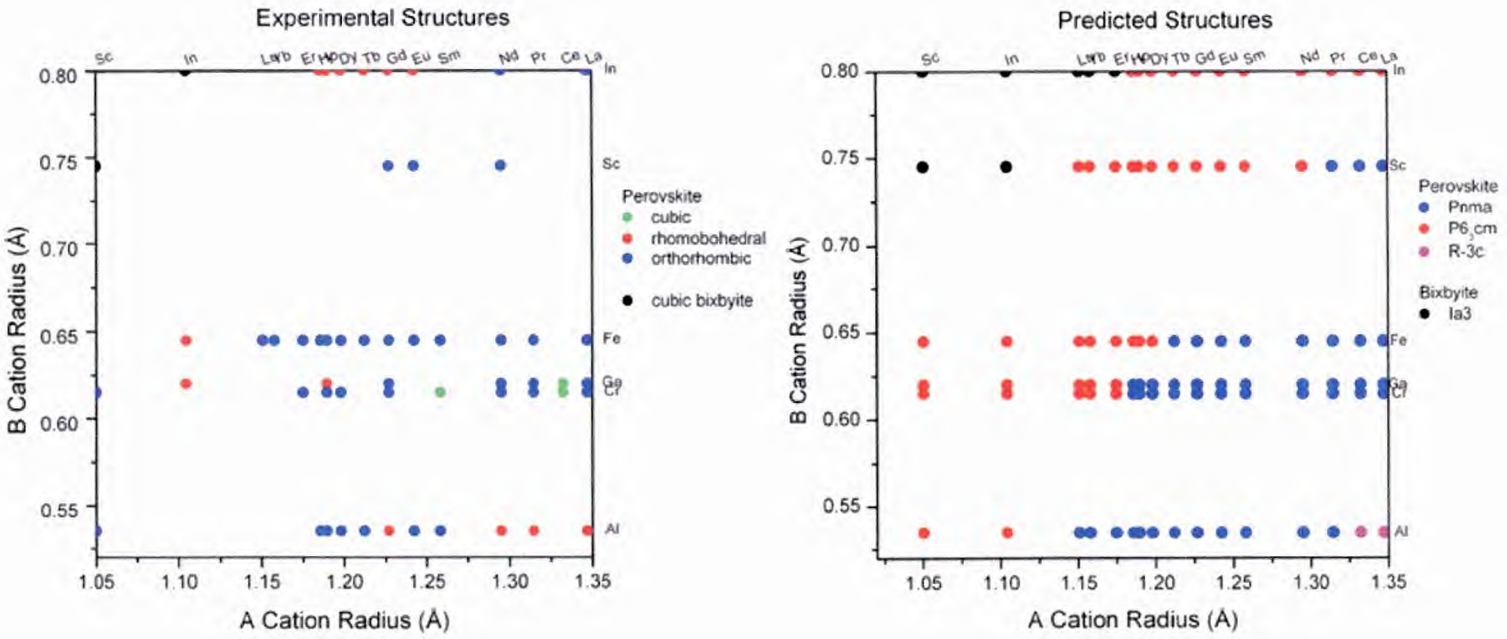


Figure 3.10: Comparison between experimental crystal structures and crystal structure predictions.

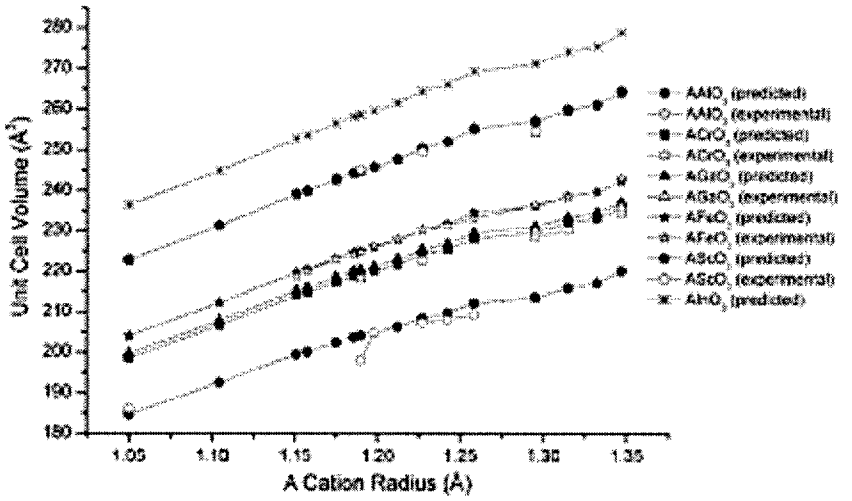


Figure 3.11: Comparison between experimentally determined and predicted unit cell volumes.

the bixbyite structure. Furthermore, a few compositions in the centre of the map, such as $YFeO_3$, do not form an ABO_3 material, but disproportionate into garnet structures (see Section 3.4).

The degree of agreement between the experimentally determined crystallography and that predicted is further seen by analysing Figure 3.11. This shows that the unit cell volumes of the predicted and experimental structures coincide to a high degree. This figure also shows the crystal structures that have been predicted but not seen experimentally also fit to trends that follow the known experimental data.

3.4 Dissociation to Garnet

Up to this point the assumption has been made that all of the compositions under consideration form as stoichiometric perovskites with a 1:1 ratio of A to B cations. This is not always the case and a number of the compositions dissociate to form garnet compositions. Two garnet compositions are stable; these are $A_3B_5O_{12}$ (spacegroup $Ia\bar{3}d$) and $A_4B_2O_9$ (spacegroup $P2_1/c$). Thus the decomposition reaction follows:

$$7ABO_3 \rightleftharpoons A_4B_2O_9 + A_3B_5O_{12} \tag{3.3}$$

The crystallography of cubic garnet, $A_3B_5O_{12}$, is shown in Figure 3.12 (with special positions in Table 3.9). This can be thought of as a distorted cubic close packed array of oxygen with isometric symmetry, with BO_6 octahedra and BO_4 tetrahedra forming a framework by alternately sharing corners. The A site forms an AO_8 dodecahedron [147]. The monoclinic garnet variant, $A_4B_2O_9$ is shown in Figure 3.13 (with special positions in Table 3.10). This form is isostructural with the mineral cuspidine ($Ca_4Si_2O_7F_2$) with the A ion being coordinated by 6 or 7 oxygen ions, and the BO_4 tetrahedra forming B_2O_7 groups by sharing an apical oxygen [148, 149] (in this regard it has some features in common with the ABO_3 $P6_3cm$ varient).

Table 3.9: Atomic positions for cubic ($Ia\bar{3}d$) garnet [150].

Site	Location	Co-ordinates
A cation	24c	$(\frac{1}{8}, 0, \frac{1}{4})$
B(1) cation	16a	(0, 0, 0)
B(2) cation	24d	$(\frac{3}{8}, 0, \frac{1}{4})$
O anion	96h	(x, y, z)

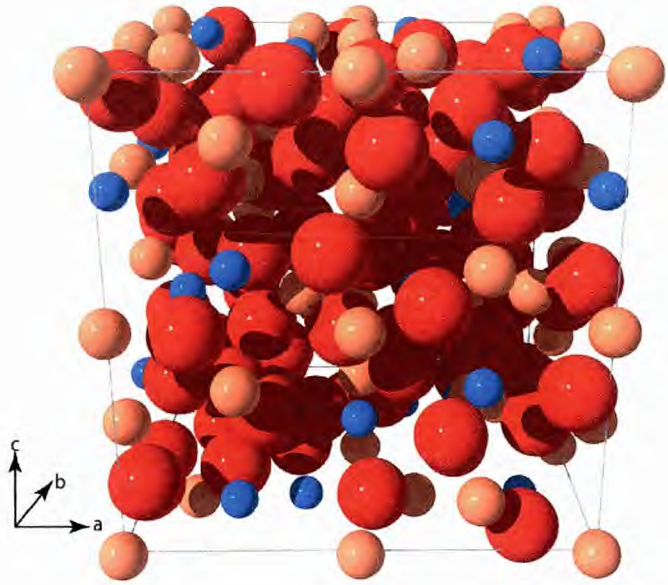


Figure 3.12: Garnet ($IA\bar{3}D$) unit cell. Blue spheres represent the A cations, yellow spheres represent the B cations, and red spheres represent oxygen.

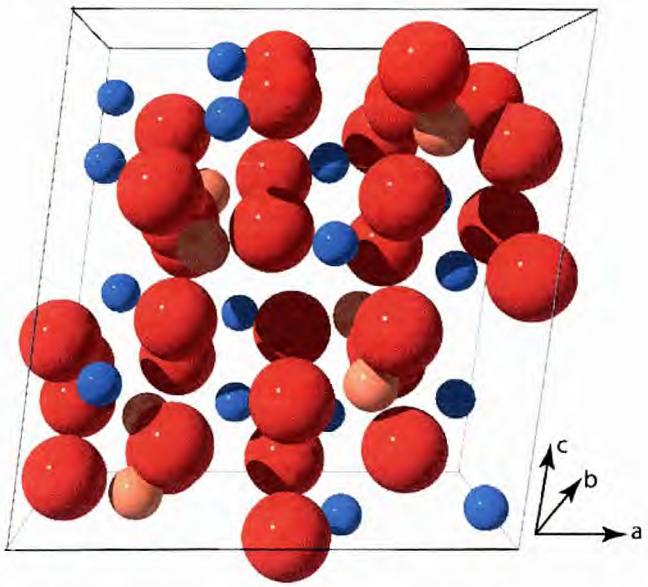


Figure 3.13: Garnet ($P2_1/c$) unit cell. Blue spheres represent the A cations, yellow spheres represent the B cations, and red spheres represent oxygen.

Table 3.10: Atomic positions for monoclinic ($P2_1/c$) garnet [150].

Site	Location	Co-ordinates
A(1-4) cations	4e	(x, y, z)
B(1-2) cations	4e	(x, y, z)
O(1-9) anions	4e	(x, y, z)

Figure 3.14 shows a series of phase diagrams for the Al_2O_3 - RE_2O_3 system (where RE = rare earth). On these and the following phase diagrams, 2:1 refers to the formation of the monoclinic garnet, $A_4B_2O_9$, and 3:5 refers to the formation of cubic garnet, $A_3B_5O_{12}$. This clearly shows that the structure of the compositions is not straightforward. It can be seen that at equilibrium Dy_2O_3, Ho_2O_3, Y_2O_3, Er_2O_3, Tm_2O_3 and Yb_2O_3 do not form perovskites when reacted with Al_2O_3 but rather dissociate to form the two garnet phases. Lu_2O_3 also does not form perovskite but instead forms only the cubic garnet. More recent work by Yoshikawa *et al.* [151] has found that several eutectic reactions can be found in this system. La_2O_3, Ce_2O_3, Pr_2O_3, Nd_2O_3 and Pm_2O_3 do not form eutectics with Al_2O_3; Sm_2O_3, Eu_2O_3 and Gd_2O_3 do form eutectics of the form $Al_2O_3/REAlO_3$; Tb_2O_3, Dy_2O_3, Ho_2O_3, Er_2O_3, Tm_2O_3, Yb_2O_3, Lu_2O_3 and Y_2O_3 also form eutectics, however of the form $Al_2O_3/RE_3Al_5O_{12}$ [151].

Figure 3.15 shows a series of phase diagrams for the Cr_2O_3 - RE_2O_3 system. It can be seen that these compounds do form stoichiometric perovskite and no garnet phase has been observed.

Figure 3.16 shows a series of phase diagrams for the Ga_2O_3 - RE_2O_3 system. It is evident that almost all of the rare earth gallate compounds do not form perovskite and indeed only La_2O_3 and Nd_2O_3 form perovskite with Ga_2O_3. However, both of these also form garnet, La_2O_3 - Ga_2O_3 only forms the monoclinic form, while

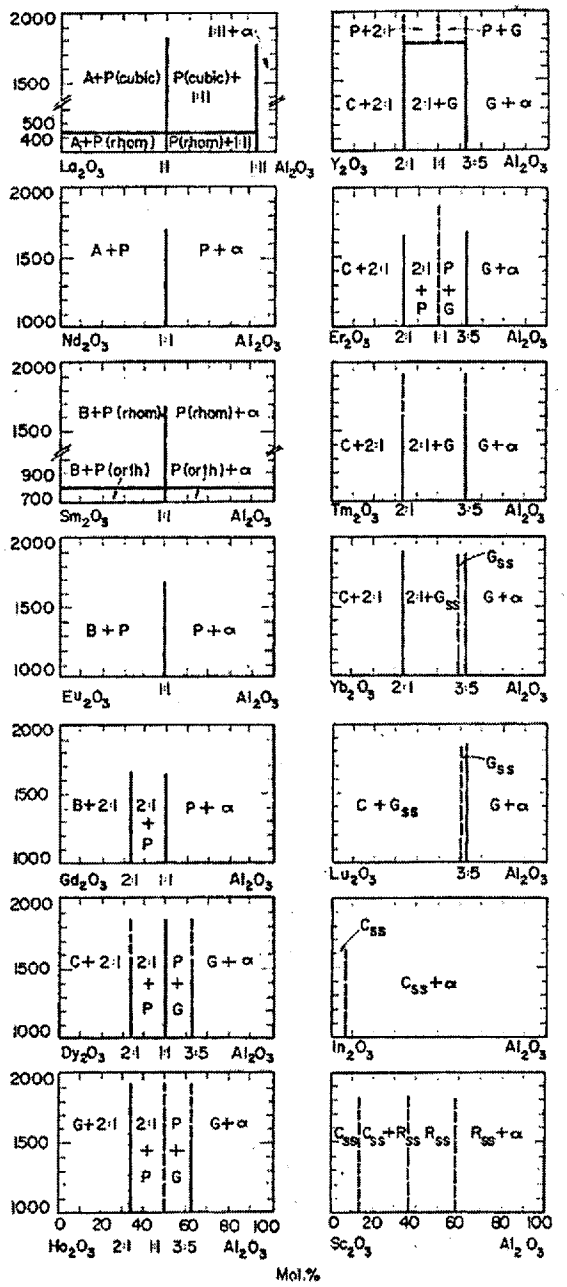


Figure 3.14: Phase diagrams for the Al_2O_3 - RE_2O_3 system [152]. Structure types: A, A type rare earth oxide; B, B type rare earth oxide; C, C type rare earth oxide; G, garnet; 1:11, beta alumina; P, perovskite; R, unknown rhombohedral symmetry; α, corundum.

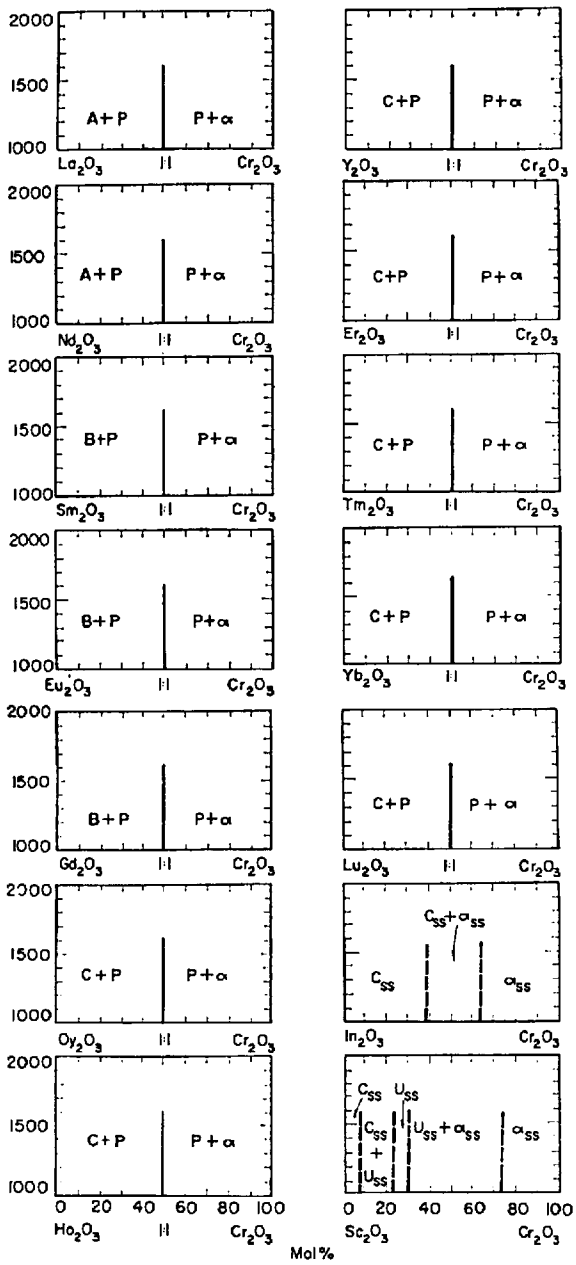


Figure 3.15: Phase diagrams for the Cr_2O_3 - RE_2O_3 system [153]. Structure types: A, A type rare earth oxide; B, B type rare earth oxide; C, C type rare earth oxide; P, perovskite; α, corundum; U, unknown, similar to kappa alumina.

Nd_2O_3 - Ga_2O_3 forms both monoclinic and cubic garnets. Sm_2O_3 and Eu_2O_3 also form both garnet structures (without perovskite formation), and the remaining rare earth sesquioxides form only the cubic garnet with gallia.

Figure 3.17 shows a series of phase diagrams for the Fe_2O_3 - RE_2O_3 system. Here, only Nd_2O_3 forms perovskite alone with Fe_2O_3. All other rare earth sesquioxides form both perovskite and cubic garnet with Fe_2O_3.

Figure 3.18 shows a series of phase diagrams for the Sc_2O_3 - RE_2O_3 system. Here the situation is changed from the previous diagrams, in that the Sc_2O_3 does not form garnet with the rare earth sesquioxides. La_2O_3, Nd_2O_3, Sm_2O_3, Eu_2O_3, Gd_2O_3 and Dy_2O_3 form stoichiometric perovskite, with all remaining rare earth sesquioxide - scandia compositions forming solid solutions of the C rare earth type structure.

Similarly in Figure 3.19 shows a series of phase diagrams for the In_2O_3 - RE_2O_3 system. Here the rare earth sesquioxides for La - Dy form perovskite, with all remaining rare earth formulations creating solid solutions of the C rare earth type structure.

The information regarding which compositions dissociate to form the garnets and those which remain perovskite is summarised in Figure 3.20.

Further to this, some of the garnet compositions have been manufactured experimentally, however only when high temperatures and pressures were applied [158]. Marezio *et al.* considered the formation of Al, Fe and Ga garnets, and found that at high temperatures and pressure even Y-Fe and Y-Al garnet could be forced to dissociate into perovskite and sesquioxide [158].

It has also proved difficult experimentally to make single phased material in the

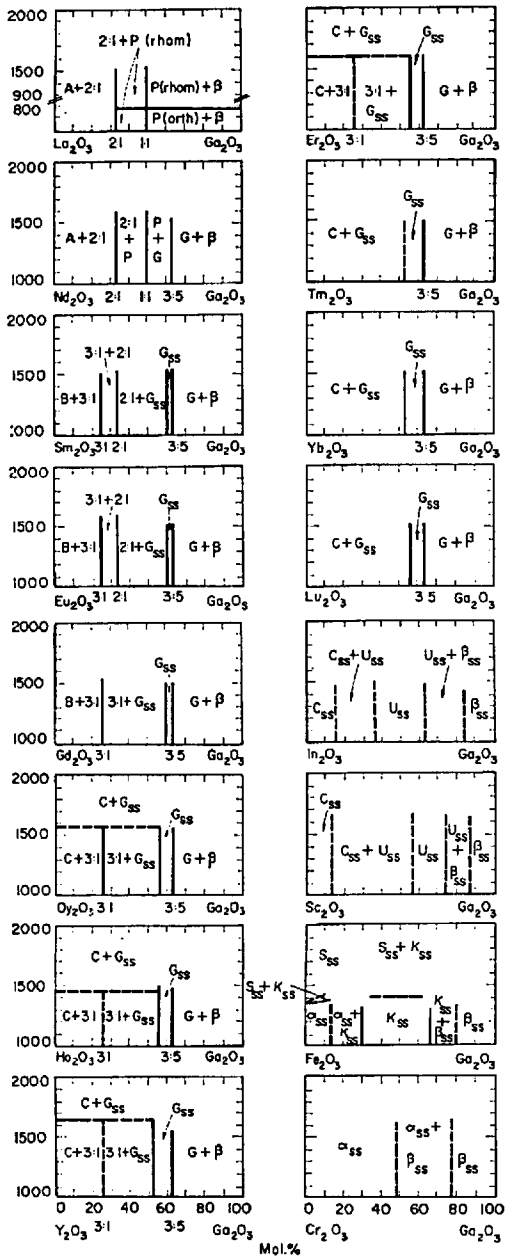


Figure 3.16: Phase diagrams for the Ga_2O_3 - RE_2O_3 system [154]. Structure types: A, A type rare earth oxide; B, B type rare earth oxide; C, C type rare earth oxide; P, perovskite; G, garnet; S, spinel; β, beta gallia; K, kappa alumina; U, unknown, similar to kappa alumina.

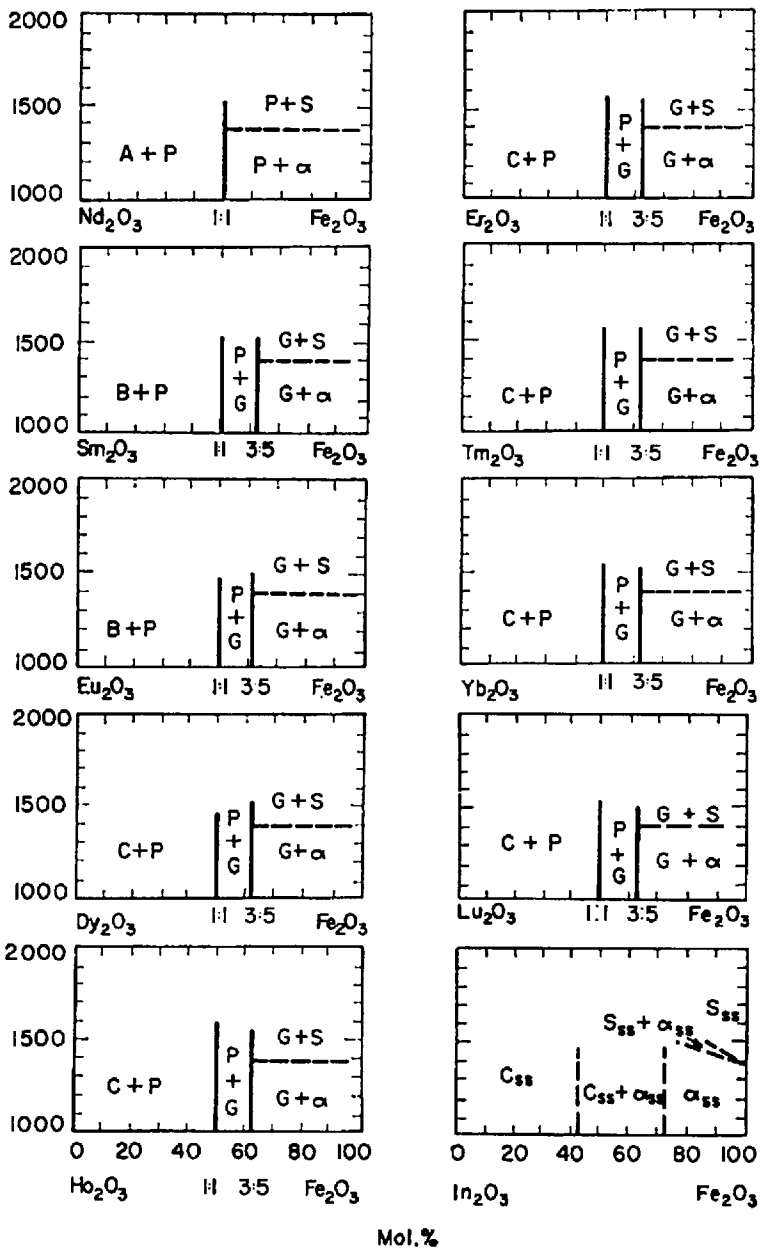


Figure 3.17: Phase diagrams for the Fe_2O_3 - RE_2O_3 system [155]. Structure types: A, A type rare earth oxide; B, B type rare earth oxide; C, C type rare earth oxide; G, garnet; P, perovskite; S, spinel; α, corundum.

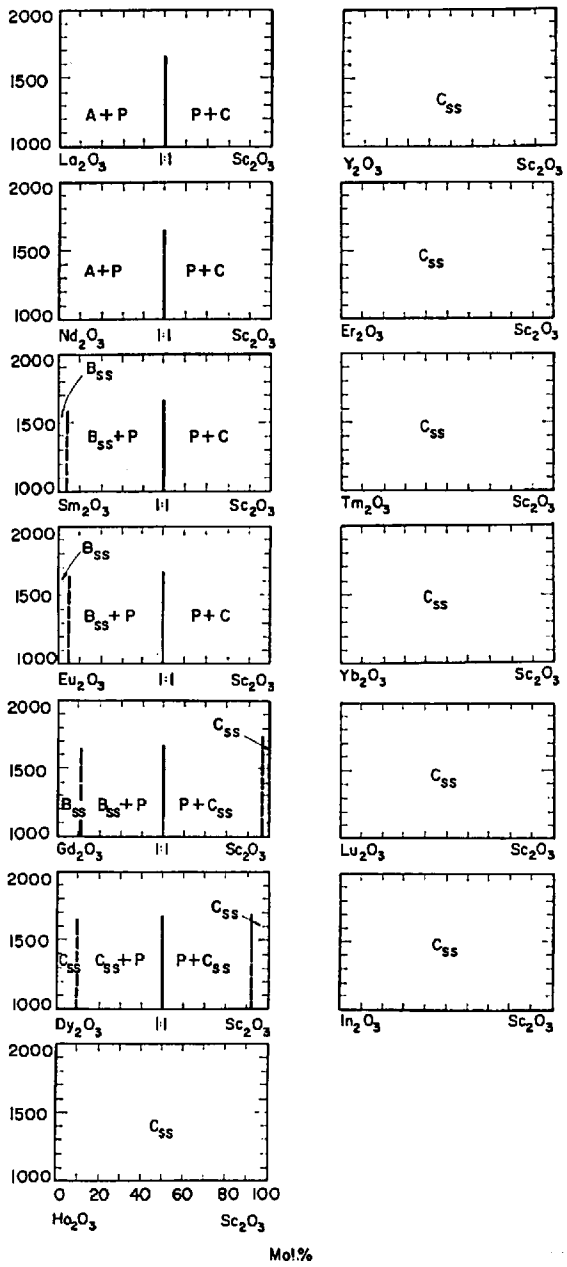


Figure 3.18: Phase diagrams for the Sc_2O_3 - RE_2O_3 system [156]. Structure types: A, A type rare earth oxide; B, B type rare earth oxide; C, C type rare earth oxide; P, perovskite.

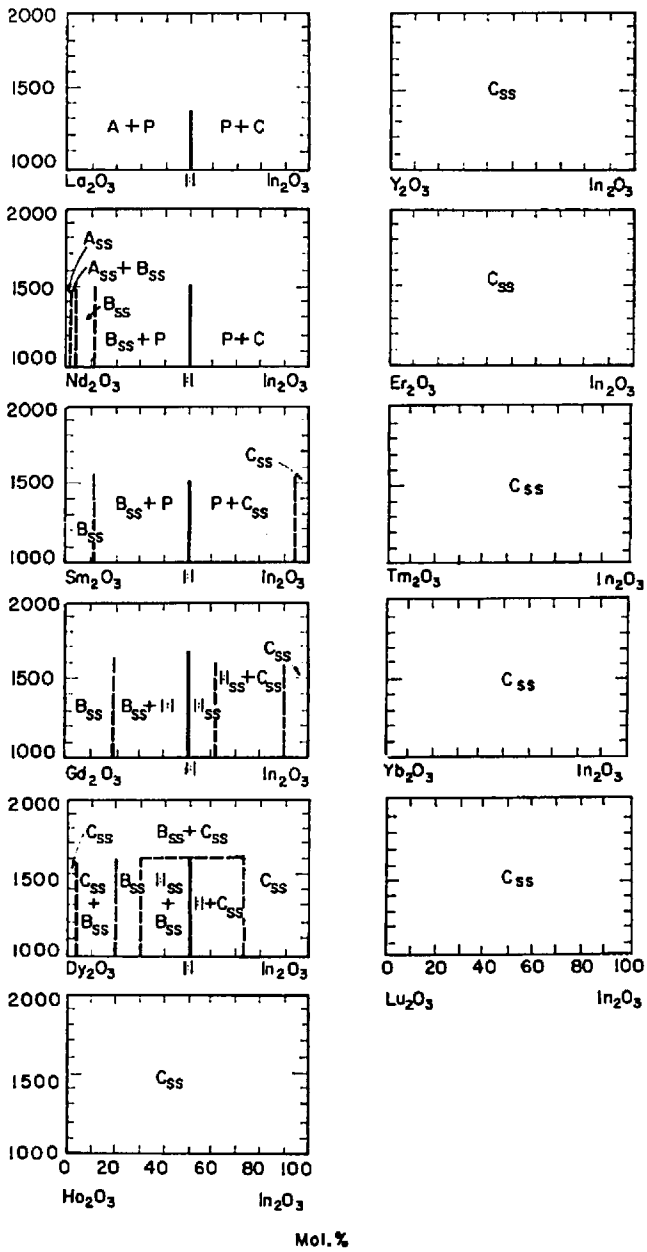


Figure 3.19: Phase diagrams for the In_2O_3 - RE_2O_3 system [157]. Structure types: A, A type rare earth oxide; B, B type rare earth oxide; C, C type rare earth oxide; P, perovskite.

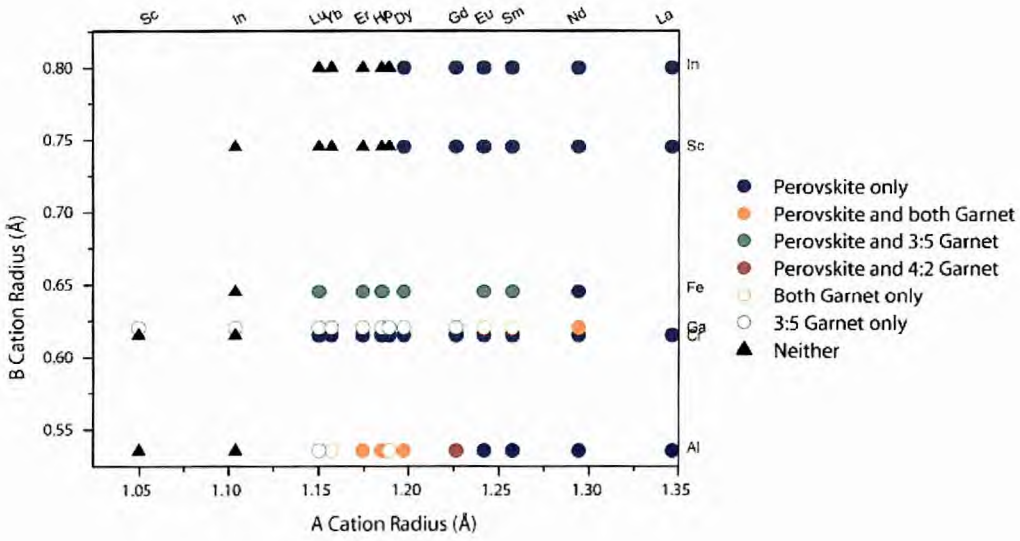


Figure 3.20: Summary of the compositions which form garnets.

region where the garnet is stable. Guo *et al.* [159] states that in attempting to form phase pure $YAlO_3$ (perovskite YAP) the garnet phase $Y_3Al_5O_{12}$ (YAG) forms as a second phase, and even when attempting to make phase pure YAG, the monoclinic garnet ($Y_4Al_2O_9$, YAM) composition forms as a second phase (along with very small amounts of YAP). Others have found even more phases when attempting to make YAG. In particular, Sim *et al.* used precipitation of hydroxides to try to form phase pure YAG, however they found that at elevated temperature some routes formed an intermediate hexagonal perovskite (rather than the expected orthorhombic) which then transformed into YAG and YAM [160, 161].

Despite this, formation of the perovskite phase is possible if considerable effort is expended. Guo *et al.* [159, 162] use a high energy ball milling procedure borrowed from metallurgy to transform a non-equilibrium Y-Al-O formulation into either YAP or YAG.

In summary, a very sensitive equilibrium exists between perovskite and garnet

phases. Consequently the processing route can induce the transformation between different phases, whilst it remains difficult to manufacture a phase pure sample of any of the phases, garnet or perovskite.

3.5 Discontinuity in the Dielectric Constant

Despite the fact that the dissociation reaction between the perovskite and two garnet phases has been known for some time, this knowledge has not yet started to influence the manufacture of electroceramics. In particular, this means comparison of predicted and experimental dielectric constants is not simple.

Experimental dielectric data is sparse for the $A^{3+}B^{3+}O_3$ compounds, however, a smooth change in the dielectric constant of a series of rare earth aluminate perovskites is suggested [163] (the results have been reproduced in Figure 3.21 for reference). This data clearly shows a gradual increase in the dielectric constant as a function of A cation radius. Such a trend might be expected if it is assumed that the crystal structure is not varying significantly from one composition to the next. The increase is then due to the increase in the polarisability of the A^{3+} cation corresponding to the increase in radius. However, if the inherent assumption that the crystal structure of the compound is constant is not valid then the situation becomes potentially much more complex. Indeed, in the phase diagrams (Figure 3.14) some of these compositions dissociate during formation into the two garnet phases.

The simulation predictions of the static dielectric constant (ϵ_r^0) are shown in Figure 3.22 and the predictions for the high frequency dielectric constant (ϵ_r^∞) are shown in Figure 3.23. In this regard it is important to bear in mind that the interionic

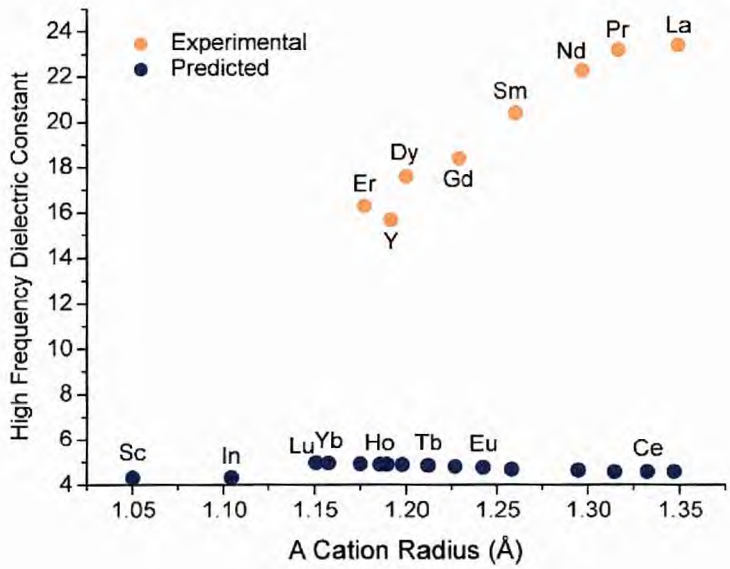


Figure 3.21: Experimentally determined high frequency dielectric constant for rare earth aluminate perovskites [163].

potential model was developed only to reproduce the perfect lattice structures and not other properties. The ϵ_r^∞ displays some evidence of the crystal structure variation, since as the stability of the orthorhombic perovskite decreases, so does ϵ_r^∞. However, if these results for the alumniate compounds are compared to the trend in the experimental dielectric data (Figure 3.21), there is a clear discrepancy. The predicted ϵ_∞ initially increases to a point where it is at the highest value for all of the perovskites, but then decreases back to a lower value. The predictions are based on the assumption that the perovskite is formed, whereas the experimental data contains possible problems since no structure verification was conducted. A similar trend can be seen for ϵ_r^0, where the highest values can be found for intermediate A cation radii aluminate materials. All other compounds have a lower value.

In addition to the difference in the trends between the experimental and predicted values of the dielectric constant, the absolute values are also clearly different. The

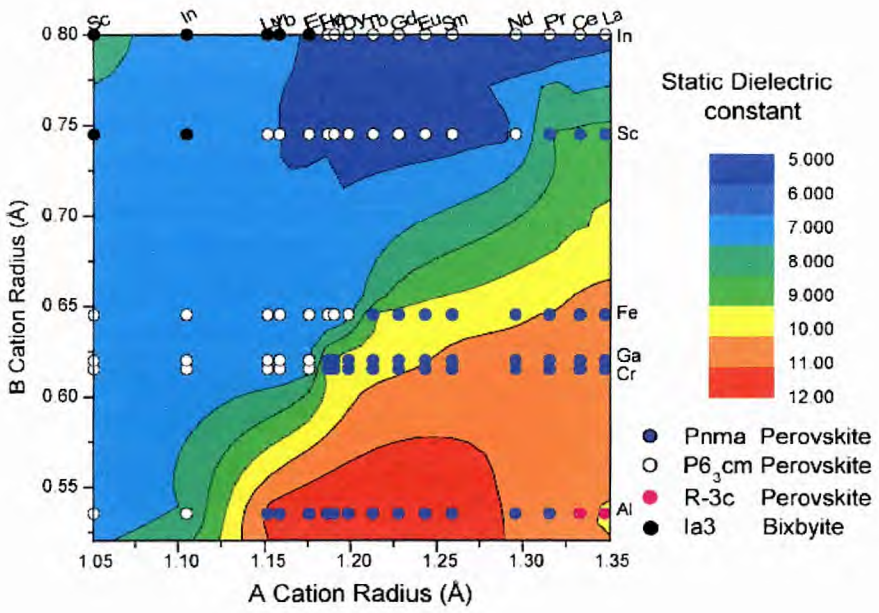


Figure 3.22: Static dielectric constant predictions for the $A^{3+}B^{3+}O_3$ compounds.

predicted values for the aluminates are too low, with ϵ_r^0 ranging from a 12 to 6. This effect could be improved with the derivation of alternative potential parameter sets, and by using a shell model for the cations. This will be discussed further in the next section.

3.6 Potential Fitting Improvements

Several approaches were used in order to improve the crystal structure predictions both to account for small inaccuracies in the lowest energy perovskite lattice predictions, to include predictions for the formation of the garnet phase and to improve the predicted dielectric constants. The important consideration was that the potentials were altered in a manner so that they maintained their internal self consistency. Full details of the methods attempted are presented in Section 2.3.6.

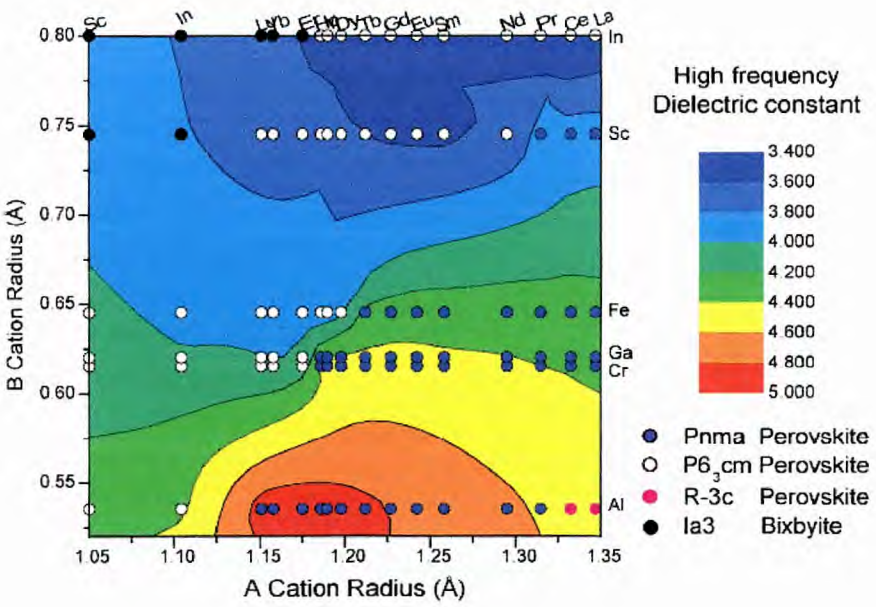


Figure 3.23: High frequency dielectric constant predictions for the $A^{3+}B^{3+}O_3$ compounds.

The first approach taken was to change the $C_{6,ij}$ parameter such that it was a function of the coordination of the cation for which it was describing. Unfortunately, the alteration of the potentials by making the $C_{6,ij}$ dependant on the coordination of the cation did not affect the structure predictions, and did not improve the agreement with experiment, also only very slight changes in the dielectric properties were seen.

Another change was the inclusion of a double exponential oxygen model (Equation 2.28, Section 2.3.6). This model was designed to decrease the bias towards the lower coordinated structures (i.e. the hexagonal $P6_3cm$) by biasing the minima in the interaction energy for the oxygen for larger separations. However, this potential model, did not improve the structure predictions either. The fact that only minor changes to the cation - anion interaction energy were made by the addition of the double exponential oxygen model can be seen by comparing the Al^{3+}-O^{2-} interaction

energies shown in Figure 2.8(b).

Using the same logic, and following an approach which has previously proved successful for simulating hydroxides [65], a damped coulombic model was included (Equation 2.29, Section 2.3.6). As with the other potential models discussed thus far, this dampening of the coulombic interaction did not affect the interaction energies of the different coordinated systems enough to improved the structure or dielectric predictions to any noticeable degree.

A further change to the potential model was the addition of shells for the cations (Section 2.3.6). The values for the shell charge and spring constant were derived from work by Grimes and Grimes on the effective polarisability of a series of ions [53,54]. This shell model was developed for improvement of the dielectric constant predictions. Values of the dielectric constant were altered by using this model, however the fit to the experimental data for the aluminate materials was not improved.

3.7 Quantum Mechanical Structure Predictions

In an attempt to improve the structure predictions using a more rigorous approach, a subset of compositions were investigated further using quantum mechanical calculation. The compositions chosen were those at the boundaries between the different crystal structure types. The rationale being that only small adjustments of the structure predictions is necessary in order to improve the predictions based on pair potential calculations. The results of these calculations are presented in Table 3.11. Unfortunately only a small number of compositions could be investigated in this way due to the considerable computational effort. For the same reason, the garnet

reaction has not been investigated due to the considerable size increase in the unit cell from the perovskite to garnet. The method is explained further in Chapter 2.

A plane wave cut-off of 480 eV was used, therefore these calculations are computationally intensive. In order to reduce the time taken per calculation the Brillouin zone was sampled at the gamma point. This work is still in progress and the results presented in this section are only preliminary.

Table 3.11: Quantum mechanically calculated lattice energies for a subset of perovskite compositions.

Compound	Lattice Energy		
	$R\bar{3}c$	Pnma	$P6_3cm$
$PrAlO_3$	-2674.01659	-2674.73150	-
$NdAlO_3$	-2939.74107	-2941.73123	-
$TbAlO_3$	-	-4898.20138	-4909.45802
$DyAlO_3$	-	-5380.42850	-5386.74393
$HoAlO_3$	-	-5940.89595	-5944.40103
$YbAlO_3$	-	-7791.63605	-7792.27850
$LuAlO_3$	-	-7158.39455	-7158.66758
$InAlO_3$	-	-2944.17758	-2944.65562
$LaInO_3$	-	-3754.64118	-3755.13198
$LaScO_3$	-	-3474.20790	-3474.22043

The results of the quantum mechanical calculations so far show that the Pnma symmetry is preferred over the $R\bar{3}c$ for $PrAlO_3$ and $NdAlO_3$ in agreement with pair potential predictions (Figure 3.10). Experiment, however, suggests that both should be $R\bar{3}c$ [102, 121].

For the remaining compositions (i.e. $TbAlO_3$ through to $LaScO_3$) these simulations suggest that the $P6_3cm$ structure is more stable than the Pnma structure which is not always in agreement with the pair potential predictions. There is agreement with

the pair potential predictions for the $LaInO_3$ which predict the $P6_3cm$ structure. Unfortunately experimentally this compound has the Pnma structure [102]. For $LaScO_3$, the quantum mechanical lattice energy difference between the hexagonal and orthorhombic structures is very small which suggests this compound will be on the boundary between $P6_3cm$ and Pnma phases. To this extent the pair potentials and quantum mechanics results agree in this case.

Discrepancies between the pair potentials and the quantum mechanics predictions are seen for the remaining compounds. For $TbAlO_3$, $DyAlO_3$, $HoAlO_3$, $YbAlO_3$, $LuAlO_3$ and $InAlO_3$, the quantum mechanics predicts that the hexagonal is the lowest energy structure yet the pair potentials only predict $InAlO_3$ to be hexagonal with the remainder being orthorhombic. Experimentally the structures are observed to be orthorhombic in agreement with pair potentials rather than quantum mechanics simulations.

The discrepancy in the quantum mechanical lattice energies may be due to the fact that calculations were performed for the gamma point only. This was to reduce the time constraints on the simulations, however further energy calculations are needed with a greater number of k points in an attempt to either improve or verify the quantum mechanical results.

Chapter 4

Disorder processes in $A^{3+}B^{3+}O_3$ compounds: implications for radiation tolerance.

The work presented in this Chapter has been published in Philosophical Magazine [164].

4.1 Introduction

4.1.1 Motivation

The radiation tolerance of perovskite phases is of importance since $(Ca,Sr)TiO_3$ compositions are a constituent of the Synroc nuclear waste package. Experimental studies have deduced that these phases undergo cation disorder leading to amor-

phisation. This in turn causes rapid leaching of radionuclides into the environment. One root of this amorphisation is the self irradiation of the ceramic by the decay of radionuclides. Cation disorder in particular induces lattice strain, due to the cation size mismatch of an A^{2+} cation on a B^{4+} site (and vice versa), but also the charge variance. The work presented in this chapter investigates the radiation tolerance of an array of perovskite compositions, where both the A and B cations adopt a 3+ valance state, by comparing the energies of the intrinsic defect processes as a function of composition. This allows for the identification of compositions that will be tolerant to intrinsic disorder processes. The initial sections of this chapter give an overview of issues and background relating to nuclear waste disposal and the radiation tolerance of ceramic materials. The results are then presented and comparisons drawn with the radiation tolerance of pyrochlore materials which have previously been investigated using the same computational approach.

4.1.2 Radioactive Waste

The 1940s and 1950s were the formative years of the nuclear industry. This was initiated by an arms race, first between the Allies and the Axis during the Second World War and then between the West[1] and the Soviet Block during the Cold-War. There was a massive drive to at first create (via the Manhattan project) and then to develop increasingly powerful nuclear weapons. The rush to attain these goals meant that insufficient attention was given to radioactive waste management and led to the use of rather basic storage disposal facilities. This is illustrated by a consideration of the economics, e.g. the US spent billions of dollars to develop nuclear weapons

[1]The West is an ideological and political distinction between nations and generally refers to western Europe and the US [165].

and commercialize nuclear power during the 1950s and 1960s whilst only spending a few hundred million to research disposal processes [166]. As such one of the major issues affecting modern society politically, socially and scientifically is radioactive waste management. In a recent white paper, the British government estimated the cost of dealing with the UK's nuclear legacy at £48 billion [167]. The clean-up cost in the US is currently costing $6 billion per year and is approximately the same as the entire US Environmental Protection Agency budget [166]. The US Department of Energy (DoE) currently estimates that $147 billion will be needed by 2070 in order to complete the clean-up [168].

The combined effect of dwindling fossil fuel supplies (estimates vary but are usually around 40 years [169, 170]), the requirement to reduce greenhouse gas emission (in line with the Kyoto protocol [171]), together with insufficient progress of renewable energy resources, leaves nuclear power generation as a highly viable energy source for the near future. As such, if anything, the volumes of radioactive waste are set to increase.

Many nuclear waste types exist, and each can be dealt with in a different manner. Nevertheless, wastes can be categorised as a being one of four types: very low, low, intermediate and high level (adapted from [167]):

Very Low Level Waste (VLLW) Hospital and general industrial waste with low activities. Proper management at the source allows disposal through conventional routes via landfill and incineration.

Low Level Waste (LLW) Hospital, research facility and general industrial waste. Principally lightly contaminated scrap such as metal, soil and clothing. Disposal is at authorised sites only.

Intermediate Level Waste (ILW) Principally from decommissioning, fuel reprocessing and reactor facilities including metal and organic materials. The heat generated is not sufficient to be of concern for storage or disposal facilities. There is currently no final management strategy for long term storage in some countries. In the UK, much of this type of waste is processed into a cementitious form contained in steel canisters.

High Level Waste (HLW) Principally from spent nuclear fuel reprocessing. The activity levels are sufficient to cause self heating of the waste to a level that causes problems for storage. As with ILW there is no final management strategy for dealing with HLW.

Since insufficient consideration was given to radioactive waste, very simple disposal techniques have historically been used. Historical disposal methods (such as those used in the UK) can lead to an inhomogeneous waste mixture. Therefore, part of the clean-up process involves examination and determination of the wastes currently in historical disposal sites [167]. Compounding the problem with historical repositories is their instability due to a build-up of explosive gases at the top of the vessel.

Ineffective stores were also used in other countries, for example in the United States at the Hanford complex [172]. Here the waste remains a significant problem despite attempts to clean up the site with schemes such as leaching the liquid waste into the soil. Since leakage and gas explosions are possible threats, the highly unstable nature of historical waste facilities has driven the development of more stable and easily managed waste forms with increased longevity [173].

Since the inception of nuclear waste management many schemes have been proposed for the long-term storage of HLW, including immobilisation in clay, encapsulation

in ceramics/glasses, land burial, dilution, geological emplacement, disposal in fault zones, ice and space and finally transmutation. Of these, separation of the most dangerous (long half life and highly radioactively toxic) followed by transmutation (the use of reactors to produce less radiotoxic products through fission) is one of the most promising approaches for dealing with the waste, yet currently, the technology is not sufficiently advanced for this to be a viable economic method for dealing with waste. Presently, modified reactors are used to generate the neutrons for the transmutation, however there is work both in the US and the UK on the use of powerful lasers to generate gamma rays to transmute atoms [174]. An example of current technology for transmutation is the fast breeder reactors which are able to transmutate actinides since an excess of neutrons is generated by the fission process, and these reactors then generate (*breed*) new fissile material (other fissile actinides) faster than it is consumed. However, such reactors are not used for waste management [175]. As a result, the current global consensus for the effective long-term disposal of radioactive waste is via encapsulation followed by geological emplacement.

Of the various types of waste, the most hazardous is HLW (including spent fuel) of which there are very large volumes; in the United States alone there are approximately 385,000 cubic metres [176] with a total activity of between 1.2 [176] and 1.6 billion Curies [97] (4.4×10^{19} to 5.9×10^{19} Bq). This waste comes from several sources: the reprocessing of spent fuel rods from nuclear power plants, the decommissioning of nuclear weapons, and the decommissioning of naval propulsion units [176]. The major issue with the disposal of HLW is the necessity to ensure that the radio-nuclides remain within the waste package, that is, they do not enter the environment. HLW may be contained in stainless steel drums and stored in specsially prepared underground repositories (further discussion of this multibarrier

concept can be found later in this Chapter). To minimize the hazards, it is currently international policy to fix the radioactive waste in a solid form before transportation.

Multi-barrier Concept

Due to the importance of preventing radiotoxic elements from entering the biosphere, one method of protection alone is insufficient. A multibarrier protocol has been developed whereby the waste is isolated from the environment via a number of different barriers [97]. Firstly the waste is encapsulated in a host matrix, either ceramic or glass. This is then placed into a metal canister such as a hermetically sealed steal container. This container is then surrounded in a metallic overpack of mild steel, pure or alloyed titanium, which acts as a protective coating for the canister during handling. In order to provide structural support against geological pressures, a sleave is added to protect the package during removal from the clean-up site. Separating the waste packages from each other and the bedrock is the backfill, this is a clay or quartz and aids heat and load transfer and compatibility of all the components in the repository. To facilitate conditioning of the groundwater, immobilisation of the radionuclides and improved compatibility, a buffer is added. Finally a filler is used to fill space between the components.

The multi-barrier disposal scheme is discussed in a technical report of the International Atomic Energy Agency [177], and by Hench [97] and Ewing *et al.* [176].

Geological Emplacement

The aim of geological emplacement is to shield humanity, and indeed the rest of the environment, from the harmful radiation emanating from the HLW by using rock

and sediment. The main principles of the emplacement strategy are reported by Ewing [178]:

1. The repository should be deep, permanent and long-term, and to utilise the radiation decrease, thermal output and toxicity as an advantage.
2. The geological history of the site is indicative of the future geological stability e.g. seismic events, indicating that the site be analysed fully before use.
3. The passive hydraulic and geochemical properties of the site must be key to the isolation e.g. depth of water table.

Many countries are planning on using geological emplacement for the storage of HLW, however, there remains a point of contention regarding the time of operation of the repositories. There are some that believe that the repositories should remain open, so that future generations with more advanced technologies have the opportunity to employ improved methods for dealing with the waste (such as transmutation). This open scheme also has the added benefit that should geological changes occur at the site, the waste can be moved. However, with an open repository, there is a continual financial burden necessary to protect the site from human intrusion, either accidental or malicious. The other choice is to seal the repository. This is favoured by those who believe that future generations should not have to manage our current nuclear legacy. Under this scheme, the repository should involve no human intervention, being sealed by backfilling [179]. The problem with the sealed approach is that suitable sites must be investigated more thoroughly since the timescales over which they should be geologically stable are immense. As such, the sites are investigated to the fullness that the current level of geological science allows, a process which is both time consuming and expensive.

There are currently two sites in the US that are under consideration for this purpose, the Waste Isolation Pilot Plant (WIPP) in New Mexico and the Yucca mountain site in Nevada [178, 180–182]. The WIPP is currently receiving transuranic wastes from defence programs [166, 178]. Characterisation of the Yucca mountain site began in 1987 [183]. Many agencies are involved in the testing of the site. For example the Environmental Protection Agency (EPA) has proposed radiation protection standards and the Nuclear Regulatory Commission (NRC) has proposed rules for implementing standards for disposal schemes. However, despite this gargantuan project, the Yucca mountain site will be unable to accept any HLW until at least 2020 [173].

Encapsulation

There has been many material types considered for the encapsulation of HLW including glasses, polyphase ceramics and concretes (see [97, 176, 184–188] for examples). On the basis of an extensive evaluation of the different waste forms, borosilicate glasses and titanate based polyphase ceramics were selected for further development in 1982 [97]. Borosilicate glass has several advantages over the polyphase ceramic waste forms. The processability of glass compared to ceramic is significant, for example the slurry-fed glass melter is a one step process. This involves a low-melting, non-radioactive glass powder being mixed with the radioactive slurry to form a homogeneous network with the radionuclei becoming trapped in the three dimensional glass network. Such a processing route causes large compositional variability, however here another benefit of the glass is seen in that the waste form is insensitive to such variations [97]. As described earlier, the waste form will be subject to heating due to the radioactive decay of the waste, and again, the thermal stability of the glass has been seen to be favourable. However, the relative economics of the glass

and ceramics waste forms is still under debate as the waste loading of the ceramic is three times that of the glass [97].

To enable the secure immobilisation of the radioactive ions, it is preferable that the ceramic material into which they are inserted shows a regular crystalline lattice with very low defect concentrations since this minimises the flux via low energy transport mechanism. When a material is subjected to radiation damage, a large number of defects (much higher than equilibrium) are formed and become "frozen" into the lattice [189]. If the defect energy is high, the radiation damage leaves a large residual (retained) energy in the lattice, and as this excess energy accumulates it eventually leads to lattice amorphisation. This condition is more significant for cation defects as their mobility in ceramics is poor, and therefore they are difficult to anneal out of the lattice. Since anion mobility is generally far higher the criteria are slightly different, the important defect processes for the recovery involve anions, most notably the anion Frenkel reaction. As such, a low retained cation energy is a necessary, but not complete condition for the radiation tolerance assessment of a material. Atomistic simulation can be used to investigate the radiation tolerance of crystalline oxides. For example, a recent study by Sickafus *et al.* [4] assessed the stability of pyrochlores (complex oxides with a fluorite-related structure) for application in HLW storage. They analysed the energy of the localized disorder, in this system, and assumed that cation disorder commenced via the anti-site reaction (Equation 4.5).

Several polyphase ceramic materials are currently being considered for the long-term encapsulation of the radioactive waste, with one of the more promising being Synroc or "synthetic rock" which was initially developed by Prof. Ted Ringwood of the Australian National University in 1978 [190,191]. Synroc is a mineral analogue that

was specifically designed to immobilise HLW and contains a series of highly durable titanate phases. There are several variants of Synroc that have been investigated for specific applications, for example, Synroc C was designed for the immobilization of liquid HLW from the reprocessing of light water reactor fuel [182]. The composition of Synroc mainly includes natural titanate materials such as zirconolite ($CaZrTi_2O_7$), hollandite ($BaAl_2Ti_6O_{16}$) and perovskite ($CaTiO_3$) [176]. Different transuranic elements are known to partition to the various phases within Synroc, e.g. neptunium (Np) will be incorporated into the zirconolite [184]. These waste elements incorporate into Synroc via a substitutional solid solution mechanism [184]. Within the Synroc phases, the elements substitute onto different lattice sites depending upon their relative ionic radii and valence. Consequently, the radiation tolerance of single perovskite phases has been investigated as part of an overall strategy to understand which of the Synroc phases are the most radiation tolerant.

Within Synroc, the low durability of the perovskite is masked by the high durability of other constituent phases [192]. The leaching of the waste elements from the perovskite phase increases with increasing damage to the crystal structure, which can be considerable - one study even found the formation of anatase (TiO_2) within a perovskite sample doped with Curium (Cm) [192].

Other schemes to immobilize the HLW are in development; one of the more promising is a Synroc-glass composite, which is being studied at the Australian Nuclear Science and Technology Organization (ANSTO), the French Atomic Energy commission and the Russian Ministry for Atomic Energy (Minatom) [182]. The reason for the interest in the Synroc-glass composite is the improved the relatively poor waste loading of the glass phase alone. The waste loading of the Synroc phase is much higher than that of the glass, Synroc-C, for example, can hold up to 30% HLW by weight [182].

Furthermore, so called vitreous waste forms often contain minor amounts of ceramic phase anyway.

Damage Types in Crystalline Materials

The radiation damage to the encapsulating matrix during disposal is relatively insignificant, yet, post-disposal radiation damage can be immense. It is estimated that the accumulated radiation dose at the end of 10,000 years is equivalent to 0.5 displacements per atom [176]. This is well within the range during which important changes in physical and chemical properties can occur, mainly the transition from a crystalline to amorphous state. When a material becomes irradiated, the energy imparted causes atomic disorder processes to occur. This disorder can lead to either swelling or, in some cases, contraction of the bulk material, which in turn causes the formation of microcracks. These microcracks are able to serve as fast migration pathways for the radioactive contaminants to escape the encasement.

It is possible for ionic materials to accommodate extensive disorder without exhibiting excessive structural deterioration. Disorder effects are mitigated to a large degree by the clustering and recombination of lattice defects during and subsequent to the irradiation bombardment. The associated lattice strains can also be accommodated by the simple relaxation of the neighbouring atoms or ions [193]. The majority of damage in ceramic materials is via elastic collisions, where nuclear particles collide with the atoms of the host lattice. If these incident particles have sufficient energy, the host atoms can become displaced, and these recoiling atoms are then able to collide with other lattice atoms causing further displacements. Given sufficient incident energy, such knock-on collisions can develop into significant collision cascades. If the radioactive particles are sufficiently fast and charged they can cause ionisation

of the host atoms so that charged defects such as excitons and polarons are formed. If nuclear reactions are induced by the incident particles, transmutation can occur whereby the unstable nuclei can radioactively decay to other atoms [193]. The alpha decay (release of a helium nucleus) of incorporated actinides causes the self damage in HLW forms and leads to a crystalline to amorphous transformation [188]. The degree to which the material becomes amorphous effects the leach rate of the HLW, and therefore the more damaged the host matrix becomes, the easier it is for the radionuclei to escape into the environment.

Perovskite Radiation Tolerance

The solid solution series of materials (Ca,Sr)TiO_3 are a component of the original compounds within Synroc [190] and as such, the majority of research concerning the radiation tolerance of perovskite materials has focused on such compositions. Waste elements are incorporated into each of the Synroc phases via a substitutional solid solution mechanism. The two phases capable of incorporating transuranic elements are zirconolite and perovskite [184]. Smaller radius ions (e.g. U^{4+}, Y^{3+} and Gd^{3+}) generally partition to zirconolite, while larger ions (e.g. Nd^{3+} and Ce^{3+}) partition to the perovskite [187]. The relative stability of the Synroc constituents upon exposure to leachants decreases from zirconolite to hollandite to perovskite [187]. Despite this, the average critical dose for the amorphisation for perovskite is 2 - 5 times higher than that for zirconolite [188].

When a perovskite is subjected to radiation damage, its cation sublattice will experience disorder, of which a common example is the antisite process, where A and B cations are "swapped". For materials such as (Ca,Sr)TiO_3, this introduces a major charge redistribution into the lattice with considerable associated strains. (This ef-

fect was first described by Zachariasen [194] for the example of metaboric acid where it was shown that an effective charge on a lattice site will cause a change in the bond lengths of the neighbouring oxygen ions). An additional factor contributing to the lattice strain associated with antisite disorder in perovskites is the significant size difference between the A and B cations.

Here studies of radiation tolerance in perovskites are extended by considering ABO_3 materials in which the A and B cations both assume formal 3+ valence states (as described in Chapter 3). One of the primary motivations for studying these 3:3 compounds is that cation disorder does not lead to a charge imbalance (although there will be some local charge redistribution in the vicinity of defects). It may be that the equivalence of the charge states leads to lower disorder energies; however, for many perovskites a significant cation size difference exists.

An exceptionally broad range of ABO_3 compositions is considered with the A cation radii ranging from Sc^{3+} (1.05 Å) to La^{3+} (1.34 Å) and the B cation radii ranging from Al^{3+} (0.535 Å) to In^{3+} (0.8 Å). Consequently, at one extreme of the compositional range the A and B cations are of closer in size. Such $A^{3+}B^{3+}O_3$ compositions no longer exhibit a perovskite-like structure, but are of the cubic bixbyite type. Previous work [146] considered the radiation tolerance of the bixbyite structure by investigating the rare earth oxides Er_2O_3 and Dy_2O_3. Both compounds were found to be highly radiation tolerant. Part of the explanation given for this observation was the similarity of the bixbyite and fluorite structures. Although the rare earth bixbyites are not within the present compositional range, this study also provided further insight into why bixbyite materials are radiation tolerant.

In this study, atomic scale computer simulation techniques were used to predict the structures and energies associated with defect formation in these compounds.

Those structures which exhibit larger energies for disorder processes will assume a greater residual or retained energy upon disorder and on this basis are assumed less radiation tolerant [4]. Such an approach proved successful in earlier work predicting the relative radiation tolerance of an extended set of materials with the pyrochlore structure [4]. Those conclusions were also supported by direct molecular dynamics simulations of cascades in pyrochlores [195]. It is acknowledged, however, that factors other than retained energy, in particular damage recovery or annealing processes, are important in determining the radiation tolerance of materials [176]. As such, the energies for those processes that form the defects necessary for transport processes are of interest.

4.1.3 Crystallography

Perovskite

In order to describe the intrinsic defect behaviour of perovskites, with a view to predicting the radiation tolerance, the structure predictions (Chapter 3) have been chosen for the case where the garnet decomposition reaction is negated. Therefore all compositions presented here are assumed to adopt the ABO_3 stoichiometry.

Pyrochlore

Since comparison will be made to pyrochlore compounds it is necessary to discuss the pyrochlore structure. The general formula for pyrochlore is $A_2B_2O_7$ and simple pyrochlores exist in two different forms: (3+, 4+) with formula $A_2^{3+}B_2^{4+}O_7$ and (2+, 5+) with formula $A_2^{2+}B_2^{5+}O_7$. However, for the purpose of this report, only

3+, 4+ pyrochlores were considered. The pyrochlore crystal structure has been widely investigated, both generally [196, 197] and for application to HLW storage [5, 198, 199]. The full pyrochlore unit cell contains eight formula units and has spacegroup $Fd\bar{3}m$ (227) [200]. The ion positions are presented in Table 4.1 and the full pyrochlore unit cell is shown in Figure 4.1. It is important to note that the atom positions have been specified relative to the origin at a B site.

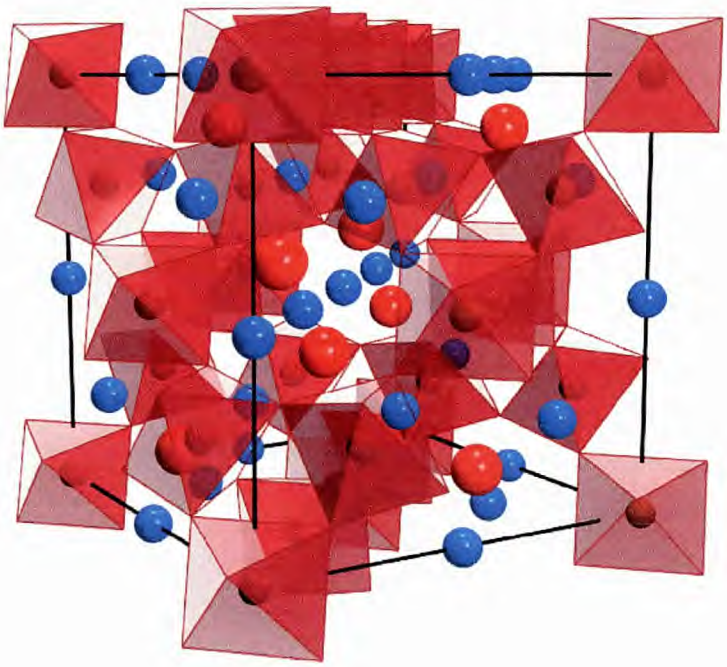


Figure 4.1: Full unit cell of pyrochlore oxide. The red octahedra represent the oxygen octahedra with oxygen ions on the vertices, the red spheres represent the 8a oxygen position and the large blue spheres represent the A^{3+} cation. The smaller B^{4+} cations are within the oxygen octahedra.

The pyrochlore structure can be considered as a defective, distorted fluorite. The general formula for the fluorite would be $(A,B)_4O_8$ compared to the pyrochlore which has one less anion, $(A_2B_2O_7)$. This oxygen vacancy causes a distortion to the surrounding oxygen ions which results in the pyrochlore structure (see Figure

Table 4.1: Atomic positions for pyrochlore oxides [150]

Site	Location	Co-ordinates
A^{3+} cation	(16d)	$(\frac{5}{8}, \frac{5}{8}, \frac{5}{8})$
B^{4+} cation	(16c)	$(\frac{1}{8}, \frac{1}{8}, \frac{1}{8})$
O(1) anion	(48f)	(x, 0, 0)
O(2) anion	(8b)	$(\frac{1}{2}, \frac{1}{2}, \frac{1}{2})$

4.1), it is noteworthy that the cations are still on fluorite sites (Table 4.1). As with the perovskite, the B cations are smaller than the A cations, and are surrounded by oxygen octahedra such that BO_6 corner sharing octahedra form sheets parallel to the (111) plane.

4.2 Results and Discussion

4.2.1 Disorder Processes

Once the lowest energy lattice structure had been identified (see Chapter 3), the individual component defect energies were calculated. Then each compound was assigned Schottky, oxygen Frenkel, cation Frenkel or antisite defect process energies by following the total defect processes described in Equations 4.1, 4.2, 4.3, 4.4 and 4.5 below. The positions of the interstitial defects necessary for Equations 4.2, 4.3 and 4.4 is given in Table 4.2.

$$A_A^X + B_B^X + 3O_O^X \rightleftharpoons V_A''' + V_B''' + 3V_O^{\bullet\bullet} + ABO_3 \tag{4.1}$$

$$O_O^X \rightleftharpoons V_O^{\bullet\bullet} + O_i'' \tag{4.2}$$

$$A_A^X \rightleftharpoons V_A''' + A_i^{\bullet\bullet\bullet} \tag{4.3}$$

$$B_B^X \rightleftharpoons V_B''' + B_i^{\bullet\bullet\bullet} \tag{4.4}$$

$$A_A^X + B_B^X \rightleftharpoons A_B^X + B_A^X \tag{4.5}$$

Table 4.2: The position of the oxygen interstitial defect as used in the oxygen Frenkel reaction (Equation 4.2).

Crystal Structure	Wyckoff Site [150]	Position
Pnma	4a	(0, 0, 0)
$R\bar{3}c$	18d	(0.5, 0, 0)
$P6_3cm$	12d	(0.875, 0.525, 0.05)
Ia3	24d	(0.25, 0.46, 0)

In a similar manner as described for perfect lattice energies, defect process energies can be represented over the full compositional range on an energy contour map. Low energy regions identify compounds for which the defect process is more favourable. In order to allow for comparison between the different defect reactions, the energies presented were normalised per defect, as dictated by a mass action analysis [201], i.e. the Schottky process has a normalisation factor of 5, whilst the antisite and Frenkel processes have normalisation factors of 2 (see Appendix A).

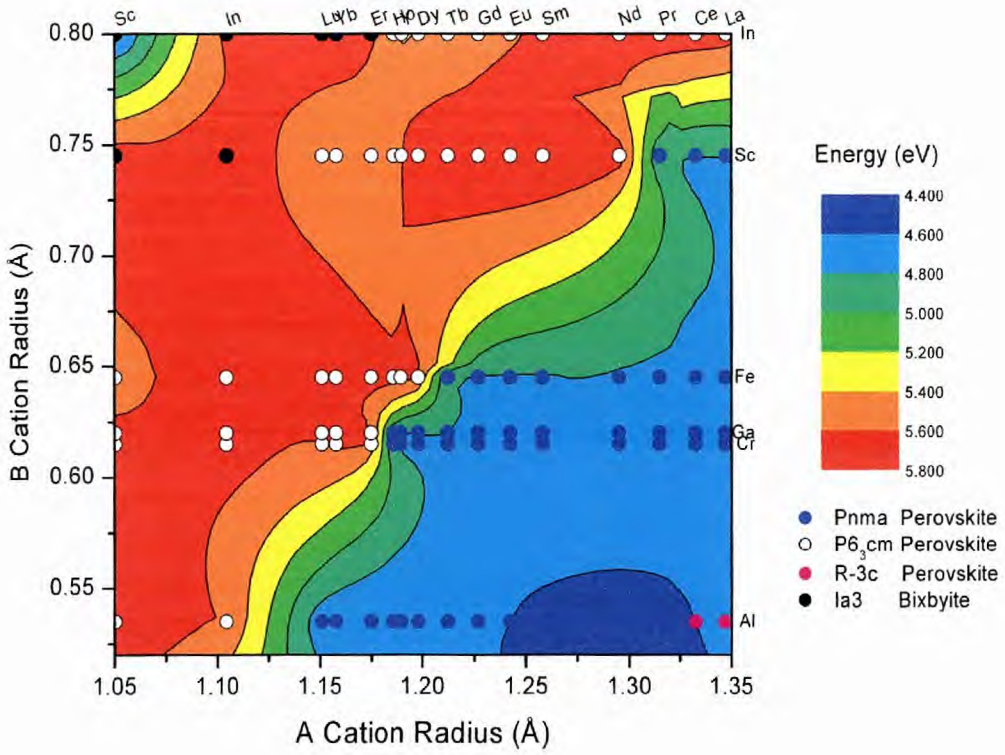


Figure 4.2: Schottky reaction energy contour map.

It can be seen from Figure 4.2 that the Schottky defect process energy (see Equation 4.1) shows considerable variation with changes in crystal structure over the compositional space. Compositions which adopt the rhombohedral ($R\bar{3}c$) and orthorhombic (Pnma) symmetries show little variation with changes in composition. As the stability of the orthorhombic phase decreases, with decreasing A^{3+} cation radii, the Schottky defect energy increases. The Schottky energy reaches a maximum of 5.7 eV for compositions which adopt the hexagonal ($P6_3cm$) symmetry. The Schottky energy then decreases for compositions which adopt the bixbyite (Ia3) symmetry.

The closer the compositions are to the classical view of the perovskite with the

corner shared octahedra, the lower the Schottky defect process energy. Within the hexagonal materials, the oxygen ions do not form octahedra, and the structure is much more open than any of the other symmetries (see Chapter 3). The more open the different ABO_3 structures, the higher the Schottky reaction energies; this is due to the higher vacancy formation energies for these materials. The closer packing of the rhombohedral and orthorhombic structures leads to lower vacancy energies since these materials are able to accommodate the extra space more readily than the hexagonal perovskite. This argument also holds true for the bixbyite materials. This is a very high symmetry structure, and here all the cation sites are surrounded by oxygen octahedra, and thus, the bixbyite structures are densely packed and they are readily able to accommodate lattice vacancies.

Figure 4.3 shows the oxygen Frenkel defect reaction energy contour map (see Equation 4.2). Perovskite compositions that exhibit the rhombohedral crystallography have the highest oxygen Frenkel defect reaction energies at 6.4 eV. The energy then decreases for those compositions adopting the orthorhombic crystallography. Moving further across Figure 4.3 (decreasing A cation radii, and increasing B cation radii), it can be seen that at the boundary between the orthorhombic and hexagonal material a step in the energy values occurs. The oxygen Frenkel reaction energies are lower for the hexagonal compositions than the other perovskite phases. The defect energies continue to decrease reaching a minimum of 3.2 eV for materials that exhibit the bixbyite structure. The general trend in the defect reaction energy for the perovskite materials shows that there is a decrease as the crystallography becomes more open. The oxygen Frenkel reaction shows competing factors, there is an energy contribution due to the formation of an oxygen vacancy, and one for the formation of an interstitial oxygen defect.

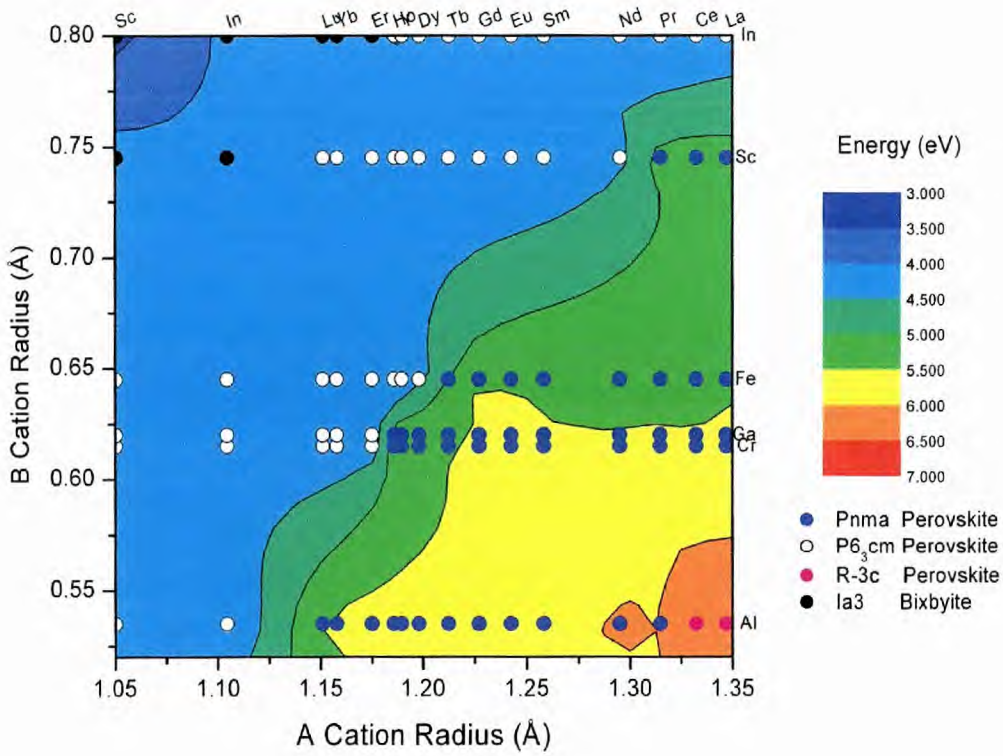


Figure 4.3: Oxygen Frenkel reaction energy contour map.

As the crystal structures become more open with the increasing distortion of the BO_6 octahedra ($R\bar{3}c$ > Pnma > $P6_3cm$) the lattice is able to accommodate the interstitial defect more readily. The bixbyite lattice is able to accommodate defects more readily again due to the nature of the lattice. Despite the fact that the bulk of the crystal structure consists of octahedra, both BO_6 and AO_6, there is a large central interstitial site which takes the form a double oxygen 6 membered ring (see Chapter 3).

The A cation Frenkel defect reaction energies (Equation 4.3) are shown in Figure 4.4. The general trend in the defect energies is similar to that for the oxygen

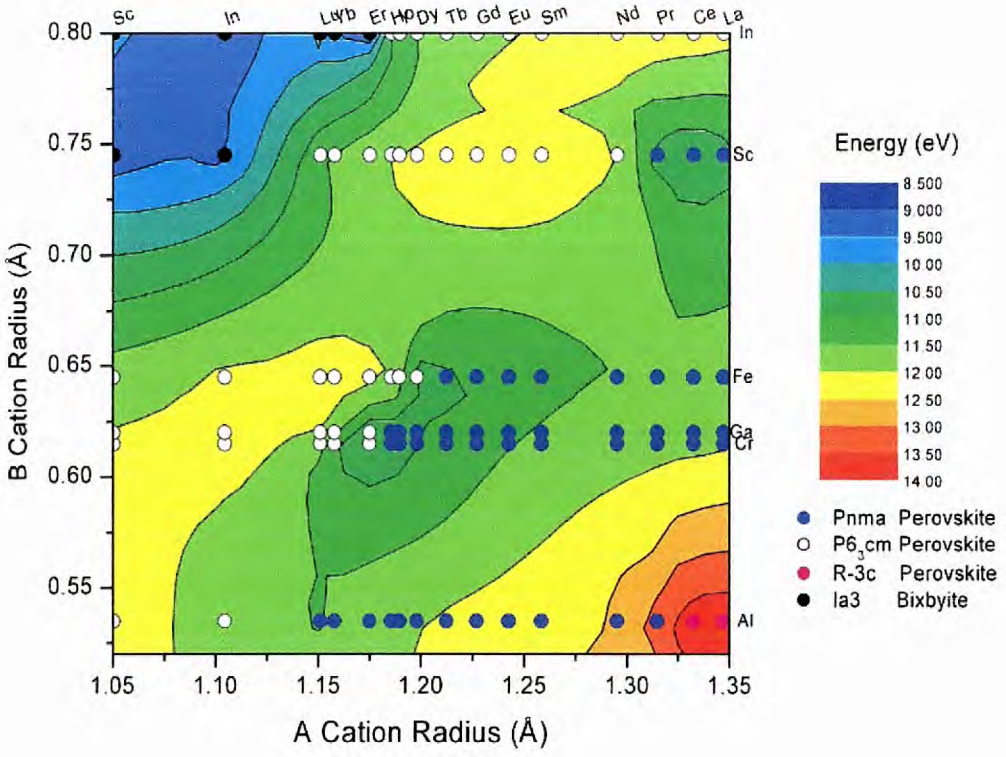


Figure 4.4: A^{3+} cation Frenkel reaction energy contour map.

Frenkel reaction energies (Figure 4.3), however the values are considerably higher, varying between 14.0 to 9.0 eV for the A cation Frenkel compared to a range of 3.2 to 6.4 eV for the oxygen Frenkel. Again the highest energy values are found for the rhombohedral perovskites. The defect energies then decrease across the orthorhombic stability region and there is somewhat of a discontinuity is seen at the boundary between the orthorhombic and hexagonal materials. The defect energy then increases slightly for these hexagonal perovskites and then drops back off for the bixbyite materials.

The reason for this energy trend is the same as that for the oxygen Frenkel reaction,

namely that the energy penalty for creating a vacancy and an interstitial defect changes with crystallography. However, since the A cation is more highly charged and larger than the oxygen anion, the lattice distortion introduced by both creating the vacancy and the interstitial defects is much larger than that for the oxygen defects, thus the higher energy obtained for the A cation Frenkel reaction component compared to the oxygen Frenkel reaction.

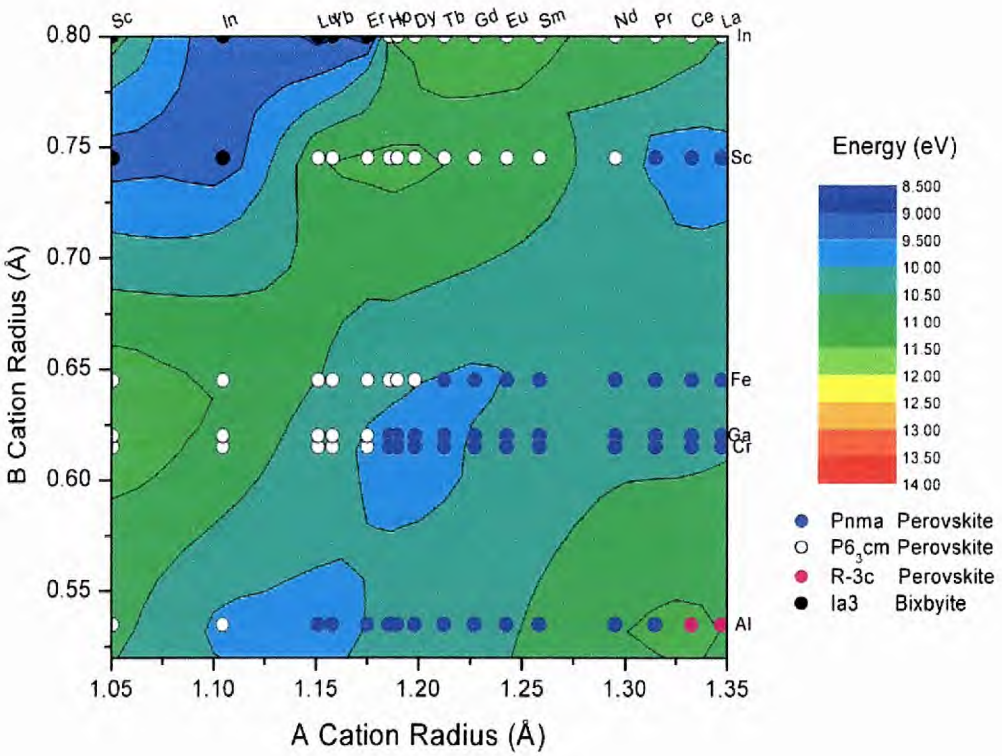


Figure 4.5: B^{3+} cation Frenkel reaction energy contour map.

The B cation Frenkel defect reaction energies (Equation 4.4) are presented in Figure 4.5. These reaction energies show considerably less variation over the compositional range than the other defect process energies, varying from a maximum of 11.0 eV

to a minimum of 9.4 eV. Here the defect energy values are intermediate to those of the oxygen Frenkel and A cation Frenkel reactions. The energy trend decreases from the rhombohedral perovskite though the orthorhombic material and reaches a minimum at the low energy boundary between the orthorhombic and hexagonal materials. The energy then increases for these hexagonal materials before decreasing again for the bixbyite compositions.

The same explanation for this trend can be made as for the oxygen and A cation Frenkel reaction energy trends, however, due to the size of the B cations being smaller than the A cations the energy values are lower due to the decreased lattice distortion created by these defects.

The observed small increases in the cation Frenkel energies (both A and B cation) for the hexagonal materials is due to the coordination of the A and B cation being lower for this structure (7 and 5 fold) than for the orthorhombic and rhombohedral perovskite structures (12 and 6 fold), thus the sizes of the cation sites are slightly smaller. The energy to create the vacancies is therefore larger due to increased lattice distortion.

The energies for the antisite defect reaction (Equation 4.5) are presented in Figure 4.6. Again, the highest energy is for the rhombohedral compositions with a value of 5.8 eV. The defect energy then decreases in a regular manner through all compositions and structures to a point where the energy is 0 eV for the bixbyite materials. A defect reaction energy of zero infers that the energy balance between the strains induced by creating the two antisite defects cancels out. This can be explained simply by consideration of the crystallography. Within the bixbyite structure each of the cation sites are octahedrally coordinated by oxygen, and as such the sites are very similar. In essence, the antisite reaction does not cause significant disorder to

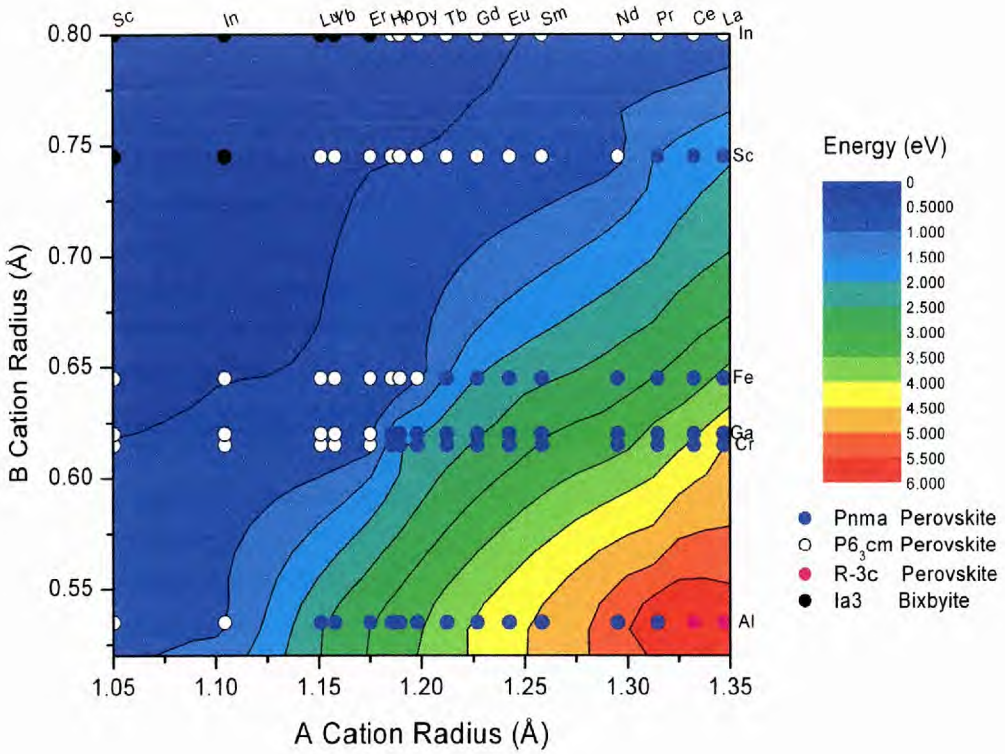


Figure 4.6: Antisite reaction energy contour map.

the lattice.

The overall trend in the antisite defect energies can be described by considering the tolerance factor (Equation 3.2). Although the tolerance factor (t) was originally derived to predict the distortion of a perovskite lattice from an idealised cubic structure, it can also be used to understand the variation exhibited by the antisite energy. This is because the tolerance factor is a relative measure of the difference in size of the A and B cations and by inference how much distortion would be necessary to accommodate an A cation at a B site and vice versa (i.e. as in the antisite reaction). In this regard, it is convenient to quantify this for the perovskite compositions

alone, such that low t values (i.e. less than 0.8) indicate that the cations fit well in opposing cation sites (i.e. an A cation on a B lattice site and vice versa), while high t values (i.e. greater than 0.8) suggest that they fit rather less well. Thus the value for a perfect cubic perovskite (i.e. 1) would imply a high antisite energy. By comparing Figures 3.9 and 4.6, it is clear that there is an excellent correlation between our calculated antisite energy and the tolerance factor.

4.2.2 Comparing Defect Processes

The Schottky, oxygen, A and B cation Frenkel and antisite reactions can be compared by considering Figures 4.2 to 4.6. It is at once apparent that the Schottky and oxygen Frenkel disorder processes show less variation in energy as a function of cation radii than the antisite process. Furthermore, the cation Frenkel reactions have much higher energies than any of the other processes. Since they are much higher in energy, the A and B cation Frenkel reactions are the least favourable processes.

The smaller predicted variation in Schottky energy as a function of cation radius is a consequence of competing factors. In the Schottky reaction (Equation 4.1) the displaced ions form new lattice and as such, the lattice energy and hence its variation with component cation radii is an important factor. This was shown in Figure 3.8 and clearly the lattice energy gain is greatest for compositions in the bottom left hand corner. The second term concerns the energy to form vacancies. Higher energies (less favourable) will result in materials with higher Madelung or electrostatic energies. Although these vary somewhat between structure types, values principally increase as the interatomic separation decreases. Thus, higher energies are expected when both the A and B cations are small, i.e. the opposite variation observed with

the lattice energy (see Figure 3.8). These electrostatic terms are therefore working in opposition, and the net effect is a smaller variation in Schottky energy as a function of cation radii. Contributions from the short range pair energies now become important. Consequently structure type boundaries where there is a change in ion coordination should show up in the Schottky energy map. In Figure 4.2, there is evidence of such a change between Pnma (VI, XII) and $P6_3cm$ (V, VII) but not $R\bar{3}c$ (VI, XII) to Pnma (VI, XII).

By comparing the results in Figures 4.2 and 4.6 it is at once evident that there is a change in lowest disorder process energy from Schottky to antisite as a function of the cation radii. If this is expressed in terms of the tolerance factor, the swap-over occurs at a t value between 0.99 and 0.98 with the antisite reaction dominant for all lower values. Thus, only in a small portion of the cation radii space (i.e. at the bottom right) does Schottky disorder dominate over antisite. Furthermore, in this region, the difference in process energies is not great, and thus materials such as $LaAlO_3$ should exhibit complex defect equilibria.

It is also possible to compare the oxygen Frenkel and antisite energies. The oxygen Frenkel energy decreases somewhat as the A cation radius increases and the B cation radius decreases, in a similar manner to the antisite process energies. Although this decreases to a value considerably below the Schottky for a majority of the compositional range, the oxygen Frenkel energy does not decrease to the same extent as the antisite and is never the dominant defect process. Again some evidence of the Pnma to $P6_3cm$ structure change is seen (Figure 4.3).

4.2.3 Implications for Radiation Tolerance

The intrinsic defect processes all effect the radiation tolerance of the ABO_3 compositions. However, predictions of the radiation tolerance that rely solely on the intrinsic defect processes are based on the retained defect process energy argument. This assumes that the greatest contribution to the retained energy upon irradiation is due to the dominant defect process (i.e. lowest energy). In this case, the tolerance of the materials essentially follows the antisite results in Figure 4.6 and radiation tolerance follows structure type in the order $R\bar{3}c$ < Pnma < $P6_3cm$ < Ia3. Clearly the perovskite-like structures are significantly less tolerant than bixbyite, although there is considerable variation between the three structures $R\bar{3}c$, Pnma and $P6_3cm$.

There is, however, an inherent limitation with this analysis. The antisite reaction only results in the formation of substitutional defects; no vacancy or interstitial defects are involved. Of course, not only will other types of defects form through radiation damage, but, as previously mentioned (Section 4.1.2), it is these latter types of defects that are necessary to help anneal damage through transport mechanisms. Since the recovery will take place with minimal external energy input unlike the high energy damage processes, it is more important to consider the oxygen sublattice, because in ceramics the anions are far more mobile than the cations. Thus, for damage evaluation and recovery, it would seem that the relative Schottky or oxygen Frenkel energies provide a valuable criteria for differentiating between compositions. If this is correct, the recovery process of all the perovskites would be similar (since the combined lowest energies in Figures 4.2 and 4.3 are almost constant as a function of radii). In this way, the main criterion for the tolerance assessment, at least when isolated defects are considered, should be the retained energy of the lattice. However, all perovskites would still be considerably less tolerant than the bixbyites.

4.2.4 Comparison to Pyrochlore/Fluorite

The perovskite defect process energies can be compared to the equivalent lowest energy defect process energies for other materials. Here, comparison is made to the fluorite and pyrochlore oxides investigated previously [4, 5]. In this case, the antisite energies of the perovskites are well above those for the zirconium containing pyrochlore/fluorite materials (e.g. $Er_2Zr_2O_7$ (0.6 eV) and $Gd_2Zr_2O_7$ (1.8 eV) [4]). As such, only selected $P6_3cm$ perovskites could be as impressively radiation tolerant as the best zirconate pyrochlores. On the other hand, the titanate pyrochlores exhibit antisite defect energies of typically 2.9 eV which is equivalent to the lowest energy for the Pnma perovskites. On this basis alone, only the most radiation tolerant Pnma perovskites would approach the tolerance of the least tolerant titanate pyrochlores. Conversely, the bixbyite materials should show excellent radiation tolerance.

The oxygen Frenkel defect energies for the perovskites (Figure 4.3) are higher than those for the pyrochlores. For example, the zirconate pyrochlores $Er_2Zr_2O_7$ and $Gd_2Zr_2O_7$ exhibit oxygen Frenkel energies of 2.5 eV and 2.0 eV respectively [5], both being lower than corresponding results for the perovskite materials. However, the titanate pyrochlores have values that are similar to the Pnma perovskites, for example, $Gd_2Ti_2O_7$ has an oxygen Frenkel energy of 5.6 eV [5]. Consequently, values for the bixbyites, which are as low as 3.0 eV, compare favorably to the titanate pyrochlores and are not significantly higher than the zirconates. On this basis the bixbyites are again predicted to be highly radiation tolerant.

Up to this point, a model has been suggested that requires antisite and oxygen Frenkel lattice defects. However, the stability of such defects depends not only on their individual energies, but also on the interactions between them. This is charac-

terised by the reduction in formation energy when the defects are associated (known as the binding energy). The work on pyrochlores considered the representative defect cluster $\{A_B^X : B_A^X : V_O^{\bullet\bullet} : O_i''\}^X$, a combination of antisite and oxygen Frenkel reactions where the defects are in their nearest neighbour positions [5].

Table 4.3: Comparison of the total defect energies for isolated defects and clusters $\{A_B^X : B_A^X\}^X$ for different compositions of perovskite and pyrochlore oxides. Note: the energies presented in this table have not been normalised. * composition is not stable as perovskite and irradiation may cause decomposition to garnet.

	Total Defect Energy (eV) $\{A_B^X : B_A^X\}^X$	
	Isolated	**Clustered**
Perovskite		
$GdAlO_3$	8.20	7.05
$LaAlO_3$	11.98	10.59
$GdFeO_3$*	4.24	4.03
$LaFeO_3$	7.44	6.30
Pyrochlore	[5]	
$Gd_2Ti_2O_7$	6.09	4.98
$La_2Ti_2O_7$	5.94	4.59
$Gd_2Zr_2O_7$	3.68	2.86
$La_2Zr_2O_7$	4.52	3.45

Interestingly, when different geometries of this cluster were investigated for pyrochlore, the oxygen Frenkel component sometimes self annihilated in the presence of the cation antisite pair (yet, when the oxygen Frenkel pair are alone, they do not annihilate). Thus in Table 4.3 for these pyrochlores the energy for the $\{A_B^X : B_A^X : V_O^{\bullet\bullet} : O_i''\}^X$ cluster are the same as for the clustered antisite pair, $\{A_B^X : B_A^X\}^X$. Such behaviour was not observed in equivalent perovskite clusters. This may in itself be a significant difference between pyrochlores and perovskites

in regard to their ability to tolerate radiation damage through damage annealing. Nevertheless, in order to compare equivalent defect clusters, energy comparisons were made for adjacent antisite pairs $\{A_B^X : B_A^X\}^X$ (see Table 4.3 for examples). It is possible to fix the defects at the clustered lattice positions, however this then is forcing an outcome for the lattice relaxation and in this case comparison would not be reliable. Critically, for perovskites the values when the defects are associated (i.e. clustered) are only modestly less than when the defects are isolated. Conversely, in pyrochlore materials, cluster formation values are considerably less than for isolated defects (Table 4.3). The larger binding energy for pyrochlores means that a significant difference between the antisite energy for $GdFeO_3$ compared to lower zirconate pyrochlore values can now be seen. The other perovskites maintain their higher defect process energies.

Clearly, for the pyrochlore materials these antisite defects are more strongly bound than for the perovskite materials. This may imply that in perovskites, as the defect concentrations increase, i.e. with damage accumulation, the retained energy increases more quickly. On this basis, all the perovskites should be significantly less radiation tolerant than pyrochlores. However, it would be appropriate to apply further analysis such as molecular dynamics (because of the great number of cluster configurations) before this can be stated with confidence.

4.3 Conclusion

By relating the energies for defect processes to radiation tolerance, predictions of how the radiation tolerance varies across an extensive series of $A^{3+}B^{3+}O_3$ compositions is possible. In this regard the intrinsic defect processes are dominated by

the antisite reaction. Certainly cation disorder is expected to be a consequence of radiation damage and as such, this is an important reaction as it is one measure of retained energy. However, damage can recover or anneal only if defects are present to mediate ion transport. Consequently, the lowest energy for either oxygen Frenkel or Schottky disorder must be considered concurrent with cation disorder. On the basis of these three reactions, the order for radiation tolerance between compositions roughly follows the perovskite tolerance factor (see Equation 3.2 and Figure 3.9). In terms of the ABO_3 crystal structure, this means that the predicted order of increasing tolerance is $R\bar{3}c$ < Pnma < $P6_3cm$ < Ia3, where $R\bar{3}c$ and Pnma are "true" perovskites and Ia3 is bixbyite. Only the formation energies for defects involved in ion transport have been calculated. Therefore, in future work, it would be valuable to construct a map for anion (and possibly cation) migration activation energies equivalent to the work on pyrochlores [28, 202].

By comparing the equivalent defects in $A_2B_2O_7$ pyrochlore oxides with previous simulations [4, 5], the relative tolerance of ABO_3 oxides can be assessed. Based on the results for isolated defects, none of the perovskites would be expected to exhibit the exceptional radiation tolerance of the zirconate or cerate pyrochlores/fluorites, i.e. $A_2Zr_2O_7$ or $A_2Ce_2O_7$ [4, 146] (the Ia3 bixbyites will be treated separately). However, the best perovskites would have a similar tolerance to the intermediate titanate pyrochlores $A_2Ti_2O_7$. When the reaction energies based on clustered defects are considered (Table 4.3), again the perovskite materials appear less tolerant than the zirconate pyrochlores.

A low energy for the antisite defect process in itself, is not sufficient for a radiation tolerant material. For the bixbyite materials, however, the oxygen Frenkel energy is similar to the oxygen Frenkel of pyrochlores. It is important to note that formation of

lattice defects is only part of the consideration of the tolerance of a material, and that the ease at which the material anneals such damage will be a major contribution. As such the energy associated with transport and the activation energy for ion migration are also significant.

Clearly, the low defect formation energies exhibited by the bixbyite oxides are consistent with these materials being approximately as radiation tolerant as the better pyrochlores. It seems logical to assume that this is in part a consequence of the similarity between the bixbyite and fluorite structures [146]. Furthermore, at higher damage, this similarity means that the bixbyite structure may be able to assume the lower symmetry disordered fluorite structure, which has been shown previously to be highly radiation tolerant [146].

It is also possible that upon irradiation, materials that lie on the cusp of the hexagonal to bixbyite boundary can also assume the cubic bixbyite (or disordered fluorite structure) since the differences in lattice energies are small. In such a case those compositions would become more radiation tolerant than in their original $P6_3cm$ phase. This may provide an interesting avenue for experimental investigation.

Finally, returning to the question originally posed in the introduction (Section 4.1.2): does the equivalence of charge between A^{3+} and B^{3+} cations in the perovskite systems imply that they show some significant degree of radiation tolerance? On the basis of this approach, the answer appears to be negative. For the $R\bar{3}c$ and Pnma (i.e. the "true" perovskites), the difference in ion size and the associated crystallography means that these materials should not be highly radiation tolerant due to the inherent lattice strains introduced upon disorder. Conversely, materials with the bixbyite structure should show considerable tolerance.

The defect energy results presented here suggest that there will be no $A^{3+}B^{3+}O_3$ perovskites as radiation tolerant as the $A_2Zr_2O_7$ zirconate pyrochlore/fluorite related compounds previously investigated [4]. The experimental data thus far are in agreement with predictions, whereby ion doses that cause amorphisation in $Er_2Ti_2O_7$ but not $Er_2Zr_2O_7$ also cause amorphisation in all the $A^{3+}B^{3+}O_3$ perovskites considered. Clearly the perovskites are not as tolerant to ion irradiation as the best fluorite related materials. Further experimental work will be needed to validate the predicted order of perovskite radiation tolerance which should be rather distinct. As such it would be interesting to reduce the ion irradiation flux to see if it is possible to differentiate between the various perovskites.

Chapter 5

Extrinsic Defect Reactions in Perovskite Materials

The work presented in this Chapter has been published in Solid State Ionics [203].

5.1 Introduction

With dwindling fossil fuel reserves [204] and increasing awareness of global warming [205, 206], attention is being directed towards renewable and non-polluting energy systems. Many schemes are presently receiving attention: wind power [207], hydroelectric [208], solar [209], nuclear [210] and oxygen conduction [211]. The Kyoto protocol [171] was created to set targets for industrialised nations to cut their greenhouse gas emissions. As part of this drive for a non-polluting, energy efficient energy system, solid oxide fuel cells (SOFCs) are being investigated with great

fervour [212–216].

The most common types of fuel cells are phosphoric acid (PAFC), molten carbonate (MCFC), proton exchange membrane (PEMFC), and solid oxide (SOFC), all named after their electrolytes. As they are made of different materials and operating temperatures, they have varying benefits, applications and challenges, but all share the potential for high electrical efficiency and low emissions [96].

A schematic of a SOFC can be seen in Figure 5.1. SOFCs are electrochemical devices that convert hydrogen from the fuel directly into electricity and heat. The reaction is driven by the continual flow of oxygen ions (O^{2-}) across an electrolyte from the cathode to the anode. At the anode, these oxygen ions combine with the hydrogen to form water (H_2O) with the release of two electrons to an external circuit. A SOFC will also utilize any carbon in the fuel (CO), which makes them more versatile when using fuels such as natural gas or propane [96, 217]. When methane (CH_4) is used as the fuel source, this is internally reformed at the SOFC anode [218]. In the case where the fuel is CO, the O^{2-} ions oxidise CO to CO_2. The two possible reactions at the anode (dependent on fuel) are therefore:

$$H_2 + \frac{1}{2}O_2 \rightleftharpoons H_2O + 2e^- \tag{5.1a}$$

$$CO + \frac{1}{2}O_2 \rightleftharpoons CO_2 + 2e^- \tag{5.1b}$$

with the corresponding reaction at the cathode:

$$\frac{1}{2}O_2 + 2e^- \rightleftharpoons O^{2-} \tag{5.2}$$

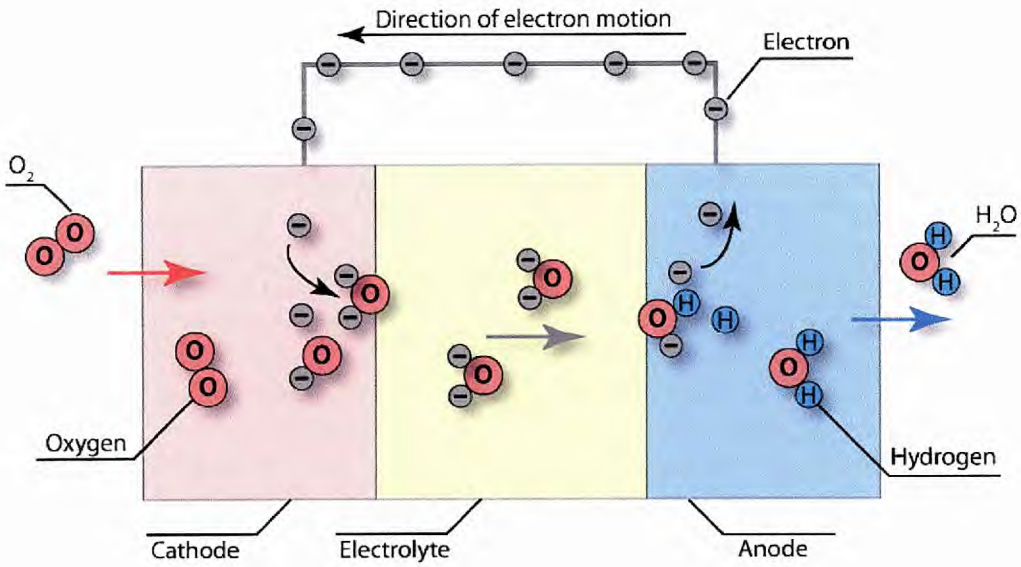


Figure 5.1: Schematic of a solid oxide fuel cell.

The total electrical conductivity (σ) of a solid is the sum of the partial conductivities of the ionic and electronic charge carriers [219]:

$$\sigma = \sum q_i \mu_i c_i \tag{5.3}$$

where q_i is the charge, μ_i is the mobility and c_i is the density of the carriers. The conductivity can be raised by increasing the carrier concentration and/or increasing the mobility of the carriers. The mobility of the charge carriers is dependent upon temperature, composition and processing (grain boundaries, dislocations etc.). The carrier concentration can be altered in two ways. Firstly, the material can be doped with aliovalent impurities that require the formation of ionic defects to maintain charge neutrality [219], or secondly, by deviations from ideal stoichiometry, i.e. either the oxidation or reduction of the material resulting in excess vacancies or interstitials [219]. For the purpose of this work, only the case where the materials

are doped was investigated.

One of the major technological problems with SOFCs is that in order to achieve high electrical conductivities they must operate at high temperatures. Currently, the best SOFCs use a doped zirconia electrolyte and in order to obtain the optimum performance from such cells they must be operated at temperatures greater than 800°C [220]. This exacerbates mechanical problems such as thermal fatigue and limits the choice of materials for interconnects and seals and necessitates the use of expensive alloys [220]. Consequently there is a drive to develop SOFC electrolytes with higher conductivities at lower temperatures [217]. $Ce_{0.9}Gd_{0.1}O_{1.95}$ is being enthusiastically developed since it yields a comparable conductivity at only 500°C [96]. These next generation SOFCs are therefore known as intermediate temperature SOFCs (IT-SOFCs).

At the present time much attention is focused on oxides with perovskite structures with the expectation of developing better cathodes [96]. It is known that ABO_3 materials such as $LaCoO_3$ [221] and $LaInO_3$ [214] can accommodate large concentrations of anion vacancies which lead to high oxygen conductivities. However, when considering the case where both the A and B cations adopt formal 3+ valance states, it is necessary to impose divalent cation substitution to increase the population of mobile oxygen vacancies. For example, in the case of $LaCoO_3$, Sr^{2+} is doped onto the La^{3+} site in order to increase the oxygen conductivity [215]. The majority of perovskite-type oxides currently in use are based on either $La_{1-x}Sr_xCoO_{3-\delta}$ or $La_{1-x}Sr_xMnO_{3-\delta}$, however, $Sm_{1-x}Sr_xCoO_{3-\delta}$ has been shown to have considerable promise [220]. The choice of divalent cation substitution is, however, expected to depend on the host lattice composition.

Another perovskite, Sr^{2+} doped $LaGaO_3$, is attracting attention as a potential

electrolyte for IT-SOFCs. Despite it having a slightly lower conductivity than $Ce_{0.9}Gd_{0.1}O_{1.95}$, it is able to operate over a wider temperature range (e.g. at 600°C where the reduction of Ce^{4+} occurs). A concern with this material, however, is the garnet dissociation reaction as described in Chapter 3, which manifests itself as second phases of $SrLaGa_3O_7$ and $La_4Ga_2O_9$ often at the grain boundaries [96]. Similar stability problems have also been found with the use of $La_{0.9}Sr_{0.1}Ga_{0.8}Mg_{0.2}O_{2.85}$. Other than altering composition or increasing temperature, the conductivity can be improved by creating thin film electrolytes, although these become very fragile and difficult to handle.

The focus of the present study was to investigate the interplay of the crystallography and doping in a subset of perovskite materials where both the A and B cations adopt formal 3+ valence states. Solution of Ba^{2+}, Ca^{2+}, Cd^{2+}, Co^{2+}, Mg^{2+} and Sr^{2+} into the Pnma and $P6_3cm$ varients of ABO_3 materials was considered (see Chapter 3 for details of the crystallography).

5.2 Defect Equilibria

Incorporation of a divalent cation onto a trivalent cation lattice site results in a charge imbalance that requires charge compensation by another lattice defect. There are three potential compensating defects: (i) a host lattice oxygen vacancy (Equations 5.4, 5.7, 5.10, 5.13 and 5.14, (ii) a dopant (2+) interstitial ion (Equations 5.5, 5.8, 5.11, 5.15 and 5.16) or (iii) a lattice self interstitial cation (Equations 5.6, 5.9, 5.12, 5.17 and 5.18). The oxygen vacancy and host interstitial mechanisms are related through the Schottky and cation Frenkel equilibria. In all equations, site and charge balance is maintained, and in Equations 5.4 to 5.12 the A:B ratio of ABO_3 is

also maintained. However, in Equations 5.13 to 5.18 the doping introduces a level of nonstoichiometry with the formation of second phase material in the form of A_2O_3 or B_2O_3.

These various mechanisms were derived as follows. Initially, if only the case where the material remains stoichiometric is considered, three outcomes are possible. Firstly, the divalent cation can dissolve onto a lattice A site (Equation 5.4), secondly onto a lattice B site (Equation 5.7), and thirdly it can dissolve onto both sites simultaneously (Equation 5.10). Reactions of these types involve the formation of excess ABO_3 lattice (via the formation of a cation antisite defect). If a stoichiometric ratio is no longer maintained, divalent ion solution onto the lattice A site can also be facilitated by a reaction in which excess A_2O_3 is formed (Equation 5.13). Equivalently, when solution is onto the lattice B site, a reaction is possible in which excess B_2O_3 is formed (Equation 5.14). Second phase formation will generally lead to the detriment of transport and electrical properties due to associated inhomogeneities.

$$2MO + 2A_A^X + B_B^X + O_O^X \rightleftharpoons 2M'_A + V_O^{\bullet\bullet} + A_B^X + ABO_3 \tag{5.4}$$

$$3MO + 2A_A^X + B_B^X \rightleftharpoons 2M'_A + M_i^{\bullet\bullet} + A_B^X + ABO_3 \tag{5.5}$$

$$3MO + 3A_A^X + B_B^X \rightleftharpoons 3M'_A + A_i^{\bullet\bullet\bullet} + A_B^X + ABO_3 \tag{5.6}$$

$$2MO + A_A^X + 2B_B^X + O_O^X \rightleftharpoons 2M'_B + V_O^{\bullet\bullet} + B_A^X + ABO_3 \tag{5.7}$$

$$3MO + 2B_B^X + A_A^X \rightleftharpoons 2M'_B + M_i^{\bullet\bullet} + B_A^X + ABO_3 \tag{5.8}$$

$$3MO + 3B_B^X + A_A^X \rightleftharpoons 3M'_B + B_i^{\bullet\bullet\bullet} + B_A^X + ABO_3 \tag{5.9}$$

$$2MO + A_A^X + B_B^X + O_O^X \rightleftharpoons M'_A + M'_B + V_O^{\bullet\bullet} + ABO_3 \tag{5.10}$$

$$3MO + A_A^X + B_B^X \rightleftharpoons M'_A + M'_B + M_i^{\bullet\bullet} + ABO_3 \tag{5.11}$$

$$6MO + 3A_A^X + 3B_B^X \rightleftharpoons 3M'_A + 3M'_B + A_i^{\bullet\bullet\bullet} + B_i^{\bullet\bullet\bullet} + 2ABO_3 \tag{5.12}$$

$$2MO + 2A_A^X + 2O_O^X \rightleftharpoons 2M'_A + V_O^{\bullet\bullet} + A_2O_3 \tag{5.13}$$

$$2MO + 2B_B^X + 2O_O^X \rightleftharpoons 2M'_B + V_O^{\bullet\bullet} + B_2O_3 \tag{5.14}$$

$$3MO + 3A_A^X \rightleftharpoons 2M'_A + M_i^{\bullet\bullet} + A_2O_3 \tag{5.15}$$

$$3MO + 3B_B^X \rightleftharpoons 2M'_B + M_i^{\bullet\bullet} + B_2O_3 \tag{5.16}$$

$$3MO + 3A_A^X \rightleftharpoons 3M'_A + A_i^{\bullet\bullet\bullet} + A_2O_3 \tag{5.17}$$

$$3MO + 3B_B^X \rightleftharpoons 3M'_B + B_i^{\bullet\bullet\bullet} + B_2O_3 \tag{5.18}$$

It is also possible for the dopant ion to dissolve onto an interstitial site with charge compensation via an oxygen interstitial defect ($MO + O_O^X \rightleftharpoons M_i^{\bullet\bullet} + O_i''$). However, reactions of this type involving oxygen excess nonstoichiometry have not been considered as the inclusion of oxygen interstitial defects into the lattice is a very high energy process (see Chapter 4).

In this study, the divalent cations being dissolved into the lattice were; Ba^{2+}, Ca^{2+}, Cd^{2+}, Co^{2+}, Mg^{2+} and Sr^{2+}. These represent common dopants used in the design of SOFC materials and have a range of ionic radii (0.89 to 1.42 Å) suitable for the perovskite compounds considered here.

Solution mechanisms were compared by generating graphs that detail solution energy (the internal energy) as a function of the radius of the dopant ion. Since the A and B lattice sites have different coordinations, an effective dopant ion radius with an intermediate coordination of eight (taken from Shannon [30]) has been chosen to facilitate this comparison. In all cases the energies reported are for the complete solution reaction normalised per defect as dictated by a mass action analysis (this

approach has been reported in detail previously [3, 222]; further details are given in Appendix A).

Solution of MO via Equation 5.4 requires knowledge of the lattice energies of MO and ABO_3, the incorporation defect energy of a substitutional M ion at an A lattice site, an A cation at a B lattice site, and the energy to form an oxygen vacancy. These were summed as dictated by equation 5.4 and it was noted that the energy of the defects such as A_A^X, B_B^X and O_O^X are zero. Energies for other solution reactions were obtained equivalently.

5.3 Results and Discussion

Solution of the divalent cations Ba^{2+}, Ca^{2+}, Cd^{2+}, Co^{2+}, Mg^{2+} and Sr^{2+} are shown in Figures 5.2 to 5.5. The solution reactions listed above in Section 5.2 are shown according to the key and can be built up by colour, symbol and line style. The VIII coordinate cation radii of the six dopant ions is shown in Table 5.1.

Table 5.1: VIII co-ordinate effective cation radii for the divalent dopant ions [30].

Cation	Effective ionic radius Å
Mg^{2+}	0.89
Co^{2+}	0.90
Cd^{2+}	1.10
Ca^{2+}	1.12
Sr^{2+}	1.26
Ba^{2+}	1.42

From Figures 5.2 to 5.5 it is evident that there are several general trends for solution of divalent ions into the four compositions. The lowest energy solution process (most

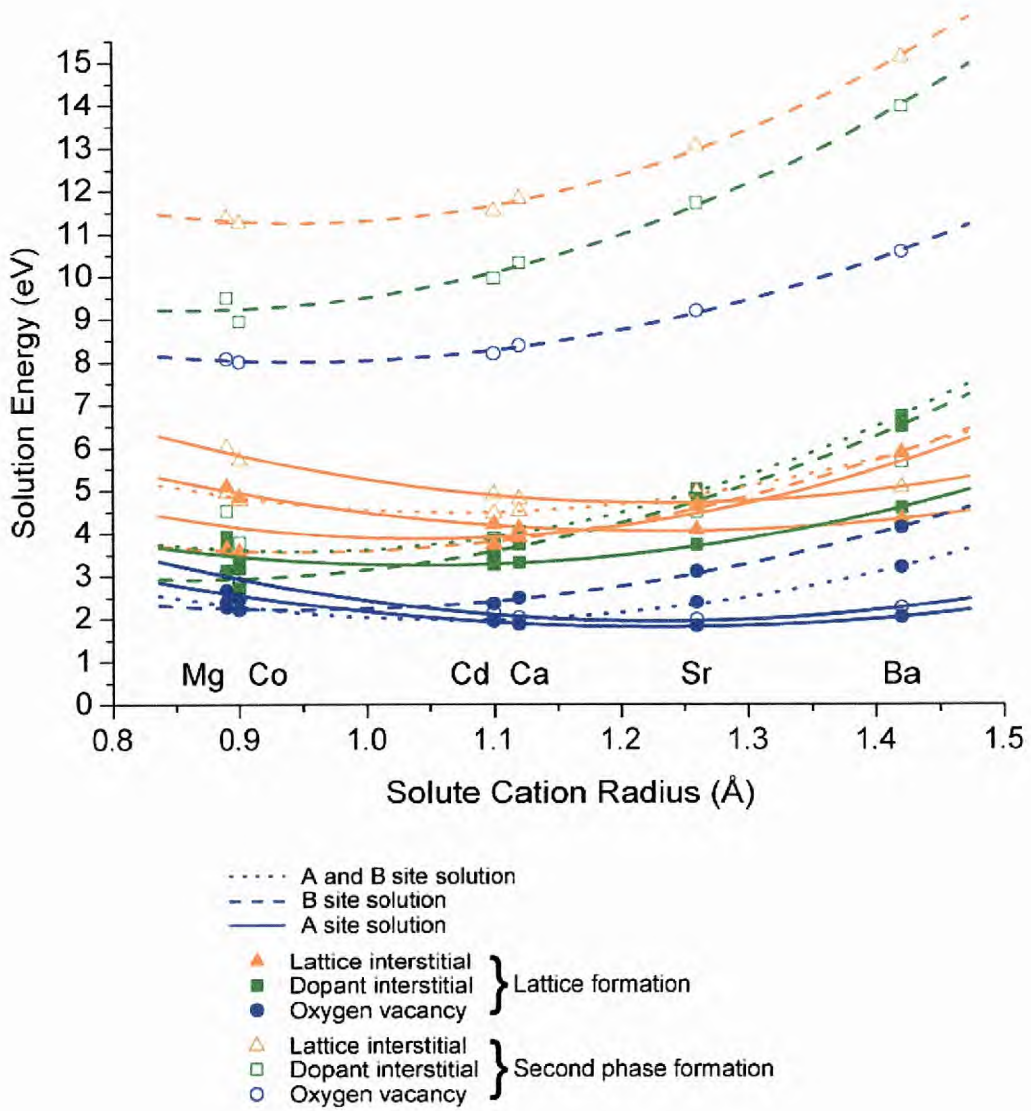


Figure 5.2: Divalent cation solution into $LaScO_3$. Note that the reference radii are La^{3+} = 1.16 Å, Gd^{3+} = 1.053 Å, Sc^{3+} = 0.87 Å and In^{3+} = 0.92 Å.

favourable) is that where the charge compensating defect is an oxygen vacancy. The lowest energy processes are also those where the perovskite remains stoichiometric (Equations 5.4, 5.7 and 5.10). Second phase formation will generally lead to detrimental transport and electrical properties of the material due to associated in-

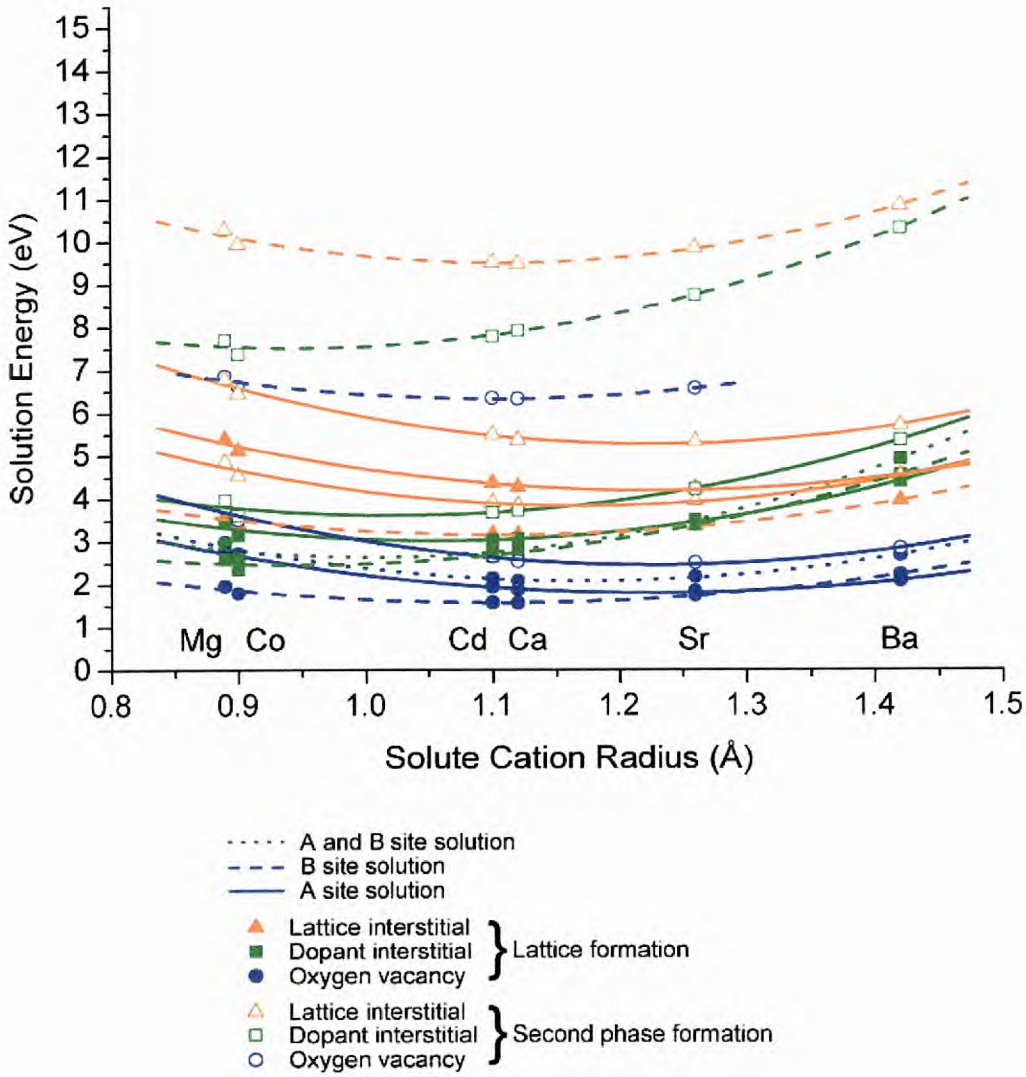


Figure 5.3: Divalent cation solution into $LaInO_3$. Note that the reference radii are La^{3+} = 1.16 Å, Gd^{3+} = 1.053 Å, Sc^{3+} = 0.87 Å and In^{3+} = 0.92 Å.

homogeneities. This trend for continued stoichiometry is therefore of benefit to the properties important for efficient application to SOFCs. It is also important to note that on doping these materials will form oxygen vacancies. Since these are important charge carriers for SOFC operation, divacancy doping is predicted to be an efficient doping process, in general agreement with experimental practice [223–225].

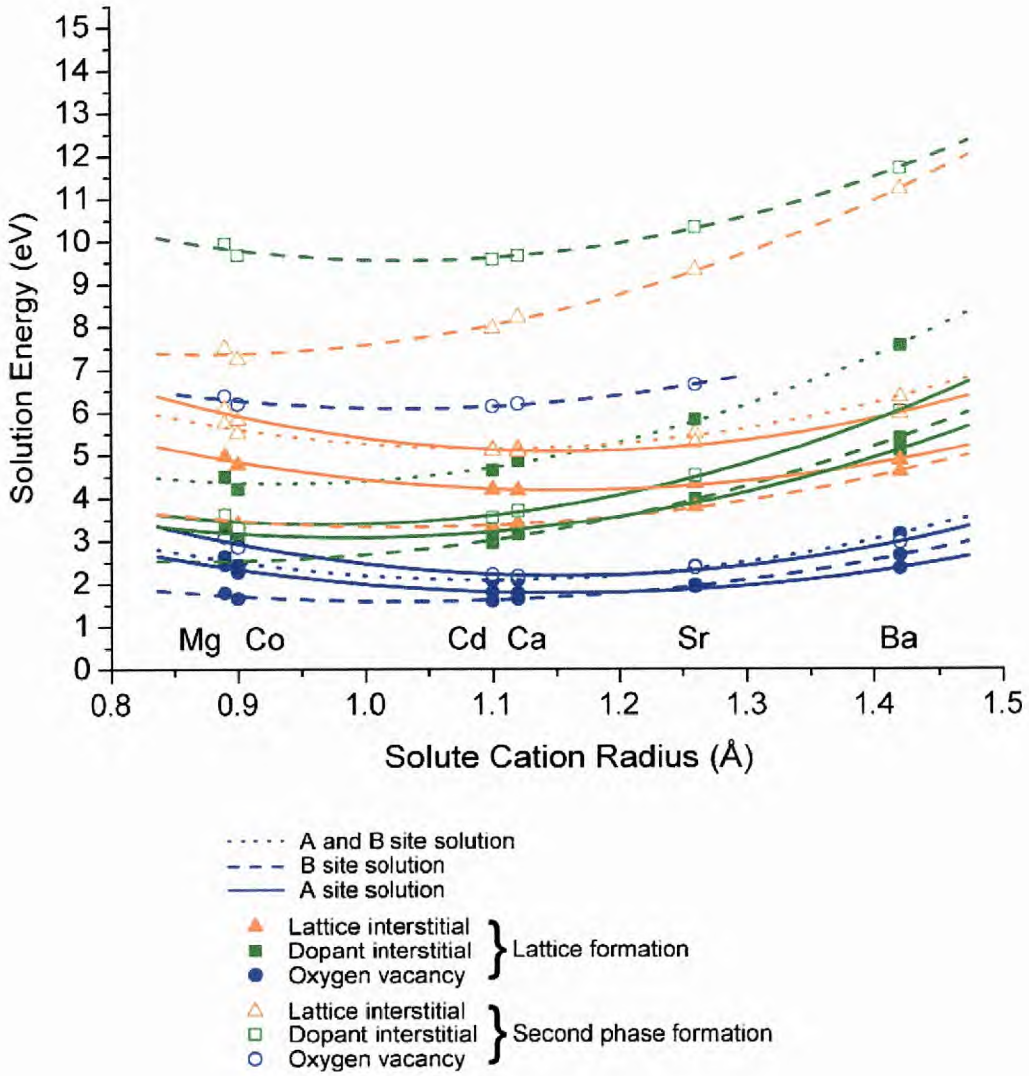


Figure 5.4: Divalent cation solution into $GdScO_3$. Note that the reference radii are La^{3+} = 1.16 Å, Gd^{3+} = 1.053 Å, Sc^{3+} = 0.87 Å and In^{3+} = 0.92 Å.

Of the four host lattices considered, $LaScO_3$ exhibits the highest overall reaction energies for solution onto the B lattice site with the formation of B_2O_3. $LaScO_3$ is the only orthorhombic (pnma) compound considered here, but it may follow that this very high energy for solution onto the B lattice site is a consequence of the host lattice crystallography. In the orthorhombic lattice, the A and B lattice sites

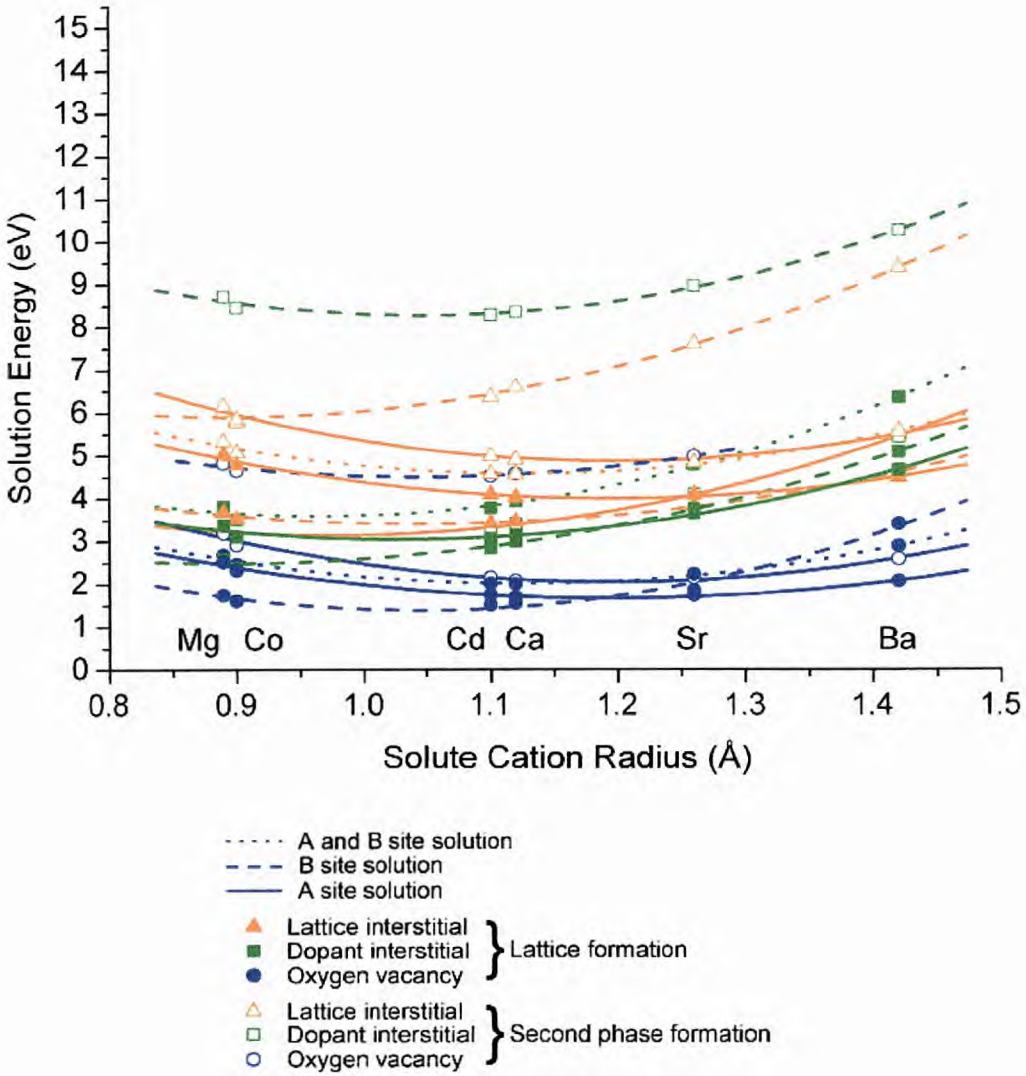


Figure 5.5: Divalent cation solution into $GdInO_3$. Note that the reference radii are La^{3+} = 1.16 Å, Gd^{3+} = 1.053 Å, Sc^{3+} = 0.87 Å and In^{3+} = 0.92 Å.

are 12 and 6 fold coordinated by oxygen, therefore, the B cation is located in the center of a BO_6 octahedra which is the smallest lattice site. Although the situation is similar for the hexagonal ($P6_3cm$) compounds, for these, the A and B lattice sites are 7 and 5 fold coordinated, the B lattice site is still smaller than the A site, but the difference is not so marked as for the orthorhombic lattice. This trend is shown

in the solution results, for example, on comparing Figures 5.2 and 5.3 it is evident that the maximum energy processes are of a far higher value for the orthorhombic phase than the hexagonal.

The relative solution energies for the three hexagonal ($P6_3cm$) materials ($LaInO_3$, $GdScO_3$ and $GdInO_3$) are similar. There are minor variations which are due to differences in the A and B cation radii, but the magnitude of the reactions is much more similar than in comparison to the orthorhombic $LaScO_3$.

In order to elucidate trends in the competing lowest energy reactions, it is necessary to consider only these lowest energy processes in more depth. Therefore, the solution reactions involving charge compensation via an oxygen vacancy are shown in Figures 5.6 to 5.9.

The general trend for the divalent solution in the four compounds is that smaller dopants (e.g. Mg^{2+}) substitute onto the smaller B lattice site, while larger dopants (e.g. Ba^{2+}) substitute onto the larger A lattice site. There is, however, a distinct difference in the solution site preference between the orthorhombic and hexagonal compounds. For the orthorhombic $LaScO_3$, the smallest of the dopants, Mg^{2+} and Co^{2+}, substitute onto the small B lattice site (Equation 5.7). At a solute cation radius of approximately 0.92 Å the lowest energy solution site changes so that solution is preferred on both the A and B lattice sites (Equation 5.10). When the solute cation radius reaches 1.1 Å, the site preference changes again, and ions larger than Cd^{2+} substitute onto the larger A lattice site (Equation 5.4).

For the hexagonal compounds the case is different; although smaller dopants again substitute onto the B lattice site, there is now no intermediate stage, and the larger dopant ions substitute only onto the A lattice site. The explanation for this is that

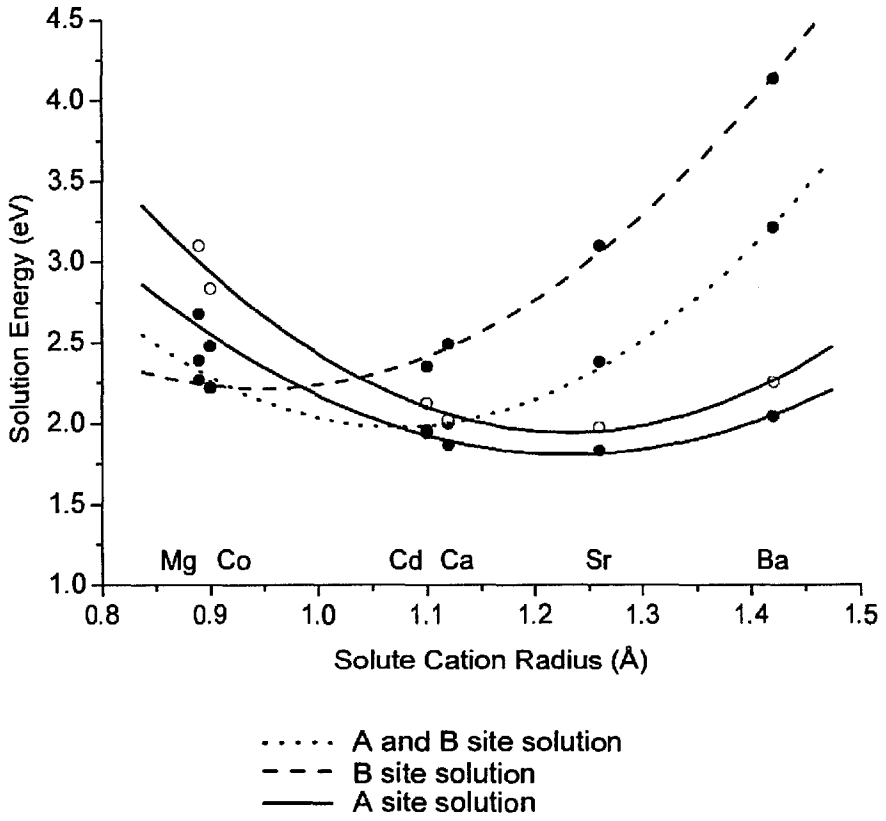


Figure 5.6: Lowest energy mechanisms for divalent cation solution into $LaScO_3$. Note that the reference radii are La^{3+} = 1.16 Å, Gd^{3+} = 1.053 Å, Sc^{3+} = 0.87 Å and In^{3+} = 0.92 Å.

the A and B lattice sites in the hexagonal materials are more comparable in size than those in the orthorhombic materials. This is due to the underlying crystallography, whereby in the hexagonal ($P6_3cm$) materials the A and B lattice sites are 7 and 5 coordinated by oxygen, whereas in the orthorhombic materials the A and B lattice sites are 12 and 6 fold coordinated by oxygen.

$GdScO_3$ is the compound with the smallest A and B cations that adopts the hexagonal $P6_3cm$ symmetry. For the small to intermediate cation radii dopants, (Mg^{2+},

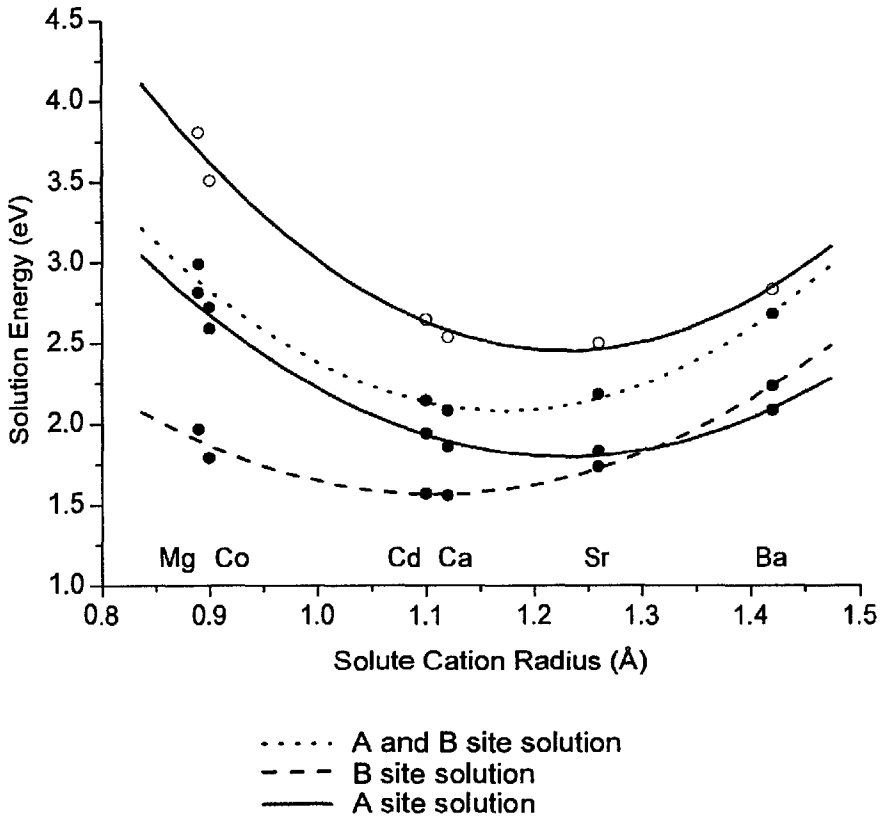


Figure 5.7: Lowest energy mechanisms for divalent cation solution into $LaInO_3$. Note that the reference radii are La^{3+} = 1.16 Å, Gd^{3+} = 1.053 Å, Sc^{3+} = 0.87 Å and In^{3+} = 0.92 Å.

Co^{2+}, Cd^{2+} and Ca^{2+}) solution is preferred onto the smaller B lattice site. It is also in this region of the graph that the overall minimum in solution energy occurs; at 1.04 Å the energy reaches a minimum of 1.3 eV, the closest dopant to this minimum is Cd^{2+}, with a radius of 1.1 Å. At a dopant radius of 1.2 Å, there is a change in preference in the solution site to solution onto the larger lattice A site, therefore Sr^{2+} and Ba^{2+} substitute onto the A lattice site.

Concentrating on the Gd^{3+} containing compounds and maintaining the hexagonal

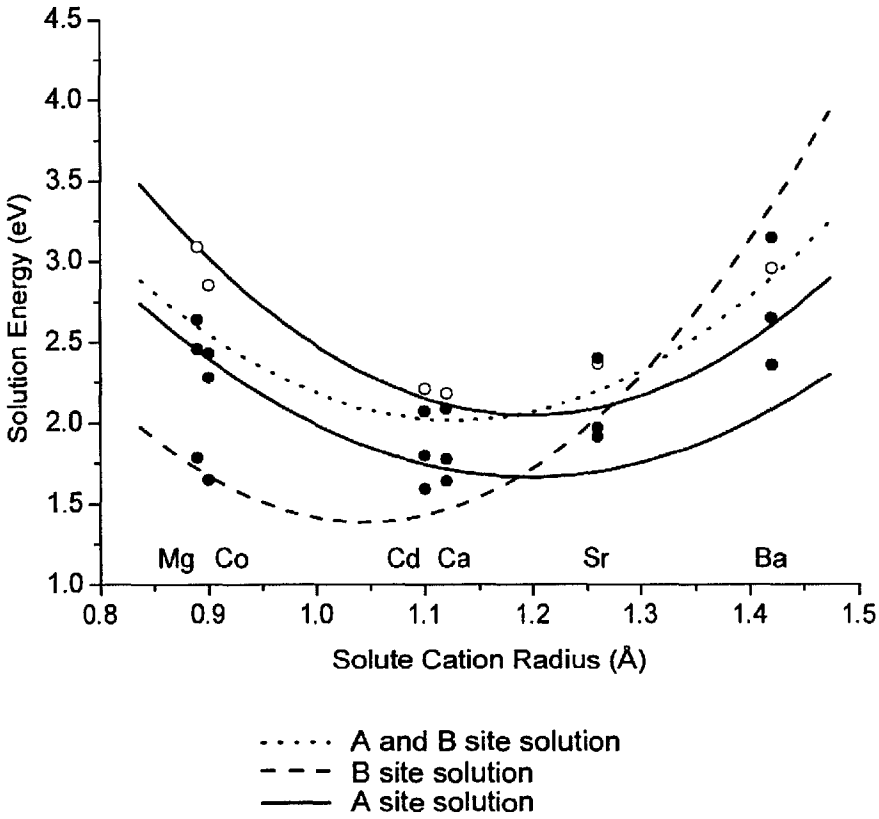


Figure 5.8: Lowest energy mechanisms for divalent cation solution into $GdScO_3$. Note that the reference radii are La^{3+} = 1.16 Å, Gd^{3+} = 1.053 Å, Sc^{3+} = 0.87 Å and In^{3+} = 0.92 Å.

crystallography, it is now pertinent to consider solution into $GdInO_3$. The trend is very similar to $GdScO_3$, with Mg^{2+}, Co^{2+}, Cd^{2+} and Ca^{2+} substituting onto the smaller B lattice site, and Sr^{2+} and Ba^{2+} substituting onto the A lattice site. The minimum in the solution energy is also very similar, 1.3 eV at a solute cation radius of 1.04 Å. The change in preference between solution onto the B and A lattice sites again occurs at a dopant radii of 1.2 Å.

If attention is now drawn to the remaining hexagonal compound, $LaInO_3$, it is clear

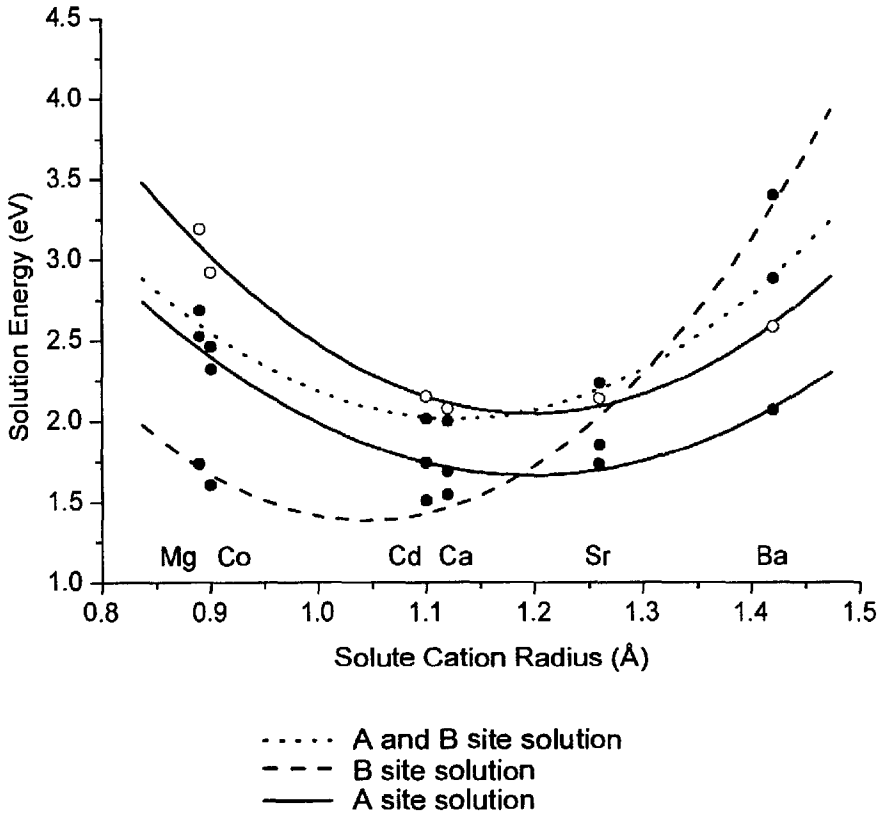


Figure 5.9: Lowest energy mechanisms for divalent cation solution into $GdInO_3$. Note that the reference radii are La^{3+} = 1.16 Å, Gd^{3+} = 1.053 Å, Sc^{3+} = 0.87 Å and In^{3+} = 0.92 Å.

that there is a difference from the trend seen with the Gd^{3+} containing compounds. Here, the smaller dopant cations again substitute onto the B lattice site, however the change over in preference for this solution site occurs at a much higher solute cation radius. Here, Mg^{2+}, Co^{2+}, Cd^{2+}, Ca^{2+} and Sr^{2+} substitute onto the B lattice site, with only Ba^{2+} substituting onto the A lattice site. Thus this change of preference occurs at the larger dopant cation radius of 1.32 Å. The overall minimum in solution energy is 1.52 eV and this occurs for Ca^{2+} (1.12 Å) solution onto the B lattice site.

The situation is different for the orthorhombic compound $LaScO_3$. Here only the smallest dopant cations (Mg^{2+} and Co^{2+}) substitute onto the B lattice site with all larger dopants (Cd^{2+}, Ca^{2+}, Sr^{2+} and Ba^{2+}) substituting onto the larger A lattice site. However, between Co and Cd in a solute cation range from 0.92 Å to 1.09 Å, solution is preferred on a combination of both the A and B lattice sites. This is a marked difference from the hexagonal materials since for these, solution onto the A and B lattice sites simultaneously is far less favourable than solution fully onto the A or B lattice sites individually for any solute cation. A further difference can be seen between $LaScO_3$ and the hexagonal materials, in that the minimum in solution energy occurs at a much higher solute cation radii (1.25 eV which corresponds to Sr^{2+} solution) and for a domain of the graph whereby solution is preferred onto the lattice A site, this minimum is also a higher energy than that for any of the hexagonal materials at 1.77 eV.

Despite the differences in solution energy, the trends between the three hexagonal materials are the same. For these hexagonal materials the minimum in the solution energy occurs at a solute cation radius that seems to be governed somewhat by the lattice A cation size. When $GdScO_3$ and $GdInO_3$ are compared, this minimum in solution energy occurs at the same point (solution cation radius of 1.04 Å) and the change in solution site preference also occurs at the same point (solute cation radius of 1.2 Å). However, when $GdInO_3$ and $LaInO_3$ are compared, both the minimum and change in solution site preference are shifted to larger solute cation radii (1.12 Å and 1.32 Å respectively). This reflects the increase in A cation size in the host lattice from Gd (1.053 Å) to La (1.16 Å).

The overall minimum in solution energy across all four compounds is for Cd^{2+} solution onto the B lattice site of $GdInO_3$. The next lowest solution is for Cd^{2+}

solution into $GdScO_3$, with Cd^{3+} solution into $LaInO_3$ and Sr^{2+} solution into $LaScO_3$ being higher still.

5.4 Conclusions

The mechanisms by which divalent ions are accommodated in ABO_3 perovskite materials have been identified by predicting solution energies as a function of dopant ion radius. For all four materials studied, these dopants are always charge compensated by oxygen vacancies. Furthermore, the smallest dopants will substitute on B sites and the largest on A sites. However, the dopant radius at which this change in lattice site preference occurs is a function of both lattice composition and crystallography.

Due to this crystallography condition for solution, the orthorhombic compound is more sensitive to solution site than the hexagonal materials. This is a result of the relative sizes of the A and B lattice sites, which in turn is related to the coordination of those sites. In the orthorhombic structure, the A and B sites are 12 and 6 fold coordinated by oxygen, and in the hexagonal material they are 7 and 5 fold coordinated by oxygen. Therefore the sites in the hexagonal materials are more similar in size than those in the orthorhombic material. This leads to only very small dopants substituting at the B lattice site, followed by an intermediate step whereby solution is facilitated onto both lattice cation sites, and finally larger cations substituting onto the large A site in the orthorhombic material. In the hexagonal materials, a majority of the dopants substitute onto the B lattice site, with only the largest substituting onto the A lattice site, and with no intermediate step.

A further consequence of this crystallographic variation is that the energy is higher for solution into the orthorhombic $LaScO_3$ than into the three hexagonal compounds ($LaInO_3$, $GdScO_3$ and $GdInO_3$). Therefore, the concentration of oxygen vacancies that would be formed is lower in the $LaScO_3$ than in the other compositions.

For the hexagonal materials, changes in the B site chemistry do not affect the doping scheme significantly. However chemistry changes on the A site do affect the doping schedule, as can be seen from comparison of $GdScO_3$ with $GdInO_3$, and $GdInO_3$ with $LaInO_3$.

For efficient SOFC operation, a high concentration of oxygen vacancies is required. The highest defect concentration occurs for the lowest solution energy. Therefore, the lower the solution energy, the more dopant will dissolve into the material, and the more charge compensating oxygen vacancies are formed. With this knowledge, it would seem that the hexagonal material, $GdIn_{1-x}Cd_xO_3$ would be the best choice for use in SOFCs. Of course, other criteria such as chemical compatibility with other materials in the system are also important. Nevertheless, the work shown here provides a useful approach for directing future research on SOFC systems.

Chapter 6

Dielectric relaxation of lithium doped ZnF_2

The work presented in this Chapter has been submitted for publication in Physica B [226].

6.1 Introduction

Many previous studies on alkaline-earth fluoride materials has considered crystals with the cubic symmetry [227–231]. Some studies have also considered materials of lower symmetries, such as tetragonal MnF_2. The reason for studying these non-cubic systems is that the physical properties have a large number of independent relationships resulting from their anisotropic nature [232].

In a study of tetragonal MnF_2 (isostructural to ZnF_2 which is shown in Figure 6.1),

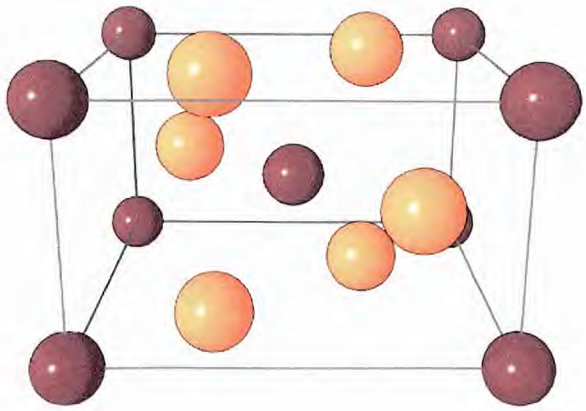


Figure 6.1: The ZnF_2 tetragonal unit cell. The orange spheres represent fluorine ions and the brown spheres represent zinc ions.

Ling *et al.* [232] suggest that the lowest energy intrinsic defect process is anion Frenkel. Studies by Catlow [233] found that the lowest energy intrinsic disorder was indeed anion Frenkel.

Several studies on tetragonal fluoride materials have noticed a split fluorine interstitial defect [232–234]. This is where two fluorine interstitial ions share a lattice site. This split type of defect occurs when an interstitial fluorine ion at an interstitial lattice site displaces a neighbouring fluorine ion from its lattice site towards the next interstitial site leaving behind a fluorine vacancy, as illustrated in Figure 6.2 which shows the orientation of this split defect cluster. Further details in relation to ZnF_2 are given in Section 6.2.

6.1.1 Dielectric Relaxation of lithium doped ZnF_2

Many materials, when subjected to an electric field, will polarize to oppose the field. This polarization can occur via two routes. The first is electronic, with the concerted

motion of the electrons in the direction of the field. The second, and for the purpose of this work most pertinent, is ionic and involves the movement of some ions from their equilibrium lattice positions. When the field is removed, the ions will generally return to their equilibrium positions. If the field is imposed on a material at a high temperature, for some extended time, and the material is subsequently quenched in the field (typically to liquid nitrogen temperature), the ionic contribution to the polarization can be frozen-in to some extent. This implies that there is an energy barrier against the relaxation of the ions back to their equilibrium positions. If the material is slowly heated, this remnant polarization will be lost once the ions gain sufficient thermal energy to overcome the barrier. This process, the dielectric relaxation, can be monitored and quantified as an electric current due to the motion of charged ions [235, 236].

It has been suggested by Roth [237,238] that zinc fluoride (ZnF_2) doped with lithium exhibits a considerable anisotropy in its dielectric properties. In particular, it exhibits a strong relaxation in [001], while the effect in [100] and [110] is several orders of magnitude lower [237]. Several mechanisms for this anisotropic dielectric relaxation have been proposed, the basis of these lies in the initial determination of the defect that charge compensates for the aliovalent Li^+ defect. Roth initially proposed a relaxation mechanism involving the movement of fluorine vacancies, as the charge compensating defects for Li^+ substitutional ions [237] (see Figure 6.3(a)). He later suggested that the anisotropy was due to the motion of Li^+ interstitial ions, as an alternative charge compensating species (see Figure 6.3(b)) [238]. The rationale behind the change in mechanism was an analysis of the experimental data which resulted in a low energy (0.32 eV) for defect cluster reorientation. Roth considered it unlikely that a vacancy model would be responsible for such a low energy but that an interstitial ion model could. The justification was based on previous observations

of low Li^+ interstitial migration energies in materials with the rutile structure [239]. In this regard, Roth suggested that the orientation of the dipole, formed by a "substitutional Li^+ ion - interstitial Li^+ ion" cluster, is initially randomised throughout the lattice with the substitutional lithium defect immobile (see Figure 6.3(b)).

Intriguingly, the anisotropy in the dielectric relaxation was only observed when the doped material was subjected to a prior heat treatment. Again, the reasoning for this treatment differed between the two Roth publications: in the first, it ensures a sufficiently high concentration of fluorine vacancies [237], and in the second it was used to dissolve defect clusters and increase the intensity of the dielectric relaxation [238].

The discrepancies between the two Roth publications was commented on by Nowick [240]. In particular, he stated that the same dielectric response in the [110] and [100] directions is not a test of the relaxation model (as proposed by Roth), but a requirement of the theory. In addition, the experimental data were re-analysed to yield a dipole reorientation energy of about 0.7 eV and as such, the necessity for an interstitial lithium mechanism was removed. Finally Nowick suggested that the dielectric anisotropy could be due merely to differences in the heat treatment of the samples.

It is noteworthy that the anisotropy in the dielectric relaxation in the lithium doped ZnF_2 could also be a result of the tetragonal crystallography of the material as described earlier.

The aim here was to use atomic scale computer simulation to predict the structures and energies of defects associated with lithium solution in ZnF_2. In this way a mechanistic basis for the defect processes that underpin such dielectric relaxation

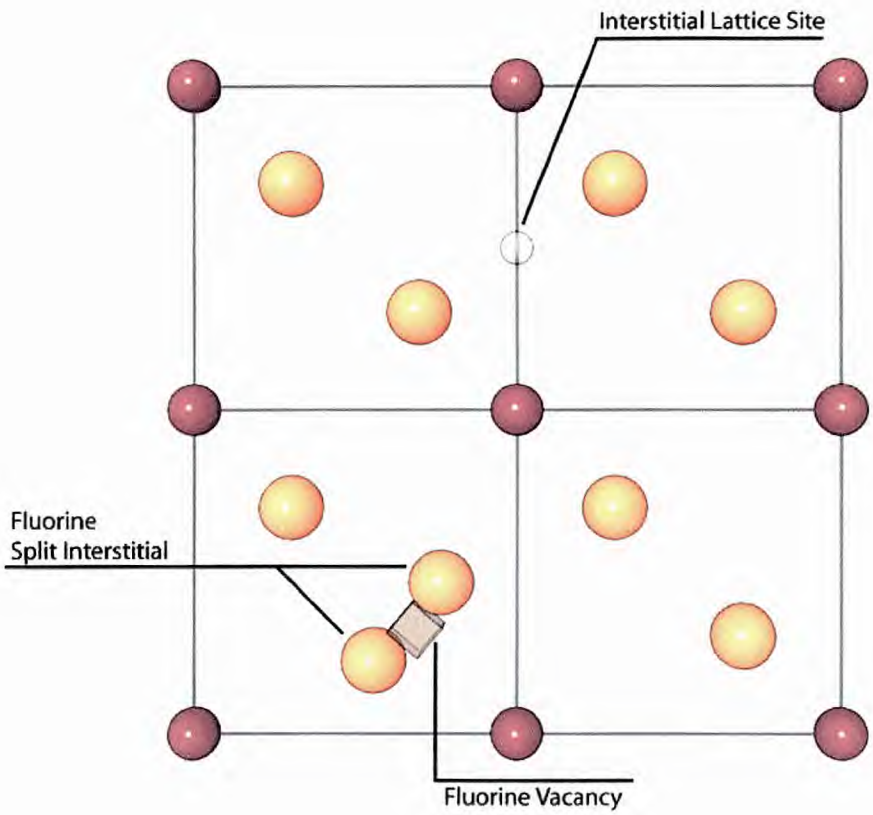
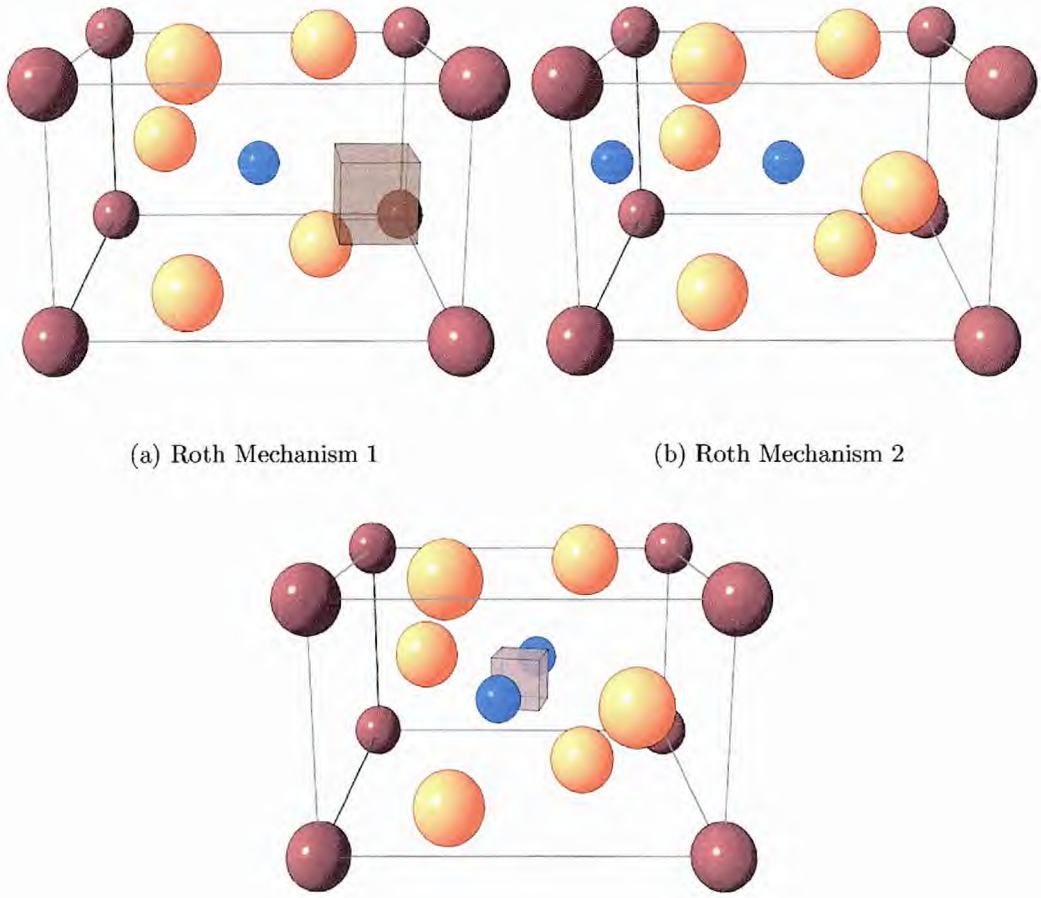


Figure 6.2: Basal plane of ZnF_2 showing the configuration of the split interstitial fluorine cluster.



(a) Roth Mechanism 1

(b) Roth Mechanism 2

(c) Levy Mechanism

Figure 6.3: The ZnF_2 tetragonal unit cell showing the three mechanisms discussed in this chapter. a) Represents a schematic of Roth's first proposed mechanism [237], b) represents a schematic of Roth's second mechanism [238], c) represents the mechanism proposed here. The transparent cube in a) represents a fluorine vacancy, the transparent cube in c) is a zinc vacancy and the blue spheres represent lithium substitutional ions in a) and b) but interstitial ions in c).

process in this material will be provided.

6.2 Results for Undoped ZnF_2

ZnF_2 adopts the tetragonal rutile crystal structure with space group 136 ($P4/mnm$). This structure can be considered as a body centered tetragonal lattice of zinc cations which are then octahedrally coordinated by the fluorine anions (see Figure 6.1). The comparison between experimental and calculated lattice parameters, presented in Table 6.1, shows excellent agreement. Elastic constants for ZnF_2 have also been reported experimentally [241–243] and a comparison with values predicted here are presented in Table 6.2. This comparison shows good agreement indicating that displacements of ions around their equilibrium positions are well reproduced.

Table 6.1: Comparison of calculated and experimental lattice parameters for ZnF_2.

	a(Å)	c(Å)	$\frac{c}{a}$	Volume (Å^3)
Calc.	4.6526	3.2046	0.6888	69.37
Expt. [244]	4.7034	3.1335	0.6662	69.32
Percentage Difference	-1.11	2.26	3.41	0.002

Table 6.2: Calculated and experimental elastic constants (x10^{11} Nm^{-2}) for ZnF_2.

	C_{11}	C_{12}	C_{13}	C_{33}	C_{44}	C_{66}
Calc.	131.8	91.4	60.8	214.2	50.1	92.4
Expt. [242,243]	126	93	84	192	39.2	80.7
Expt. [241]	130	97	89	199	39.5	81.4

Since a lithium doped material is under investigation, the lithium-fluorine potential was derived so that the predicted lattice parameter of LiF, (space group 225 ($Fm\bar{3}m$) [245]) reproduces the experimental data, i.e. a lattice parameter of 4.027 Å.

The energies for intrinsic defect processes in ZnF_2 were also calculated (see Appendix A for details on the normalisation of the defect energies). The results, shown in Table

6.3, suggest that the anion Frenkel reaction is slightly preferred (lower energy) over the Schottky reaction while the cation Frenkel energy is substantially higher. The anion Frenkel defects (i.e. the fluorine vacancy and fluorine interstitial) are therefore the majority intrinsic defects in this material. However, the Schottky reaction is only slightly higher in energy than the anion Frenkel. This reaction will therefore also provide an important concentration of intrinsic defects.

Table 6.3: Normalised, intrinsic defect process energies (eV) for ZnF_2.

Schottky	Anion Frenkel	Cation Frenkel
2.59	2.17	4.31

Finally, when the defects are allowed to cluster, it was found that interstitial F^- adopts a split-interstitial configuration similar to that observed in other fluorite structures [24,233]. In this, the interstitial fluorine ion displaces a lattice F^- ion into a neighbouring interstitial site. Thus, the two F^- ions effectively share the vacant fluorine lattice site that is created. The split-interstitial configuration remains in the ab lattice plane (see Figure 6.2).

6.3 Solution mechanisms for LiF doped ZnF_2

The incorporation of monovalent Li^+ ions onto divalent zinc sites requires charge compensation. This can be facilitated in one of three ways: via a Zn^{2+} interstitial ion (Equation 6.1), a Li^+ interstitial ion (Equation 6.2) or a F^- vacancy (Equation 6.3). Using Kröger-Vink notation [3], these are:

$$2LiF + 2Zn_{Zn}^{X} \rightleftharpoons 2Li'_{Zn} + Zn_i^{\bullet\bullet} + ZnF_2 \tag{6.1}$$

$$2LiF + Zn_{Zn}^{X} \rightleftharpoons Li'_{Zn} + Li_i^{\bullet} + ZnF_2 \tag{6.2}$$

$$LiF + Zn_{Zn}^{X} + F_F^{X} \rightleftharpoons Li'_{Zn} + V_F^{\bullet} + ZnF_2 \tag{6.3}$$

The normalised energies for these processes are reported in Table 6.4 (see Appendix A for details of the normalisation process). It is clear that the energies of these extrinsic defect processes are considerably smaller than those for intrinsic processes. As such, at equilibrium, extrinsic defects will dominate over intrinsic defects.

Initially, it is assumed that the defects remain spatially isolated, and the lowest energy charge compensating defect is a Li^+ interstitial (Equation 6.2). However, Equation 6.3 which describes charge compensation via a F^- vacancy is only 0.19 eV higher, and may on this basis alone yield a further minor, yet significant, concentration of defects.

The coulombic interaction between the isolated defects leads to the formation of defect clusters. The lowest energy solution process, based on defect clusters, still involves compensation via a Li^+ interstitial defect (Equation 6.2). This mechanism is now substantially favoured over the other two reactions (Table 6.4). The reason for this is that the Li^+ interstitial/substitution pair undergoes considerable lattice relaxation when clustering occurs, into a split interstitial configuration, which lowers the overall solution energy. (This is isostructural to the split F^- interstitial ion reported in the intrinsic defect analysis). The structure of this cluster, as shown in Figure 6.3(c), consists of two equivalent Li^+ interstitials either side of a vacant zinc site (i.e. $\{Li_i^{\bullet} : V''_{Zn} : Li_i^{\bullet}\}^X$ rather than $\{Li'_{Zn} : Li_i^{\bullet}\}^X$). This is the referred to as the Levy Mechanism shown in Figure 6.3(c).

Table 6.4: Solution and cluster binding energies (eV) for Li^+ accommodation in ZnF_2.

Solution Mechanism	Charge Compensating Defect	Solution Energy		Cluster Binding Energy
		Isolated*	Clustered	
Reaction 6.1	$Zn_i^{\bullet\bullet}$	2.22	1.82	-4.84
Reaction 6.2	$Li_i^{\bullet}$	1.27	0.73	-1.81
Reaction 6.3	$V_F^{\bullet}$	1.46	1.52	-1.40

* note: these energies have been normalised as described in Appendix A.

Equation 6.4 describes the equilibrium between Li^+ ions when isolated and when part of a defect cluster (indicated by braces).

$$Li'_{Zn} + Li_i^{\bullet} \rightleftharpoons \{Li_i^{\bullet} : V''_{Zn} : Li_i^{\bullet}\}^X \tag{6.4}$$

The corresponding mass action equation is [3];

$$\frac{\left[\{Li_i^{\bullet} : V''_{Zn} : Li_i^{\bullet}\}^X\right]}{[Li'_{Zn}]\,[Li_i^{\bullet}]} = \exp\left(\frac{-\Delta H_b}{kT}\right) \tag{6.5}$$

where ΔH_b is the cluster binding enthalpy, k is the Boltzman constant, T is the absolute temperature and square brackets indicate a concentration. Using the electroneutrality condition between the charged defects (Equation 6.6), Equation 6.5 can be simplified to yield an expression for the ratio of lithium in clusters to that which is isolated (see Equation 6.7).

$$[Li'_{Zn}] = [Li_i^{\bullet}] \tag{6.6}$$

$$\frac{\text{clustered}}{\text{isolated}} = \frac{\left[\{Li_i^{\bullet} : V''_{Zn} : Li_i^{\bullet}\}^X\right]}{2\,[Li'_{Zn}]} \tag{6.7}$$

If the assumption is made that the total lithium concentration is 100 ppm, as stated by Roth in the experimental studies [237], at the heat treatment temperature of 473 K and the calculated cluster binding energy -1.81 eV (Table 6.4), this ratio has the value $3\text{x}10^7$; *ergo*, at equilibrium, Li^+ ions will be in the form of clusters. On the basis of this analysis, the reason for the heat treatment given by Roth in his second paper [238], that is, to dissolve the clusters, is therefore not valid.

It is also possible to use the calculated defect energies to predict an equilibrium solution limit for Li^+ and compare this against the value given by Roth [237]. In this case, it is assumed that defect clusters dominate and Equation 6.2 is re-written in the form:

$$2LiF + Zn_{Zn}^{X} \rightleftharpoons \{Li_i^{\bullet} : V_{Zn}'' : Li_i^{\bullet}\}^{X} + ZnF_2 \tag{6.8}$$

The corresponding reduced mass action equation is;

$$\left[\{Li_i^{\bullet} : V_{Zn}'' : Li_i^{\bullet}\}^{X}\right] = \exp\left(\frac{-\Delta H_{sol}}{kT}\right) \tag{6.9}$$

where $\Delta H_{sol} = 0.73$ eV, which is the cluster solution energy given in Table 6.4. Using Equation 6.9 the equilibrium solution limit at 473 K is 0.01 parts per million (ppm). This is substantially below the 100 ppm Li^+ ion concentration value suggested to be present by Roth [237].

An assumption of the above analysis is that the Li^+ ion content can reach equilibrium. It is therefore necessary to confirm that the kinetics of the Li^+ interstitial defect are sufficiently fast as to allow access to equilibrium or even for defect clustering to occur in a non-equilibrium material. The migration activation energy for an isolated Li^+ interstitial ion to migrate through the ZnF_2 lattice was therefore calculated. The migration energy in the [001] direction was determined to be 0.01 eV (Figure 6.4), whilst in the basal (ab) plane, the lowest migration activation energy in the [110] direction was 0.9 eV. Since there is an equivalent atomic layer rotated by 90° at the mid point in the unit cell (a translation of $\frac{c}{2}$), and thus the migration in <110> is 0.9 eV (Figure 6.5).

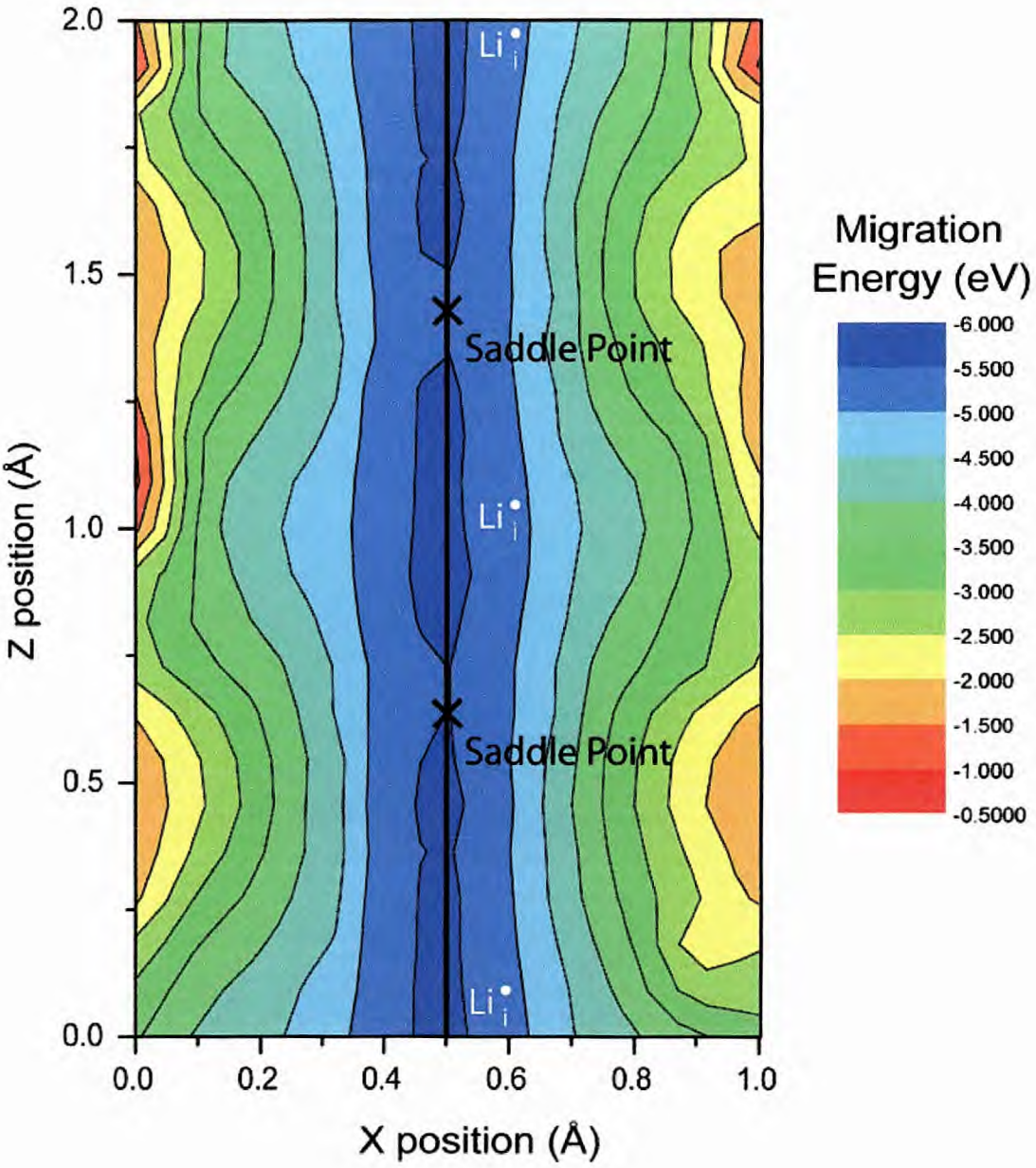


Figure 6.4: Isolated Interstitial Li^+ migration in the [001]. The line indicates the lowest energy pathway.

Since interstitial Li^+ ion migration along [001] is a much lower energy process, it is probable that the isolated Li^+ defects migrate along the [001] until they are either

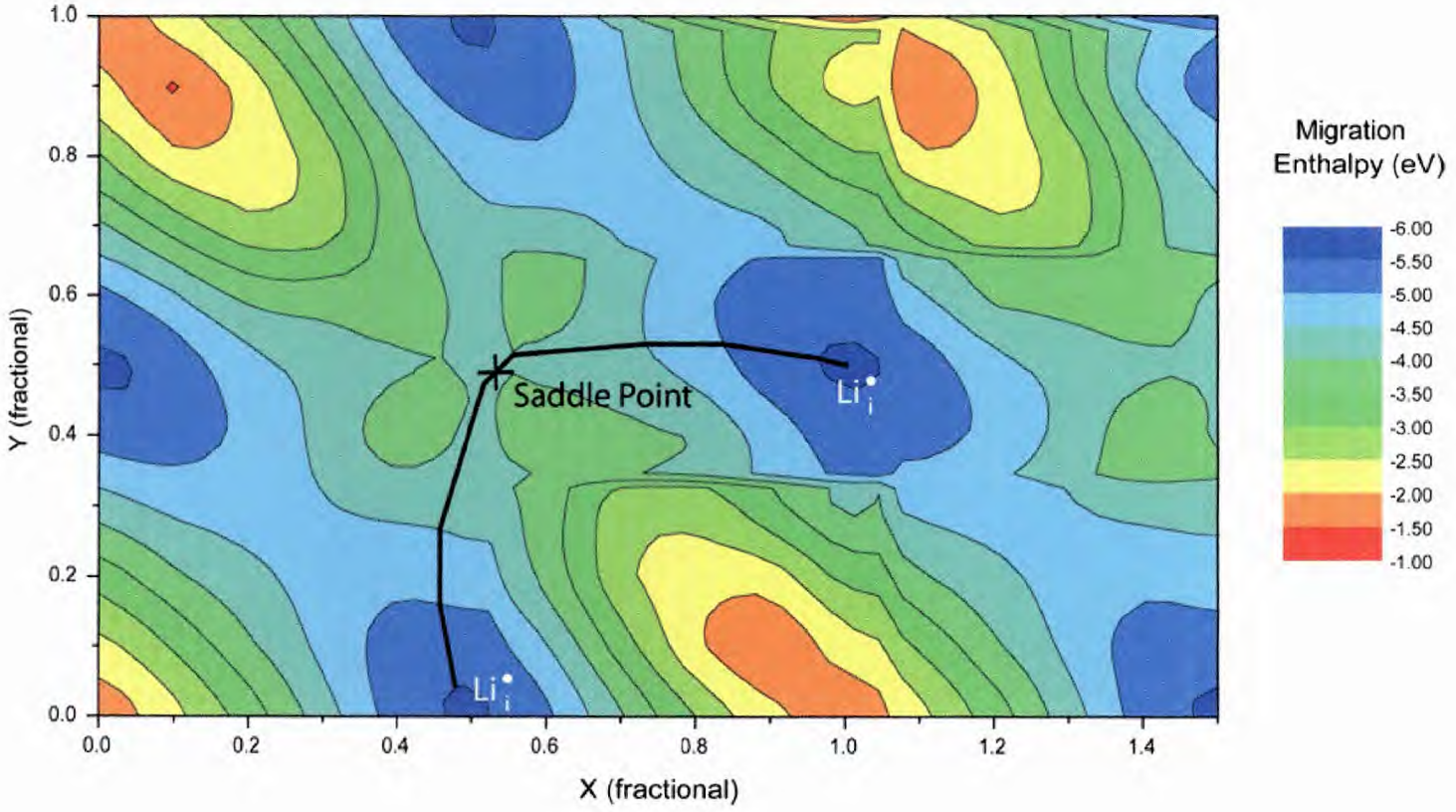


Figure 6.5: Isolated Interstitial Li^+ migration in the ab plane. The line indicates the lowest energy pathway.

trapped in vacant zinc sites, or become part of clusters.

The situation where the Li^+ ion is initially trapped at a zinc site was therefore also considered. In this case, the calculated activation energy is that necessary to move the Li^+ from the substitutional site (leaving behind a vacancy) into a nearest stable interstitial site. If that interstitial site remains in the ab plane, the activation energy is 5.0 eV (the migration energy contour map for this migration is shown in Figure 6.6). If the interstitial migration has a component in the c direction, the activation energy is 3.1 eV (shown in Figure 6.7). In either case, clearly, if the Li^+ defect is trapped at a vacant zinc site, the activation energy is very high.

It is apparent from the earlier analysis that the Li^+ defects take the form of split clusters sharing a vacant zinc lattice site. It therefore follows that there may be some component of the migration that would involve the migration of one of the lithium defects away from this split configuration to a neighbouring interstitial lattice site. This case is shown in Figure 6.8. It is clear that the only migration that is possible is to the 1^{st} interstitial site;, such motion would require an activation energy of 1.5 eV, with migration to a subsequent interstitial sites requiring an additional 2 eV (see Figure 6.8). However, consideration of Table 6.5 shows that when a polarising field is removed, and the lattice is able to respond (relax) to the defect, the split interstitial configuration is adopted once again, i.e. there is effectively no energy barrier for the lattice to relax back to allow the split configuration to reform from a 2^{nd} neighbour split.

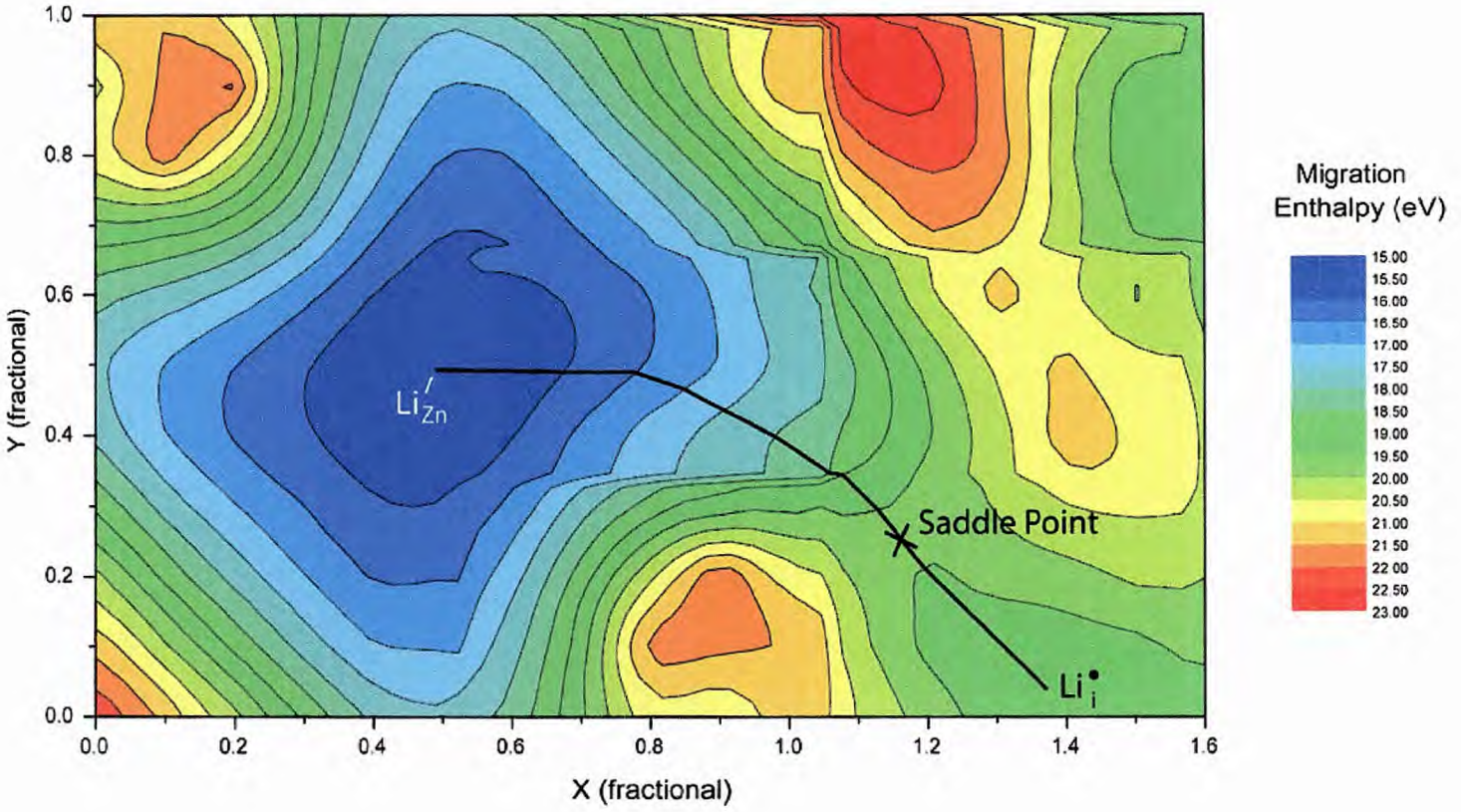


Figure 6.6: Isolated Substitutional Li^+ migration in the ab plane. The line indicates the lowest energy pathway.

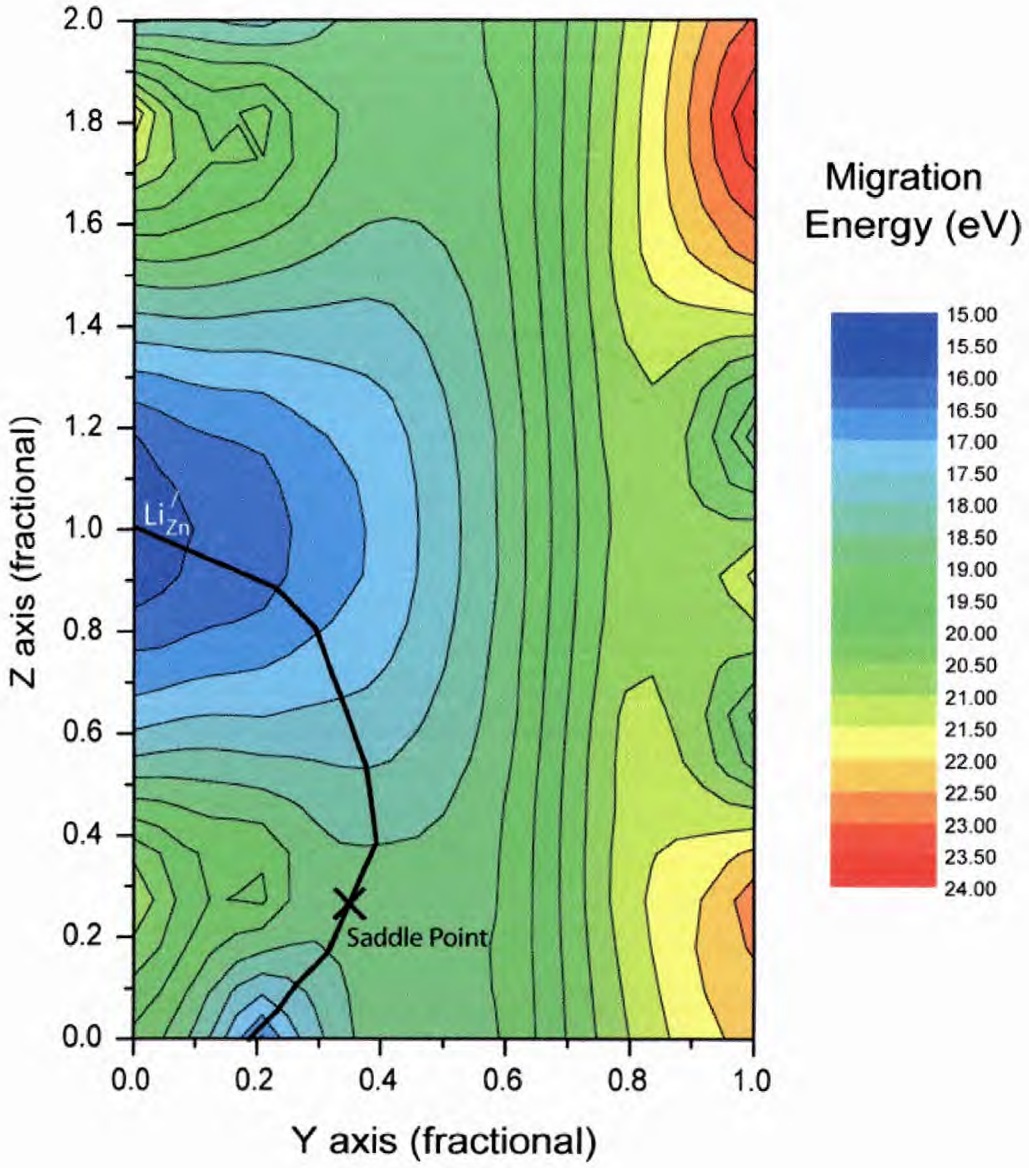


Figure 6.7: Isolated substitutional Li^+ migration in the ac plane. The line indicates the lowest energy pathway.

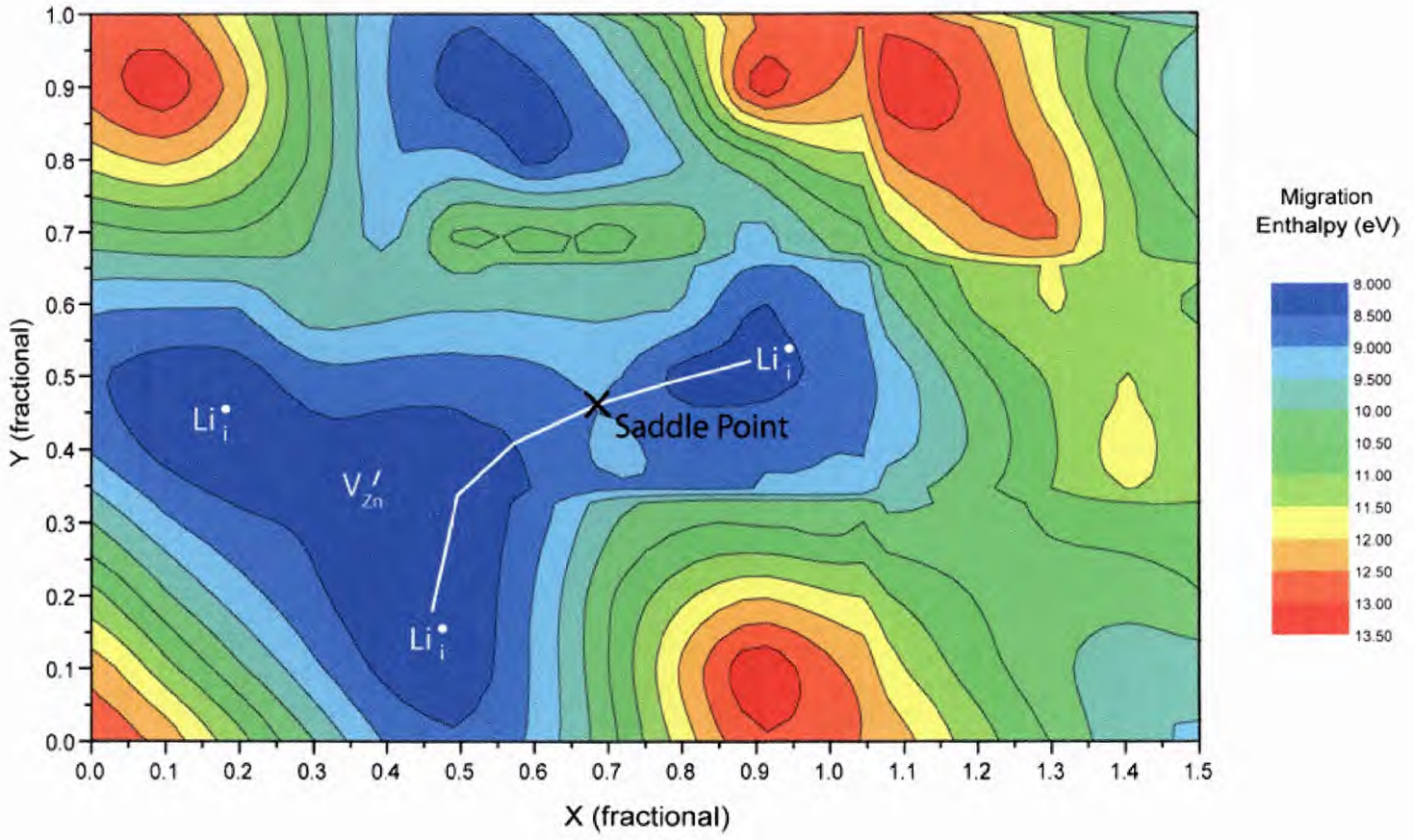


Figure 6.8: Li^+ migration in the ab plane starting from the split defect orientation. The line indicates the lowest energy pathway.

Table 6.5: $\{Li_i^{\bullet} : V_{Zn}'' : Li_i^{\bullet}\}$ cluster energies (eV).

Cluster Neighbour Positions	Relaxation	No Relaxation	Difference
1st	0.73	1.39	0.66
2nd	0.73	1.64	0.91
3rd	1.81	1.85	0.04

6.4 Discussion on the Dielectric Relaxation

Solution energy calculations clearly support the second of Roth's models, i.e. that the dielectric relaxation is governed by lithium interstitial ions. However, the cluster configuration predicted here (Figure 6.3(c)) is quite distinct from the models envisaged by Roth (as shown in Figures 6.3(a) and 6.3(b)). The implications of this to the dielectric relaxation process must now be considered.

First, the way in which this defect cluster couples to an applied field must be investigated. This split lithium cluster is a trimer defect (i.e. +:2-:+) oriented in the [150] direction. As such, if a field is applied parallel to the ab plane, this defect will not couple to the field without reorientation towards the dipole configuration envisaged by Roth (compare Figures 6.3(a) and 6.3(b)). In order to calculate the energies associated with this reorientation, one Li^+ defect is restricted to remain at the substitutional (vacant zinc) site and the Li^+ interstitial is allowed to relax. The calculated energy difference between the two configurations is 0.66 eV (Table 6.5) which is the same as that suggested as the dipole reorientation energy as reanalysed by Nowick [240]. The resulting calculated dipole of the Roth cluster is 7.0×10^{-29} *Cm*. The problem with this model is, however, when no field is present the defect relaxes back to the split orientation with essentially no energy barrier.

When a field is applied in the [001] direction, the split interstitial defect cluster will

couple with the field and form a dipole most readily by the relaxation of both $Li_i^{\bullet}$ defects in a [001] direction. If the field imparts the same energy (i.e. 0.66 eV) to displace the $Li_i^{\bullet}$ ions, a similar dipole of $2.9\text{x}10^{-29}$ Cm is formed. Once again, when the field is removed, the Li^+ ions will relax back to the $\{Li_i^{\bullet} : V_{Zn}'' : Li_i^{\bullet}\}$ tripole defect with no net polarization of the lattice. Thus, reorientation of the equilibrium defect cluster cannot result in a dielectric relaxation of the type observed by Roth [237,238].

In order to investigate the possible role of the equilibrium lithium cluster in the dielectric relaxation response, the energy of the cluster was considered as a function of defect separation. This was facilitated by placing one Li^+ at a substitutional site and the second Li^+ ion at first, then second and finally third neighbour interstitial sites. Table 6.5 shows the formation energy of the cluster constrained (unrelaxed) and after lattice relaxation. It is immediately clear that when the two Li^+ ions are in either 1st or 2nd neighbour positions (see Figure 6.9) and unconstrained, subsequent energy minimization results in a relaxation to the "split-interstitial" defect orientation. Only, in the 3rd neighbour position do they remain apart; i.e. there is an energy barrier against relaxation to the split interstitial configuration. The resulting 3rd neighbour configuration as shown in Figure 6.9 is oriented in the [203] direction and as such has very similar dipole components both in the ab plane and in the [001] direction. However, the existence of symmetry related equivalent orientations of the 3rd neighbour cluster means that in a purely [001] field, a distribution of such defects can together have a net dipole only in the [001] direction (e.g. [203] + $[\bar{2}03]$ and [023] + $[0\bar{2}3]$). Unfortunately, the equivalent holds true for a field applied in the ab plane (e.g. [203] + $[02\bar{3}]$ etc.) so it is also possible to construct a dipole response that is restricted to the ab plane.

On the basis of the above analysis, the split Li^+ interstitial cluster cannot be re-

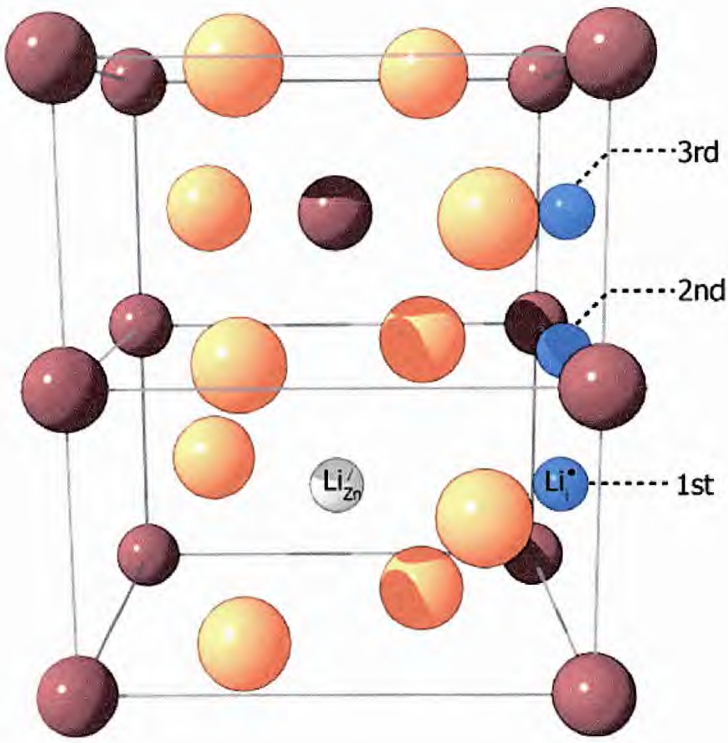


Figure 6.9: The ZnF_2 tetragonal unit cell showing the three different unrelaxed neighbour positions (denoted by the blue spheres) of the Li^+ interstitial defect (1^{st}, 2^{nd}, 3^{rd}) which together with the Li'_{Zn} defect (denoted by the white sphere) will generate the defect cluster $\{Li'_{Zn} : Li_i^{\bullet}\}^x$.

sponsible for the anisotropic dielectric relaxation reported by Roth [237]. However, the earlier solution energy analysis suggests that Roth's material was far from equilibrium. The supersaturated solid solution consisted of essentially immobile substitutional Li^+ ions and charge compensating Li^+ interstitial ions. These later defects are confined to move preferentially in [001] (compare Figures 6.4 and 6.5). Once they encounter a Li^+ substitutional ion they become trapped and form the split Li^+ interstitial cluster. Any untrapped Li^+ interstitial ions will move in [001] subject to an applied field. It is the displacement of these non-equilibrium, residual defects that may conceivably result in a polarization of the crystal. Certainly such a polar-

ization will occur much more strongly in [001] than in the ab plane. Furthermore, the polarization will decay once the temperature is raised to overcome the activation energy barrier. Nevertheless, such defects should eventually become trapped and as such the anisotropic relaxation effects may be subject to a form of thermal cycling fatigue.

Chapter 7

Conclusions

7.1 Crystal Structure Predictions for Perovskites

The results presented in the preceding chapters show a high degree of agreement with experimental work when the situation is limited to where the A and B cation ratio remains stoichiometric, i.e. the perovskite structure is maintained and not permitted to dissociate to form garnet.

When the constituent cation radii are highly disparate, a rhombohedral $R\bar{3}c$ structure is adopted; as the radii become more similar, first an orthorhombic Pnma structure results, followed by a hexagonal $P6_3cm$ structure. Finally as the cation radii become most similar (for the compounds under consideration) a cubic bixbyite is formed. One of the major driving forces for the change in crystal structure is the change in the oxygen sublattice, as at small distortions, the BO_6 octahedra begin to tilt away from their ideal cubic orientations forming rhombohedral and orthorhombic symmetries, and then as the lattice strain increases, the octahedra themselves

are broken, such that for the $P6_3cm$ structure the A and B cation sites are seven and five coordinated respectively.

Structure and defect energies have been predicted for a number of compounds that have not previously been reported. These include a number of compounds within the $AAlO_3$, $ACrO_3$, $AGaO_3$, $AFeO_3$, $AScO_3$ and $AInO_3$ regions.

Changes in the potential model are unable to describe the dissociation of the perovskite to garnets. It is possible that a new potential model is needed, or that subtly different potential sets should be utilised for the garnet and perovskite symmetries (however this in turn would introduce consistency problems).

7.2 Intrinsic Defect Processes in Perovskites: Implications for Radiation Tolerance

The antisite reaction is the dominant intrinsic defect reaction mechanism for the majority of the 3:3 perovskite compounds under consideration. When the constituent cation radii are highly disparate (the $R\bar{3}c$ and the least distorted Pnma structures being dominant) the Schottky reaction is the dominant process. For the $P6_3cm$ compounds, the Schottky reaction energy is higher than the anion Frenkel reaction energy. The cation Frenkel reaction energy is always the highest energy process.

By relating the energies for defect processes to radiation tolerance, predictions of how the radiation tolerance varies across an extensive series of $A^{3+}B^{3+}O_3$ compositions is possible. Disorder on the cation sublattice is a direct effect of irradiation and is a major contributing factor to the retained energy, while disorder on the oxygen

sublattice defines the recovery processes. The combined effect of these processes are therefore necessary to predict the radiation tolerance of the materials. A low energy for the antisite defect process in itself, is insufficient for a radiation tolerant material. Therefore, the combined effect of the defect processes is used to predict the radiation tolerance, which follows the classical perovskite tolerance factor in that tolerance increases $R\bar{3}c < Pnma < P6_3cm < Ia3$.

By comparing the equivalent defects in $A_2B_2O_7$ pyrochlore oxides with previous simulations, the relative tolerance of ABO_3 oxides can be assessed. Significant for the bixbyite forming materials, the oxygen Frenkel energy is similar to the oxygen Frenkel of pyrochlores. For example, on such a basis, none of the perovskites would be expected to exhibit the exceptional radiation tolerance of the zirconate or cerate pyrochlores/fluorites. However, the best perovskites would have a similar tolerance to the intermediate titanate pyrochlores.

Clearly, the low defect formation energies exhibited by the bixbyite oxides are consistent with these materials being approximately as radiation tolerant as the better pyrochlores. It seems logical to assume that this is in part a consequence of the similarity between the bixbyite and fluorite structures [146].

Finally, the equivalence of charge between A^{3+} and B^{3+} cations in the perovskite systems does not aid the tolerance of the perovskites as the difference in ion size and the associated crystallography means that these materials should not be highly radiation tolerant due to the inherent lattice strains introduced upon disorder. Conversely, materials with the bixbyite structure should show considerable tolerance.

7.3 Extrinsic Defect Processes in Perovskites

For the four compositions considered ($GdInO_3$, $GdScO_3$, $LaInO_3$, $LaScO_3$), the lowest energy compensation reaction is the oxygen vacancy mechanism for all divalent solute cation radii. Furthermore, the smallest dopants will substitute on B sites and the largest on A sites. However, the dopant radius at which this change in lattice site preference occurs is a function of both lattice composition and crystallography.

Due to this crystallographic condition for solution, the orthorhombic compound is more sensitive to solution site than the hexagonal materials. This is due to the relative sizes of the A and B lattice sites, which in turn is related to the coordination of those sites. Very small dopants substitute exclusively at the B lattice site in the orthorhombic material, followed by an intermediate stage whereby solution occurs on both lattice cation sites, and finally larger cations substitute only onto the large A site. In the hexagonal materials, most of the dopants substitute onto the B lattice site, with only the largest substituting onto the A lattice site, with no intermediate stage.

A further consequence of this crystallographic variation is that the energy is higher for solution into the orthorhombic $LaScO_3$ than into the three hexagonal compounds ($LaInO_3$, $GdScO_3$ and $GdInO_3$). Therefore, the concentration of oxygen vacancies that would be formed is lower in the $LaScO_3$ than in the other compositions.

7.4 Lithium doped Zinc Fluoride

Solution energy calculations clearly support the case that the dielectric relaxation is governed by lithium interstitial ions. The split lithium interstitial cluster configuration predicted here is, however, quite distinct from models previously put forward. (This is isostructural to the split F^- interstitial ion reported in the intrinsic defect analysis). The cluster consists of two equivalent Li^+ interstitials either side of a vacant zinc site (i.e. $\{Li_i^{\bullet} : V_{Zn}'' : Li_i^{\bullet}\}^X$).

The split Li^+ interstitial cluster cannot be responsible for the anisotropic dielectric relaxation due to its symmetry and inability to couple into a field. However, solution energy analysis suggests that the experimental material was far from equilibrium. The supersaturated solid solution consisted of essentially immobile substitutional Li^+ ions and charge compensating Li^+ interstitial ions. These latter defects are confined to move preferentially in [001]. Any untrapped Li^+ interstitial ions will move in [001] subject to an applied field. It is the displacement of these non-equilibrium, residual defects that may conceivably result in a polarization of the crystal. Certainly such a polarization will occur much more strongly in [001] than in the ab plane. Furthermore, the polarization will decay once the temperature is raised to overcome the activation energy barrier. Nevertheless, such defects should eventually become trapped and as such the anisotropic relaxation effects may be subject to a form of thermal cycling fatigue.

Chapter 8

Further Work

8.1 Simulation Studies

Crystal Structure Predictions

While much has been learnt from the current simulation studies, the crystal structure predictions for the current set of $A^{3+}B^{3+}O_3$ materials should be revisited so that the dissociation of the perovskite to the two garnets can be further investigated. At present, there are limitations in the potential model such that the same consistent set of potentials are unable to predict both the different perovskite phases and the formation of the garnets. A useful tool to overcome this limitation would be quantum mechanical calculations. Initial results for the perovskite materials have been presented here, however a more in depth study should be able to determine more clearly the structural boundaries for crystal structure changes. This will present a significant challenge due to the size of the unit cells; the smallest cell is the rhombo-

hedral ($R\bar{3}c$) perovskite with 16 ions, the next in size is the orthorhombic (Pnma) perovskite with 32 ions, the largest perovskite is the hexagonal ($P6_3cm$) with 48 ions, whilst the garnets are significantly larger than any of these with the smaller having 96 ions per cell and the largest with 256 ions per cell. The size of the unit cells for the hexagonal perovskite and the two garnet phases means that quantum mechanical simulations on these structures are hugely demanding computationally.

The compositional range investigated with pair potentials should be extended to encompass a larger array of compounds ranging from corundum oxides e.g.(Al_2O_3), bixbyite and La_2O_3 structure. A proposed expansion of the ionic radii space is provided in Figure 8.1. This would allow for more significant crystal structure variations to be compared, and in turn aid in the understanding of the inter dependence of crystal structure variation and dominant defect processes. For example, Figure 8.1 shows that the corundum structures are likely to be developed when both the A and B cations are small, outside the scope of the current investigation.

Additionally, new potential parameter sets could be developed to better describe the lattice. Those currently planed are a new breathing shell model in which the radius of the oxygen shell is allowed to alter with respect to the local atomic environment. The breathing shell model is useful as it better describes how the electron density of an ion is deformed as the surrounding atoms squeeze it. It is possible that the breathing shell model may not be sufficiently flexible to describe the wide array of ion environments since this is still a centrosymmetric model. Therefore elliptical distortions to the shell model could also be incorporated, thus allowing the shell to breath and distort.

The free-energy of the system should also be calculated in order to account for the effect of temperature on the lattice. This essentially raises the calculation tem-

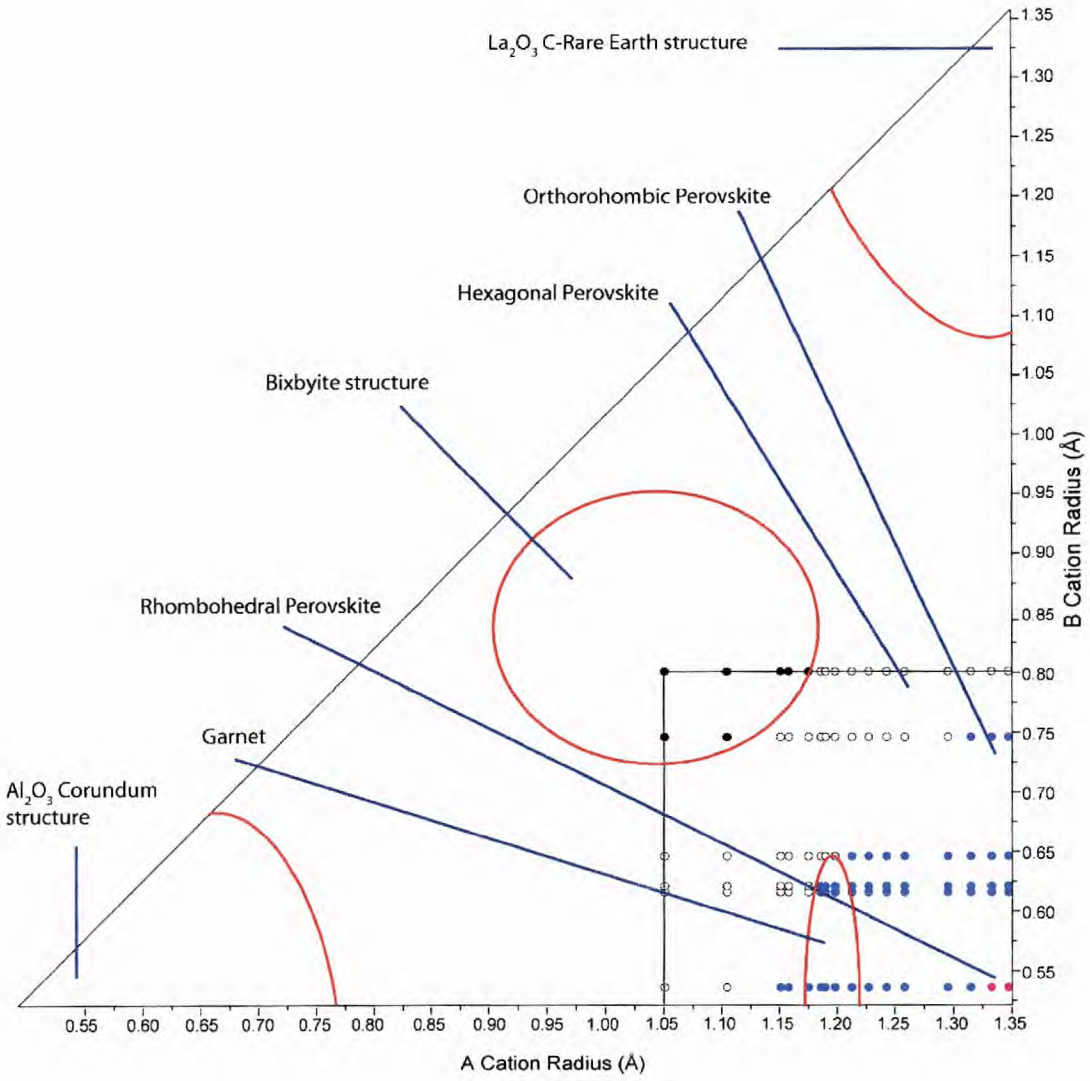


Figure 8.1: Proposed extension to the crystallographic space modelled.

perature from zero kelvin to better compare with the experimental data which is afterall mostly derived from room temperature measurements. Currently the GULP code [88] only calculates the Helmholz free energy, however, the newer SHELL code [246] is able to calculate the Gibbs free energy. The Helmholtz free energy does not contain the pressure-volume (PV) term that is included in the Gibbs free energy, and is therefore only a measure of the internal energy of the system rather

than the enthalpy of the system.

Radiation Tolerance

The effect of defect clusters was considered only briefly in the course of this thesis, however, defect association plays a major role in determining materials properties. Therefore, the way in which the intrinsic defects associate within the perovskite materials should be investigated further. Defect clustering is not only of significance to the radiation tolerance of the materials, it also gives information regarding the behaviour of the majority intrinsic defects and will be an important precursor to further studies of these perovskite materials for many potential applications, from dielectric resonators to SOFCs.

During the storage of radioactive waste, one problem that is encountered is that the defects formed lead to lattice swelling. This in turn leads to micro-cracking which provides fast ion migration pathways and thus leaching of the waste ions into the environment. This effect can be modelled by calculating the defect volumes of both the isolated and defect clusters. These volumes can be determined by two different approaches which should be compared. The first is via the construction of a supercell in which the defect concentrations can be altered. The volume of this cell is then determined and compared to the value of an equivalent perfect lattice cell. The second approach calculates the defect volume by comparing defect calculations conducted under constant volume and constant pressure conditions [247].

Defect migration studies could also be used to investigate defect recovery processes that occur in the perovskites post irradiation damage. These could be carried out either using the static lattice method employed in this thesis for the work on the

dielectric relaxation of lithium doped zinc fluoride, or via a molecular dynamics approach.

Extrinsic Defect Processes

Since the defect of importance for SOFCs is the oxygen vacancy, the clustering of the intrinsic defects is particularly important as this will help develop an understanding of possible trapping mechanisms for the majority charge carriers and a better measure of the defect concentrations.

The doping studies should be expanded to include the substitution of different ions onto both the A and the B lattice sites. This would lead to complex defect association and the interaction energies between defects would then also need to be determined.

The transport of ions through the lattice should be studied with particular attention to the mobility of oxygen anions and oxygen vacancies. It is the conductivity of these species that underpins the SOFC efficiency. This can be achieved using molecular dynamics calculations, however if the timescales that need to be modelled are larger than can normally be handled with standard techniques, accelerated dynamics approaches can be employed [21, 248].

Dielectric Relaxation of ZnF_2

In order to more fully understand the motion of the lithium defect within zinc fluoride, molecular dynamics calculations should be conducted. Such calculations would

be able to more conclusively determine the possible migration paths of these defects. It would also be useful to conduct supercell calculations in which the concentration of the defects can be altered. A further method can be employed which uses a combination of static lattice energy minimization and Monte Carlo procedures [249]. In this combined approach, the energy minimization process identifies the configuration with the lowest lattice energy (i.e. the perfect lattice structure), the Monte Carlo procedure is then used to sample higher energy states for use with a defined thermodynamic analysis. Energy minimization is applied after each random redistribution of defects to obtain the energy corresponding to each new arrangement. This would further the argument that the lithium defects do indeed cluster in zinc fluoride.

Also, to consider the anisotropic dielectric response of the doped ZnF_2 more fully, it would be useful to compare similar doping schemes in related tetragonal fluoride materials such as MgF_2 and NiF_2.

8.2 Experimental Studies

Crystal Structure Predictions

The temperature dependant crystal structure of the $A^{3+}B^{3+}O_3$ compounds should be determined using modern *in situ* X-ray diffraction techniques. Much of the current experimental structural data is inconsistent and dates back to before the 1960s. There are also some regions of the composition field where no data exists to describe ion positions. There are also structural data which would appear erroneous, for example there is evidence that the material is a perovskite, yet investigations

by other authors show that the perovskite phase is unstable at room temperature and that the material should disassociate into two garnet phases. This fundamental research is important because the $A^{3+}B^{3+}O_3$ materials are used in a variety of industrial applications, and in order to make real advances, it is vital to understand the optimisation of properties (an example of this is given in Chapter 3 for the discussion of the dielectric properties).

Data on the evolution of the structures as a function of temperature would enable the illustration of the interconnections between the different crystallographies. This is also important as many of the applications of these perovskite compounds require their operation at elevated temperatures. This work should also look at the structural evolution to very low temperatures so that more consummate comparison can be made with the calculated predictions.

Radiation Tolerance

Further experimental work will be needed to test the prediction that the perovskites are less radiation tolerant than all the fluorite related materials. It would also be interesting to carry out a series of experiments as a function of ion irradiation fluence to see if it is possible to differentiate between the various perovskites and relate this to the predictions made herein.

Extrinsic Defect processes

The next step in determining the suitability of the perovskite compounds for SOFC applications is to measure the oxygen conduction across specimens, both pure and

doped. This would allow for accurate operating temperatures to be calculated and the relative suitability of different materials to be assessed. Some of the current problems being encountered when using certain compositions is that they dissociate partially and form second phases at the grain boundaries. These phases are of the garnet type. Therefore if these phases are formed explicitly there should be no second phase formation, and the compositions can be tested for their conductivity properties.

Dielectric Relaxation of ZnF_2

Current experimental results suggest a significant anisotropy in the dielectric response to an electric field. The simulation studies suggest that this dielectric anisotropy is due to non-equilibrium defects. Such defects should eventually become trapped and as such the anisotropic relaxation effects may be subject to a form of thermal cycling fatigue. An experiment based on this premise may provide one way of further investigating this material. Alternatively, samples could be subjected to higher temperature heat treatments so that they are closer to obtaining an equilibrium defect configuration. In this latter case, a significant anisotropic response would not be expected. In order to compare the response of the ZnF_2 lattice to the electric field, it would be useful to compare equivalent experiments to other tetragonal fluoride materials such as MgF_2 and NiF_2.

Bibliography

[1] S. Vyas, R. W. Grimes, D. J. Binks, and F. Rey. Metastable solid solutions of alumina in magnesia. *Journal of Physics and Chemistry of Solids*, 58(10): 1619–1624, 1997.

[2] C. R. A. Catlow and B. E. F. Fender. Calculations of defect clustering in $Fe_{1-x}O$. *Journal of Physics C: Solid State Physics*, 8:3267–3279, 1975.

[3] F.A. Kroger. The chemistry of imperfect crystals. volume 2, page 82. North-Holland Publishing Company, Ltd., 2nd edition, 1974.

[4] K. E. Sickafus, L. Minervini, R. W. Grimes, J. A. Valdez, M. Ishimaru, F. Li, K. J. McClellan, and T. Hartmann. Radiation tolerance of complex oxides. *Science*, 289(5480):748–751, 2000.

[5] L. Minervini, R. W. Grimes, and K. E. Sickafus. Disorder in pyrochlore oxides. *Journal of the American Ceramic Society*, 83(8):1873–1878, 2000.

[6] J. S. Oliveira, C. G. Bailey, J. B Jones-Oliveira, D. A. Dixon, D. W. Gull, and M. L. Chandler. A computational model for the identification of biochemical pathways in the krebs cycle. *Journal of Computational Biology*, 10(1):57–82, 2003.

[7] R. Chignola and E. Milotti. Numerical simulation of tumor spheroid dynamics. *Physica A-Statistical Mechanics and Its Applications*, 338(1-2):261–266, 2004.

[8] A. T. Brunger and L. M. Rice. In J. H. Kalivas, editor, *Adaptation of Simulated Annealing to Chemical Optimisation Problems*. Elsevier, 1995.

[9] D. Cubero, N. Quirke, and D. F. Coker. Electronic transport in disordered n-alkanes: From fluid methane to amorphous polyethylene. *Journal of Chemical Physics*, 119(5):2669–2679, 2003.

[10] D. Cubero, N. Quirke, and D. F. Coker. Electronic states for excess electrons in polyethylene compared to long-chain alkanes. *Chemical Physics Letters*, 370 (1-2):21–25, 2003.

[11] A. P. Dhanarajan, J. Urban, and R. A. Siegel. A model for a hydrogel-enzyme chemomechanical oscillator. In *Nonlinear Dynamics in Polymeric Systems*, volume 869 of *ACS Symposium Series*, pages 44–57. 2004.

[12] M. A. Glaser, N. A. Clark, E. Garcia, and D. M. Walba. Quantum chemistry based force fields for soft matter. *Spectrochimica Acta Part A-Molecular and Biomolecular Spectroscopy*, 53(8):1325–1346, 1997.

[13] S. S. Patnaik, S. J. Plimpton, R. Pachter, and W. W. Adams. *Liquid Crystals*, 19:213–220, 1995.

[14] C. R. A. Catlow, R. G. Bell, and J. D. Gale. Computer modelling as a technique in materials chemistry. *Journal of Materials Chemistry*, 4(6):781–792, 1994.

[15] H. A. Bethe and N. D. Mermin. A conversation about solid-state physics. *Physics Today*, 57(6):53–56, 2004. 825.

[16] C. R. A. Catlow, J. D. Gale, and R. W. Grimes. Recent computational studies in solid-state chemistry. *Journal of Solid State Chemistry*, 106(1):13–26, 1993.

[17] G. E. Moore. Cramming more components onto integrated circuits. *Electronics*, 38(8), 1965.

[18] C. R. A. Catlow, C. M. Freeman, and R. L. Royle. Recent studies using static simulation techniques. *Physica B & C*, 131(1-3):1–12, 1985.

[19] R. Car and M. Parrinello. Unified approach for molecular dynamics and density-functional theory. *Physics Review Letters*, 55(22):2471–2474, 1985.

[20] Dierk Raabe. *Computational materials science: The simulation of materials, microstructures and properties.* Wiley-VCH, Weinheim, 1^{st} edition.

[21] A. F. Voter. A method for accelerating the molecular dynamics simulation of infrequent events. *Journal of Chemistry and Physics*, 106(11):4665–4677, 1997.

[22] G. Busker, A. Chroneos, R. W. Grimes, and I. W. Chen. Solution mechanisms for dopant oxides in yttria. *Journal of the American Ceramic Society*, 82(6): 1553–1559, 1999.

[23] Abramowski. *Atomistic simulations of the uranium/oxygen system.* PhD thesis, Imperial College of Science Technology and Medicine, 2001.

[24] K. J. W. Atkinson, R. W. Grimes, and S. Owens. Defects and transport in NiF_2. *Solid State Ionics*, 150:443–448, 2002.

[25] C. R. A. Catlow, R. James, W. C. Mackrodt, and R. F. Stewart. Defect energetics in α-Al_2O_3 and rutile TiO_2. *Physical Review B*, 25(2):1006–1026, 1982.

[26] L. Minervini, R. W. Grimes, Y. Tabira, R. L. Withers, and K. E. Sickafus. The oxygen positional parameter in pyrochlores and its dependence on disorder. *Philosophical Magazine A-Physics of Condensed Matter Structure Defects and Mechanical Properties*, 82(1):123–135, 2002.

[27] L. Minervini, M. O. Zacate, and R. W. Grimes. Defect cluster formation in M_2O_3-doped CeO_2. *Solid State Ionics*, 116(3-4):339–349, 1999.

[28] M. Pirzada, R. W. Grimes, L. Minervini, J. F. Maguire, and K. E. Sickafus. Oxygen migration in $A_2B_2O_7$ pyrochlores. *Solid State Ionics*, 140(3-4):201–208, 2001.

[29] D. A. Fletcher, R. F. McMeeking, and D. Parkin. The United Kingdom chemical database service. *Journal of Chemical Information and Computer Sciences*, 36(4):746–749, 1996.

[30] R. D. Shannon. Revised effective ionic radii and systematic studies of interatomic distances in halides and chalcogenides. *Acta Crystallographica*, A32: 751–767, 1976.

[31] M. Born and J.E. Mayer. Zur Gittertheorie der Ionenkristalle. *Zeitschirft fur Physik*, 75:1, 1932.

[32] M. Born and J.E. Mayer. Dispersion and polarizability and the van der Waals potential in the Alkali Halides. *Journal of Chemical Physics*, 1:270, 1933.

[33] J. H. Harding. Computer simulation of defects in ionic solids. *Reports on Progress in Physics*, 53:1403–1466, 1990.

[34] David Jason Binks. *Computer modelling of zinc oxide and related oxide ceramics.* PhD, University of Surrey, 1994.

[35] B. I. Bleaney and Bleaney. B. Electricity and magnetism. page 33. Oxford University Press, 2nd edition, 1968.

[36] M. P. Allen and D. J. Tildesley. *Computer Simulation of Liquids.* Clarendon Press, Oxford, 1987.

[37] P. P. Ewald. Die berechung optischer und electrostatischer gitterpotentiale. *Annalen der Physik*, 64:253–287, 1921.

[38] C. Kittel. *Introduction to Solid State Physics.* John Wiley & Sons, Inc., New York, 1st edition, 1954.

[39] C. Kittel. *Introduction to Solid State Physics.* John Wiley & Sons, Inc., New York, 5th edition, 1976.

[40] Mario P. Tosi. Cohesion of ionic solids in the Born model. *Solid State Physics*, 16:1–120, 1964.

[41] C. R. A. Catlow and M. J. Norgett. Technical Report AERE-M2936, Harwell Laboratory, 1976.

[42] A. F. Kapustinskii. Lattice energy of ionic crystals. *Quarterly Reviews, Chemical Society*, 10(3):283–294, 1956.

[43] J. D. Gale. Empirical potential derivation for ionic materials. *Philosophical Magazine B-Physics of Condensed Matter Statistical Mechanics Electronic Optical and Magnetic Properties*, 73(1):3–19, 1996.

[44] M. Born and A. Landé. *Verhandlungen der Deutschen Physik Gesellschaft*, 21/24:210, 1918.

[45] F. London. Theorie und systematik der molekularkrafte. *Zeitschrift für Physik*, 63:245–279, 1930.

[46] F. London. Properties and applications of molecular forces. *Zeitschrift für Physikalische Chemie (B)*, 11:222–251, 1930.

[47] R. Eisenschitz and F. London. Über das varhältnis der van der waalsschen kräfte zu den homöopolaren bindungskräften. *Zeitschrift für Physik*, 60:491, 1930.

[48] H. Margenau. Surface energy of liquids. *Physical Review*, 38:365–371, 1931.

[49] J. E. Lennard-Jones. On the determination of molecular fields. I. from the variation of the viscosity of a gas with temperature. *Proceedings of the Royal Society of London Series A*, 106(738):441–462, 1924.

[50] J. E. Lennard-Jones. On the determination of molecular fields. II. from the equation of state of a gas. *Proceedings of the Royal Society of London Series A*, 109(738):463–477, 1925.

[51] J. E. Lennard-Jones and A. E. Ingham. On the calculation of certain crystal potential constants, and on the cubic crystal of least potential energy. *Proceedings of the Royal Society of London Series A*, 107(744):636–653, 1925.

[52] P. W. Fowler, P. J. Knowles, and N. C. Pyper. Calculations of 2-body and 3-body dispersion coefficients for ions in crystals. *Molecular Physics*, 56(1): 83–95, 1985.

[53] N. W. Grimes and R. W. Grimes. Dielectric polarizability of ions and the corresponding effective number of electrons. *Journal of Physics-Condensed Matter*, 10(13):3029–3034, 1998.

[54] N. W. Grimes and R. W. Grimes. Analysis of oxide dielectric data and the quantum theory of atomic polarizability. *Journal of Physics-Condensed Matter*, 9(31):6737–6747, 1997.

[55] R. W. Grimes and S. P. Chen. The influence of ion size on the binding of a charge compensating cobalt vacancy to M^{3+} dopant ions in CoO. *Journal of Physics and Chemistry of Solids*, 61(8):1263–1268, 2000.

[56] M. M. Kuklja. Defects in yttrium aluminium perovskite and garnet crystals: Atomistic study. *Journal of Physics-Condensed Matter*, 12(13):2953–2967, 2000.

[57] J. A. Chisholm, D. W. Lewis, and P. D. Bristowe. Classical simulations of the properties of group-III nitrides. *Journal of Physics: Condensed Matter*, 11(22):L235–L239, 1999.

[58] C. R. A. Catlow, editor. *Computer Modelling in Inorganic Crystallography.* Academic Press, Inc., 1st edition, 1997.

[59] B. G. Dick and A. W. Overhauser. Theory of the dielectric constants of alkali halide crystals. *Physical Review*, 112(1):90–103, 1958.

[60] I. D. Faux and A. B. Lidiard. The volumes of formation of Schottky defects in ionic crystals. *Zeitschrift für Naturforschung A*, 26:62–68, 1971.

[61] C. R. A. Catlow and W. C. Mackrodt. Theory of simulation methods for lattice and defect energy calculations in crystals. In C. R. A. Catlow and W. C. Mackrodt, editors, *Computer Simulation of Solids*, Lecture Notes in Physics. Springer-Verlag, Berlin, 1982.

[62] U. Schroder. A new model for lattice dynamics ("breathing shell model"). *Solid State Communications*, 4(7):347–349, 1966.

[63] M. J. L. Sangster. Interionci potentials and force constant models for rocksalt structure crystals II. *Journal of Physics and Chemistry of Solids*, 35:195200, 1974.

[64] J. H. Harding. The practical calculation of interatomic potentials. *Molecular Simulation*, 4(5):255–168, 1990.

[65] S. E. Redfern, R. W. Grimes, and R. D. Rawlings. The hydroxylation of t-ZrO_2 surfaces. *Journal of Materials Chemistry*, 11(2):449–455, 2001.

[66] N. F. Mott and M. J. Littleton. Conduction in polar crystals. I. electrolytic conduction in solid salts. *Transactions of the Faraday Society*, 34:485–499, 1938.

[67] F. Agullo-Lopez, C. R. A. Catlow, and P. D. Townsend. Point defects in materials. pages 341–372. Academic Press Limited, London, 1 edition, 1988.

[68] G. Henkelman and H. Jonsson. Improved tangent estimate in the nudged elastic band method for finding minimum energy paths and saddle points. *Journal of Chemical Physics*, 113(22):9978–9985, 2000.

[69] G. Mills and H. Jonsson. Quantum and thermal effects in H_2 dissociative adsorption: Evaluation of free energy barriers in multidimensional quantum systems. *Physical Review Letters*, 72(7):1124–1127, 1994.

[70] P. W. Atkins and Friedmanm R. S. *Molecular Quantum Mechanics*. Oxford University Press, Oxford, 3rd edition, 1997. 16-20 pp.

[71] M. Born and J. R. Oppenheimer. Zur quantentheorie der molekeln. *Annalen der Physik*, 84:457–484, 1927.

[72] M. D. Segall, P. J. D. Lindan, M. J. Probert, C. J. Pickard, P. J. Hasnip, S. J. Clark, and M. C. Payne. First-principles simulation: ideas, illustrations and the castep code. *Journal of Physics: Condensed Matter*, 14(11):2717–2744, 2002.

[73] J. C. Slater. The self consistent field and the structure of atoms. *Physical Review*, 32(3):339–348, 1928.

[74] D. R. Hartree. The wave mechanics of an atom with a non coulomb field. I. Theory and methods. *Proceedings of the Cambridge Philosophical Society*, 24: 89–110, 1928.

[75] P. W. Atkins and Friedmanm R. S. Molecular quantum mechanics. pages 215–216. Oxford University Press, Oxford, 3rd edition, 1997.

[76] W. Pauli. *General Principles of Quantum Mechanics.* Springer-Verlag, Berlin, 1980.

[77] P. W. Atkins and Friedmanm R. S. Molecular quantum mechanics. pages 301–304. Oxford University Press, Oxford, 3rd edition, 1997.

[78] P. Hohenberg and W. Kohn. Inhomogeneous electron gas. *Physical Review*, 136(3B):B864–B871, 1964.

[79] W. Kohn and L. J. Sham. Self-consistent equations including exchange and correlation effects. *Physical Review*, 140(4A):A1133–A1138, 1965.

[80] L. J. Sham and W. Kohn. One-particle properties of an inhoomogeneous interacting electron gas. *Physical Review*, 145(2):561–567, 1966.

[81] P. W. Atkins and Friedmanm R. S. Molecular quantum mechanics. page 178. Oxford University Press, Oxford, 3rd edition, 1997.

[82] E. Fermi. A statistical method for the determination of some properties of atoms. II. application to the periodic system of the elements. *Zeitschrift für Physik*, 48:73, 1928.

[83] L. H. Thomas. The calculation of atomic fields. *Proceedings of the Cambridge Philosophical Society*, 23:542–548, 1927.

[84] J. C. Slater. A simplification of the hartree-fock method. *Physical Review*, 81 (3):385–390, 1951.

[85] I. H. Lee and R. M. Martin. Applications of the generalized-gradient approximation to atoms, clusters, and solids. *Physical Review B*, 56(12):7197–7205, 1997.

[86] R. O. Jones and O. Gunnarsson. The density functional formalism, its applications and prospects. *Reviews in Modern Physics*, 61:689–746, 1989.

[87] M. Leslie. Technical Report DL/SCI/TM31T, SERC Daresbury Laboratory, 1982.

[88] J. D. Gale. Gulp: A computer program for the symmetry-adapted simulation of solids. *Journal of the Chemical Society, Faraday Transactions*, 93(4):629–637, 1997.

[89] J. D. Gale. Gulp: Technical report. Technical report, Royal Institution of Great Britain, 1994.

[90] M. J. Norgett. A general formulation of the problem of calculating the energies of lattice defects in ionic crystals. Technical Report R.7650 HL74/335, Atomic Energy Research Establishment, Harwell, 1974.

[91] M. J. Norgett. A users guide to HADES. Technical Report R.7015 HL72/550, Atomic Energy Research Estabishment, Harwell, 1972.

[92] E. H. Isaaks and R. M. Srivastava. *Applied geostatistics.* Oxford University Press, New York, 1989.

[93] John C. Davis. *Statistics and data analysis in geology.* John Wiley & Sons, 2nd edition, 1986.

[94] Microcal Software Inc. Origin:version 6, 1999.

[95] M. W. Davidson and G. F. Lofgren. Photomicrography in the geological sciences. *Journal of Geological Education*, 39:403–422, 1991.

[96] N. P. Brandon, S. Skinner, and B. C. H. Steele. Recent advances in materials for fuel cells. *Annual Review of Materials Research*, 33:183–213, 2003.

[97] L. L. Hench, D. E. Clark, and A. B. Harker. Review: Nuclear waste solids. *Journal of Materials Science*, 21:1457–1478, 1986.

[98] W. Piekarczyk, W. Weppner, and A. Rabenau. Dissociation pressure and gibbs energy of formation of $Y_3Fe_5O_{12}$ and $YFeO_3$. *Materials Research Bulletin*, 13: 1077–1083, 1978.

[99] J. L. Garcia-Munoz, J. Rodriguezcarvajal, P. Lacorre, and J. B. Torrance. Neutron-diffraction study of $RNiO_3$ (R = La, Pr, Nd, Sm) - electronically induced structural-changes across the metal- insulator-transition. *Physical Review B-Condensed Matter*, 46(8):4414–4425, 1992.

[100] O. Muller and R. Roy. *The Major Ternary Structural Families.* Crystal Chemistry of Non-Metallic Materials. Springer-Verlag, 1974.

[101] A. M. Glazer. The classification of tilted octahedra in perovskites. *Acta Crystrystallographica*, B28:3384–3392, 1972.

[102] C. J. Howard, B. J. Kennedy, and B. C. Chakoumakos. Neutron powder diffraction study of rhombohedral rare-earth aluminates and the rhombohedral

to cubic phase transition. *Journal of Physics-Condensed Matter*, 12(4):349–365, 2000.

[103] Ralph W. G. Wyckoff. *Crystal structures*, volume 2: Inorganic Compounds RX_n, R_nMX_2, R_nMX_3. John Wiley & Sons, 2nd edition, 1964.

[104] V. M. Goldshmidt. Geochemische verteilungsgesetze der elememte VII. die gesetze der krystallochemie. *Norske Videnskaps - Akademi, Matemtsik - Naturvidenskapelig Klasse I, Skifter, Oslo*, 2, 1926.

[105] Douglas J. du Boulay. *Structure, vibration and electron density in Neodynium-Iron-Boride and some rare-earth perovskite oxides.* PhD thesis, The University of Western Australia, 1996.

[106] A. Munoz, J. A. Alonso, M. J. Martinez-Lope, J. L. Garcia-Munoz, and M. T. Fernandez-Diaz. Magnetic structure evolution of $NdMnO_3$ derived from neutron diffraction data. *Journal of Physics-Condensed Matter*, 12(7):1361–1376, 2000.

[107] L. Vasylechko, L. Akselrud, W. Morgenroth, U. Bismayer, A. Matkovskii, and D. Savytskii. The crystal structure of $NdGaO_3$ at 100K and 293K based on synchrotron data. *Journal of Alloys and Compounds*, 297(1-2):46–52, 2000.

[108] C. J. Howard and B. J. Kennedy. The orthorhombic and rhombohedral phases of $LaGaO_3$ - a neutron powder diffraction study. *Journal of Physics-Condensed Matter*, 11(16):3229–3236, 1999.

[109] T. Hashimoto, N. Tsuzuki, A. Kishi, K. Takagi, K. Tsuda, M. Tanaka, K. Oikawa, T. Kamiyama, K. Yoshida, H. Tagawa, and M. Dokiya. Analysis of crystal structure and phase transition of $LaCrO_3$ by various diffraction measurements. *Solid State Ionics*, 132(3-4):181–188, 2000.

[110] S. Geller and P. Romo. Refinement of the structure of scandium sesquioxide. *Zeitscrift fuer Kristallographie, Kristallgeometrie, Kristallphysik, Kristallchemie*, 124:136–142, 1967.

[111] Greendan J. E., M. Bieringer, J. F. Britten, and D. M. Giaquinta. Synthesis, crystal structure, and unusual magnetic properties of $InMnO_3$. *Journal of Solid State Chemistry*, 116:118–130, 1995.

[112] Robert Ian Hines. *Atomistic simulation and ab-initio studies of polar solids.* Phd, Bristol, 1997.

[113] L. E. Russel, D. L. Harrison, and N. H. Brett. Perovskite-type compounds based on plutonium. *Journal of Nuclear Materials*, 2(4):310–320, 1960.

[114] N. L. Allan, M. J. Dayer, D. T. Kulp, and W. C. Mackrodt. Atomistic lattice simulations of the ternary fluorides AMF_3 (A = Li, Na, K, Rb, Cs; M = Mg, Ca, Sr, Ba). *Journal of Materials Chemistry*, 1(6):1035–1039, 1991.

[115] A. Wold and R. Ward. Perowskite-type oxides of cobalt, chromium and vanadium with some rare earth elements. *Journal of the American Chemical Society*, 76:1029–1030, 1954.

[116] A Ruggiero and R Ferro. Ortogalliti di elementi delle terre rare. *Atti della Accademia Nazionale dei Lincei, Classe di*, 17:48–50, 1954.

[117] M Tanaka, T Shishido, H Horiuchi, N Toyota, D Shindo, and T Fukuda. Structure studies of $CeAlO_3$. *Journal of Alloys and Compounds*, 192:87–89, 1993.

[118] V G Zubkov, I F Berger, Z M Pesina, G V Bazuev, and G P Shveikin. Neutron-diffraction study of the crystal structure of rare earth orthovanadites. *Doklady Akademii Nauk*, 31(6):459–461, 1985.

[119] M. Marezio, J. P. Remeika, and P. D. Dernier. The crystal chemistry of the rare earth orthoferrites. *Acta Crystallographica*, B26:2008–2022, 1970.

[120] T. Mori, K. Aoki, N. Kamegashira, T. Shishido, and T. Fukuda. Crystal structure of $DyMnO_3$. *Materials Letters*, 42(6):387–389, 2000.

[121] S. Geller and V. B. Bala. Crystallographic studies of perovskite-like compounds. II. rare earth aluminates. *Acta Crystallographica*, 9:1019–1025, 1956.

[122] Z A Zaitseva and A L Litvin. Specification of crystal structure of neodymium and gadolinium chromite. *Dop. Ak. Nauk Ukr. RSR Ser. B-Geol. Khim. Biol. Nauki*, pages 994–997, 1978.

[123] P A Amanyan, E V Antipov, V A Antonov, P A Arsen'ev, K S Bagdasarov, A M Kevorkov, L M Kovba, and A V Rakhmatulin. The synthesis and structure of $GdScO_3$. *Zhurual Neorganicheskoi Khimii*, 32:2087–2091, 1987.

[124] N. Sakai, H. Fjellvag, and B. C. Hauback. Structural, magnetic, and thermal properties of $La_{(1-t)}Ca_{(t)}CrO_{(3-\delta)}$. *Journal of Solid State Chemistry*, 121(1): 202–213, 1996.

[125] H. Falcon, A. E. Goeta, G. Punte, and R. E. Carbonio. Crystal structure refinement and stability of $LaFe_xNi_{1-x}O_3$ solid solutions. *Journal of Solid State Chemistry*, 133(2):379–385, 1997.

[126] P. R. Slater, J. T. S. Irvine, T. Ishihara, and Y. Takita. The structure of the oxide ion conductor $La_{0.9}Sr_{0.1}Ga_{0.8}Mg_{0.2}O_{2.85}$ by powder neutron diffraction. *Solid State Ionics*, 107(3-4):319–323, 1998.

[127] J Rodriguez-Carvajal, M Hennion, F Moussa, A H Moudden, L Pinsard, and A Revcolevschi. Neutron-diffraction of the Jahn-Teller transition in stoichio-

metric $LaMnO_3$. *Physical Review B: Condensed Matter*, pages 3192–6192, 1998.

[128] A Wold, R J Arnott, and W J Croft. The reaction of rare earth oxides with a high temperature form of rhodium (III) oxide. *Inorganic Chemistry*, 2:972–974, 1963.

[129] M Eitel and J E Greedan. A high resolution neutron diffraction study of the perovskite $LaTiO_3$. *Journal of Less-Common Metals*, 116:95–104, 1986.

[130] H Seim, H Fjellvag, and B C Hauback. Non-stoichiometric $LaVO_3$. II. powder neutron diffraction study of crystal and magnetic structure for $La_{1-x}VO_3$, 0.00<x<0.10. *Acta Chemica Scandinavica (43,1989-)*, 52:1301–1306, 1998.

[131] H. Taguchi. Spin state of cobalt ion in $Nd(Cr_{1-x}Co_x)O_3$. *Journal of Solid State Chemistry*, 122(2):297–302, 1996.

[132] H. Taguchi. Effect of spin state of Ni^{3+} ions on electrical properties of $Nd(Cr_{1-x}Ni_x)O_3$. *Journal of Solid State Chemistry*, 134(2):382–387, 1997.

[133] H. Taguchi. Relationship between crystal structure and electrical properties of $Nd(Cr_{1-x}Fe_x)O_3$. *Journal of Solid State Chemistry*, 131(1):108–114, 1997.

[134] I. Plaza, E. Palacios, J. Bartolome, S. Rosenkranz, C. Ritter, and A. Furrer. Neutron diffraction study of $NdScO_3$ below 1K - magnetic structure and hyperfine enhanced polarization of Nd. *Physica B*, 234:635–636, 1997.

[135] Z. Jirak, J. Hejtmanek, K. Knizek, and R. Sonntag. Structure and properties of the $Pr_{1-x}K_xMnO_3$ perovskites (x=0-0.15). *Journal of Solid State Chemistry*, 132(1):98–106, 1997.

[136] R. J. Hill and I. Jackson. The thermal-expansion of $ScAlO_3$ - a silicate perovskite analog. *Physics and Chemistry of Minerals*, 17(1):89–96, 1990.

[137] N L Ross. High pressure study of $ScAlO_3$ perovskite. *Physics and Chemistry of Minerals (Germany)*, 25:597–602, 1998.

[138] T Shinike, G Adachi, and J Shiokawa. Crystal structures and some physical properties of perovskite type vanadates of lanthanide-series elements. *Denki Kagaku Oyobi Kogyo Butsuri Kagaku*, 48:258–262, 1980.

[139] A. Bombik, B. Lesniewska, J. Mayer, A. Oles, A. W. Pacyna, and J. Przewoznik. Solid solutions $TbFe_{1-x}Al_xO_3$ ($0 \leq x \leq 1$): Structure and magnetic behaviour. *Journal of Magnetism and Magnetic Materials*, 168(1-2):139–148, 1997.

[140] N L Ross. Distortion of $GdFeO_3$ -type perovskites with pressure: A study of $YAlO_3$ to 5 GPa. *Phase Transitions*, 58:27–41, 1996.

[141] S Geller and E A Wood. Crystallographic studies of perovskite-like compounds. I. rare earth orthoferrites and $YFeO_3$, $YCrO_3$, $YAlO_3$. *Acta Crystallographica*, 9:563–568, 1956.

[142] P. Coppens and M. Eibschutz. Determination of the crystal structure of yttrium orthoferrite and refinement of gadolinium orthoferrite. *Acta Crystallographica*, 19:524–531, 1965.

[143] I. Sosnowska, R. Przenioslo, P. Fischer, and V. A. Murashov. Neutron diffraction studies of the crystal and magnetic structures of $BiFeO_3$ and $Bi_{0.93}La_{0.07}FeO_3$. *Journal of Magnetism and Magnetic Materials*, 160:384–385, 1996.

[144] A. Ruggiero and R. Ferro. Ortoalluminati, ortocromiti e ortoferriti di elementi terre rare. *Gazzetta Chimica Italiana*, 85:892–897, 1955.

[145] G. Thornton, B. C. Tofield, and A. W. Hewat. A neutron-diffraction study of $LaCoO_3$ in the temperature-range 4.2K $\leq$ T $\leq$ 1248K. *Journal of Solid State Chemistry*, 61(3):301–307, 1986.

[146] Kurt E. Sickafus, James A. Valdez, Jesse R. Williams, Robin W. Grimes, and Heather T. Hawkins. Radiation induced amorphization resistance in A_2O_3-BO_2 oxides. *Nuclear Instruments and Methods in Physics Research Section B: Beam Interactions with Materials and Atoms*, 191(1-4):549–558, 2002.

[147] S. Utsunomiya, L. M. Wang, S. Yudintsev, and R. C. Ewing. Ion irradiation induced amorphization and nano crystal formation in garnets. *Journal of Nuclear Materials*, 303:177–187, 2002.

[148] H. Yamane, S. Sakamoto, S. Kubota, and M. Shimada. Preparation and phase transition of $Gd_4(Al_{1-x}Ga_x)_2O_9$ solid solutions. *Journal of Materials Science*, 36:307–311, 2001.

[149] M. S. Lehmann, A. N. Christensen, H. Fjellvag, R. Feidenhans'l, and M. Nielsen. Strcture determination by use of pattern decomposition and the Rietveld method on synchrotron X-ray and neutron powder data; the structures of $Al_2Y_4O_9$ and I_2O_4. *Journal of Applied Crystallography*, 20(2):123–129, 1987.

[150] N. F. Henry and K. Lonsdale, editors. *International Tables for X-Ray Crystallography*, volume 1 of *Symmetry Groups*. The Kynoch Press, 1952.

[151] A. Yoshikawa, Hasegawa. K., J. H. Lee, S. D. Durbin, B. M. Epelbaum, D. H. Yoon, T. Fukuda, and Y. Waku. Phase identification of $Al_2O_3/Re_3Al_5O_{12}$ and

$Al_2O_3/ReAlO_3$ (RE = Sm-Lu, Y) eutectics. *Journal of Crystal Growth*, 218: 67–73, 2000.

[152] S. J. Schneider, R. S. Roth, and J. L. Waring. Phase equilibria in systems involving rare earth oxide. Part II. Solid state reactions in trivalent rare earth oxide systems. *Journal of Research of the National Bureau of Standards*, 65A (4):364, 1961.

[153] S. J. Schneider, R. S. Roth, and J. L. Waring. Phase equilibria in systems involving rare earth oxide. Part II. Solid state reactions in trivalent rare earth oxide systems. *Journal of Research of the National Bureau of Standards*, 65A (4):367, 1961.

[154] S. J. Schneider, R. S. Roth, and J. L. Waring. Phase equilibria in systems involving rare earth oxide. Part II. Solid state reactions in trivalent rare earth oxide systems. *Journal of Research of the National Bureau of Standards*, 65A (4):365, 1961.

[155] S. J. Schneider, R. S. Roth, and J. L. Waring. Phase equilibria in systems involving rare earth oxide. Part II. Solid state reactions in trivalent rare earth oxide systems. *Journal of Research of the National Bureau of Standards*, 65A (4):369, 1961.

[156] S. J. Schneider, R. S. Roth, and J. L. Waring. Phase equilibria in systems involving rare earth oxide. Part II. Solid state reactions in trivalent rare earth oxide systems. *Journal of Research of the National Bureau of Standards*, 65A (4):370, 1961.

[157] S. J. Schneider, R. S. Roth, and J. L. Waring. Phase equilibria in systems involving rare earth oxide. Part II. Solid state reactions in trivalent rare earth

oxide systems. *Journal of Research of the National Bureau of Standards*, 65A (4):372, 1961.

[158] M. Marezio, J. P. Remeika, and P. D. Dernier. High pressure synthesis of $YGaO_3$, $GdGaO_3$ and $YbGaO_3$. *Materials Research Bulletin*, 1:247–255, 1966.

[159] X. Guo and K. Sakurai. Formation of yttrium aluminum perovskite and yttrium aluminum garnet by mechanical solid state reaction. *Japanese Journal of Applied Physics*, 39(3A):1230–1234, 2000.

[160] S.-M. Sim, K. A. Keller, and T.-I. Mah. Phase formation in yttrium aluminium garnet powders synthesized by chemical methods. *Journal of Materials Science*, 35:713–717, 2000.

[161] Z. Jin and Q. Chen. An assesment of the $AlO_{1.5}$-$YO_{1.5}$ system. *Calphad*, 19 (1):69–79, 1995.

[162] X. Guo and K. Sakurai. Crystallization of yttrium aluminum perovskite at around room temperature. *Journal of Materials Science Letters*, 19:451–452, 2000.

[163] S-Y. Cho, I-T. Kim, and K. S. Hong. Microwave dielectric properties and applications of rare-earth aluminates. *Journal of Materials Research*, 14(1): 114–119, 1999.

[164] M. R. Levy, R. W. Grimes, and K. E. Sickafus. Disorder in $A^{3+}B^{3+}O_3$ compounds: implications for radiation tolerance. *Philosophical Magazine*, 84(6): 533–545, 2004.

[165] R. Kagan. *Paradise and Power: America and Europe in the New World Order.* Atlantic Books, London, UK, 2004.

[166] A. M. Beauchesne and J. Boese. Cleaning up america's nuclear weapons compex a govenor's guide. Technical report, National Govenors' Association, Center for Best Practices, Washington, D.C., 2000.

[167] Managing the nuclear legacy: A strategy for action. Technical report, Secretary of State for Trade and Industry, London (UK), 2002.

[168] Accelerating cleanup: Paths to closure. Technical Report DOE/EM-0362, Department of Energy, Office of Environmental Management, Washington, D.C. (United States), June 1998.

[169] B. Holmes and N. Jones. Brace yourself for the end of cheap oil. *Newscientist*, 179(2406):9, 2nd August 2003.

[170] UK close to losing status as oil exporter. *The Times*, 9th July 2004.

[171] United Nations. Report of the conference of the parties on its third session, held at Kyoto from 1 to 11 December 1997. Technical Report FCCC/CP/1997/7/Add.1, Framework Convention on Climate Change, 18 March 1997.

[172] Long-lived legacy: managing high-level and transuranic waste at the doe nuclear weapons complex. Technical Report OTA-BP-O-83, U. S. Congress, Office of Technology Assessment, Washington DC, 1991.

[173] Complex cleanup: The environmental legacy of nuclear weapons production. Technical Report OTA-O-484, U. S. Congress, Office of Technical Assessment, Washington, D. C., 1991.

[174] J. Hogan. How to create and destroy clements in a flash of light. *New Scientist*, (2409), 23 August 2003.

[175] P. D. Wilson. Basic principles. In P. D. Wilson, editor, *The Nuclear Fuel Cycle from Ore to Wastes*. Oxford University Press, Oxford, 1st edition, 1996.

[176] R. C. Ewing, W. J. Weber, and F. W. Clinard Jr. Radiation effects in nuclear waste forms for high-level radioactive waste. *Progress in Nuclear Energy*, 29 (2):63–127, 1995.

[177] Scientific and technical basis for geological disposal of radioactive wastes. Technical Report STI/DOC/010/413, International Atomic Energy Agency, Vienna, Austria, 2003.

[178] R. C. Ewing. Radioactive waste - less geology in the geological disposal of nuclear waste. *Science*, 286(5439):415–, 1999.

[179] The environmental and ethical basis of geological disposal of long-lived radioactive wastes. a collective opinion of the nea radioactive waste management committee. Technical report, Nuclear Energy Agency - OECD, Paris, 1995.

[180] James E. Mielke. Proposed high-level nuclear waste repository: Yucca mountain site characterisation process, May 27 1999.

[181] Richard A. Kerr. Nuclear waste disposal: Science and policy clash at yucca mountain. *Science*, 288(5466):602–, 2000.

[182] Uranium Information Centre Ltd. Synroc: Nuclear issues briefing paper 21, 2001.

[183] A reporter's guide to yucca mountain. Technical report, Environmental Health Center National Safety Council, Washington, D.C. (United States), 2001.

[184] B. D. Begg, E. R. Vance, and S. D. Conradson. The incorporation of plutonium and neptunium in zirconolite and perovskite. *Journal of Alloys and Compounds*, 271-273:221–226, 1998.

[185] G. Leturcq, T. Advocat, K. Hart, G. Berger, J. Lacombe, and A. Bonnetier. Solubility study of Ti,Zr-based ceramics designed to immobilize long-lived radionuclides. *American Mineralogist*, 86(7-8):871–880, 2001.

[186] B. E. Burakov, E. B. Anderson, D. A. Knecht, M. A. Zamoryanskaya, E. E. Strykanova, and M. A. Yagovkina. Synthesis of garnet/perovskite-based ceramic for the immobilization of Pu-residue waste. In *Materials Research Society Scientific basis for Nuclear Waste Management*, volume 556, pages 55–62. Materials Research Society, 1999.

[187] G. R. Lumpkin, K. L. Smith, and M. G. Blackford. Partitioning of uranium and rare-earth elements in synroc - effect of impurities, metal additive, and waste loading. *Journal of Nuclear Materials*, 224(1):31–42, 1995.

[188] K. L. Smith, N. J. Zaluzec, and G. R. Lumpkin. In situ studies of ion irradiated zirconolite, pyrochlore and perovskite. *Journal of Nuclear Materials*, 250(1): 36–52, 1997.

[189] B. P. Uberuaga, R. Smith, A. R. Cleave, F. Monralenti, G. Hnkelman, R. W. Grimes, A. F. Voter, and K. E. Sickafus. Structure and mobility of defects formed from collision cascades in MgO. *Physical Review Letters*, 92 (11):115505, 2004.

[190] A. E. Ringwood, S. E. Kesson, N. G. Ware, W. Hibberson, and A. Major. Immobilisation of high level nuclear reactor wastes in synroc. *Nature*, 278, 1979.

[191] A. E. Ringwood and P. M. Kelly. Immobilization of high-level waste in ceramic waste forms. *Philosophical Transactions of the Royal Society of London Series A-Mathematical Physical and Engineering Sciences*, 319(1545):63–82, 1986.

[192] K. Kuramoto, H. Mitamura, T. Banba, and S. Muraoka. Development of ceramic waste forms for actinide-rich waste - radiation stability of perovskite and phase and chemical stabilities of Zr- and Al-based ceramics. *Progress in Nuclear Energy*, 32(3-4):509–516, 1998.

[193] D. S. Billington and J. H. Crawford Jr. Radiation damage in solids. Princeton University Press, Princeton, New Jersey, US, 1st edition, 1961.

[194] W. H. Zachariasen. The crystal chemistry of monoclinic metaboric acid. *Acta Crystallographica*, 16:385–389, 1963.

[195] J. A. Purton and N. L. Allan. Displacement cascades in $Gd_2Ti_2O_7$ and $Gd_2Zr_2O_7$: a molecular dynamics study. *Journal of Materials Chemistry*, 12 (10):2923–2926, 2002.

[196] M. A. Subramanian, G. Aravamudan, and G. V. Subba Rao. Oxide pyrochlores - a review. *Progress in Solid State Chemistry*, 15:55–143, 1983.

[197] E. Aleshin and R. Roy. Crystal chemistry of pyrochlore. *Journal of the American Ceramic Society*, 45(1):15–25, 1962.

[198] J. Lian, X. T. Zu, K. V. G. Kutty, J. Chen, L. M. Wang, and R. C. Ewing. Ion-irradiation-induced amorphization of $La_2Zr_3O_7$ pyrochlore. *Physical Review B*, 66(5):054108, 2002.

[199] J. Lian, L. Wang, J. Chen, K. Sun, R. C. Ewing, J. Matt Farmer, and L. A. Boatner. The order-disorder transition in ion-irradiated pyrochlore. *Acta Materialia*, 51(5):1493–1502, 2003.

[200] R. W. G. Wyckoff. Chapter IXD: Compounds $R_xM_yX_7$. In *Crystal Structures*, volume 3: Inorganic Compounds $R_X(MX_4)_y$, $R_x(M_nX_p)_y$, Hydrates and Ammoniates. Interscience Publishers, New York, 2^nd edition, 1956.

[201] F.A. Kroger and H. J. Vink. Relations between the concentration of imperfections in crystalline solids. In F. Seitz and D. Turnbull, editors, *Solid State Physics: Advances in research an applications*, volume 3, pages 307–435. Academic Press Inc., New York, 1956.

[202] R. E. Williford and W. J. Weber. Computer simulation of Pu^{3+} and Pu^{4+} substitutions in gadolinium zirconate. *Journal of Nuclear Materials*, 299(2): 140–147, 2001.

[203] M. R. Levy, B. C. H. Steele, and R. W. Grimes. Divalent cation solution in $A^{3+}B^{3+}O_3$ perovksites. *Solid State Ionics*, 175(1-4):349–352, 2004.

[204] Alejandro Eggers Moreno. Fossil-fuel dependency - do oil reserves foretell bleak future. *San Francisco Cronicle*, April 2 2004.

[205] J. M. Gregory, P. Huybrechts, and S. C. B. Raper. Threatened loss of the greenland ice-sheet. *Nature*, 428(6983):616, 2004.

[206] J. T. Emmert, J. M. Picone, J. L. Lean, and S. H. Knowles. Global change in the thermosphere: Compelling evidence of a secular decrease in density. *Journal of Geophysical Research*, 109:A02301, 2004.

[207] D. Knight. Wind is fastest growing power sector. *Inter Press Service*, January 16 2002.

[208] Hydropower: Seting a course for our energy future. Technical Report DOE/GO-102004-1981, U. S. Department of Energy: Energy Efficiency and Renewable Energy, July 2004.

[209] D. Hochschild and A. Hochschild. Big energy v.s solar. *Los Angeles Times*, August 11 2002.

[210] G. Lean. Nuclear power "can't stop climate change". *The Independent*, June 26 2004.

[211] A. Casanova. A consortium approach to commercialized westinghouse solid oxide fuel cell technology. *Journal of Power Sources*, 71:65–70, 1998.

[212] M. Dokiya. SOFC system and technology. *Solid State Ionics*, 152-153:383–392, 2002.

[213] H. Ullmann, N. Trofimenko, F. Tietz, D. Stover, and A. Ahmad-Khanlou. Correlation between thermal expansion and oxide ion transport in mixed conducting perovskite-type oxides for SOFC cathodes. *Solid State Ionics*, 138 (1-2):79–90, 2000.

[214] H. P. He, X. J. Huang, and L. Q. Chen. Sr-doped $LaInO_3$ and its possible application in a single layer SOFC. *Solid State Ionics*, 130(3-4):183–193, 2000.

[215] S. J. Skinner. Recent advances in perovskite-type materials for solid oxide fuel cell cathodes. *International Journal of Inorganic Materials*, 3(2):113–121, 2001.

[216] D. Lybe, W. P. Poulson, and M. Mogensen. Conductivity of A- and B- site doped $LaAlO_3$, $LaGaO_3$, $LaScO_3$ and $LaInO_3$ perovskites. *Solid State Ionics*, 128:91–103, 2000.

[217] J. B. Goodenough. Oxide-ion electrolytes. *Annual Review of Materials Research*, 33:91–128, 2003.

[218] E. P. Murray, T. Tsai, and S. A. Barnett. A direct-methane fuel cell with a ceria-based anode. *Nature*, 400:649–651, 1999.

[219] P. Knauth and H. L. Tuller. Solid-state ionics: Roots, status, and future prospects. *Journal of the American Ceramic Society*, 85(7):1654–1680, 2002.

[220] Stephen J. Skinner. Recent advances in perovskite-type materials for SOFC cathodes. *Fuel Cells Bulletin*, 4(33):6–12, 2001.

[221] S. Kim, Y. L. Yang, R. Christoffersen, and A. J. Jacobson. Oxygen permeation, electrical conductivity and stability of the perovskite oxide $La_{0.2}Sr_{0.8}Cu_{0.4}Co_{0.6}O_{3-x}$. *Solid State Ionics*, 104(1-2):57–65, 1997.

[222] K. J. W. Atkinson, R. W. Grimes, M. R. Levy, Z. L. Coull, and T. English. Accommodation of impurities in α-Al_2O_3, α-Cr_2O_3 and α-Fe_2O_3. *Journal of the European Ceramic Society*, 23:3059–3070, 2003.

[223] T. Ramos and A. Atkinson. Oxygen diffusion and surface exchange in $La_{1-x}Sr_xFe_{0.8}Cr_{0.2}O_{3-\delta}$ (x=0.2, 0.4 and 0.6). *Solid State Ionics*, 170(3-4): 275–286, 2004.

[224] A. J. Jennings and S. J. Skinner. Thermal stability and conduction properties of the $La_xSr_{2-x}FeO_{4+\delta}$ system. *Solid State Ionics*, 152-153:663–667, 2002.

[225] H-K. Lee. Electrochemical characteristics of $La_{1-x}Sr_xMnO_3$ for solid oxide fuel cell. *Materials Chemistry and Physics*, 77(3):639–646, 2003.

[226] M. R. Levy, K. J. W. Atkinson, O. H. Odili, and R. W. Grimes. Dielectric relaxation of lithium doped zinc fluoride. *Physica B*, submitted.

[227] C. R. A. Catlow. The defect properties of anion-excess alkaline-earth fluorides: I. low defect concentrations. *Journal of Physics C: Solid State Physics*, 9:1845–1857, 1976.

[228] C. R. A. Catlow. The defect properties of anion-excess alkaline-earth fluorides: II. intermediate and high dopant concentrations. *Journal of Physics C: Solid State Physics*, 9:1859–1869, 1976.

[229] H. B. Johnson, N. J. Taylor, G. R. Miller, and I. B. Cutler. Electrical and mechanical relaxation in CaF_2 doped with NaF. *Journal of Physics and Chemistry of Solids*, 30:31–42, 1968.

[230] C. R. A. Catlow and M. J. Norgett. Shell model calculations of the energies of formation of point defects in alkaline earth fluorides. *Journal of Physics C: Solid State Physics*, 6:1325–1339, 1973.

[231] A. R. Allnatt and P. S. Yuen. Defect interactions in ionic fluorite structures: II. 2:2:2 clusters in CaF_2 doped with YF_3. *Journal of Physics C: Solid State Physics*, 9:431–437, 1976.

[232] S. Ling and A. S. Nowick. Defects and mass transport in rutile-structured fluorides. I. experiment. *Physical Review B*, 40(5):3266–3277, 1989.

[233] A. N. Cormack, C. R. A. Catlow, and S. Ling. Defects and mass transport in rutile-structured fluorides. II. computer simulation. *Physical Review B*, 40(5): 3278–3284, 1989.

[234] A. S. Nowick. Dielectric and anelastic relaxation of crystals containing point defects. II. *Advances in Physics a quarterly supplement of the Philosophoical Magazine*, 16(61):2–47, 1967.

[235] C. Bucci and R. Fieschi. Ionic thermoconductivity. method for the investigation of polarization in insulators. *Physical Review Letters*, 12(1):16–19, 1964.

[236] C. Bucci and R. Fieschi. Ionic thermocurrents in dielectrics. *Physical Review*, 148(2):816–823, 1966.

[237] T. A. Roth. Dielectric relaxation of ZnF_2:LiF and its crystallographic orientation dependence. *Journal of Applied Physics*, 42(1):246–249, 1971.

[238] T. A. Roth. Dielectric relaxation fo ZnF_2:LiF. *Journal of Applied Physics*, 44 (3):1056–1060, 1973.

[239] O. W. Johnson. One-dimensional diffusion of Li in rutile. *Physical Review*, 136(1A):A284–A290, 1964.

[240] A. S. Nowick. Comments on "Dielectric relaxation of ZnF_2:LiF". *Journal of Applied Physics*, 44(11):5169–5170, 1973.

[241] S. Hart. *South African Journal of Physics*, 1:65, 1978.

[242] J. C. Jamieson and D. S. Rimai. *Bulletin of the American Physical Society*, 22:353, 1977.

[243] D. S. Rimai. Pressure dependence of the elastic moduli of single crystal ZnF_2. *Physical Review B*, 16(5):2200–2204, 1977.

[244] John K. Vassiliou. Pressure and termperature dependence of the static dielectric constants and elastic anomalies of ZnF_2. *Journal of Applied Physics*, 59 (4):1125–1135, 1986.

[245] K. Recker, F. Wallrafen, and K. Dupre. *Naturwissenschaften*, 75:156, 1988.

[246] M. B. Taylor, G. G. Barrera, N. L. Allan, T. H. K. Barron, and W. C. Mackrodt. Shell - a code for lattice dynamics and structure optimisation of ionic crystals. *Computer Physics Communications*, 109:135–243, 1998.

[247] C. R. A. Catlow, J. Cornish, P. W. M. Jacobs, and A. B. Lidiard. The thermodynamics of characteristic defect parameters. *Journal of Physics C: Solid State Physics*, 14:L121–L125, 1981.

[248] A. F. Voter, F. Montalenti, and T. C. Germann. Extending the time scale in atomistic simulation of materials. *Annual Reviews of Materials Research*, 32: 321–346, 2002.

[249] M. O. Zacate and R. W. Grimes. Combined monte-carlo, energy minimisation analysis of Al/Fe disorder in Ca_2FeAlO_5 brownmillerite. *Philosophical Magazine A*, 80(4):797–807, 2000.

Appendix A

Thermodynamics and Normalisation

A.1 Reaction Equilibria

The following derivation is based on that of Kröger and Vink [201]. The laws of thermodynamics state that, at equilibrium, the sum of the thermodynamic potentials of the reactants is equal to the sum of the thermodynamic potential of the products, i.e.

$$\sum_i n_i \mu_i = 0 \tag{A.1}$$

where n_i is the number of atoms of i in the reaction and μ_i is its corresponding thermodynamic potential:

$$\mu_i = h_i - Ts_i \tag{A.2}$$

where h_i and s_i are the partial enthalpy and partial entropy of i. μ_i is also a function of x_i, the concentration of i, and it follows from statistics (providing that the system is closed) that:

$$\mu_i = (\mu_i)_\circ + kTlnx_i \tag{A.3}$$

where $(\mu_i)_\circ$ is the thermodynamic potential of i under standard conditions (273 K). Combining A.3 and A.1;

$$\sum n_i \left((\mu_i)_\circ + kTlnx_i\right) = 0 \tag{A.4}$$

$$\Rightarrow \sum n_i(\mu_i)_\circ + \sum n_i kTlnx_i = 0 \tag{A.5}$$

$$\Rightarrow \sum n_i lnx_i = \frac{-\sum n_i(\mu_i)_\circ}{kT} \tag{A.6}$$

$$\Rightarrow \Pi x_i^{n_i} = \exp\left(\frac{-\sum n_i(\mu_i)_\circ}{kT}\right) \tag{A.7}$$

where $\Pi x_i^{n_i}$ is the product of $x_i^{n_i}$ with different values of i, the values of n_i corresponding to the products is positive, with that corresponding to the reactants is negative. The law of mass action states that this is equal to the equilibrium constant, K;

$$\Pi x_i^{n_i} = K \tag{A.8}$$

Combining A.7, A.8 and A.2;

$$K = \exp\left(\frac{\sum n_i(s_i)_\circ}{kT}\right) \cdot \exp\left(\frac{-\sum n_i(h_i)_\circ}{kT}\right) = C\exp\left(\frac{-\sum n_i(h_i)_\circ}{kT}\right) \tag{A.9}$$

where C is the reaction constant for the process. For a reaction in thermodynamic equilibrium, $\sum n_i(h_i)_\circ$ is the reaction energy. For example, for the Schottky reaction, this is the enthalpy for the total Schottky process.

A.2 Thermodynamic Approximations

The reaction energies presented in this thesis are internal energies. As such they do not account for the entropy or PV (pressure × volume) components in the Gibbs free energy. The reason this approximation does not cause a significant error is that the reaction energies calculated here are used to discuss relative rather than absolute values.

The approximation detailed below is taken from Kröger [3]. If an equilibrium exists between two reactants A and B and two products C and D:

$$aA + bB \rightleftharpoons cC + dD \tag{A.10}$$

The equilibrium condition can then be applied:

$$\frac{[C]^c[D]^d}{[A]^a[B]^b} = K = \exp\left(\frac{-\Delta G}{kT}\right) \tag{A.11}$$

where K is the equilibrium constant for the reaction, ΔG is the Gibbs free energy, k is the Boltzmann constant, T is the temperature kelvin and square brackets indicate a concentration. This relationship can then be expanded using $\Delta G = \Delta H - T\Delta S$ with H being the enthalpy and S being the entropy:

$$K = \exp\left(\frac{-\Delta H}{kT}\right) \cdot \exp\left(\frac{\Delta S}{k}\right) \tag{A.12}$$

If the change in entropy (ΔS) is small, it follows that $\exp\left(\frac{\Delta S}{k}\right) \approx 1$. Hence, the approximation is possible:

$$\frac{[C]^c[D]^d}{[A]^a[B]^b} \approx \exp\left(\frac{-\Delta H}{kT}\right) \tag{A.13}$$

It is therefore possible to assume that $\Delta G \approx \Delta H$ for this type of equilibrium with no external stimulus. This approximation has been used successfully in the past, for example Zacate *et al.* [27].

A.3 Normalisation Factor Worked Examples

A.3.1 Schottky Defect Process

In order to compare different defect reactions, with different numbers of defects, an equivalence must be determined. This equivalence is that the reaction energies are

normalised per defect following the approach detailed below for the worked example of a Schottky process in a perovskite ABO_3.

$$A_A^X + B_B^X + 3O_O^X \rightleftharpoons V_A''' + V_B''' + 3V_O^{\bullet\bullet} + ABO_3 \tag{A.14}$$

Electroneutrality condition:

$$3[V_O^{\bullet\bullet}] = [V_A'''] + [V_B'''] \tag{A.15}$$

Corresponding Equation of State:

$$[V_O^{\bullet\bullet}]^3[V_A'''][V_B'''] = \exp\left(\frac{-\Delta H}{kT}\right) \tag{A.16}$$

For a pure Schottky reaction it also follows that $[V_A'''] = [V_B''']$ so that the electoneutrality condition gives;

$$3[V_O^{\bullet\bullet}] = 2[V_A'''] \tag{A.17}$$

and

$$3[V_O^{\bullet\bullet}] = 2[V_B'''] \tag{A.18}$$

Substituting the neutrality conditions into the equation of state the concentrations of the individual defects can be expressed as,

$$\frac{9}{4}[V_O^{\bullet\bullet}]^5 = \exp\left(\frac{-\Delta H}{kT}\right) \tag{A.19}$$

$$[V_O^{\bullet\bullet}] = \sqrt[5]{\frac{4}{9}} \exp\left(\frac{-\Delta H}{\mathbf{5}kT}\right) \tag{A.20}$$

It can be seen from the above equation that the normalisation factor (in bold) for the Schottky process is 5. The same approach can also be applied to the other defects in the reaction, however, different pre-exponential multipliers will develop as is illustrated by the case for V_A'''.

If we want to solve for the V_A''' defect concentration we can again use the charge neutrality conditions to give;

$$\left(\frac{2}{3}\right)^3 [V_A'''']^5 = \exp\left(\frac{-\Delta H}{kT}\right) \tag{A.21}$$

$$[V_A''''] = \left(\frac{2}{3}\right)^{\frac{3}{5}} \exp\left(\frac{-\Delta H}{\mathbf{5}kT}\right) \tag{A.22}$$

A.3.2 Anion Frenkel disorder and extrinsic defects in ZnF_2

The anion Frenkel reaction in ZnF_2 is;

$$F_F^X \rightleftharpoons F_i' + V_F^{\bullet} \tag{A.23}$$

and the corresponding mass action equation [201] is;

$$\frac{[F_i'][V_F^{\bullet}]}{[F_F^X]} = \exp\left(\frac{-\Delta H_F}{kT}\right) \tag{A.24}$$

where ΔH_F is the total calculated energy for Equation A.23.If this is the dominant reaction then electroneutrality would dictate that;

$$[F_i'] = [V_F^{\bullet}] \tag{A.25}$$

and Equation A.24 can be rewritten to yield;

$$[F_i'] = \exp\left(\frac{-\Delta H_F}{2kT}\right) \tag{A.26}$$

The energy that is of significance in order to determine the F^- ion interstitial concentration (or fluorine vacancy concentration) is therefore $\Delta H_F/2$. The value 2 is the normalization factor for this reaction. An equivalent analysis for extrinsic reactions can also be carried out. For example, assuming Equation 6.8, for Li^+ solution, so that Li^+ interstitial compensation is dominant (Chapter 6), electroneutrality would dictate that;

$$[Li_i^{\bullet}] = [Li'_{Zn}] \tag{A.27}$$

and the mass action equation becomes;

$$[Li'_{Zn}] = \exp\left(\frac{-\Delta H_{sol}}{2kT}\right) \tag{A.28}$$

The energies for the isolated defect reactions reported in this thesis have been normalized. When defect clusters are formed, the component defect positions are spatially correlated. This limits the configurational contribution and alters the mass

action equations so that the normalization factor becomes unity (in the case where all defects are bound into a cluster).

Appendix B

Presentations and Publications

Publications

K.J.W. Atkinson, Robin W. Grimes, Mark R. Levy, Zoe L. Coull, Tim English, *Accommodation of impurities in* α-Al_2O_3, α-Cr_2O_3 *and* α-Fe_2O_3, Journal of the European Ceramic Society, 23 (2003) 3059-3070.

Mark R. Levy, Robin W. Grimes, Kurt E. Sickafus, *Disorder processes in* $A^{3+}B^{3+}O_3$ *compounds: implications for radiation tolerance*, Philosophical Magazine, 84 (2004) 533-545.

Mark R. Levy, Brian C.H. Steel, Robin W. Grimes, *Divalent Cation Solution in* $A^{3+}B^{3+}O_3$ *Perovskites*, Solid State Ionics, 175 (2004) 349-352.

Mark R. Levy, K.J.W. Atkinson, Oneyka H. Odili, Robin W. Grimes, *Dielectric Relaxation of Lithium Doped Zinc Fluoride*, Submitted to: Physica B.

Conference Presentations

Dielectric Constant Prediction Maps for $A^{3+}B^{3+}O_3$ Compositions, 104^{th} Annual Meeting of the American Ceramics Society, Indianapolis, IN., USA, 18^{th} April - 24^{th} April 2004.

Structure Prediction Maps for $A^{3+}B^{3+}O_3$ Compositions, 106^{th} Annual Meeting of the American Ceramics Society, Indianapolis, IN., USA, 18^{th} April - 24^{th} April 2004.

Divalent Cation Solution into a series of $A^{3+}B^{3+}O_3$ Perovskites, Keynote Presentation, 14th International Solid State Ionics Conference, Monterey, CA., USA, 23rd - 27^{th} June 2003.

Composition Defect Maps for $A^{3+}B^{3+}O_3$ Perovskites, 14^{th} International Solid State Ionics Conference, Monterey, CA., USA, 23^{rd} - 27^{th} June 2003.

Composition Defect Maps for $A^{3+}B^{3+}O_3$ Perovskites, Computer Simulations in Advanced Materials, Paris, France, 5^{th} - 6^{th} June 2003.

Composition Defect Maps for $A^{3+}B^{3+}O_3$ Perovskites, 104^{th} Annual Meeting of the American Ceramics Society, St. Louis MO., USA, 29^{th} April - 2^{nd} May 2002.